A SPECTROSCOPIC STUDY OF UNSTABLE SPECIES IN THE GAS PHASE

A Thesis submitted to the
University of Southampton
for the degree of
Doctor of Philosophy

Jonathan Barr

Department of Chemistry
Faculty of Science
University of Southampton
December 2000

UNIVERSITY OF SOUTHAMPTON

ABSTRACT

FACULTY OF SCIENCE

DEPARTMENT OF CHEMISTRY

Doctor of Philosophy

A Spectroscopic Study of Unstable Species in the Gas Phase

by Jonathan Barr

This thesis contains the results of spectroscopic investigations on several unstable gas phase species. Two techniques were used: photoelectron spectroscopy with a synchrotron photon source, and resonance enhanced multiphoton ionization (REMPI) spectroscopy.

Chapter 1 contains an introduction to the photoelectron and REMPI spectroscopic techniques. In Chapter 2 the experimental apparatus used for the study of short lived molecules with photoelectron spectroscopy using synchrotron radiation is described. Chapter 3 outlines the fundamental principles of photoelectron spectroscopy using both fixed and tunable wavelength radiation such as that found at a synchrotron source.
In Chapter 4 photoionization of the OH and OD radicals, produced from the H + NO_2 and D + NO_2 reactions, has been studied in the photon energy region 13.0-17.0 eV. A comparison of vibrationally specific OH and OD CIS spectra, and photoelectron spectra recorded at resonant wavelengths, has allowed a more complete assignment of structure observed in earlier photoionization mass spectrometric measurements. These assignments have been supported by the results of Franck-Condon calculations. Photoelectron spectra recorded for the first bands of OH and OD at resonant photon energies have allowed more extensive vibrational structure to be obtained than has previously been recorded by PES experiments performed with inert gas discharge photon sources.
In Chapter 5 the photoionization behaviour of $O_2(a^1\Delta_g)$ is studied in the photon energy region 12.5-19.0 eV. Suggestions are made for the nature of the highly excited states of O_2 associated with the observed structure in the CIS spectra, based on available ionization energies and spectroscopic constants of known ionic states accessible from $O_2(a^1\Delta_g)$.

In Chapter 6 the experimental apparatus used in the REMPI spectroscopic studies of Ar·NO, Kr·NO and $(CO)_2$ is described. Chapter 7 contains the details of the theoretical models used to interpret the (2+1) REMPI spectra of rare gas-NO (Rg·NO) complexes. In Chapter 8 the results of REMPI studies on the Ar·NO and Kr·NO van der Waals complexes are presented. For both complexes significant deviation from a T-shaped structure is found in their excited states, although it was not possible to determine the absolute position of the rare gas atom within experimental uncertainty. From the REMPI spectra dissociation energies of 582 and 803 cm^{-1} were derived for the $\tilde{E}^2\Sigma^+$ states of Ar·NO and Kr·NO respectively. Chapter 9 describes the results of preliminary REMPI studies on $(CO)_2$.

Chapter 10 describes a statistical technique for determining the number of ions contained in an ion trap mass spectrometer

In Chapter 11 conclusions are drawn from the work presented in this thesis and suggestions for further work are made.

MEMORANDUM

This thesis is an account of original research performed by the author in the Chemistry Department, University of Southampton, between October 1997 and September 2000. Where findings of other work have been used, due reference has been given.

ACKNOWLEDGEMENTS

The University of Southampton is acknowledged for the award of a studentship, which was funded by the Ministry of Defence. Additionally, I would like to acknowledge the role of my supervisor, Professor John Dyke, for his support and advice throughout the course of my PhD studies. Dr Tim Wright and Dr Stuart Gamblin also figured prominently in the laser and photoelectron spectroscopy sections of this work respectively.

Of the many helpful people at the Daresbury synchrotron source, without whom this work would not be possible, I would like to thank Dr John West who is able to combine the role of world scientific leader and comprehensible teacher with ease. He was always available, usually at unsociable times, for us to tap his vast knowledge of all things synchrotron and beyond.

At all stages of this work I was very grateful for the help and advice of Dr Alan Morris who it seemed to me had almost magical powers in solving the numerous problems that occurred in the laboratory.
The Chemistry Department at Southampton is blessed with excellent workshop and glassblowing facilities whose staff could not be more helpful. Much of the work in this thesis would not have been impossible without their help.

Finally I would like to thank the other members of the PES group in Southampton, Dr Ed Lee, Dr Alberto Defanis, Levi Beeching, Nicole Hooper and Paul Mack who together with other members of the Chemistry Department helped make my stay in Southampton all the more enjoyable.

Table Of Contents

CHAPTER 4- STUDY OF THE OH AND OD RADICALS WITH PHOTOELECTRON SPECTROSCOPY USING SYNCHROTRON RADIATION

CHAPTER 5: A STUDY OF $O_2(A^1\Delta_G)$ WITH PHOTOELETRON SPECTROSCOPY USING SYNCHROTRON RADIATION

CHAPTER 6: EXPERIMENTAL APPARATUS FOR REMPI SPECTROSCOPIC STUDIES OF VAN DER WAALS COMPLEXES 110

CHAPTER 7 THEORETICAL METHODS USED TO INTERPRET (2+1) REMPI SPECTRA OF 'RARE-GAS'-NO COMPLEXES

Chapter 1: Introduction

The work described in this thesis aims to study unstable species in the gas phase using spectroscopic techniques. Unstable species, including complexes, clusters and radicals are currently receiving a great deal of attention from the chemistry community as a result of recent developments in experimental and theoretical methods. This work is especially relevant to atmospheric and combustion chemistry where extreme conditions often give rise to significant concentrations of unstable species.

The first part of this thesis (Chapters 2-5) is concerned with the study of the photoionization behaviour of two species, OH and O_2 ($a^1\Delta_g$), which play key roles in atmospheric and combustion processes. The experimental and theoretical techniques used to study these molecules are described in Chapters 2 and 3 respectively, whilst some background to their atmospheric relevance is described at the beginning of Chapters 4 and 5. An introduction to the photoelectron spectroscopy of short-lived molecules using synchrotron radiation is provided below (1.1).

The NO and CO complexes studied in the second part of this thesis (Chapters 6 to 9) were studied using Resonance Enhanced Multiphoton Ionization Specroscopy (REMPI). The experimental and theoretical methods used for this work are detailed in Chapters 6 and 7, whilst a short introduction to the REMPI technique is provided below (1.2.2). Some background to the NO and CO complexes is also given in this Chapter (1.2.1).

1.1 Photoelectron spectroscopy of short-lived molecules using synchrotron radiation

The study of a reactive intermediate with photoelectron spectroscopy (PES) using monochromatized synchrotron radiation (see chapter 2) should allow more information to be obtained on the molecular ionic states produced and the associated photoionization processes[1,2,3] than a PES study with a low pressure discharge of an inert gas as the photon source.[4,5,6,7]

In particular

(i) a study of the relative band intensities in the valence photoelectron spectrum of a small molecule as a function of the ionizing photon energy can provide valuable information to assist in band assignment,

(ii) the inner-valence region of the molecule under study can be probed and it is in this region where a complete breakdown of the one-electron ionization model often occurs,

(iii) measurement of photoelectron angular distributions at fixed photon energy allows information on photoionization dynamics to be obtained, and

(iv) an autoionization resonance (see Chapter 3), once identified, can give rise to extra structure over that observed in a photoelectron spectrum recorded off resonance.[8,9,10,11,12] This effect was first observed by Price[13] for the oxygen molecule where the neon discharge resonance lines coincided with a resonance in O_2; the resulting photoelectron spectrum showed considerably more vibrational structure than one taken using the helium discharge line.

It was feature (iv) which initially attracted the Southampton PES group to use synchrotron radiation because in a number of previous investigations some of the valence photoelectron bands of the reactive species studied, when recorded with a HeI (21.22 eV) photon source, showed an intense adiabatic component with very little intensity in other vibrational components. Such an observation for the first photoelectron band of a short-lived molecule is particularly disappointing, since measurement of the vibrational level separations in the ground ionic state is usually one of the main objectives of the experiment.[14,15]

In order to achieve the aim of feature (i) the constant ionic state (CIS) technique is used, in which the photoelectron spectrometer is set on a particular ionic vibrational level known to belong to the species of interest, and the exciting wavelength is then scanned in synchronism with the electron spectrometer voltage (which establishes the kinetic energy at which electrons are detected- See Chapter 2). In this way a relative partial ionization cross section of the molecule is obtained, and new structure in the continuum is observed. In fact,

very little is known about the ionization continua of short-lived molecules and this method is an ideal way of obtaining such information.

Feature (iii) requires the polarization properties of the SR source, for which the principal component of the E-vector is horizontal, to measure angular distribution parameters. This facility can be important in identifying the ionic symmetries associated with new structure observed in the photoelectron spectra, as well as being a powerful method of showing the presence of weak underlying structure in the photoionization continuum. There is no such work described in this thesis, although the Southampton PES group has recently completed a successful study on the angle resolved photoelectron spectroscopy of $O_2(a^1\Delta_g)$[16].

The relative lack of synchrotron studies of reactive intermediates compared to those using a laboratory discharge source[4,5,6,7] is in part because the molecules to be studied are reactive and corrosive and the sources used do not interface well with the ultra-high vacuum (UHV) systems essential on modern synchrotron radiation (SR) sources, which are based on electron storage rings. Not only is contamination damaging to the strorage ring, the main impact being on beam lifetime, but it has an even worse effect on beam line optical components. Rapid deterioration of the efficiency of the reflecting surfaces occurs, and in extreme cases the light output can deteriorate by a factor of 100 over a period of a few days.[3] To overcome this the optical systems are kept in vacuum systems where the pressure is 10^{-9} mbar or better, and, more importantly, the identity of the residual gases in the vacuum system is established using mass spectrometry. In particular, the presence of hydrocarbons can be detected in this way, and steps can be taken, such as glow discharge and bake-out, to remove them. The aim is a partial pressure of such contaminants in the region of 10^{-13} mbar. The other main reason that short-lived molecules are rarely studied on SR sources is because the methods of preparation can be complex and their development has required extensive laboratory work which is not routinely transferable to a SR source environment, particularly where RF heating is required, or fluorine abstraction is to be used.

Two short-lived molecules, CS and SO, were studied previous to this work with photoelectron spectroscopy using synchrotron radiation[17,18] . Prominent spectral features were observed in the photoionization continuua of SO ($X^3\Sigma^-$) and CS ($X^1\Sigma^+$) using the CIS method to reveal the presence of many excited Rydberg states which are parts of series converging to limits of the excited ion. Furthermore, by focussing on resonant regions,

photoelectron spectra were obtained with extended vibrational progressions, and with the aid of Franck-Condon calculations (see Chapter 3) these assisted with the identification of the observed structure. The extended vibrational structure also allowed values of ω_e^+ and $\omega_e x_e^+$ to be better determined than the corresponding values obtained from the off-resonant spectra; as compared with the more presise constants obtained from ionic emission spectroscopy[19]. This demonstrated that a resonant photoelectron spectrum can be used to provide reliable ionic state vibrational constants for states which exhibit very little vibrational structure in an off-resonant spectrum, e.g., a HeI (see Chapter 2) photoelectron spectrum.

1.2 Resonance Enhanced Multiphoton Ionization (REMPI) Spectroscopy of Rare Gas-NO Complexes

1.2.1 NO Complexes

Almost thirty-five years ago, Narcisi and Bailey used a rocket-borne spectrometer to measure the positive ion composition of the low to mid-latitudes of the D-region of the Earth's ionosphere[20]. Prior to these measurements, it had been reported that the principal source of positive ions throughout this region of the atmosphere (at altitudes of 65-90 km) is ionization of nitric oxide by solar Lyman-α radiation[21]. This conclusion has since been confirmed by several other workers[22,23,24,25]. It was discovered by Narcisi and Bailey, however, that at altitudes below ≈82 km in the D-region of the ionosphere, the dominant positive ion species are hydrated hydronium complexes of the form, $(H_2O)_n \cdot H_3O^+$, where n is an integer[20]. The apparent contradiction in the observations that ionization of NO is the primary source of ions in the lower mesosphere, but that hydrated hydronium ions are the dominant positive ion species below 82 km, can be resolved if a reaction scheme exists by which nitric oxide ions, NO^+, may be efficiently converted into hydrated hydronium complexes[23,24,25,26].

It is widely believed that the formation of $(H_2O)_n \cdot H_3O^+$ in the lower regions of the mesosphere relies on the hydration of NO^+, with the ion-molecule complex, $H_2O \cdot NO^+$, being a vital intermediate in the generation of hydrated hydronium species[27,28,29]. The $H_2O \cdot NO^+$ complex may be formed by the direct reaction of NO^+ and H_2O in the presence of a third-body, but although laboratory based measurements using stationary and flowing afterglow techniques have shown that this reaction is rapid[30,31], in the atmospheric region of

interest the concentration of water is low. There is a relatively large partial pressure of nitrogen and carbon dioxide[32], however, and it is more probable that free NO^+ would initially react with either of these two species[33,34,35]. It has been therefore proposed that the dominant mechanism for generating $H_2O{\cdot}NO^+$ in the lower mesosphere does not involve the direct association of NO^+ with H_2O, but instead consists of a series of ion-molecule reactions relying on the formation and subsequent reactions of $N_2{\cdot}NO^+$ and $CO_2{\cdot}NO^+$ [23,33,35,36,37]. The important ion-molecule reactions in this scheme may be summarized as follows, where X and Y=H_2O, N_2 or CO_2 and M is a third body:

$$NO^+ + X + M \rightarrow X \cdot NO^+ + M \qquad \textbf{Association/Dissociation Reaction}$$

$$X \cdot NO^+ + Y \rightarrow Y \cdot NO^+ + X \qquad \textbf{Switching Reaction}$$

The ion-molecule chemistry of NO^+ and hydrated hydronium complexes is also important in ion-mobility spectrometry (IMS)[38]. This form of mass spectrometry operates at atmospheric pressure, and the technique relies on measurement of the products of ion-molecule reactions occurring in gases at thermal equilibrium. The complexes, $H_2O{\cdot}NO^+$, $N_2{\cdot}NO^+$ and $(H_2O)_n{\cdot}H_3O^+$ have all been detected in IMS systems[39] and it is plausible that the reaction scheme used to describe the chemistry of the D-region of the ionosphere may also be relevant to the chemistry of ion-mobility systems.

As part of the overall aim to understand better the mechanism by which the $X{\cdot}NO^+$ complexes of atmospheric significance (where X=H_2O, CO_2 and N_2) are converted to hydrated hydronium complexes, it is of fundamental interest to investigate the ion-molecule interactions which exist in these species. In order to describe fully the strength of the intermolecular interaction in these complexes it is necessary to consider both the dissociation energy of the complexes, D_0^+, and the thermodynamic stability of each complex. The entropic factors involved in the thermodynamic stability may be evaluated if the geometry and fundamental frequencies of the vibrational modes of the complex are known. The dissociation energy of a given $X{\cdot}NO^+$ complex (where X=H_2O, CO_2, N_2) may be calculated from equation (1.1) if the adiabatic ionization energies of the complex, $IE_{X{\cdot}NO}$, and free NO, IE_{NO}, are known together with the dissociation energy of the neutral complex, D_0.

$$D_0^+ = D_0 + IE_{X\cdot NO} - IE_{NO} \qquad \ldots(1.1)$$

It has been demonstrated previously that the ionization energies and ionic vibrational frequencies of nitric oxide and NO complexes may be precisely measured using the combined techniques of multiphoton ionization (MPI) and zero kinetic energy pulsed field ionization (ZEKE-PFI) spectroscopy[40,41,42,43]. Usually, the ZEKE technique involves exciting to high lying Rydberg states which are just below an ionization threshold through an intermediate electronic state, in a multi-photon process. It is usually necessary to characterise the intermediate electronic state in order to provide a complete interpretation of the ZEKE spectra.

Recently, a study of the $\tilde{A}^2\Sigma^+$ state of Ar·NO using REMPI spectroscopy was used to aid the analysis of the ZEKE spectrum of $Ar\cdot NO^+$.[43] The work in this thesis involves the characterization of the $\tilde{E}^2\Sigma^+$ states of rare gas-NO complexes using REMPI spectroscopy. Subsequently, it should be possible to probe more of the $Rg\cdot NO^+$ potential energy surface as a consequence of the different Franck-Condon factors that exist between the $\tilde{E}^2\Sigma^+$ state and the ground ($\tilde{X}^1\Sigma^+$) state of $Ar\cdot NO^+$, compared to those that exist between the $\tilde{A}^2\Sigma^+$ neutral state and the ground ionic state. This fundamental work on the Rg·NO systems should be of great assistance in the corresponding future investigations of the atmospherically relevant $X\cdot NO^+$ systems ($X=N_2$, H_2O, CO_2).

1.2.2 Resonance Enhanced Multiphoton Ionization (REMPI) Spectroscopy

The technique of REMPI spectroscopy is based on the fact that in the presence of sufficiently intense radiation, a molecule, M, in its ground electronic state may absorb a number of photons, generating the ion, M^+, and a photoelectron, e^-.[44,45] The probability of a multiphoton process occurring is greatly increased if the energy of a single photon, or number of photons, is equal to the energy of a transition between the ground electronic state and a real, electronically excited state of the molecule, M*; in this situation, the ionization is described as resonantly enhanced. The general description of a resonantly enhanced multiphoton ionization process where monochromatic radiation is employed may be written as follows:

$$M \xrightarrow{nh\nu} M^* \xrightarrow{mh\nu} M^+ + e^- \qquad \ldots(1.2)$$

In the situation where only one laser is used, the multiphoton ionization process is termed one-colour. Equation (1.2) describes a one-colour (n+m) REMPI process: the electronically excited state, M*, is resonant at the energy of n-photons, and after the population of the excited neutral state, absorption of a further m-photons is required to generate the ion, M^+. It is not necessary for the excitation and ionizing photons to be of the same frequency; ionization may occur *via* a two-colour (n+m′) REMPI process, which may be described as follows, where the frequencies, ν_1 and ν_2 are not equal:

$$M \xrightarrow{nh\nu_1} M^* \xrightarrow{mh\nu_2} M^+ + e^- \qquad \ldots(1.3)$$

Coherent n-photon transitions from the ground electronic state to the resonant intermediate state, M*, proceed *via* virtual states (see 7.2.2) if n is greater than one. Schematic representations of one-colour (1+1) and (2+1) REMPI processes are presented in Figure 1.1.

The cross-sections for multiphoton excitations are small[46] and it is therefore necessary to use a high powered radiation source, such as a laser, in order to generate a radiation field sufficiently intense to observe MPI processes. Considering an (n+m) or (n+m′) REMPI process, the excitation probability, P, for a resonant n-photon transition is given by the following[47]:

$$P = \int \sigma_n I^n dt \qquad \ldots(1.4)$$

where σ_n represents the cross-section for an n-photon absorption and I denotes the radiation intensity. Values of P calculated assuming typical values[46] of σ_n and I are presented in Table 1.1.

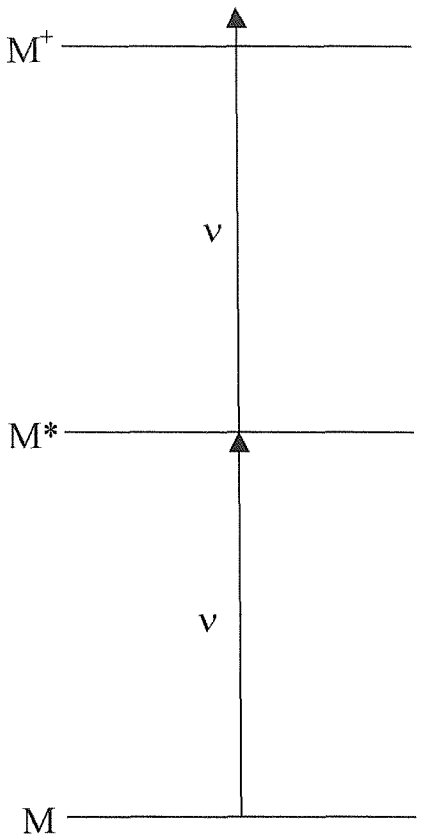

(a) (1+1) REMPI Excitation

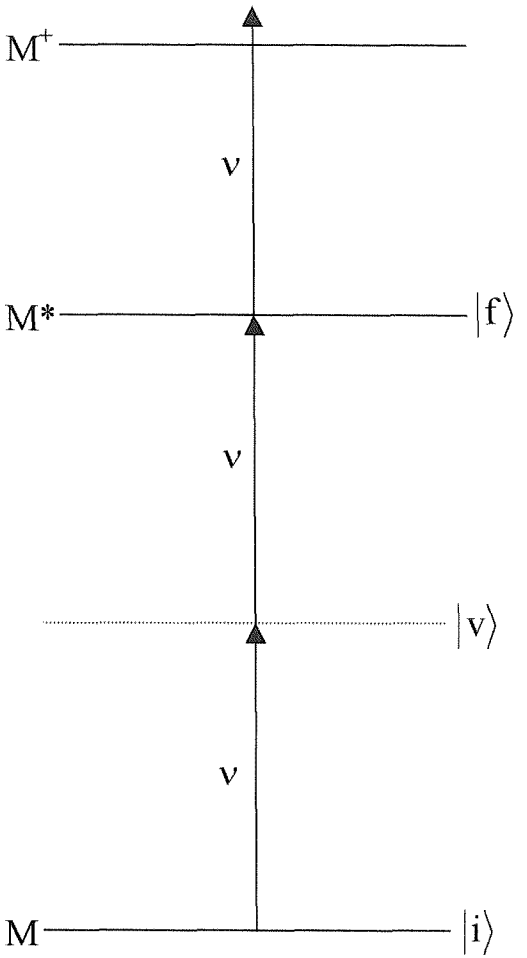

(b) (2+1) REMPI Excitation

Figure 1.1: Schematic Representations of (1+1) and (2+1) REMPI Excitation Schemes
Note $|i\rangle$ and $|f\rangle$ denote real states; $|v\rangle$ denotes a virtual state.

n	σ_n	P
1	10^{-17} cm^2	0.1
2	10^{-50} cm^4s	10^{-10}
3	10^{-84} cm^6s^2	10^{-20}

Table 1.1: Typical excitation probabilities for resonant n-photon transitions. P is calculated assuming a photon intensity, I, of 10^{24} photons $cm^{-2}s^{-1}$, and a pulse width of 10ns.

The general technique of resonance enhanced multiphoton ionization may be used to study the properties of the resonant intermediate state, M*. In a one-colour experiment, where a number of molecules, M, are irradiated by monochromatic radiation, the yield of ions generated as a function of laser wavelength may be measured in order to record an (n+m) REMPI spectrum. Whenever the photon energy, nhν, is resonant with the energy of a transition between the ground electronic state and a rovibrational level in the excited electronic state, if the transition moment and laser intensity are sufficiently strong, an enhancement of the ion signal will be observed. In the situation where MPI experiments are performed on a gaseous mixture, consisting of different molecules of different masses, different ions will be formed through various MPI processes. The (n+m) REMPI spectrum of a particular species may be recorded, however, by employing some form of mass analysis to separate the various ion masses enabling the ion yield at a given mass to be selectively measured as a function of laser wavelength.

1.3 Summary

The aim of this work was to study the structure and bonding of unstable species in the gas phase using two techniques, photoelectron spectroscopy with synchrotron radiation and laser multiphoton ionization . This has been achieved by studying the structure and bonding of the transient molecules OH and $O_2(a^1\Delta_g)$, and also van der Waals complexes of NO with

a rare gas atom. The photoelectron spectroscopic studies of OH and $O_2(a^1\Delta_g)$ described in Chapters 2-5 utilise the tunability of a synchrotron source in order to observe superexcited states which provide new insight on the photoionization behaviour of these species. The complexes of rare gas atoms (Ar and Kr) with NO are studied using the REMPI technique (Chapters 6-8); the mass selective nature of this technique is particularly suited for use with a supersonic expansion where a mixture of species are often formed. Analysis of the REMPI spectra allows information concerning the structure and bonding in electronically excited states of the complexes to be derived. A preliminary REMPI investigation of $(CO)_2$ is described in Chapter 9. Finally, in Chapter 10 a statistical method for the determination of the number of ions in a quadrupole ion trap mass spectrometer is described.

In Chapter 11, the significant conclusions drawn from each aspect of the work presented in this thesis are summarised, and suggestions for continuing and extending the studies are proposed.

1.4 References

1. J. B. West, in *Applications of Synchrotron Radiation,* edited by C. R. A. Catlow and G. N. Greaves (Blackie and Son, Glasgow, 1990).

2. J. B. West, in *Vacuum ultraviolet Photoionization and Photodissociation of Molecular Clusters,* edited by C. Y. Ng (World Scientific, Singapore, 1991)

3. I. Nenner and J. A. Beswick, in *Handbook on Synchrotron Radiation,* Vol. II. Edited by G. V. Marr (Elsevier, Amsterdam, 1987).

4. J. M. Dyke, L. Golob, N. Jonathan, A. Morris and M. Okuda, *J. Chem.Soc.Faraday Trans.* **270**, 1818 (1974).

5. J. M. Dyke, V. Butcher, M. C. R. Cockett, M. Feher, A. Ellis, A. Morris, and M. H. Zamanpour, *Philos. Trans. R. Soc. London. Sect. A.* **324**, 197 (1988).

6. J. M. Dyke, A. Morris, and N. Jonathan, *Int. Rev. Phys. Chem.* **2**, 3 (1982).

7. J. Baker, M. Barnes, M. C. R. Cockett, J. M. Dyke, A. M. Ellis, E. P. F. Lee A. Morris and H. Zamanpour, *J. Electron. Spectrosc, Relat. Phenom.* **51**, 487 (1990).

8. D. M. P. Holland, J. B. West, and M. A. Hayes, *Chem. Phys.* **148**, 241 (1990).

9. K. Codling, A. C. Parr, D. L. Ederer, R. Stockbauer, J. B. West, B. E. Cole, and J. L. Dehmer, *J. Phys. B.* **14**, 657 (1981).

10. P. Natalis, J. E. Collin, J. Delwiche, G. Caprace and M. J.Hubin, *J. Elec. Spec. Rel. Phenom.* **17**, 205 (1979).

11. J. A. R. Samson. *Phys. Rep.* **28c**, 303 (1976).

12. T. Reddish, A. A. Cafolla, and J. Comer, *Chem. Phys.* **130**, 149 (1988).

13. W. C. Price, *Molecular Spectroscopy,* edited by P. Hepple (London: Institute of Petroleum).

14. J. M. Dyke, *J. Chem. Soc. Faraday Trans. 2* **83**, 67 (1987).

15. M. C. R. Cockett, J. M. Dyke, and H. Zamanpour, in *Vacuum Ultraviolet Photoionization of Molecules and Clusters,* edited by C. Y. Ng (World Scientific, Singapore 1991).

16. L. Beeching, A. DeFanis, J. M. Dyke, S. D. Gamblin, N. Hooper and A. Morris, J. B. West, *J. Chem. Phys.* **112** (4), 1707 (2000).

17. J. M. Dyke, S. D. Gamblin, D. Haggerston, A.Morris, S. Stranges, J. B. West, T. G. Wright and A. E. Wright, *J. Chem. Phys.* **108** (15), 6258 (1998).

18. J. M. Dyke, D. Haggerston, A. Morris, S. Stranges, J. B. West, T. G. Wright and A. E. Wright, *J. Chem. Phys.* **106**(3), 821 (1997).

19. D. Cossart, *J. Mol. Spectrosc.* **167**, 11 (1994).

20. R. S. Narcisi and A. D. Bailey, *J. Geophys. Res.* **70**, 3687 (1965).

21. M. Nicolet, *Mem. Instr. R. Meteorol. Belg.* **19**, 83 (1945).

22. M. G. Heaps and J. M. Heimerl, *J. Atm. Terr. Phys.* **42**, 733 (1980).

23. G. C. Reid, *Planet Space Sci.* **25**, 275 (1977).

24. B. G. Hunt, *J. Atm. Terr. Phys.* **35**, 1755 (1973).

25. R. E. Huffman, D. E. Paulsen, J. C. Larrabee and R. B. Cairns, *J. Geophys. Res.* **76**,1028 (1971).

26. D. Smith, N. G. Adams and D. Grief, *J. Atm. Terr. Phys.* **39**, 513 (1977).

27. F. C. Fehsenfeld and E. E. Ferguson, *J. Geophys. Res.* **74**, 2217 (1969).

28. W. C. Lineberger and L. J. Puckett, *Phys. Rev.* **187**, 286 (1969).

29. F. C. Fehsenfeld and E. E. Ferguson, *J. Geophys. Res.* **74**, 5743 (1969).

30. F. C. Fehsenfeld, M. Mosesman and E. E. Ferguson, *J. Chem. Phys.* **55**, 2120 (1971).

31. C. J. Howard, H. W. Rundle and F. Kaufman, *J. Chem. Phys.* **55**, 4772 (1971).

32. U. S. Standard Atmosphere Supplements, 1966, Superintendent of Documents, U. S. Govt. Printing Office, Washington, D. C. 20402.

33. D. B. Dunkin, F. C. Fehsenfeld, A. L. Schmeltekopf and E. E. Ferguson, *J. Chem. Phys.* **54**, 3817 (1971).

34. F. Arnold and D. Krankowsky, *J. Atm. Terr. Phys.* **39**, 625 (1977).

35. R. Johnsen, C. M. Huang, M. A. Biondi, *J. Chem. Phys.* **63**, 3374 (1975).

36. E. E. Ferguson. *Rev. Phys.* **9**, 997 (1971).

37. L. Thomas, *J. Atm. Terr. Phys.* **38**, 61 (1976).

38. G. A. Eiceman and Z. Karpas, *Ion Mobility Spetrometry* (CRC Press, Boca Raton, 1994).

39. S. H. Kim, K. R. Betty and F. W. Karasek, *Anal. Chem.* **50**, 2007 (1978).

40. G. Reiser, W. Habenicht, K. Müler-Dethlefs and E. W. Schlag, *Chem. Phys. Lett.* **152**, 119 (1988).

41. I. Fischer, A. Strobel, J. Staecker, G. Niedner-Schatteburg, K. Müller-Dethlefs and V. E. Bondybey, *J. Chem. Phys.* **96**, 7171 (1992).

42. M. Takahashi, *J. Chem. Phys.* **96**, 2594 (1992).

43. A. M. Bush, J. M. Dyke, P. Mack, D. M. Smith and T. G. Wright, *J. Chem. Phys.* **108**, 406 (1998).

44. P. M. Johnson, M. R. Berman and D. Zakheim, *J. Chem. Phys.* **62**, 2500 (1975).

45. G. Petty, C. Tai and F. W. Dalby, *Phys. Rev. Lett.* **34**, 1207 (1975).

46. M. N. R. Ashfold and J. D. Howe, *Annu. Rev. Phys. Chem.* **45**, 57 (1994).

47. M. N. R. Ashfold and J. D. Prince, *Contemp. Phys.* **29**, 125 (1988).

Chapter 2: Experimental apparatus for the study of short-lived molecules with photoelectron spectroscopy using synchrotron radiation

2.1 Introduction

A number of ultraviolet photoelectron spectrometers have been built at Southampton and elsewhere[1,2,3,4,5,6] to study short-lived molecules. The main components of an ultraviolet photoelectron spectrometer are: a radiation source, an ionisation chamber, an electron lens, a hemispherical energy analyser and an electron detector. The spectrometer used in this work, designed by Dr A. Morris, is modular, with separate chambers for the ionisation region and electron analyser, separated by narrow entrance slits. Each chamber is evacuated by a turbomolecular pump; this differential pumping system ensures that contamination of the analyser is minimised. The modular design also allows for easy and rapid access for cleaning contaminated areas, such as the ionisation chamber.

The basic principle of the spectrometer is relatively simple[7]. The sample, in a gaseous form and flowing continuously, is admitted into the ionisation region and intersected by the radiation source where ionisation occurs. A small fraction of the photoelectrons produced then pass through the slits in the boxes which enclose the ionisation region. Next the electrons pass through an electron lens, where they are focussed, and subjected to an accelerating/retarding voltage. After passing through the final slit in the focussing lens, the electrons enter the hemispherical electrostatic deflection analyser, where the electrons are separated on the basis of their kinetic energy. Electrons of an appropriate energy, selected by the voltage applied to the analyser hemispheres, pass between the interior surfaces of the analyser before exiting through another slit, where upon they are detected. By fixing the voltages applied to the hemispheres and sweeping the accelerating/retarding potential on the electron lens, electrons with different kinetic energies can be detected, and a spectrum of intensity vs. electron kinetic energy can be recorded.

Schematic diagrams of the photoelectron spectrometer used in this work are shown in Figures 2.1 and 2.2.

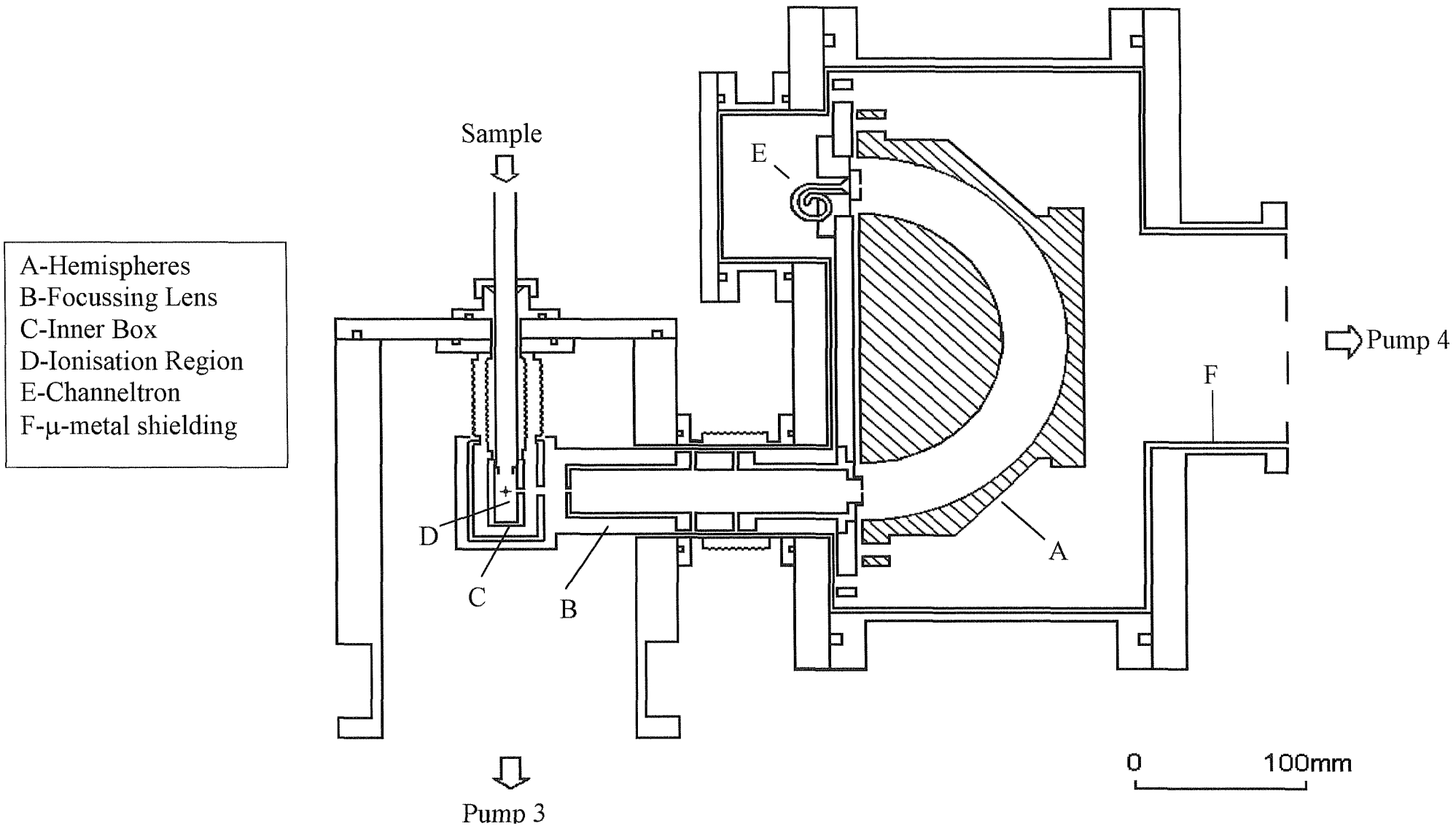

Figure 2.1: Schematic diagram of the photoeletron spectrometer

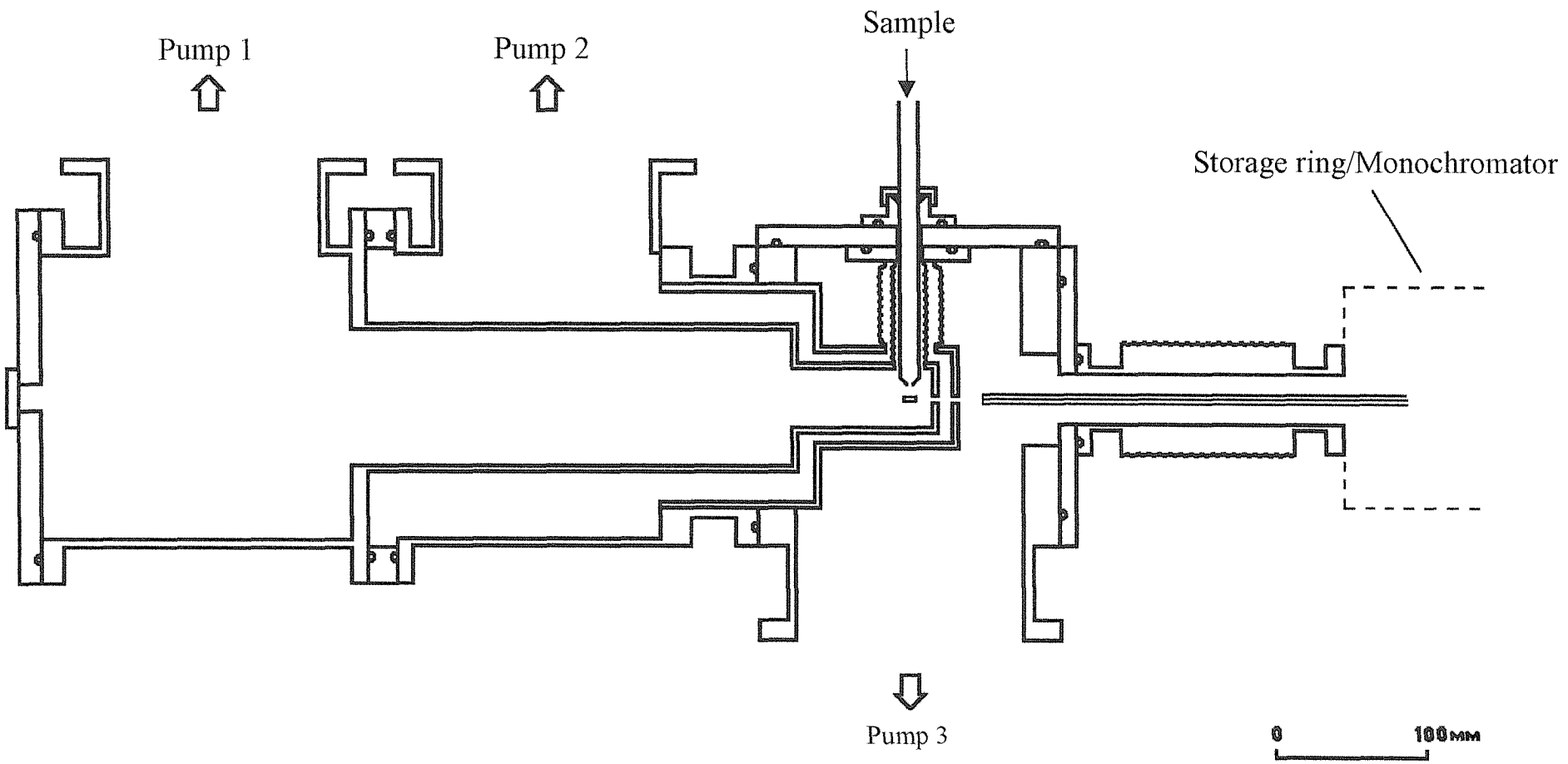

Figure 2.2: Side elevation schematic diagram of the photoelectron spectrometer

2.2 The Vacuum System

The spectrometer must be evacuated to low pressures ($P<10^{-5}$ mbar), otherwise the VUV radiation will be absorbed, photoelectrons will be scattered, and the detector will not operate.

The differential pumping system adopted in the apparatus used, consists of four turbomolecular pumps, each backed by its own rotary pump. The ionisation region is enclosed within two boxes. The boxes are closed, apart from a 2 mm circular aperture at the front to collimate the photon beam, the slits (10 mm × 2 mm) which point towards the electron analyser, and a 12 mm diameter hole at the top for the introduction of the sample. Most of the sample gas in the inner box is removed via a 360 ls^{-1} turbo pump (Pump 1 in Fig 2.2, Leybold Turbovac 361). Gas that escapes through the slits on the inner box is pumped away by a 400 ls^{-1} turbomolecular pump (Pump 2 in Fig 2.2, Leybold Turbovac 361C). A third turbomolecular pump (Pump 3 in Fig 2.2, Leybold Turbovac 1000) maintains the vacuum between the spectrometer and the synchrotron source by collecting any gas that enters the ionisation chamber. An ionisation gauge measures the pressure outside the boxes, whose base value is 2×10^{-7} mbar, rising to between 5×10^{-6} and 5×10^{-5} mbar when gas is admitted. The pressure inside the inner box is estimated to be at least one order of magnitude higher. No appreciable change in the beam-line pressure is observed when gas is admitted. Pressures in the spectrometer are measured by ionisation gauges and read by an Edwards AGC controller. Because pumps 1 and 2 receive a heavy load of gases, which are often corrosive, both have corrosion resistant coatings. They are also fitted with purge valves to reduce bearing contamination and extend the operational lifetime when pumping corrosive gases. The electron analyser region is also held under vacuum using a fourth, horizontally mounted tubomolecular pump (Pump 4, Leybold Turbovac 600). Using this pumping arrangement contamination of the monochromator optics is kept to a minimum.

2.3 The Hemispherical Electron Analyser

The electron analyser consists of two 180° hemispherical sectors. The inner and outer sectors are constructed from aluminium, and have radii R_I and R_0 of 80 and 120 mm respectively. In order to select electrons with mean pass energy E_{pass}, the sectors must be at potentials V_i and V_o given by[7,8]:

$$V_i = E_{pass}\frac{R_0}{R_i} \qquad \ldots(2.1)$$

and

$$V_0 = E_{pass}\frac{R_i}{R_0} \qquad \ldots(2.2)$$

The contribution of the finite width of the analyser slits to the full width at half maximum (FWHM) of a photoelectron band is approximately[9]

$$\Delta E_{FWHM} = \frac{\Delta S}{R_i + R_0}E_{pass} \qquad \ldots(2.3)$$

In equation (2.3) ΔS is the common width of the entrance and exit slits, $\Delta S=\Delta S_{entrance}=\Delta S_{exit}$. For the analyser geometry used in this work (ΔS=1mm) the ΔE_{FWHM} is equal to 25 and 50 meV for pass energies of E_{pass}=5 and 10 eV respectively. Narrower slits and lower pass energy would give rise to higher resolution, but at the expense of a lower electron transmission. A further important contribution to the FWHM arises from contact potentials that may cause the electron beam to spread, accelerate or decelerate. To minimise these potentials the inner surfaces of the analyser are coated with a conductive layer of graphite. Contamination of the electron optics from the reactive gases used usually leads to the resolution and transmission of the spectrometer deteriorating with time so that regular cleaning and replacement of the graphite coating is essential to regenerate the best conditions for recording high quality spectra.

2.4 The Electron Lens

The laboratory based photoelectron spectrometers used in Southampton record spectra by sweeping the voltages on the hemispheres, so that the kinetic energy of the transmitted electrons is scanned. This procedure has the disadvantage of giving different resolution and transmission for electrons with different kinetic energies. The apparatus used in this work has an analyser that operates at a constant pass energy, typically 5 or 10 eV. The electrons are accelerated (or retarded) by a lens so that they enter the analyser with the appropriate energy for transmission. Hence spectra are recorded with constant transmission and resolution.

The lens is constructed from three electrically isolated, coaxial, cylindrical aluminium elements. The first element is earthed, so that electrons in this segment retain their initial kinetic energy after ionization. The third element is at a voltage $V_3=E_{pass}-E_1$, with E_1 the original energy of the electrons, so that when moving from the first to the third element these electrons are accelerated or decelerated to the pass energy E_{pass}.

2.4.1 The Focus Curve

The second element of the lens is at a potential V_2, and acts as a focusing element. The value of V_2 must be such that the exit slit of the lens becomes the optical image of the entrance slit. A focus curve is generated by plotting acceptable values of V_2 against the electron kinetic energy. Focus curves for various lens geometries have been calculated by Harting and Read[10], but were determined empirically in this work. This is performed by optimising V_2 so that the intensity of a particular electron signal is maximized for a range of kinetic energies at the selected analyser pass energy. A fourth order polynomial is fitted to a plot of $(E_1+V_2)/E_1$ vs E_{pass}/E_1, and the coefficients are passed to the controlling software which is then able to calculate the optimum focusing voltage V_2 at a particular electron kinetic energy.

At the Daresbury Synchrotron Radiation Source (SRS), the data for the focus curve were obtained by observing the $Ar^+(3p^5, {}^2P_{3/2})\leftarrow Ar(3p^6, {}^1S_0)$ line at different photon energies. In Southampton only the HeI discrete line source is available, and the different electron kinetic energies are obtained by observing O_2 photoelectron bands.

2.5 Shielding

Stray electric and magnetic fields must be removed since these can affect the paths of the electrons which are to be analysed. Electrostatic fields cannot penetrate the metal frame of the spectrometer, but extra effort must be made to minimize the magnetic fields. The laboratory based photoelectron spectrometers in Southampton are enclosed by three orthogonal pairs of Helmoltz coils, in which currents are adjusted to minimise the magnetic fields within them. Space constraints at the synchrotron radiation source do not permit such an arrangement and so instead the critical regions of the spectrometer: the ionization region, the lens, the analyser and the detector, are surrounded by a 2 mm-thick layer of μ-metal, an alloy with high magnetic permeability.

2.6 Electron detection and control system

Electrons that traverse the analyser and pass through the exit slit are detected by a single channel electron multiplier (channeltron). The electron pulses produced by the channeltron are preamplified and passed to an Ortec 590A amplifier, whose output goes to a CAMAC counter (Hytec 350A) and then to a computer. The output from the amplifier is also passed to a ratemeter for visual display of the signal.

Voltages applied to the spectrometer, and signals received from it, are controlled by a computer via a modular CAMAC system, with supporting NIM units and power supplies. The potentials for the focussing and retarding elements of the lens are set by Kepco APH500M and BOP100-1M power supplies respectively, controlled by analog converters (DACs), Hytec 650 and 620, in the CAMAC crate, that are scanned by the computer.

The control software allows the collection of photoelectron and constant ionic state (see later) spectra at the Daresbury SRS, as well as their graphical display.

2.7 Preparation of the sample

The short lifetimes (~0.1 ms) of the reactive molecules studied in this work mean that they must be produced *in situ* for spectroscopic investigation. Methods that are commonly used to produce such species are fast atom-molecule reactions, pyrolysis, photolysis and gas-solid reactions.

The fast atom-molecule route was used to produce the OH radical via the rapid reaction[9]

$$H+NO_2 \rightarrow OH+NO \qquad \ldots(2.4)$$

The rate constant of this reaction is 1.1×10^{-10} $cm^3 molecule^{-1} sec^{-1}$ at room temperature[11]. Hydrogen atoms were produced by microwave discharging molecular hydrogen flowing through a 12 mm bore glass inlet system. In order to prevent low energy electrons produced in the discharge from entering the ionization region, the side inlet tube has three 90° bends. Helium is added to help sustain the discharge, and the inner surface of the glass tube is coated with phosphoric acid to reduce hydrogen atom recombination. NO_2 is added to the $H/H_2/He$ mixture through a 1 mm bore inner tube which passes down the centre of the main inlet system. The inner tube may be moved, allowing the position of the $H+NO_2$ mixing point above the photon beam to be adjusted.

The OH radicals produced by the reaction (2.4) undergo rapid secondary reactions:

$$OH+OH \rightarrow H_2O+O \qquad \ldots(2.5)$$

$$O+O+M \rightarrow O_2+M \qquad \ldots(2.6)$$

These reduce the yield of OH radicals and also give rise to H_2O bands in the spectra that can overlap with those from OH. This is a common problem when studying PES of reactive intermediates. In order to reduce the concentration of secondary products in the ionization region, the precursors must be mixed close to the photon beam, but not so close as to prevent reaction (2.4) from proceeding. The optimum mixing distance was found to be 30 mm above the photon beam. OD was produced via the same method as OH, using D_2 instead of H_2.

$O_2(a^1\Delta_g)$ was produced by flowing molecular oxygen through a microwave discharge. It is known that $O_2(a^1\Delta_g)$ is the dominant excited molecular product from such a discharge, but also atomic oxygen in its ^3P ground state and a negligible amount of $O_2(b^1\Sigma_g^+)$ are present.[12] From the published HeI photoionization cross sections of the $a^1\Delta_g$ and $X^3\Sigma_g^-$ states of O_2 [Ref. 13], and with the relative intensities observed in HeI photoelectron spectra

recorded for a typical discharge, the yield of $O_2(a^1\Delta_g)$ is estimated to be approximately 15%.

2.8 The Synchrotron Radiation Source

The spectra discussed in Chapters 4 and 5 were all recorded using the Daresbury Synchrotron Radiation Source (SRS), beamline 3.2, as the photon source[14]. This beamline is configured to output radiation in the vacuum ultraviolet region (10-40 eV), at high resolution, for the study of processes such as ionisation in atoms and molecules. The production of radiation at a synchrotron source[15,16,17] can be described as follows:-

Any charged particle subjected to acceleration will emit radiation. When the particle velocity is low, the emission, which is in the radiofrequency range, is very weak, and is of little use as an experimental source. However, relativistic particles, that is those with velocity v≈c, where c is the speed of light, may emit intense radiation of a far more useful energy. Such radiation is termed synchrotron radiation (SR), after the instrument in which it may be produced.

The classical picture of emission from a circulating particle is a toroidal pattern, which, due to relativistic effects, is distorted into a narrow cone in the instantaneous direction of motion of the charged particle, whilst maintaining the dipole polarisation in the orbital plane. This emission, being tangential to the circular orbit, may be observed as a fan of radiation extending around the ring, mostly confined within the plane of the ring as the divergence is small.

In a synchrotron, particles, usually electrons, are constrained by strong magnetic fields to move on an approximately circular path at a fixed frequency ν, given by[18]:

$$\nu = \frac{v}{2\pi R} \quad \text{Hz} \qquad \ldots(2.7)$$

R, the orbit radius in meters, is equal to 3.3 E/B, where B is the magnetic field strength in Tesla and E is the energy of the circulating particle in GeV[18].

The energy radiated by a single particle on one orbit, E_o, is[18]

$$E_o = \frac{4\pi e^2 \gamma^4}{3R} \qquad \ldots(2.8)$$

where $\gamma = E/m_0c^2$, m_o being the rest mass of the particle. The m_o^{-4} term in Equation (2.8) reveals why electrons are more widely used that protons for the production of SR – at the same kinetic energy an electron radiates $\sim 10^{13}$ times as much as a proton. For an electron, the radiated energy may be rewritten as[18]:

$$E_o = \frac{88.5E^4}{R} \quad \text{keV} \qquad \ldots(2.9)$$

and the total power, P, emitted by a circulating electron current of I ampères, is

$$P = 88.5E^3IB \quad \text{kW} \qquad \ldots(2.10)$$

For a synchrotron source such as the Daresbury SRS storage ring, with E=2 GeV, B=1.2 T, I=250 mA, and R=5.6 m, the single-orbit emission is
$E_o \approx 250$ keV, $P \approx 60$ kW.

Synchrotron radiation is sampled from a small opening angle, proportional to $1/\gamma$, and for E=2 GeV, this divergence is <1 mrad, which corresponds to an orbit length of $\sim R/\gamma$. A radiation pulse of duration τ will appear in the laboratory frame to be relativistically reduced to $R/c\gamma^3$, and harmonics of the orbit frequency up to τ^{-1} will be observable. Therefore frequencies up to γ^3 times the orbital period (usually ~ 1 MHz) may be observed; these are not resolvable due to the high densities of the higher harmonics and the natural spread in the orbital period, so that the emitted spectrum is effectively continuous between the microwave and X-ray regions.[18]

Synchrotron emission may be characterised by a "critical" wavelength, λ_c, which bisects the total emitted power over the full wavelength range. This is defined by $\lambda_c = 5.6RE^{-3}$ Å; as the electron energy is increased, the critical wavelength shortens.

A useful measure of the emission is the photon flux, normally defined as the number of emitted photons per second per mrad of horizontal angle in a 0.1% bandwidth, which is given by[18]:

$$N(\lambda) = 2.5 \times 10^{14} \mathrm{E} \mathrm{G}_1 \mathrm{I} \qquad \ldots(2.11)$$

where G_1 is a function of (λ/λ_c), and is known as a Universal function. The maximum flux is emitted at $\sim 4\lambda_c$. It falls slowly to longer wavelengths, whilst it falls sharply to shorter wavelengths, and is only useable for $\lambda > 0.1\lambda_c$.

The polarisation of the emitted radiation is predominantly within the plane of the orbit – within that plane, the orbiting electron appears as an oscillating dipole – and normal to the instantaneous direction of motion, so that to an experimental station the SR is predominantly linearly polarised in the horizontal plane. Moving out of the plane of the orbit, the polarisation falls, becoming elliptical with a horizontal component usually around 75%. The collimation of the radiation, that is the degree to which it leaves the plane of the ring, depends upon the critical wavelength: for a given λ_c, the out of plane divergence rises as λ increases, so that the X-ray emission does not diverge appreciably, but the VUV radiation spreads rather more significantly. For a given wavelength, the divergence falls as λ_c is increased, so that high-energy synchrotron rings provide more divergent radiation, especially at long wavelengths.

At the Daresbury SRS, electrons are circulated with an energy of 2 GeV in a storage ring[19], which incorporates several ports through which radiation is allowed to propagate. Initially electrons, produced at a hot cathode, are taken to 100 keV energy by a linear accelerator, or "linac". This directs the electrons into a small booster synchrotron, which accelerates them further to 400 MeV, and feeds them in pulses (or "bunches") into the main storage ring, in which final acceleration to 2 GeV kinetic energy is effected by radiofrequency fields. The electron beam is constrained upon its (approximately) circular path by bending magnets, into which are built many of the radiation ports, in particular that leading to Beamline 3.2. The storage ring may be operated with either one pulse of orbiting electrons ("single-bunch mode") or with many such bunches ("multi-bunch mode"); the former is used for time-

resolved spectroscopy and does not provide sufficient light flux to be applicable to PES, so all the spectra in this work were obtained during multi-buch operation.

Beamline 3.2 may be considered as consisting of three parts: pre-monochromator optics, the monochromator itself, and post-monochromator optics, as shown in Figure 2.3.

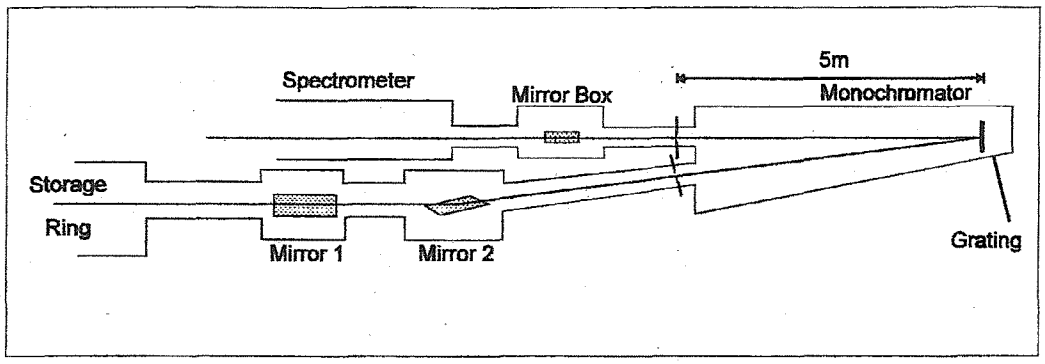

Figure 2.3: Beamline 3.2 Optics

The pre-monochromator system consists of a pair of mirrors that separate a component of the synchrotron radiation and focuses it onto the monochromator. These mirrors (labelled Mirror 1 and Mirror 2 in Figure 2.3) are of importance for aligning the beam after each fill of the ring.

The monochromator itself is a 5-metre, normal incidence McPherson model, with two gratings (interchangeable under vacuum) to cover a wide photon energy range.[20] Slit assemblies at the entrance and exit of the monochromator allow adjustment of the bandwidth of transmitted radiation, typically in the range 0.4-1.0 Å, which at 21.2 eV photon energy corresponds to 15-35 meV.

A third mirror box is situated beyond the monochromator and contains a focusing mirror which directs the photon beam into the spectrometer and also protects the monochromator from contamination. The mirror box chamber acts as a further stage of differential pumping between the spectrometer and monochromator and, by deflecting the photon beam through a narrow angle, removes any direct line-of-sight between the (possibly reactive) sample under study and the monochromator grating. A glass capillary constrains the radiation beam in its

propagation from this mirror box to the spectrometer, and also allows for a pressure difference between the ionization chamber of the spectrometer and the mirror box.

The monochromator drive mechanism is connected to two encoders, that provide a read-out of the wavelength of the selected radiation. These encoders should read zero when the monochromator is set to zero order, but it is usually the case that a small correction is required. After optimization of the pre-monochromator mirrors, the monochromator position is adjusted to maximize photon flux at zero order. The difference of the final encoder readings from zero is used as a correction to the wavelength given by these encoders whilst recording spectra. It is this reading that is recorded by the controlling software, and is saved with the photoelectron and CIS spectra that are obtained.

2.9 Calibration of the photon source and alignment of the spectrometer

The wavelength scale is calibrated by comparing the measured energies of the resonances in the CIS spectra (see later) of $O^+(2p^3, {}^4S)\leftarrow O(2p^4, {}^3P)$, $Xe^+(5p^5, {}^2P_{3/2})\leftarrow Xe(5p^6, {}^1S_0)$ and $Ar^+(3p^5, {}^2P_{3/2})\leftarrow Ar(3p^6, {}^1S_0)$ in the photon energy regions 13.5-18.5 eV, 20.0-23.5 eV and 26.0-30.0 eV with their nominal values from references 21 and 22. The changes in the photon energy scale after calibration were less than 50 meV.

The spectrometer must be aligned with the beam-line at the beginning of a beam-time allocation. Feet are attached to the base frame of the spectrometer to allow vertical adjustment. Horizontal adjustment is achieved via two plates that are also mounted to the base frame.

2.10 Types of Spectra

2.10.1 Photoelectron Spectra

A conventional photoelectron spectrum is recorded at fixed photon energy. In this case, the electron intensity is recorded as a function of the electron kinetic energy, which is scanned by adjusting the lens potentials. This provides a map of ionic states, and allows the determination of the energy required for ionisation to each one.

2.10.2 Constant Ionic State Spectra

A constant ionic state (CIS) spectrum is recorded by measuring the intensity of electrons corresponding to a given ionisation process as the photon energy changes, that is the ionisation energy is fixed. In order to accomplish this the measured kinetic energy is changed synchronously with the photon energy. A CIS spectrum yields the partial photoionisation cross-section into a particular ionic state, and may show discrete structure when the photon energy is resonant with a transition to an excited neutral state. By recording such a spectrum a map of autoionising states is obtained; the natures of these states may be deduced, and new ionisation limits may even be extrapolated from the spectra.

2.11 Summary

A photoelectron spectrometer used for the study of reactive intermediates with a synchrotron radiation source has been described in this chapter. The spectrometer has been used to study the photoionization behaviour of $O_2(a^1\Delta_g)$ and OH and the results of this work are presented in Chapters 4 and 5.

2.12 References

1. D. C. Frost, S. T. Lee, C. A. McDowell and N. P. C. Westwood, *J. Elec. Spec. Rel. Phenom.* **12**, 95 (1977).

2. N. Jonathan, D. J. Smith and K. J. Ross, *Chem. Phys. Lett.* **9**, 217 (1971).

3. J. M. Dyke, L. Golob, N. Jonathan, A. Morris, M. Okuda and D. J. Smith, *J. Chem. Soc. Faraday Trans. II.* **70**, 1818 (1974).

4. J. M. Dyke, N. Jonathan and A. Morris, in *Electron Spectroscopy: Theory, Techniques and Applications,* ed C. R. Brundle and A. D. Baker, Academic Press (1979).

5. A. Morris, N. Jonathan, J. M. Dyke, P. D. Francis, N. Keddar and J. D. Mills, *Rev. Sci. Instrum.* **55**, 172 (1984).

6. J. M. Dyke, A. Morris and N. Jonathan, *Int. Rev. Phys. Chem.* **2**, 3 (1982).

7. J. H. D. Eland, *Photoelectron Spectroscopy*, Butterworths, London (1984).

8. J. W. Rabalais, *Principles of Ultraviolet Photoelectron Spectroscopy,* Adam Hilger, Bristol (1977).

9. A. Poulin and D. Roy, *Journal of Physics E: Scientific Instruments,* **11**, 35 (1978).

10. E. Harting and F. H. Read, *Electrostatic Lenses,* Elsevier, Amsterdam (1976).

11. P. P. Benard and M. A. A. Clyne, *Journal of the Chemical Society, Faraday Transaction II,* **73**, 394 (1977).

12. N. Jonathan, M. Okuda, K. J. Ross and D. J. Smith, *Journal of the Chemical Society, Faraday Transaction II,* **70**, 1810 (1974).

13. W. J. van der Meer, P. van der Meulen, M. Volmer and C. A. de Lange, *Chem. Phys,* **126**, 385 (1988).

14. D. M. P. Holland, J. B. West, A. A. MacDowell, I. H. Munro and A. G. Beckett, *Nuclear Instruments and Methods in Physics Research,* **B44,** 233 (1989).

15. J. Schwinger, *Phys. Rev.* **75**, 1912 (1949).

16. J. D. Jackson and J. Wiley, *Classical Electrodynamics,* New York (1962).

17. W. K. H. Panovsky and M. Phillips, *Classical Electricity and Magnetism,* Addison Wesley, London (1962).

18. S. Krinsky, M. L. Perlman and R. E. Watson, in *Handbook on Synchrotron Radiation,* ed. E. E. Koch, North-Holland, Amsterdam (1983).

19. J. B. West, *Rev. Sci. Instrum.* **63**, 1597 (1992).

20. D. M. P. Holland, J. B. West, A. A. Macdowell, I. H. Munro and A. G. Beckett, *Nucl. Instrum. Methods Phys. Res. B.* **44**, 233 (1989).

21. C. Moore, *Atomic Energy Levels,* circular 467, United States National Bureau of Standards (1949).

22. R. P. Madden, D. L. Ederer and K. Codling, *Physical Review Letters,* **117**, 136 (1969).

Chapter 3: Fundamental principles relevant to the photoelectron spectroscopy study of reactive intermediates with synchrotron radiation

3.1 Photoelectron spectroscopy with a fixed wavelength radiation source

The primary aim of conventional photoelectron spectroscopy (PES) is to provide information on the ionic states of atoms and molecules. The basis for PES is the photoelectric effect, which was first observed experimentally by Hertz[1], and later investigated theoretically by Einstein[2]. Irradiation of a sample molecule with sufficiently energetic photons causes ionisation of that sample. Typically, photons of several tens of electron volts in energy are required, and suitable photon sources are those emitting vacuum ultraviolet (VUV) or X-radiation. The photoelectric effect may be summarised, for a molecule M, as:

$$M+h\nu \rightarrow M^{+}+e^{-}$$

The free electron, or photoelectron, will have a kinetic energy determined to a first approximation by the photon energy, $h\nu$, and the energy of the molecular orbital from which it was ejected. Ionization from each orbital gives rise to at least one ionic state, with each ionisation process yielding electrons of a specific kinetic energy. A photoelectron spectrum is recorded by counting photoelectrons produced per unit time over a range of kinetic energies, with the photon energy fixed, and it thus provides a map of ionic states of a molecule. In a photoelectron spectrum, one band will be observed for ionisation to each ionic state accessed.

The resolution achievable in a PES experiment is typically in the region of 200 cm^{-1}, and hence only vibrational structure can be resolved. This usually allows an estimation of the vibrational constant ω_e^+ in an ionic state, and perhaps also the anharmonicity constant $\omega_e x_e^+$. An analysis of the shape of the vibrational pattern in a PES band may allow an estimate of the change in equilibrium geometry between the neutral and ionic states.

Photoelectron spectroscopy has evolved into two branches, using radiation in different wavelength ranges to ionise the sample. When an X-ray source is used, both valence and core electrons may be ejected, and the technique is termed X-ray photoelectron

spectroscopy (XPS), or Electron Spectroscopy for Chemical Analysis (ESCA). This method was pioneered by Siegbahn[3] in 1964, mainly for the study of solid samples. If vacuum ultraviolet (VUV) radiation is used to photoionize the sample[4,5,6] then only valence electrons can be ejected, but higher resolution is achievable at these lower photon energies. This method is known as Ultraviolet Photoelectron Spectroscopy (UPS) or, more commonly, just Photoelectron Spectroscopy (PES). It is this latter technique that is used to study unstable diatomic molecules in this work.

The technique is relatively simple in principle, requiring only a photon source and an energy analyser. There are, however, a number of practical difficulties, most notably with the maintenance of the vacuum required for the whole apparatus and the prevention of chemical contamination; the latter requirement is particularly important in the study of unstable molecules where methods used to prepare molecules of interest in the gas phase often involve the use of "dirty" precursors. Rare gas discharge lamps are the most commonly used photon source; a list of suitable rare gas discharges may be found in reference [7]. Such lamps tend to allow the use of only one or two photon energies for a given rare gas, and only the helium emission lines (HeI at 21.22 eV and HeII at 40.81 eV) are sufficiently energetic to ionise any sample that may be studied.

The ionisation processes that are allowed in photoelectron spectroscopy are governed by selection rules for the electronic and vibrational changes that may occur on ionisation[8].

3.1.1 Electronic Selection Rules

The probability for photoionization from an initial, neutral state to a final, ionised state (which includes both the ion and the free electron) is proportional to the square of the modulus of the transition moment integral M. This latter quantity may be written as[8]:

$$M = \left\langle \Psi'^{*} \middle| \mu \middle| \Psi''^{*} \right\rangle \qquad \ldots(3.1)$$

where ψ' and ψ'' are the total wavefunctions describing the initial and final states respectively. μ is the electric dipole operator, since photoionisation arises from an interaction of the molecule with the oscillating electric field of the radiation.

The Born-Oppenheimer approximation, which proposes that the relative time-scales of nuclear and electronic motion permit their mathematical separation, may be applied, so that each wavefunction ψ may be considered as the product of a nuclear wavefunction and an electronic wavefunction[22]. The nuclear wavefunction, $\psi_v(R)$, is a function of the nuclear coordinates, R, and is treated simply as a vibrational function. The electronic wavefunction, $\psi_e(R,r)$, is a function of both nuclear co-ordinates and electronic co-ordinates, r. However, variation of ψ_e with R is slow, and to a first approximation may be neglected. This procedure, combined with the separation of the operator μ into electronic and nuclear terms μ_e and μ_n leads to:

$$M = \langle \Psi_e'^* | \mu_e | \Psi_e'' \rangle \langle \Psi_v'^* | \Psi_v'' \rangle + \langle \Psi'^*_e | \Psi_e'' \rangle \langle \Psi_v'^* | \mu_n | \Psi_v'' \rangle \qquad \ldots(3.2)$$

The second term in this expression vanishes due to the orthogonality of Ψ_e' and Ψ_e'', so that the transition probability becomes proportional to:

$$|M|^2 = \left| \langle \Psi_e'^* | \mu_e | \Psi_e'' \rangle \right|^2 \left| \langle \Psi_v'^* | \Psi_v'' \rangle \right|^2 = |M_e|^2 |M_v|^2 \qquad \ldots(3.3)$$

The electronic selection rules derive from the integral, M_e, which must be non-zero for a transition to be allowed. Electronic wavefunctions with different spin values are orthogonal, so the total spin of the system must remain constant upon ionisation. Since the photoelectron has half-integral spin, the spins of the molecule and ion must differ after ionisation by $\pm 1/2$.

Only single-electron transitions are permitted in photoionisation, for if a second electron were simultaneously excited, the initial and final state wavefunctions would differ by two orbitals ; the orthogonality of molecular orbitals would lead to M_e vanishing, and hence such many-electron transitions are forbidden[22]. This condition may be relaxed should electronic relaxation or correlation become significant.

There is no restriction on the change in orbital angular momentum in the molecule upon ionisation, since the ejected electron may leave with whatever angular momentum is required to compensate for this change.

3.1.2 Vibrational Selection Rules

The probability of a vibrational change occuring during the ionisation process is proportional to [8,7]:

$$|M_v|^2 = \left|\left\langle \Psi_v'^* \middle| \Psi_v'' \right\rangle\right|^2 \qquad \ldots(3.4)$$

This quantity, known as the Franck-Condon factor, or FCF, reveals that the intensity of a vibrational component within an electronic band is established by the overlap of the vibrational wavefunctions in the initial and final states.

Both narrow and broad bands are frequently observed in photoelectron spectra, which has led to the definition of two different ionisation energies. The adiabatic ionisation energy[7], or AIE, is the energy required to ionise from the lowest vibrational level of a molecule to the lowest vibrational level of an ionic state, as in the process

$$M^+, v^+=0 \leftarrow M, v''=0$$

The vertical ionisation energy (VIE)[7] is the energy required to ionise from the lowest vibrational level of a molecule to an ionic state vibrational level with a geometry that gives a maximum value for the overlap integral in equation (3.4). The VIE is measured at the most intense portion of a (non-overlapped) photoelectron band.

As mentioned previously, the vibrational structure in a photoelectron band, if resolved, may yield further information on the associated ionic state. The separations, ΔG, between successive components provide an estimate of the ionic state vibrational constant (ω_e^+).

The vibrational levels in an electronic state of a diatomic molecule may be described by an anharmonic oscillator[7] expression:

$$G_v = \omega_e(v+1/2) - \omega_e x_e (v+1/2)^2 \qquad \ldots(3.5)$$

from which ΔG may be derived as:

$$\Delta G = \omega_e - 2\omega_e x_e (v+1) \qquad \ldots(3.6)$$

where v is the vibrational quantum number of the first of the two levels in the ionic state. In heavier molecules, the spin-orbit splitting constant, A, may also be obtained for an ionic state, from resolved spin-orbit separations within each vibrational component.

Ionisation from a non-bonding molecular orbital tends to leave the equilibrium bond length in the ion, r_e^+, essentially the same as that in the initial neutral state. In such a case a narrow photoelectron band would be expected, with ω_e^+ similar to ω_e'', but only a rough estimate of ω_e^+ will be obtained since few vibrational separations will be measurable.

Ionisation of a bonding electron weakens the internuclear bond, increasing its equilibrium length and lowering the vibrational constant (ω_e^+) in the ion relative to that in the ground neutral state. Since $r_e^+ > r_e''$, a broad progression should be observed in the photoelectron band, from which it should be found that $\omega_e^+ < \omega_e''$. The loss of an electron from an antibonding orbital leads to a shorter, stronger bond, and a higher vibrational constant (ω_e^+) in the ion compared to that of the neutral molecule. A fairly broad photoelectron band will usually result, similar to that in the bonding case.

Thus, for a diatomic molecule, comparisons of measured values of ω_e^+ with the (usually well known) ω_e'' of the ground state, along with a consideration of the shape of the photoelectron band, may allow the bonding nature of each orbital from which ionisation occurs to be determined. Moreover, knowing the values of ω_e'', $\omega_e x_e''$, r_e'', ω_e^+ and $\omega_e x_e^+$, it is possible to calculate the Franck-Condon envelope for a given photoelectron band several times, using a range of plausible values of r_e^+. The best fit of the computed profile to the experimental spectrum should occur for the most accurate value of r_e^+; this method has been used to determine r_e^+ to within ± 0.005 Å by this method for some molecules[9,10,11].

The Franck-Condon factor calculations presented in this work were performed using the computer program CONFRON[12].

This program models both initial and final states with the Morse potential V(r), defined as:

$$V(r) = D_e[1 - \exp(-a(r - r_e))]^2 \qquad \ldots(3.7)$$

where D_e, the dissociation energy of the electronic state, and the constant a can be expressed in terms of the constants, ω_e and $\omega_e x_e$ in equation (3.5) as:-:

$$D_e = \frac{\omega_e^{\ 2}}{4\omega_e x_e}$$

$$a = \left[\frac{8\pi^2 c\mu\omega_e x_e}{h}\right]^{\frac{1}{2}}$$

For each state, the program iteratively solves the Schrödinger equation to obtain vibrational wavefunctions. It then determines the overlap of the initial and final state wavefunctions; the spectroscopic constants ω_e, $\omega_e x_e$ and r_e in each state must be supplied- if any of these are not known, CONFRON must be provided with an estimated value. It is found, as might be expected, that variation in r_e in a state has the strongest effect on the computed profile, modification of ω_e has a lesser effect, and changes in the anharmonicity constant ($\omega_e x_e$) within a reasonable range make very little difference.

To summarise, a well-resolved photoelectron spectrum of a diatomic molecule may allow the derivation of adiabatic and vertical ionisation energies and spectroscopic constants (ω_e^+, $\omega_e x_e^+$ and r_e^+) for a number of ionic states provided ω_e, $\omega_e x_e$ and r_e have been well determined for the ground state by other spectroscopic methods. In many cases, however, determination of the ionic constants is not possible, usually because the spectral resolution is insufficient, but occasionally because a photoelectron band may be distorted by a resonant effect (See 3.2). In such a case, analysis of the Franck-Condon envelope of the band may lead to an erroneous value being derived for the ionic equilibrium bond length r_e^+; the vertical ionisation energy derived from such a band may also be incorrect. In this case the experimental vibrational envelope depends on the Franck-Condon factor between the initial state and the resonant state, as well as the Franck-Condon factor between the resonant

state and the ion. This is made use of in Chapters 4 and 5 when considering the resonant photoelectron spectra of OH and $O_2(a^1\Delta_g)$ recorded with synchrotron radiation.

3.2 Photoelectron Spectroscopy with a tuneable wavelength radiation source

Above the first ionisation threshold there exists a profusion of neutral states, to which photoabsorption may occur when the photon energy matches the transition energy. Such resonant absorption processes may compete with direct photoionisation, and the decay mechanisms of these superexcited states can have a strong effect on the photoionisation cross-section at resonant photon energies. By using a tuneable wavelength source, such as synchrotron radiation, it is possible to map out these superexcited states which may be detected as fluctuations in partial photoionisation cross sections.

Excited neutral states may be classified into two categories- valence and Rydberg –although the distinctions between the two are often difficult to make (and states of each type may mix with each other)

3.2.2 Valence and Rydberg States

In atomic systems, the valence shell consists of atomic orbitals with the same principal quantum number as that of the highest occupied orbital in the ground state.[13] Therefore in atoms a valence state is one which is produced by exciting electrons within the valence shell. An atomic Rydberg state is obtained when an electron is promoted outside the valence shell. In molecules composed of elements of the same period, such as CO, a molecular valence shell may be defined in the same way, as the principal quantum numbers of the outermost orbitals of each atom are the same. In other cases, for example CS, there is no clear definition of a molecular valence shell, so a sensible description of molecular valence and Rydberg states cannot be based on such a concept.

A Rydberg state may also be defined as one whose excitation energy, E_R, obeys the Rydberg formula[13]:

$$E_R = IE - \frac{R}{(n^*)^2} \qquad \ldots(3.8)$$

where R is the Rydberg constant and n* is an effective principal quantum number. Each Rydberg state is a member of a series converging to a particular ionisation limit of energy IE. This definition is suitable for both atomic and molecular systems. In a molecule, a Rydberg state is considered to be pseudo-atomic, since to an electron in a spatially extensive Rydberg orbital, the molecular core will appear as a point charge, leading to near-hydrogenic behaviour. The extent of the departure from hydrogenic behaviour is contained within the effective quantum number, n*, which may be rewritten as $n^*=n-\delta$, where n is the principal quantum number of the Rydberg orbital and δ is termed the quantum defect. For $\delta=0$, the Rydberg orbital is exactly described by a hydrogenic atomic orbital. The magnitude of the quantum defect reflects the degree of penetration of the Rydberg orbital into the molecular core, which is strongly dependent on the radial distribution function of that orbital, and on the nuclear charges of the atoms from which the molecule is constructed. The radial probability distribution functions of atomic s orbitals have fairly large amplitudes close to the nucleus, whilst those of p orbitals have less amplitude at short radius, and d orbitals even less[14]. Thus the s orbitals experience the highest effective nuclear charge, so the quantum defect for an ns Rydberg orbital is high. Quantum defects for np and nd orbitals are progressively lower as the degree of penetration of those orbitals decreases. A Rydberg orbital tends to be particularly non-penetrating if there is no occupied "precursor" core orbital of the same symmetry[14]. For example, a Li 2p atomic orbital has no precursor (there is no 1p orbital), and so is a non-penetrating Rydberg orbital. The same is not true of the Na 3p orbital, since there is an occupied 2p precursor orbital; hence, although the Na 3p orbital is Rydberg, it experiences some core penetration and has a higher quantum defect than that in lithium[14].

In a heavy atom or molecule, the greater nuclear charge tends to make quantum defects larger than in a light system, where the electron-core interactions are weaker. Typical values of δ for first row atoms (e.g. C, N, O) and second row atoms (e.g. Si, P, S) are given in table 3.1.[15]

	δ(ns)	δ(np)	δ(nd)
1st Row	1.0	0.5	0.1
2nd Row	2.0	1.5	0.3

Table 3.1: Typical values of δ for first row atoms (e.g. C, N, O) and second row atoms (e.g. Si, P, S)

Molecular Rydberg orbitals will normally be characteristic of a particular atom in the molecule, so in a diatomic molecule, where A and B are from rows 1 and 2 respectively, some Rydberg states may exhibit quantum defects typical of A, and others may have δ values closer to those expected for B.

Every ionic state in an atom or molecule will have Rydberg series converging to it. Since the ionic core interacts only weakly with the Rydberg electron, the core will closely resemble the ionic state that lies at the series limit, and so the spectroscopic constants for a member of the Rydberg series will be similar to those of the ion core. The similarity of the Rydberg state to the ion at the series limit grows as the principal quantum number of the Rydberg orbital increases, so that as the ionisation limit is reached there is a seamless transition into the continuum.[16] The quantum defect, δ, in a series also tends towards an asymptotic limit with increasing n. This convergence is a consequence of the nature of high-n Rydberg orbitals: as n increases, the average radius of the Rydberg orbital grows rapidly. An electron in a spatially extensive orbital spends much more time at a distance from the core than close to it, and so it interacts less strongly with the core, and the Rydberg state resembles more closely the ion .

In a molecular system, every vibrational level in each ionic state may be considered as a limit for a Rydberg series. Thus, two descriptions of Rydberg series are possible. Firstly, one may consider that each ionic state lies at the limit of a series of discrete members M_n, and that each state M_n may be vibrationally excited. Each Rydberg state may be treated as having its own vibrational quantum number v_n, and its own spectroscopic constants. Alternatively, by treating each level v^+ of a state M^+ as a series limit, there are multiple

series of single levels, each of which has a certain vibrational excitation in the core. In general the former picture is more useful, especially when an observed Rydberg state exhibits extensive vibrational structure and may be considered in its entirety.

The average radius of a Rydberg orbital is proportional to $(n^*)^2$; for high values of n the Rydberg molecule can extend over more than 100 Å. Such large molecules have high collisional cross-sections, and the reactions (mainly charge-transfer) of highly excited Rydberg states have generated considerable interest.[17]

The overall symmetry of a Rydberg state is determined by the coupling of the angular momenta of the excited electron and the ionic core. In a diatomic molecule the Rydberg orbital may be assigned a principal quantum number n and an azimuthal quantum number l, so that as in atomic systems there are ns, np, nd... series. The cylindrical form of a diatomic molecule requires that another label, λ, be attached to each orbital, depending on the projection of the orbital angular momentum along the internuclear axis, denoting σ, π, δ... symmetry. Thus examples of Rydberg orbitals are $3s\sigma$, $5p\sigma$, $5p\pi$, $4d\sigma$, $4d\pi$, $4d\delta$ etc, or $nl\lambda$ in general. These subdivisions of the p and d (and higher) orbitals each have a slightly different quantum defect as they do not interact with the cylindrical core in exactly the same manner. A Rydberg state may thus be described by the ionic core around which it is built, that is the limiting state to which it converges, and the symmetry of the Rydberg orbital, an example being the well-known $H^3\Pi_u$ Rydberg state of oxygen: $(a^4\Pi_u)3s\sigma_g$ or, in general, $(M^+)nl\lambda$. As n increases, however, and the electron interacts less strongly with the core, λ tends to lose its importance and the Rydberg electron is better described simply by l. In this work most of the observed Rydberg states have low principal quantum numbers, and λ is a useful quantitiy in these cases.

The orbital angular momentum of the Rydberg electron may be determined experimentally, by determining the quantum defect for a state. This may be used in conjunction with the symmetry of the ionic core to determine the symmetry of the Rydberg state. In cases where a band is sufficiently well-resolved to obtain rotational structure in the upper state, and thus derive the symmetry of that state, it is possible to determine the symmetry of the ion at the series limit, which may also be unknown.

3.2.3 Decay Mechanisms

The effect on the photoionization cross section of absorption to a super-excited state will depend on the subsequent decay which may occur by one of a number of routes. These mechanisms may be summarised as follows, for a diatomic molecule AB:

(a) Re-radiation: $AB+hv \rightarrow AB^* \rightarrow AB+hv$

(b) Predissociation: $AB+hv \rightarrow AB^* \rightarrow A+B$

(c) Ion pair formation: $AB+hv \rightarrow AB^* \rightarrow A^+ + B^-$

(d) Autoionisation: $AB+hv \rightarrow AB^* \rightarrow AB^+ + e^-$

Fluorescent re-radiation is known to occur from Rydberg states, but will normally only take place if other decay channels are unavailable. The radiative lifetime of an excited state of a diatomic molecule is typically of the order of 10^{-8} s, whilst autoionisation and predissociation are frequenctly observed to be more rapid than one vibrational period, which is the order of 10^{-13} s. Hence, fluorescent decay is not usually competitive with the other decay processes. Mechanisms (b), (c) and (d) are only viable if the excited state lies above the threshold for formation of the respective products – if this is not the case, then re-radiation must occur, although not necessarily to the ground state of AB.

Predissociation arises from the interaction of the bound state AB* with an unbound one, resulting in a radiationless transition to the repulsive state and the fragmentation of the molecule. This tends to take place over a fairly narrow energy range, in the region where the two potential curves intersect[18], and may not affect all the vibrational and rotational levels of AB*. Ion pair formation is a special case of predissociation, in which two ionic products are formed[19]. No photoelectron is emitted in this mechanism, so that photoelectron spectra should be unaffected by ion pair formation.

Autoionisation is another radiationless transition, one that occurs when the excited neutral state interacts with an ionisation continuum that exists at the same energy. The transition from the excited state to the ion occurs by the loss of an electron, and this can have a profound effect on the overall ionisation cross-section and photoelectron envelope. There are four possible types of autoionisation mechanism: rotational, vibrational, spin-orbit and electronic[20].

When a Rydberg state $(M^+)nl\lambda$ lies above the threshold for ionisation to the particular ionic state M^+, due to rotational or vibrational excitation in the core, rotational and vibrational autoionisation may occur. For example, a Rydberg state $(M^+)nl\lambda$ of sufficiently high n, with one quantum of vibrational excitation ($v^*=1$), may lie above threshold for formation of M^+, $v^+=0$. The Rydberg state may autoionise by transfer of vibrational energy from the core to the excited electron, which then leaves. This vibrational autoionisation requires a strong interaction between the core and the Rydberg electron, and also involves a breakdown of the Born-Oppenheimer approximation, since nuclear and electronic motions are correlated in this mechanism. Vibrational autoionsation has been observed in molecular hydrogen[20], but seems to be less prevalent in more complex systems. Studies of vibrational autoionisation have revealed that the process favours the minimum possible change in vibrational quantum number, usually $\Delta v=-1$ [Ref. 20 and 21]. Since the separation between consecutive vibrational levels in the ion is relatively small, only Rydberg states of high n that converge to the upper v^+ level will lie above the lower v^+ level. Since the probability of absorption to Rydberg states is approximately a function of $(n^*)^{-3}$
[Ref. 22], excitation to, and thus autoionisation from these states is weak; hence vibrational autoionisation is not considered to be an important process in most molecules. The same applies to rotational autoionisation. Spin-orbit autoionisation is only observable where the spin-orbit coupling constant in the limiting ionic core is large, such as in argon, where the resonant series converging to $Ar^+ {}^2P_{1/2}$ are observed to autoionise into $Ar^+ {}^2P_{3/2}$.

Electronic autoionisation involves a transition from a Rydberg state built upon one (excited) ionic state interacting with a continuum associated with a lower one[23]. Rydberg states based upon the ground ionic state cannot autoionise electronically, therefore, but a state $(M_2^+)nl\lambda$ may autoionise into both the M_0^+ and M_1^+ continua.

Electronic autoionisation is a result of interactions between the Rydberg state and the continuum and may be visualised in one of two ways. Either the excited core relaxes to a lower-energy configuration, and the energy so released is transferred to the Rydberg electron, or the Rydberg electron returns to its original orbital and the excess energy is used to eject another electron, again leaving the ion in the less-excited state. Either way, autoionisation is a two-electron process, requiring the close approach of the Rydberg electron to the core; only electronic motions are involved, so the Born-Oppenheimer approximation still holds. Electronic autoionisation is found to be the dominant

autoionisation process in most diatomic molecules, where there are sufficient excited ionic states to yield fairly high densities of Rydberg states several eV above the first ionisation threshold.

In the work presented in this thesis, superexcited states are probed by recording constant ionic state (CIS) spectra. A CIS spectrum monitors the intensity of a single photoelectron feature as the photon energy is scanned; when the photon energy is coincident with a transition to an autoionising state, discrete structure can be observed in the CIS spectrum.

3.3 Reactive Intermediates

Short-lived species, both neutral and ionised, are of great importance in combustion processes, in atmospheric and astrophysical chemistry. Reaction intermediates, despite being present in low concentrations, can have a major influence on the gas-phase chemistry. Due to experimental difficulties, short-lived molecules of fundamental importance in these areas have not been thoroughly studied, and their electronic structure may be complex, requiring sophisticated theoretical treatments..

The Southampton PES group has concentrated on the study of reactive intermediates as its main research topic. Initial work was performed on short-lived molecules, formed in the gas phase in discharges[10,24,25] or by chemical reaction[26]; this has progressed to the studies of the vapour above heated inorganic solids[27,28] and of chemiionisation reactions[29]. A review of PES investigations performed in Southampton using HeI (21.22 eV) and HeII (40.81 eV) radiation from discharge lamps can be found in Ref 30 and a review on the work performed to date with synchrotron radiation is contained in Ref. 31.

The study of reactive species involves many experimental difficulties, as does their preparation, and a good deal of specialised knowledge and equipment is required. Once these obstacles have been overcome, however, there is a wealth of information to be obtained from photoelectron spectroscopy of these often intriguing molecules.

3.4 Summary

The basic principles outlined in this chapter are relevant to the study of short-lived molecules with synchrotron radiation. These are applied to the analysis of the results of synchrotron studies on $O_2(a^1\Delta_g)$ and OH, described in Chapter 4 and 5.

3.5 References

1. H. Hertz, *Ann. Phys.* **31**, 983 (1887).

2. A. Einstein, *Ann. Phys.* **17**, 132 (1905).

3. K. Siegbahn, C. Nordling, A. Fahlman, R. Nordberg, K. Hamrinn, J. Hedman, G. Johansson, T. Bergmark. S. E. Karlsson, I. Lindgren and B. Lindberg, *Nova Acta Regia Soc. Sci. Upsal. Ser. IV.* **20**, (1967).

4. F. I. Vilesov, B. L. Kurbatov and A. N. Terenin, *Dokl. Akad. Nauk SSSR* **138**, 1329 (1961).

5. M. I. Al-Joboury and D. W. Turner, *J. Chem. Soc.* 5141 (1963).

6. M. I. Al-Joboury and D. W. Turner, *J. Chem. Phys.* **37**, 3007 (1962).

7. J. H. D. Eland, *Photelectron Spectroscopy,* Butterworths, London (1984).

8. J. W. Rabalais, *Principles of Ultraviolet Photoelectron Spectroscopy,* Adam Hilger, Bristol (1977).

9. N. Jonathan, A. Morris, M. Okuda, K. J. Ross and D. J. Smith, *Farad. Disc. Chem. Soc.* **54**, 1-8 (1972).

10. N. Jonathan, D. J. Smith and K. J. Ross, *Chem. Phys. Lett.* **9**, 217-218 (1971).

11. J. H. D. Eland, *J. Chem. Phys.* **72**, 6015 (1980).

12. C. A. de Lange, H. J. Bakker and O. Grabandt, *J. Mol. Struc.* **173**, 221 (1988).

13. A. B. F. Duncan, *Rydberg Series in Atoms and Molecules,* Academic Press, New York (1971).

14. M. B. Robin, *Higher Excited States of Polyatomic Molecules,* Academic Press, New York (1974).

15. C. E. Moore, *Atomic Energy Levels,* National Bureau of Standards, Washington (1949).

16. U. Fano and J. W. Cooper, *Phys. Rev.* **137**, 1364 (1965).

17. F. B. Dunning and R. F. Stebbings, in *Rydberg States of Atoms and Molecules,* ed. R. F. Stebbings and F. B. Dunning, Cambridge University Press, Cambridge (1983).

18. G. Herzberg, *Spectra of Diatomic Molecules,* Van Nostrand, New Jersey (1950.

19. K. P. Lawley and R. J. Donovan, *J. Chem. Soc. Faraday Trans.* **89**, 1885 (1993).

20. R. S. Berry, *J. Chem. Phys.* **45**, 1228 (1966).

21. J. Berkowitz and W. A. Chupka, *J. Chem. Phys.* **51**, 2341 (1969).

22. J. Berkowitz, *Photoabsorption, Photoionisation and Photoelectron Spectroscopy,* Academic Press, New York (1979).

23 A. L. Smith, *J. Quant. Spectr. Radiat. Tranfer.* **10**, 1129 (1970).

24. N. Jonathan, A. Morris, K. J. Ross and D. J. Smith, *J. Chem. Phys.* **54**, 4954 (1971).

25. N. Jonathan, A. Morris, M. Okuda, K. J. Ross and D. J. Smith, *Farad. Disc. Chem. Soc.* **54**, 1 (1972).

26. L. Andrews, J. M. Dyke, N. Keddar, N. Jonathan and A. Morris, *J. Am. Chem. Soc.* **106**, 229 (1984).

27. J. M. Dyke, N. Jonathan, E. P. F. Lee and A. Morris, *J. Chem. Soc. Faraday Trans. II.* **72**, 1385 (1976).

28. J. M. Dyke, D. Haggerston, A. E. Wright, A. Morris, E. van Lenthe and J. C. Snijders, *J. Elec. Spec. Rel. Phenom.* **85**, 23 (1997).

29. M. C. R. Cockett, J. M. Dyke, A. M. Ellis, M. Feher and T. G. Wright, *J. Elec. Spec. Rel. Phenom.* **51**, 529 (1990).

30. M. C. R. Cockett, J. M. Dyke and H. Zamanpour, in *Vacuum Photoionisation and Photodissociation of Molecules and Clusters,* edited by CY Ng, World Scientific, London (1991).

31. J. D. Barr, L. Beeching, A. DeFanis, J. M. Dyke, S. D. Gamblin, N. Hooper, A. Morris, S. Stranges, J. B. West, A. E. Wright and T. G. Wright, *J. Elec. Spec. Rel. Phen.* **108**, 47 (2000).

Chapter 4- Study of the OH and OD radicals with photoelectron spectroscopy using synchrotron radiation

4.1 Introduction

The hydroxy radical (OH) plays an important role in the chemistry of the Earth's atmosphere,[1,2] combustion processes,[3] and the interstellar medium.[4] For example, it plays a dominant role in the day-time chemistry of the troposphere where it initiates free radical chain reactions leading to the oxidation of most trace constituents.[1,2] The ultraviolet (UV) photophysics of this molecule and the properties of ground and excited states are therefore of fundamental importance. Although the low-lying electronic states of the neutral molecule have been extensively studied by experiment[5,6,7,8,9,10,11,12] and theory,[13,14,15] the UV absorption spectrum at wavelengths shorter than 1200 Å is poorly resolved[11] and resonant states above the first ionization energy have only been observed by photoionization mass spectrometry (PIMS).[16,17] A Zero electron kinetic energy (ZEKE) study on the ground ionic states of OH and OD was performed by Wiedmann *et.al*[18] .

The ground state ($X^2\Pi$) electronic configuration of OH is

$$1\sigma^2 2\sigma^2 3\sigma^2 1\pi^3$$

where each 1π molecular orbital consists of an O $2p_\pi$ atomic orbital and is thus nonbonding in character, and the 3σ orbital is a bonding orbital consisting of H 1s and O $2p_\sigma$ contributions.

The $(1\pi)^{-1}$ ionization produces the $X^3\Sigma^-$, $a^1\Delta$, and $b^1\Sigma^+$ states of OH^+, while the $(3\sigma)^{-1}$ ionization gives rise to the $A^3\Pi$ and $c^1\Pi$ ionic states.[19,20] The He I (21.22 eV) photoelectron spectrum (PES) of OH, prepared via the F + H_2O reaction, shows all three bands associated with the $(1\pi)^{-1}$ ionization.[20] They exhibit nonbonding envelopes with adiabatic ionization energies (AIEs) of 13.01, 15.17, and 16.61 eV. For the $(3\sigma)^{-1}$ ionization, only the $OH^+(A^3\Pi)\leftarrow OH(X^2\Pi)$ band was observed[20] because of the poor transmission of the spectrometer above 18.0 eV which prevented observation of the $OH^+(c^1\Pi)\leftarrow OH(X^2\Pi)$

band. As expected the OH^+ ($A^3\Pi$)←OH ($X^2\Pi$) band (AIE=16.48 eV) is broad with vibrational separations smaller than in the ground state neutral molecule.[20]

Table 4.1 lists symmetries and ionization energies of ionic states which are accessible by one photon ionization from the ground state of OH and OD using a He I (21.22 eV) radiation source.

State of OH^+ Accessed	Ionization	AIE (eV)	Reference
$X^3\Sigma^-$	$(1\sigma)^{-1}$	13.01	20
$a^1\Delta$	$(1\sigma)^{-1}$	15.17	20
$b^1\Sigma^+$	$(1\sigma)^{-1}$	16.61	20
$A^3\Pi$	$(3\sigma)^{-1}$	16.48	20
$c^1\Pi$	$(3\sigma)^{-1}$	18.30	21,22

Table 4.1: Symmetries and adiabatic energies (AIEs) of the states of OH^+ and OD^+ accessible from photoionization of the neutral ground state with He I radiation (21.22 eV).

The most detailed spectroscopic study of OH^+ is that of Merer *et al.* who studied the $X^3\Sigma^-$←$A^3\Pi$ emission system.[23] In that work, the OH^+ $A^3\Pi$ state was shown to be strongly perturbed by the $b^1\Sigma^+$ state and analysis of the rotational structure in the UV emission spectrum, which accounted for excited state perturbations, enabled accurate spectroscopic constants to be derived for the $X^3\Sigma^-$, $A^3\Pi$ and $b^1\Sigma^+$ ionic states. The only experimental observation of the $c^1\Pi$ state of OH^+ has been by laser photofragmentation spectroscopy of the [$c^1\Pi$, $v'=3$]←[$b^1\Sigma^+$, $v''=0$] transition.[24] This work measured the [$c^1\Pi$, $v'=3$]←[$b^1\Sigma^+$, $v''=0$] transition energy as 2.29 eV. When this is combined with the OH^+ ($b^1\Sigma^+$)←OH ($X^2\Pi$) AIE of 16.61 eV (Ref. 20) and vibrational separations computed

for OH^+ ($c^1\Pi$) by *ab initio* molecular orbital calculations,[25] the AIE for the OH^+ ($c^1\Pi$)←OH ($X^2\Pi$) ionization can be derived as 18.30 eV.

Although the lowest-lying states of OH have been extensively studied by theoretical methods,[14,15,26] the position and spectroscopic properties of neutral states near or above the first ionization threshold are not well established.[13,26] Potential curves for the first five electronic states of OH^+ have been calculated by the multireference double excitation configuration interaction (MRDCI) method[25] and molecular constants derived from the computed potential curves are in good agreement with available experimental values and those derived from other calculations.[27,28]

Excited states of OH which autoionize to OH^+ states have been observed by PIMS.[16,17] In the work of Dehmer,[16] which covered the photon energy region 13.0-16.5 eV, just one Rydberg series was identified converging to the $a^1\Delta$ ionic limit. Cutler *et al.*[17] repeated this work on both OH and OD in the photon energy range 13.0-18.2 eV and assigned two additional Rydberg series converging to the $b^1\Sigma^+$ and $A^3\Pi$ ionic limits. Rotational structure, extending over ~0.08 eV, associated with the transition $[OH^*(a^1\Delta,3d), v'=0]$←$[OH(X^2\Pi), v''=0]$ was recorded although no analysis of this structure was presented. Also, for the $[OH^*(A^3\Pi,3d), v']$←$[OH(X^2\Pi), v''=0]$ absorption, components were observed with $v'=0,1$, and 2. For higher values of principal quantum number (n=4-8), only the $v'=0$←$v''=0$ components could be identified but positions of the other vibronic transitions (i.e., $v'=1,2$←$v''=0$ for each n) were suggested based on results of earlier PES work.

The purpose of this work was to record constant ionic state (CIS) spectra of the $[X^3\Sigma^-, v^+=0,1]$ and $[a^1\Delta, v^+=0]$ vibronic states of OH^+ and OD^+ and thus to determine the excitation energies of neutral states which autoionize into these vibrational channels. It was anticipated that the vibrational specificity of the CIS technique would help to determine the nature of those states unassigned in earlier PIMS studies,[16,17] and would also allow the identification of previously unobserved Rydberg states. In addition, once resonant energies are identified, then photoelectron spectra can be recorded which can exhibit extra vibrational structure in the first photoelectron band helping to confirm possible Rydberg state assignments.

4.2 Results and Discussion

4.2.1 Photoelectron spectra of OH and OD at 21.22 eV

Figure 4.1 shows photoelectron spectra recorded at the synchrotron source at a photon energy of 21.22 eV for the H + NO_2 reaction (See Section 2.7) with the H_2/He discharge on and off. As can be seen from this figure, only a very small amount of NO_2 is present in the discharge-on spectrum. The spectra obtained are in good agreement with those recorded previously by Katsumata and Lloyd[19] (who also used the H+NO_2 method to produce OH) using a He I (21.22 eV) photon source, clearly showing the first two photoelectron bands of OH at 13.01 and 15.17 eV AIE corresponding to the ionizations
$[OH^+ (X^3\Sigma^-), v^+=0,1] \leftarrow [OH(X^2\Pi), v''=0]$ and
$[OH^+ (a^1\Delta), v^+=0] \leftarrow [OH(X^2\Pi), v''=0]$, respectively. As well as bands associated with H_2, H, NO, and OH, signals arising from H_2O, O, and O_2 were also observed in the discharge-on spectrum. These are thought to arise from the secondary reactions:

$$OH+OH \rightarrow H_2O+O,$$

$$O+O+M \rightarrow O_2+M$$

Photoelectron spectra recorded for the D+NO_2 reaction were very similar to those shown in Fig. 4.1 except that, as expected, the vibrational spacings observed in the OD, D_2O, and D_2 bands were less than in the OH, H_2O, and H_2 bands. The measured vibrational separations for the first photoelectron bands of OH and OD are 0.37 and 0.26 meV respectively (2984 and 2100 cm^{-1}). Figure 4.2 shows the 11.0-14.0 eV ionization energy region of the photoelectron spectrum recorded for the D+NO_2 reaction. It shows the first two vibrational components of the first band of OD corresponding to the ionization
$[OD^+(X^3\Sigma^-), v^+=0,1] \leftarrow [OD(X^2\Pi), v''=0]$.

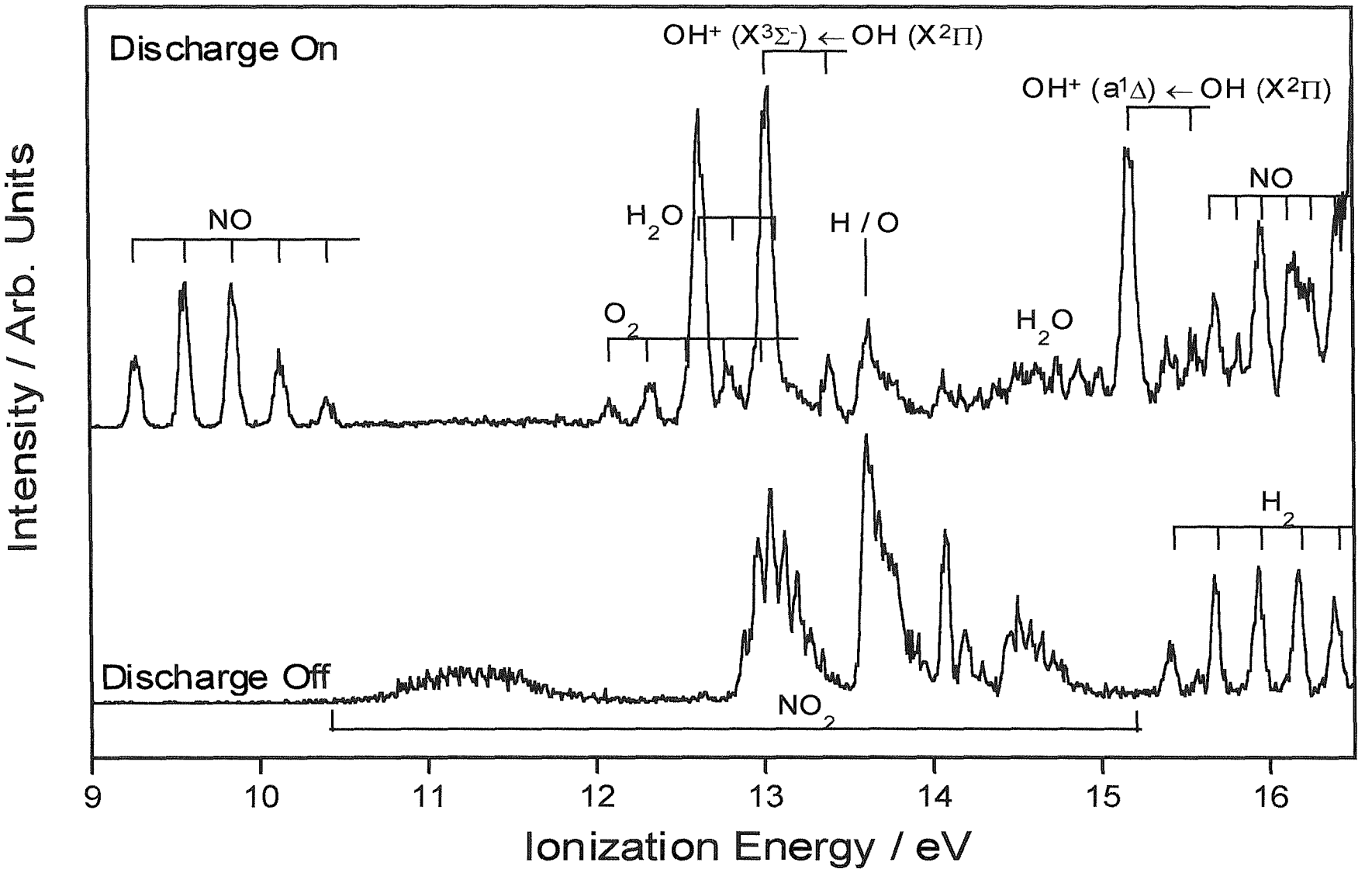

Figure 4.1: Photoelectron spectra recorded for the reaction mixture H_2/He+NO_2 with the microwave discharge on and off, at a photon energy of 21.22 eV. NO_2 was added to the H_2/He mixture ~30 cm after the H_2/He discharge and ~ 3 cm above the photon beam

Figure 4.2: Photoelectron spectrum recorded in the ionization energy region 11.0-14.0 eV, for the D_2/He + NO_2 reaction mixture with the microwave discharge on and hv=21.22 eV

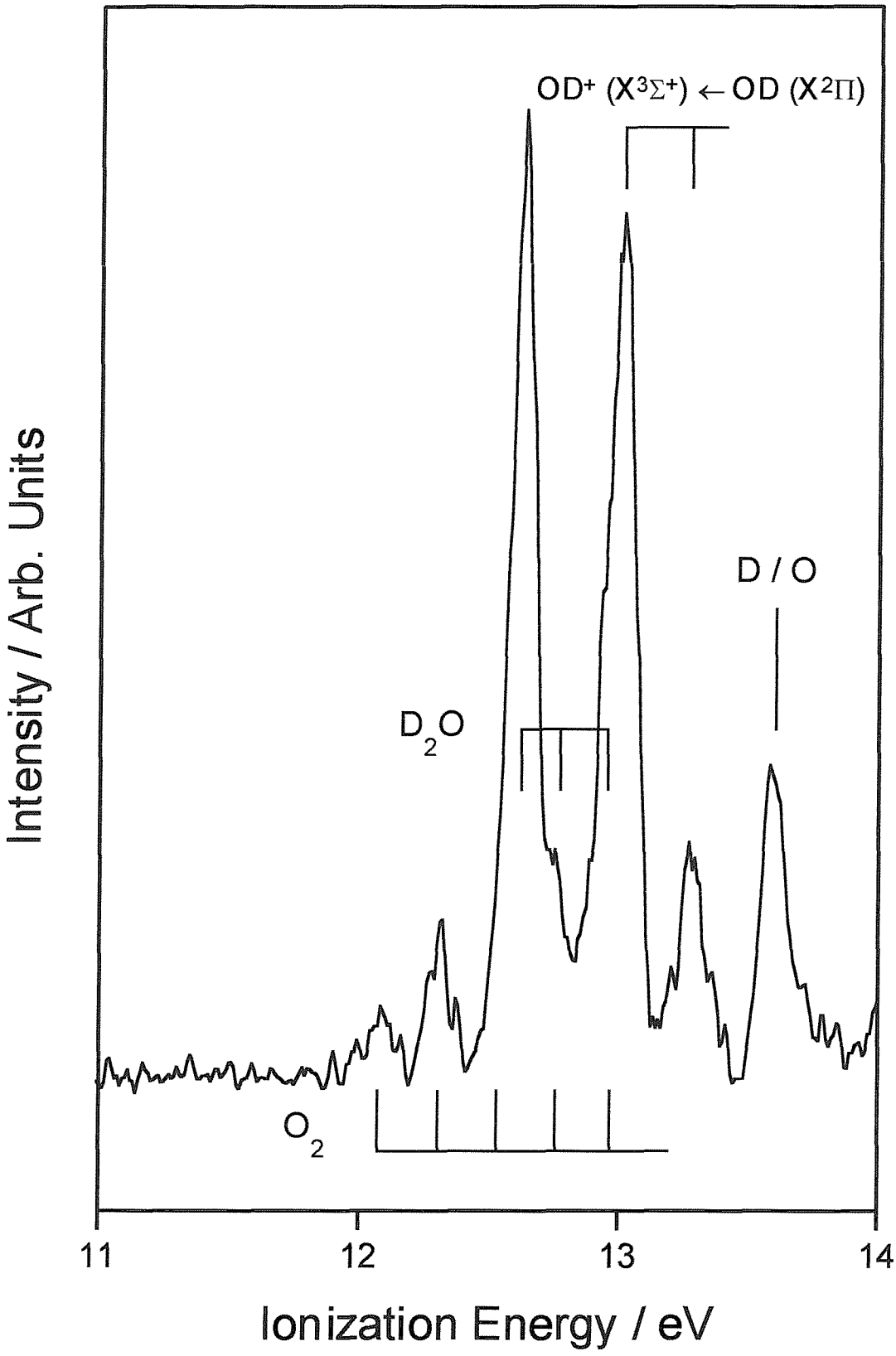

4.2.2 CIS Spectra for the $X^3\Sigma^-$, $v^+=0,1$ and $a^1\Delta$, $v^+=0$ states

For both OH and OD, CIS spectra were recorded in the photon energy range 13.0-17.0 eV for the first two vibrational components of the first band and the first vibrational component of the second band. The measured ionization energies of these features are 13.01, 13.38 and 15.17 eV for OH and 13.01, 13.27 and 15.17 eV for OD.

Since the CIS technique cannot distinguish between electrons with the same kinetic energy arising from different species, then it is possible that atoms or molecules with an ionization energy very close to that of OH and OD may give rise to contaminant features in the OH or OD CIS spectra. It can be seen from Figure 4.1 that the adiabatic component of the first band of OH (13.01 eV ionization energy) overlaps with the third vibrational component of the second band of unreacted NO_2 (13.02 eV) and is close to the third vibrational component of the first band of water (13.07 eV) and the fifth vibrational component of the first band of oxygen (12.97 eV). Separate CIS spectra of pure samples were therefore recorded for these potential contaminants over the 13.0-17.0 eV photon energy range. The CIS spectra of NO_2 and H_2O did not show any significant resolved structure. The CIS spectrum of O_2 did exhibit many sharp resonances, but since the most intense of these occur at energies corresponding to regions of flat baseline in the OH CIS spectra, then the contribution of O_2 features to the OH CIS spectrum was concluded to be negligible. Similar experiments undertaken on the sixth and seventh vibrational components of the first band of O_2 (13.19 and 13.40 eV ionization energy) and the sixth vibrational component of the second band of NO_2 (13.27 eV) led to the conclusion that these molecules did not contribute to CIS spectra recorded for the second vibrational components of the first bands of OH and OD (at 13.38 and 13.27 eV ionization energy, respectively).

A more significant contaminant is NO, which despite displaying only five vibrational components in its first band in the 21.22 eV photoelectron spectrum,[29] is known to have many sharp resonances in the 13.0-17.0 eV photon energy region.[30] Recording photoelectron spectra at these resonant energies may extend the vibrational profile of the first NO band at least as far as the onset of the second band (15.65 eV).[29] Therefore, NO was also studied separately by recording CIS spectra at positions of the $[NO^+ (X^1\Sigma^+), v^+=14, 15, \text{and } 16] \leftarrow [NO (X^2\Pi), v''=0]$ ionizations (at ionization energies of 12.96, 13.17 and 13.42 eV) and at ionization energies used to record the OH and OD CIS

spectra (13.01, 13.27, 13.38, and 15.17 eV). It was found that NO contributes a total of seven peaks to the CIS spectra recorded for OH and OD. Apart from these features, the positions of all other peaks in the CIS spectra recorded for OH and OD are in good agreement with those observed previously in mass-resolved PIMS spectra[16,17] and so can be confidently assigned to OH and OD. However, the vibrational-state specificity of the CIS spectra of this work should assist spectral assignment.

The CIS spectrum of the $[OH^+(X^3\Sigma^-), v^+=0]\leftarrow[OH(X^2\Pi), v''=0]$ ionization over the photon energy range 13.0-17.0 eV is shown in Figure 4.3. One feature which can be identified as an NO resonance is marked in this figure with an asterisk. For all the other significant peaks, effective principal quantum numbers, n*, were calculated assuming the resonant state to be the v′=0 level of a Rydberg state based upon $a^1\Delta$, $b^1\Sigma^+$, $A^3\Pi$, or $c^1\Pi$ ionic cores using the AIEs given in the introduction. From these preliminary values of n*, two Rydberg series were identified, one in the 13.0-15.3 eV photon energy region converging to the $a^1\Delta$ ionic limit [an ($a^1\Delta$, nd) series] and one in the 14.8-17.0 eV region converging to the $A^3\Pi$ ionic limit [an ($A^3\Pi$, nd) series]. The first series has been identified previously in the photoionization work of Dehmer[16] and both series have been observed in the PIMS work of Cutler *et al.*[17] These two series will be considered in detail before the remaining structure is discussed.

The $(a^1\Delta,nd)\leftarrow X^2\Pi$ series

Figure 4.4 shows the $v^+=0$ and $v^+=1$ CIS spectra of the $[OH^+(X^3\Sigma^-, v^+]\leftarrow[OH(X^2\Pi), v''=0]$ ionization over the photon energy range 13.0-15.2 eV. Many of the most intense peaks in the $v^+=0$ spectrum arise from transitions to autoionizing states which form a Rydberg-like series converging to the $a^1\Delta$ ionic limit. At least five components of the series are clearly observed and their energies, calculated n* values and quantum defects are listed in table 4.2

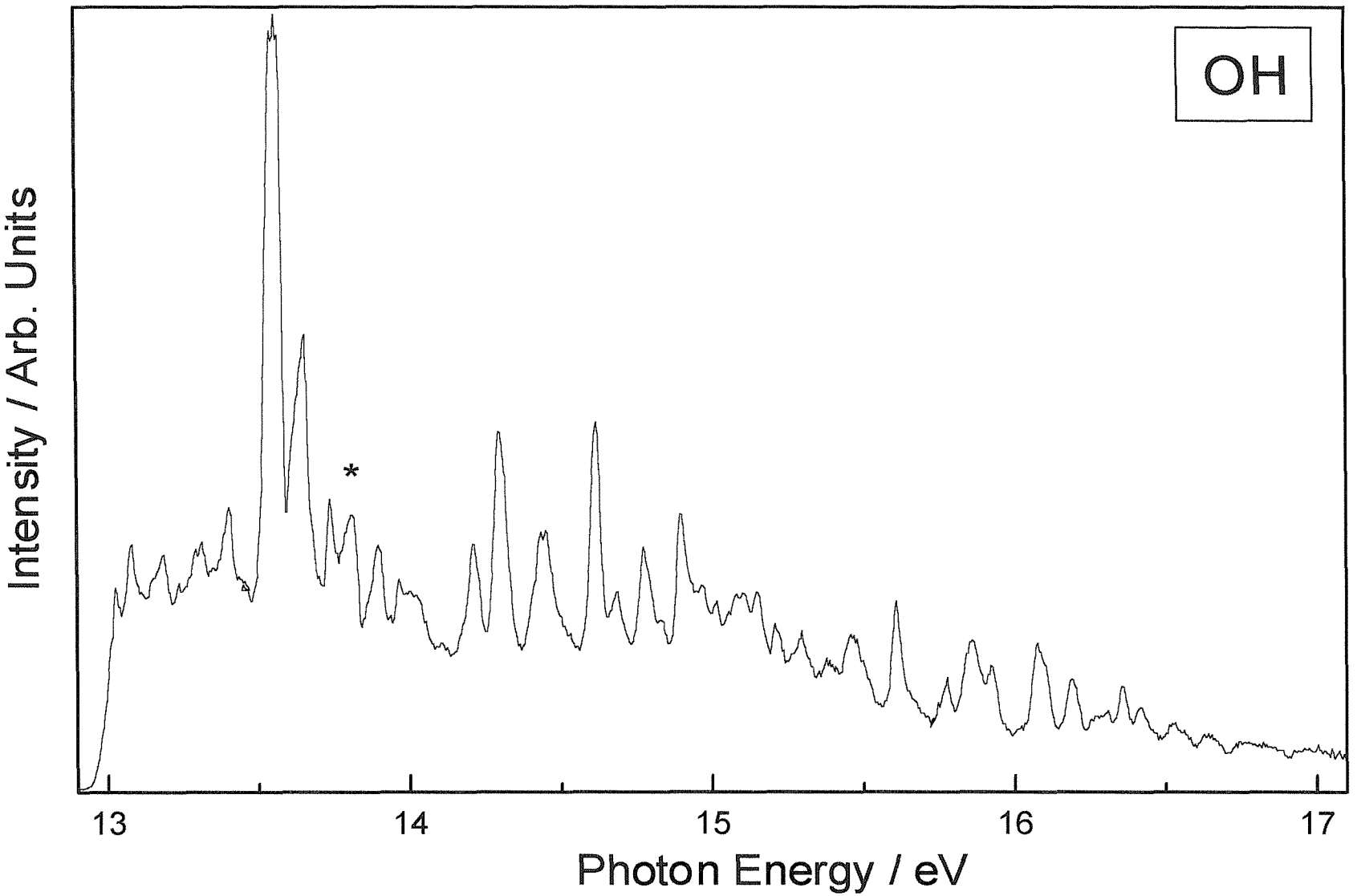

Figure 4.3: CIS spectrum recorded for [$OH^+(X^3\Sigma^-)$, $v^+=0$] in the photon energy range 13.0-17.0 eV. A peak which may be due to an NO resonance is marked with an asterisk(*).

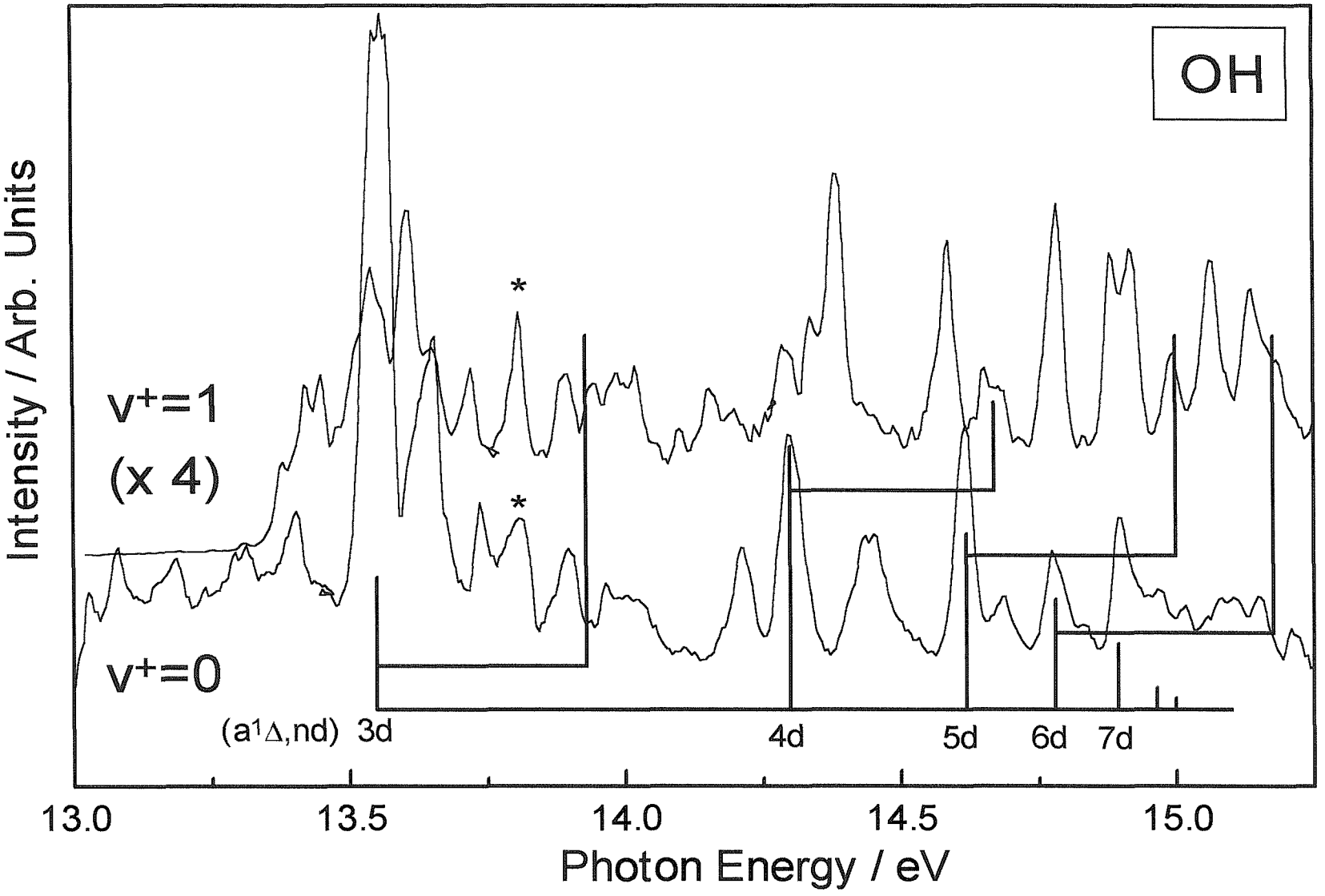

Figure 4.4: CIS spectra recorded for [$OH^+(X^3\Sigma^-)$, v^+=0 and 1] in the photon energy range 13.0-15.25 eV. Peaks which may be due to NO resonances are marked with an asterisk (*). The positions of OH* v′=0 and 1 resonances are indicated for each Rydberg state.

Energy (eV)	n*	Quantum defect δ	Rydberg Orbital
13.550	2.90	0.10	3d
14.300	3.95	0.07	4d
14.620	4.97	0.03	5d
14.785	5.94	0.06	6d
14.895	6.97	0.03	7d

Table 4.2: Resonances in the CIS of the $[OH^+(X^3\Sigma^-, v^+] \leftarrow [OH(X^2\Pi), v''=0]$ ionization over the photon energy range 13.0-15.2 eV assigned to Rydberg series members.

This series may be tentatively extended to include the weak features at around 14.96 and 15.00 eV. The mean quantum defect (δ) of this series is ~0.05 or ~1.05, suggesting either an nd or (n+1)s excited state assignment, both of which are reasonable considering the almost wholly O 2p character of the orbital from which the electron has been promoted and the $\Delta l=\pm 1$ atomic electric dipole selection rule for one-photon absorption. Unfortunately, the calculated position of the ($a^1\Delta$, 3s) component (n*~1.9) is at approximately 1.6 eV below the OH^+ ($X^3\Sigma^-$) onset, assuming δ=1.05, and so it was not possible to distinguish between the two assignments. Nevertheless, the ($a^1\Delta$, nd) series assignment is preferred for the following reasons.

There are two known Rydberg states of OH below the first ionization limit, which have been experimentally characterized: the $D^2\Sigma^-$ and $3^2\Sigma^-$ states[8,9,10] at excitation energies from the ground state of 10.14 and 10.86 eV, as determined by resonance-enhanced multiphoton ionization (REMPI) spectroscopy.[8,9,10] The lower-lying Rydberg state, the $D^2\Sigma^-$ state, is known to have an outermost half-filled orbital, which is of mixed 3s-3pσ character.[7] Its

excitation energy from the ground state gives n*=2.18, with n=3 and δ=0.82, where the δ value is between those expected for s and p Rydberg orbitals (1.0 and 0.6, respectively). For the $3^2\Sigma^-$ state, calculations[9] indicate that the occupied Rydberg orbital is also of mixed s-p character, with approximately equal s and p contributions in the Franck-Condon accessible region from the ground state. The transition energy of 10.86 eV, when combined with the first AIE of OH, gives n*=2.52, i.e., n=3, δ=0.48 (or n=4, δ=1.48, since in Ref. 8 the occupied Rydberg orbital was assumed to be a 4sσ orbital). Hence in Rydberg states of low n, which are nominally s or p in character, s-p mixing seems to be prevalent, and consequently if the series observed in the present work corresponds to a nominal (n+1)s excited state series, then values of δ which differ noticeably from 1.0 would be expected. Therefore, as the derived quantum defect is ~0.05 or ~1.05 for nominal nd or (n+1)s excited states, the lower value of δ(0.05), and thus an assignment to an nd series, is preferred for the Rydberg series shown in Figure 4.4.

To assist in the assignment of the ionic core associated with the Rydberg series shown in Figure 4.4, a procedure adopted successfully in similar earlier work[31,32,33] was used to compute Franck-Condon factors for the initial excitation and the subsequent autoionization steps, i.e., Franck-Condon factors were computed for processes 4 and 5 below:

$$OH^*, v' \xleftarrow{h\nu} [OH, (X^2\Pi), v'' = 0] \qquad (4)$$

$$[OH^+(X^3\Sigma^-), v^+] + e^- \leftarrow [OH^*, v'] \qquad (5)$$

In these calculations the OH ($X^2\Pi$), OH*, and OH^+ ($X^3\Sigma^-$) states were represented by Morse potentials specified using the well established values of r_e, ω_e and $\omega_e x_e$ for OH ($X^2\Pi$) and OH^+ ($X^3\Sigma^-$), and assuming OH* to be well represented by the r_e, ω_e and $\omega_e x_e$ values of the chosen ionic core.[23,34] Simulated CIS relative intensities were obtained by multiplying the Franck-Condon factors for both steps together. The OH results for v^+=0 and v^+=1 for v′=0-5 for OH* states with $a^1\Delta$ and $A^3\Pi$ ionic cores are shown in Fig. 4.5 together with those for OD. The calculations confirm the expectation that because the equilibrium bond length of the $a^1\Delta$ ion is so similar to that of both the neutral and ionic ground states, only v′=0 Rydberg states should be observed in the v^+=0 CIS spectrum and only v′=1 Rydberg states

should be observed in the $v^+=1$ CIS spectrum for OH* states with OH^+ ($a^1\Delta$) cores. In practice, there are features in the $v^+=1$ CIS spectrum separated from the [($a^1\Delta$,nd),$v'=0$] ($n=4$, 5 and 6) positions by approximately the OH^+ ($a^1\Delta$)0-1 vibrational spacing [2960 cm^{-1} (Ref. 20)]. Although it is difficult to estimate the level of the nonresonant background, the intensity of the $n=4$, $v'=0$ component in the $v^+=0$ spectrum is approximately eight times that of the $n=4$, $v'=1$ component in the $v^+=1$ spectrum, in rather poor agreement with the computed ratio based on relative intensities derived from the computed Franck-Condon factors (~5:1). Despite the fact that the $n=3$, $v'=0$ feature at 13.55 eV is very intense in the $v^+=0$ CIS spectrum, there is no obvious $n=3$, $v'=1$ component in the $v^+=1$ CIS spectrum at the correct vibrational spacing. This may be due to a dissociative state interacting with the OH*, $v'=1$ level or a breakdown of the Franck-Condon principle. Non-Franck-Condon behaviour has previously been recognised in photoionization spectra recorded for the $v'=0$-3 levels of OH ($X^3\Sigma^-$, $3p\sigma$)$D^2\Sigma^-$.[9] This can arise when molecular Rydberg orbitals evolve rapidly with internuclear distance and display Cooper minima in their photoionization cross sections.[9,35] The result is that the electronic transition moment is not constant with internuclear distance.

Figure 4.6 shows the [$OD^+(X^3\Sigma^-)$,$v^+=0,1$] CIS spectrum over the photon energy range 13.0-15.25 eV. The $v^+=0$ spectrum shows a broadly similar profile to the [$OH^+(X^3\Sigma^-)$,$v^+=0$] spectrum, consistent with much of the structure arising from the $v'=0$ Rydberg states, and the ($a^1\Delta$,nd) series observed in the OH CIS spectrum is also observed in the OD CIS spectrum. The $v'=1$ members of this series are difficult to observe in the $v^+=1$ spectrum since they are shifted to positions which overlap with more intense features. Nevertheless, there are features at the corresponding vibrational spacing from the [($a^1\Delta$,nd), $v'=0$] positions. In contrast to OH, there is a sharp feature at the expected [($a^1\Delta$, 3d), $v'=1$] position in the $v^+=1$ spectrum of OD.

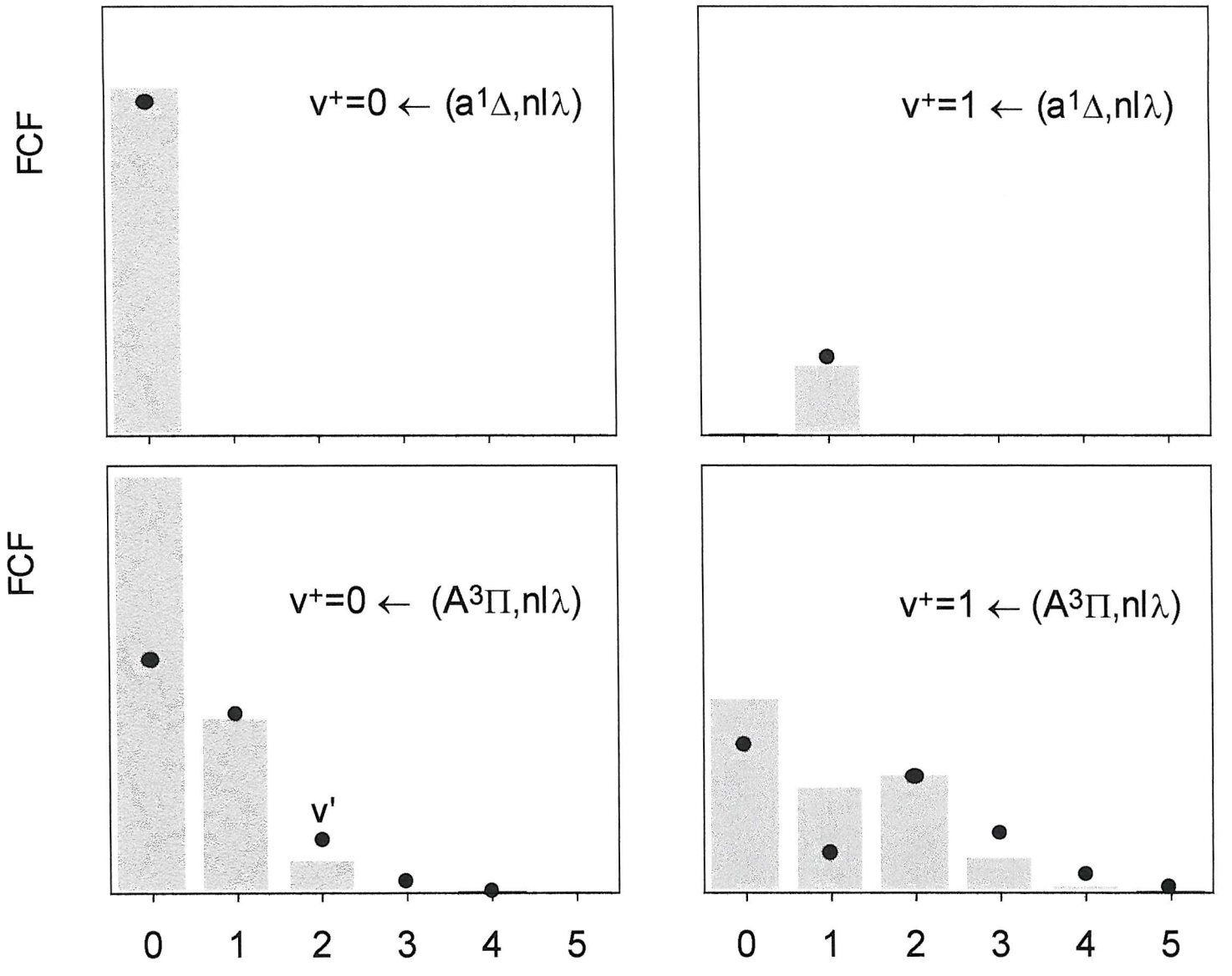

Figure 4.5: Simulated CIS spectra for [$OH^+(X^3\Sigma^-)$, v^+=0 and 1]. OH Rydberg states, denoted as OH*, are modelled on $a^1\Delta$ and $A^3\Pi$ ionic cores. CIS envelopes calculated for OH are indicated by bars and the corresponding envelopes for OD are denoted by circles

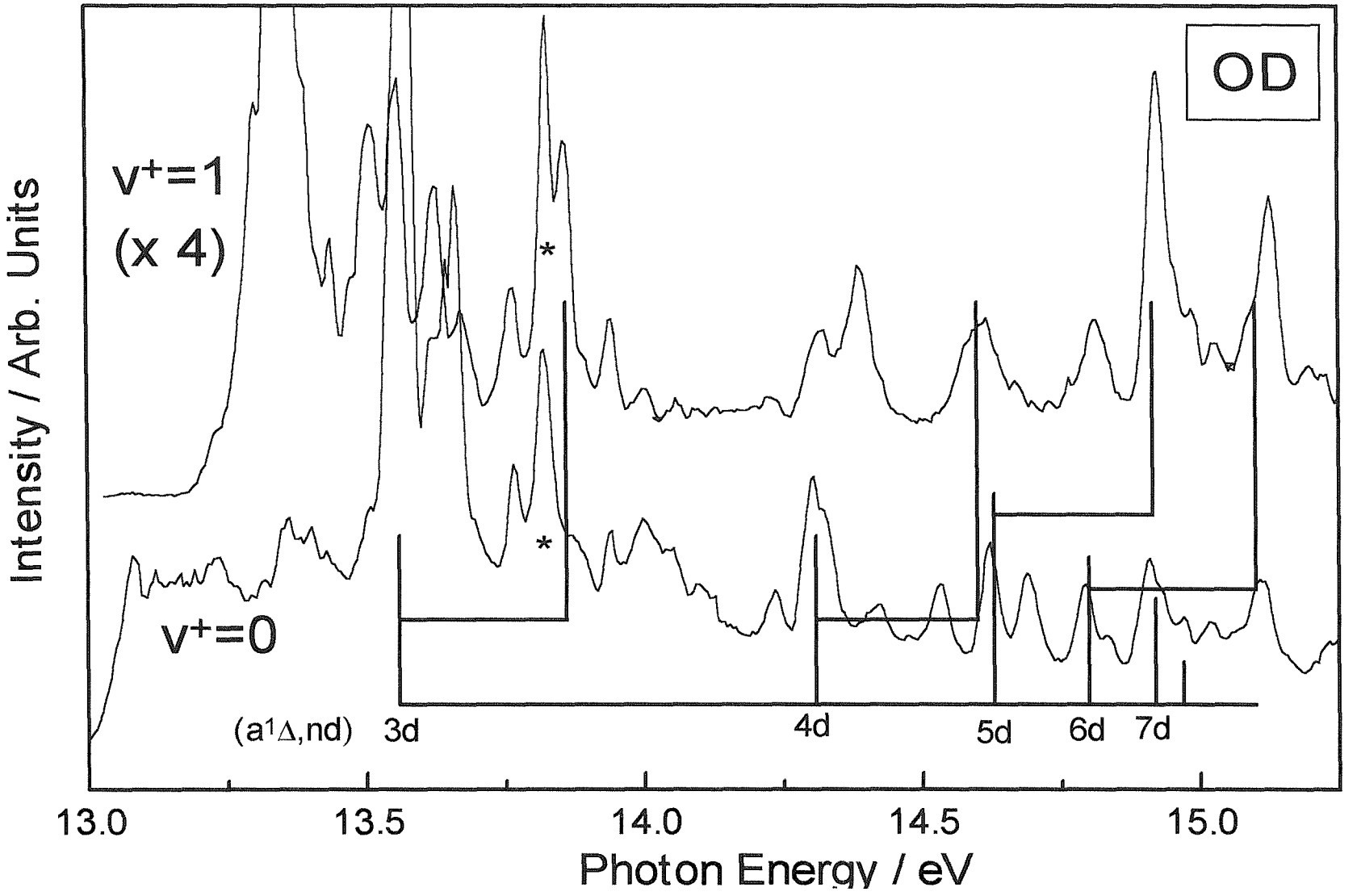

Figure 4.6: CIS spectra recorded for [$OD^+(X^3\Sigma^-)$, v^+=0 and 1] in the photon energy range 13.0-15.25 eV. Peaks which may be due to NO resonances are marked with an asterisk (*). The positions of OD* v′=0 and 1 resonances are indicated for each Rydberg state

The $(A^3\Pi,nd)\leftarrow X^2\Pi$ series

Figure 4.7 shows the [OH^+ ($X^3\Sigma^-$),v^+=0,1] and [$OH^+(a^1\Delta)$, v^+=0] CIS spectra over the photon energy range 14.8-17.0 eV. A consideration of the possible values of n* for each of the peaks in this region identified one Rydberg series converging to the $A^3\Pi$ ionic limit. Table 4.3 lists the energies, effective principal quantum numbers (n*) of the series members.

Energy (eV)	n*	Quantum defect δ	Rydberg Orbital
14.88	2.92	0.08	3d
15.61	3.95	0.05	4d
15.93	4.97	0.03	5d
16.10	5.98	0.02	6d
16.20	6.97	0.02	7d

Table 4.3: Resonances in the CIS of the [$OH^+(a^1\Delta$, v^+=0]$\leftarrow$[$OH(X^2\Pi)$, v''=0] and [$OH^+(X^3\Sigma^-)$,v^+=0,1]$\leftarrow$[$OH(X^2\Pi)$,v''=0] ionizations over the photon energy range 14.8-17.0 eV assigned to Rydberg series members.

This series could be assigned as an $(A^3\Pi,nd)$ series or an $[A^3\Pi,(n+1)s]$ series with quantum defects of ~0.03 or ~1.03. However, the $(A^3\Pi,nd)$ upper state assignment is preferred, as the positions of the major components shown in Figure 4.7 are very close to those expected from adding 1.31 eV [the $OH^+(A^3\Pi)$-$OH^+(a^1\Delta)$ separation] to the main components of the $(a^1\Delta,nd)$ series in Fig. 4.4. (Values of 14.86, 15.61, 15.93, 16.09 and 16.20 eV are obtained in this way.)

Calculated Franck-Condon profiles for CIS spectra involving an $A^3\Pi$ based Rydberg state are shown in the bottom half of Fig. 4.5 and indicate that OH*v'=0 and 1 components

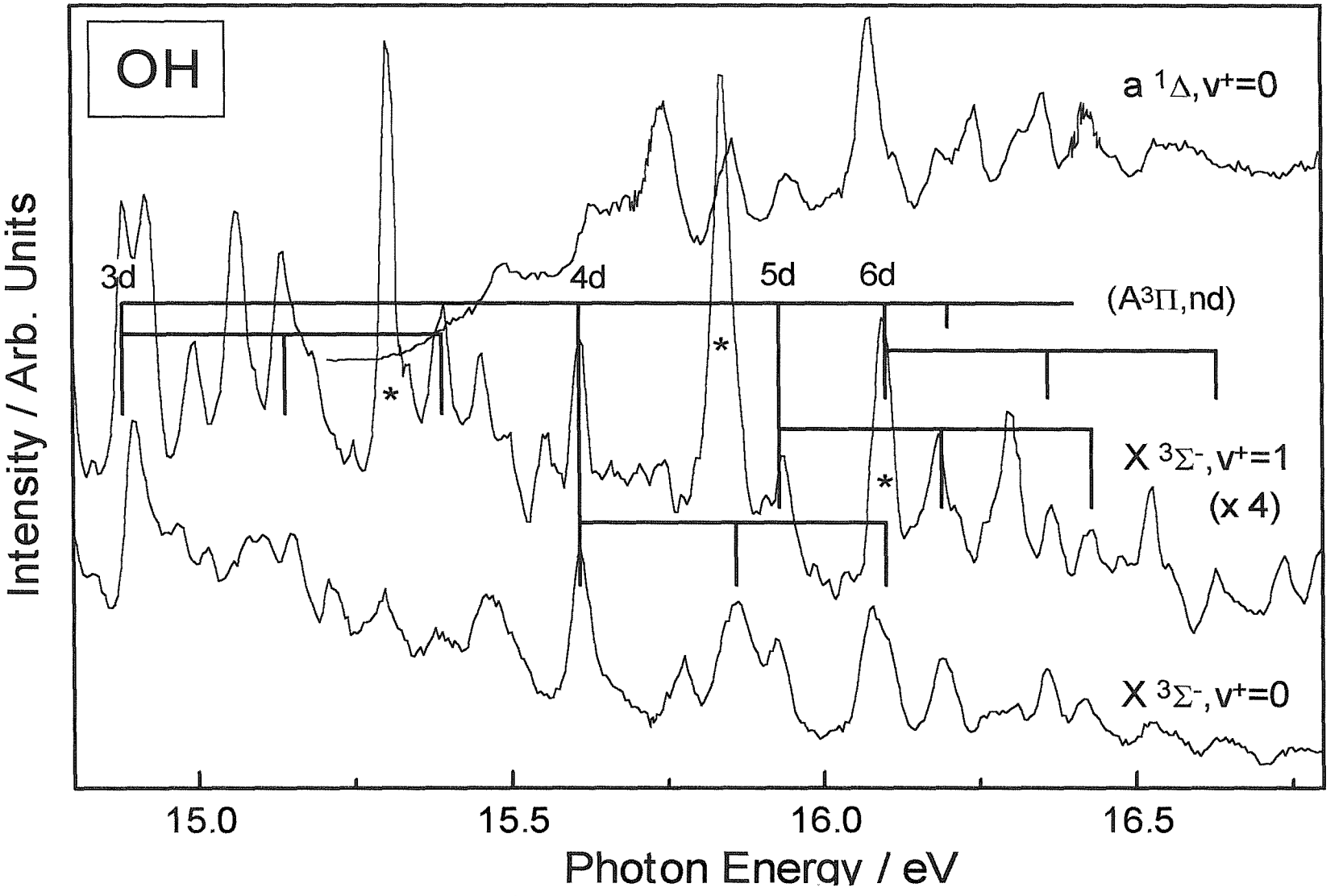

Figure 4.7: CIS spectra recorded for [$OH^+(X^3\Sigma^-)$, v^+=0 and 1] and [$OH^+(a^1\Delta)$, v^+=0] in the photon energy range 14.8-16.8 eV. Peaks which may be due to NO resonances are marked with an asterisk (*). The positions of OH* v′=0 and 1 resonances are indicated for each Rydberg state.

should be observed with appreciable intensity in the $[OH^+ (X^3\Sigma^-),v^+=0]$ channel and OH*, v′=0, 1 and 2 should be observed in the $[OH^+(X^3\Sigma^-),v^+=1]$ channel. Vibrationally excited components of $(A^3\Pi,nd)$ (n=3-6) states are clearly observed in $[OH^+ (X^3\Sigma^-),v^+=0,1]$ CIS spectra and have separations very close to that of the $A^3\Pi$ ionic state [1974 cm^{-1} (Ref. 23)]. Many of these vibrational features overlap with other members of the $(A^3\Pi,nd)$ series, members of the earlier $(a^1\Delta,nd)$ series and NO contaminating bands (three NO features are marked with an asterisk in Fig. 4.7). As a result it is difficult to estimate the vibrational envelope of a single observed band. Nevertheless, it can be seen that no more than three vibrational components are observed for a particular value of n and the first two appear to be comparable in intensity to each other and stronger than the third in qualitative agreement with the results of Franck-Condon calculations.

Because the equilibrium bond lengths of the $a^1\Delta$ and $X^3\Sigma^-$ ionic states are so similar, bands arising from autoionization to $OH^+(a^1\Delta)$ should exhibit the same vibrational profile in the $OH^+(a^1\Delta)$ CIS spectrum as that already observed in the $[OH^+(X^3\Sigma^-),v^+=0]$ CIS spectrum, at least for those resonant levels that can autoionize to both cationic states. The ionization onset shown in Figure 4.7 of the $[a^1\Delta,v^+=0]$ CIS spectrum is not sharp because of experimental difficulties in detecting low energy electrons at the time of this experiment. However, between 15.5 and 16.5 eV photon energy this spectrum does show significant structure. The positions of most of the observed resonances coincide with those already observed in the $OH^+(X^3\Sigma^-)$ CIS spectra as components of the $(A^3\Pi,nd)$ series. Despite this agreement, the $[a^1\Delta, v^+=0]$ and $[X^3\Sigma^-, v^+=0]$ CIS spectra do differ in detail although the exact reason for these differences is not clear at present. Figure 4.8 shows the $[X^3\Sigma^-, v^+=0,1]$ and $[a^1\Delta, v^+=0]$ CIS spectra of OD over the photon energy range 14.8-17.0 eV. All of the main $(A^3\Pi,nd)$ excited state features observed in the CIS spectrum of OH are observed in the OD spectrum. The assignment of the OH spectrum is supported by the fact that those peaks assigned to v′=0 resonances are observed at approximately the same resonant energies for OD and that the positions of the v′=1 and v′=2 resonances are reduced by an amount consistent with the expected isotopic vibrational shift. However, only semi-quantitative agreement was obtained with the results of the Franck-Condon calculations. For example, these calculations suggest that in the

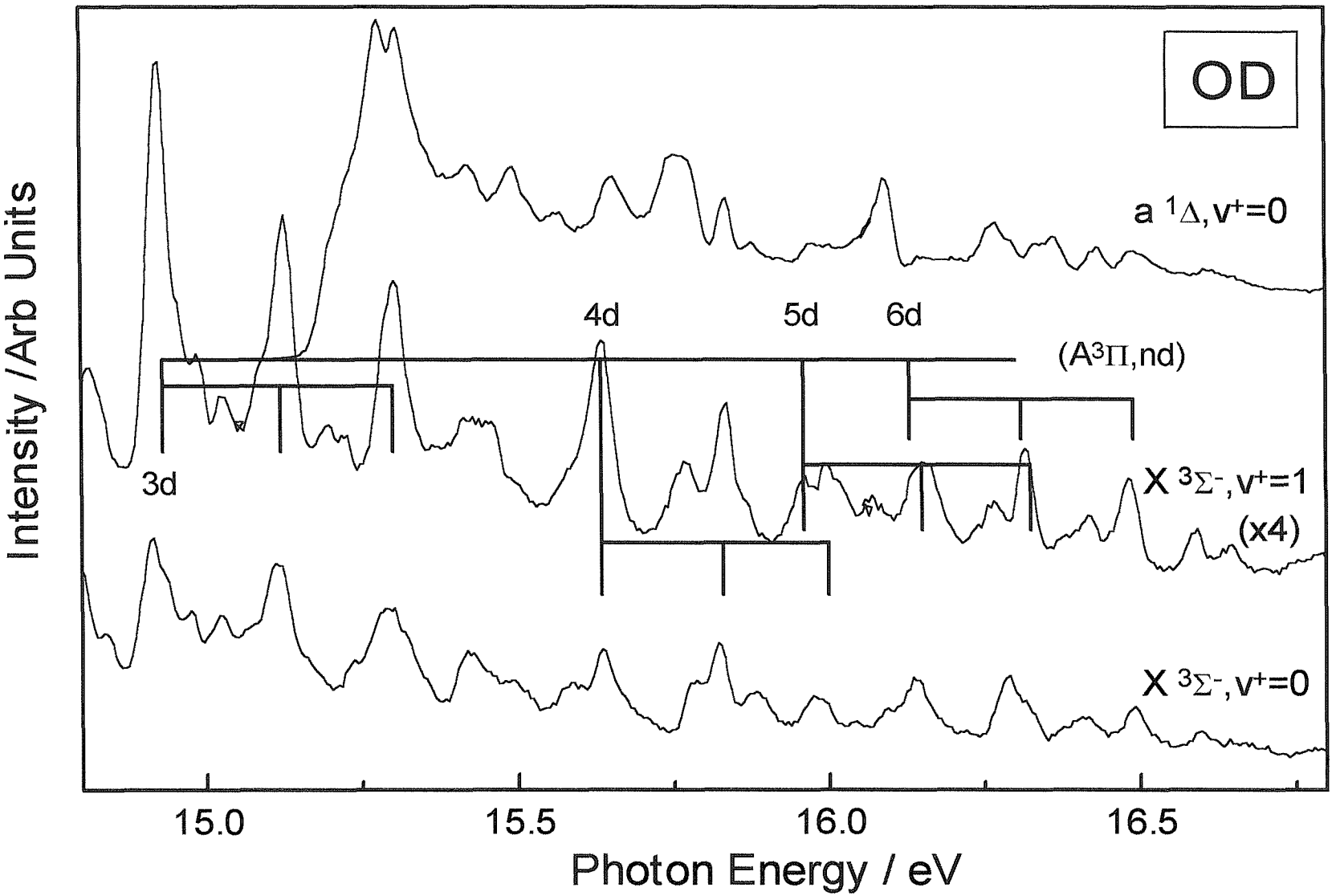

Figure 4.8: CIS spectra recorded for [$OD^+(X^3\Sigma^-)$, v^+=0 and 1] and [$OD^+(a^1\Delta)$, v^+=0] in the photon energy range 14.8-16.8 eV. Peaks which may be due to NO resonances are marked with an asterisk (*). The positions of OD* v′=0 and 1 resonances are indicated for each Rydberg state.

$[X^3\Sigma^-,v^+=1]$ CIS spectrum, the intensity of the $v'=1$ component of an $(A^3\Pi,nd)$ Rydberg state should be less than both the $v'=0$ and $v'=2$ components. However, in the $[X^3\Sigma^-, v^+=1]$ CIS spectrum, the $(A^3\Pi,4d)$ resonance, which is relatively free from band overlap, rather than following the Franck-Condon predictions, appears to show a steady drop in intensity over the three observed components from $v'=0$ to $v'=2$.

4.2.3 On resonance photoelectron spectra

In addition to recording CIS spectra, photoelectron spectra of the first photoelectron bands of OH and OD were recorded at photon energies corresponding to observed resonances. A number of these are shown in Fig. 4.9 together with a typical off-resonance spectrum of OH recorded at 21.22 eV photon energy [Fig. 4.9(a)]. In all of these spectra, the first band of H_2O (or D_2O) at 12.62 eV ionization energy was approximately constant in intensity and therefore intensity changes can be estimated relative to this band on changing the photon energy.

Increased vibrational intensities were observed in the OH first band at resonant wavelengths since the Franck-Condon factors for autoionization of a resonant state, OH* (or OD*), to the $X^3\Sigma^-$ state of OH^+ (or OD^+) are different from those for direct ionization. The contribution to the first photoelectron band for this resonant process was simulated by computing Franck-Condon factors for the autoionization step:

$$OH^+(X^3\Sigma^-),v^+=0\text{-}7 \leftarrow OH^*,v'$$

Calculations were carried out for OH* Rydberg states based on all four characterized excited ionic cores and the results for $a^1\Delta$ and $A^3\Pi$ based Rydberg states (with $v'=0,1,2$, and 3) are shown in Figure 4.10. As previously, since the equilibrium bond length of the $a^1\Delta$ ionic state is so similar to that of both the neutral and ionic ground states, the computed Franck-Condon factors indicate that autoionization from a Rydberg state based on the $a^1\Delta$ ionic core should occur with no change in vibrational quantum number. The photoelectron spectrum recorded at a photon energy of
14.30 eV, corresponding to excitation to an $(a^1\Delta ,4d),v'=0$ state, is shown in Fig. 4.9(b). As expected, this spectrum shows considerable enhancement of the $v^+=0$ component relative to

Figure 4.9: Photoelectron spectra recorded for the first band of OH (a)-(g) and OD (h). The photon energies used to obtain each spectrum are given in each diagram, as well as the resonant neutral state assignments for the on-resonance spectra (b)-(h). The positions of vibrational components in the first photoelectron band, as calculated from established ionic state constants, are indicated by combs in each diagram.

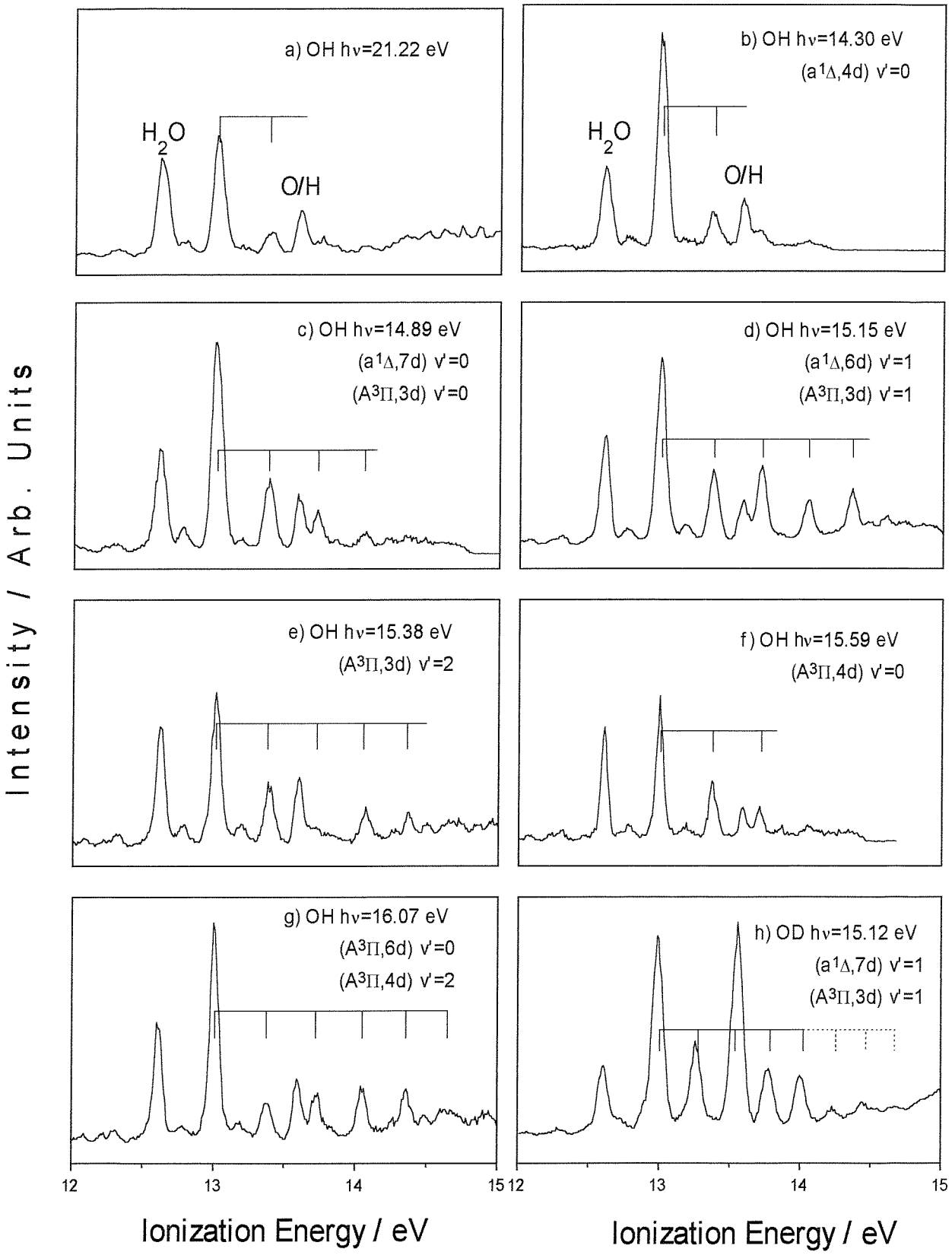

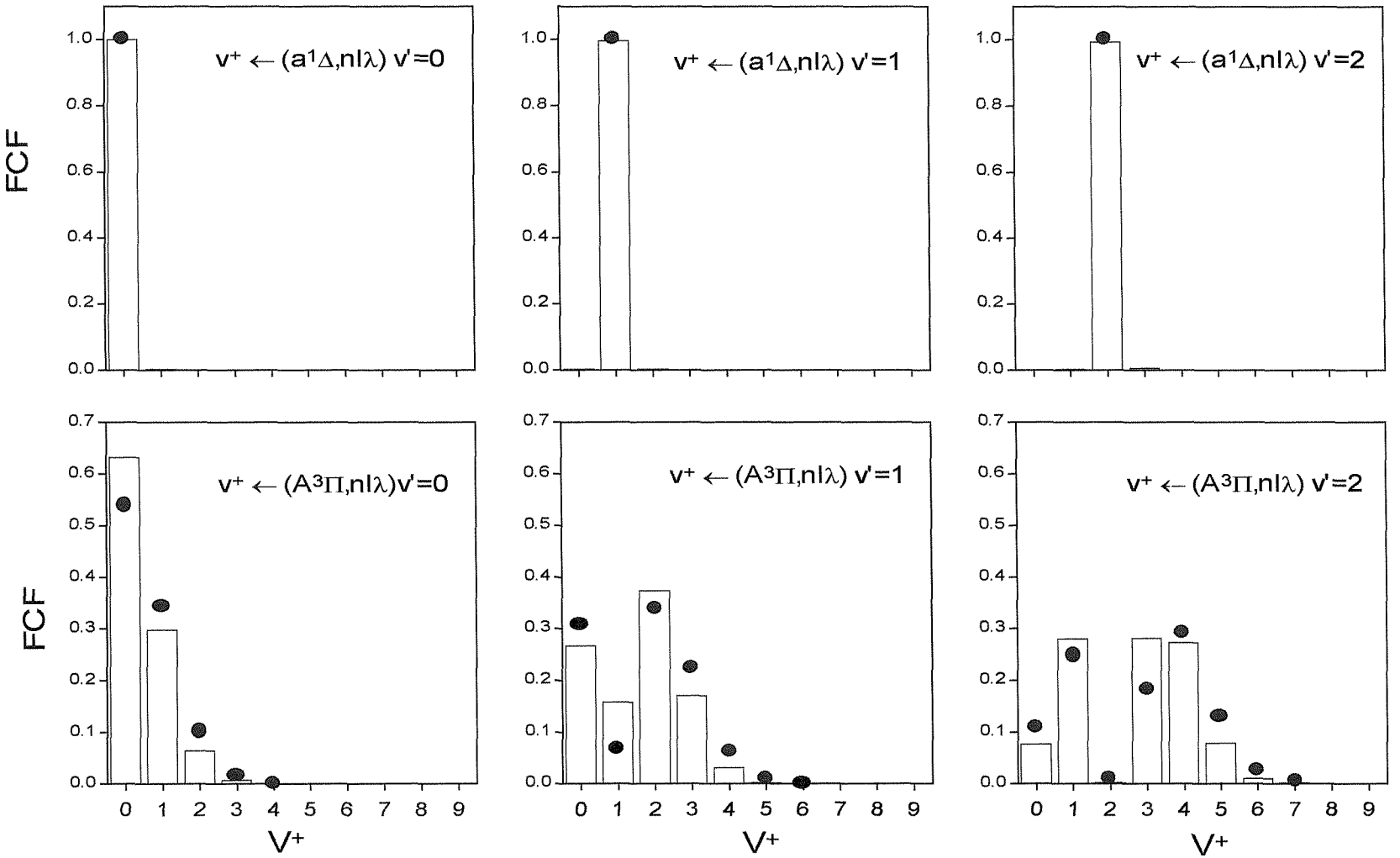

Figure 4.10: Simulated Franck-Condon envelopes for the first photoelectron band of OH arising from $[OH^+(X^3\Sigma^-),v^+]\leftarrow[OH^*,v']$ for resonant transitions to v'=0, 1, and 2, where OH* is modeled on $a^1\Delta$ and $A^3\Pi$ ionic cores. The computed Franck-Condon factors for OH are indicated by bars and the corresponding results for OD by circles.

the off-resonant spectrum [Fig. 4.9(a)]. It also shows a small enhancement of the $v^+=1$ $OH^+(X^3\Sigma^-)$ component, suggesting either excitation to a second resonance state at this photon energy or deviation from the Franck-Condon predictions.

All of the other on-resonant photoelectron spectra shown in Figure. 4.9 were recorded at photon energies which correspond to resonances with one or more $(A^3\Pi,nd)$ states which, in contrast to the $(a^1\Delta,nd)$ resonances, are expected to show enhanced intensity in a number of different v^+ channels. All of these spectra show reasonable agreement of their vibrational envelopes with the computed Franck-Condon profiles (see Fig. 4.10), bearing in mind that contributions from more than one calculated envelope need to be considered in most cases. The only example of an excitation energy which clearly corresponds to an $(A^3\Pi,nd)v'=0$ resonance, with no other contribution, is the $(A^3\Pi,4d)$ resonance at 15.59 eV photon energy. The photoelectron spectrum recorded at this energy [Fig. 4.9(f)] exhibits just three observable components, in agreement with the computed Franck-Condon envelope, although the $v^+=0$ component is less intense and the $v^+=2$ component is more intense, relative to the $v^+=1$ component, than the calculations suggest. The photoelectron spectrum recorded at 15.38 eV photon energy provides an example of an unoverlapped $(A^3\Pi,nd)v'=2$ resonance for which Franck-Condon calculations predict a very distinct vibrational profile with a minimum at $v^+=2$ and significant intensity in $v^+=3$ and 4. These features are reproduced in the experimental spectrum [Fig. 4.9(e)].

Perhaps the most significant on-resonance photoelectron spectra are those recorded at 15.15 and 16.07 eV photon energy [Figs. 4.9(d) and 4.9(g)] in which vibrational components up to $v^+=4$ are clearly observed for the first time by PES.

As can be seen from the CIS spectra in Fig. 4.7, there are contributions to each of these photoelectron spectra from at least two resonant states and it is difficult to estimate their relative cross sections. Nevertheless, it can be noted that the relative intensity of the $v^+=4$ component in the 15.15 eV spectrum is greater than that expected from only the $(A^3\Pi,3d),v'=1$ state, and that the relative intensity of the $v^+=2$ component in the 16.07 eV spectrum is anomalously large when one considers that the $(A^3\Pi,4d),v'=2$ resonant state should not autoionize to this channel as judged from the computed Franck-Condon factors. These results indicate that the Franck-Condon model, although qualitatively useful, is not

providing quantitative agreement with observed vibrational relative intensities. Reasons for this have been described earlier.

A number of on-resonant photoelectron spectra of OD were recorded but their interpretation was handicapped by masking of the $v^+=2$ feature by a significant O or D atom signal at an ionization energy of 13.61 eV. It was also found that, at many interesting resonant energies, high vibrational levels ($v^+=18$-23) of the first band of NO were observed in the 13.87-14.90 eV ionization energy region and exhibit positions and spacing almost coincident with those expected for the higher vibrational components ($v^+>3$) of OD. Nevertheless, it is interesting to compare the OD spectrum recorded at 15.12 eV [Fig. 4.9(h)] with that of OH at 15.15 eV [Fig. 4.9(d)] since both show autoionization from an $(A^3\Pi,3d),v'=1$ and an $(a^1\Delta,nd),v'=1$ state. Allowing for the isotopic shift of the vibrationally excited components and the overlap of
$[OD^+(X^3\Sigma^-), v^+=2]$ component with O or D atoms, the two experimental profiles are similar, both clearly exhibiting enhancement in $v^+=3$ and 4. The stronger features up to and including $v^+=4$ were all found to be due to OD, but the weaker features above $v^+=4$ in the OD spectrum are attributed to NO.

4.2.4 Other features in the CIS spectra

There are a number of strong features in the CIS spectra of OH and OD which do not belong to the $(a^1\Delta,nd)$ and $(A^3\Pi,nd)$ series so far assigned. These features were also observed in the earlier PIMS experiments but were not assigned.[16,17] The more intense unassigned features are at 14.785 and 15.060 eV in the $[OH^+(X^3\Sigma^-), v^+=1]$ CIS spectrum (these features are also seen weakly in the corresponding $v^+=0$ CIS spectrum), at 14.210 and 14.440 eV in the $[OH^+(X^3\Sigma^-), v^+=0]$ CIS spectrum and at 14.390 and 14.590 eV in the $[OH^+(X^3\Sigma^-), v^+=1]$ CIS spectrum. All six features can be seen in Figure 4.11.

Considering the 14.785 and 15.060 eV features first, the separation between these peaks is close to the vibrational spacing in $OH^+(A^3\Pi)$ and, assuming the peak at 14.785 eV to be the first vibrational component, n* for a state at this excitation energy and with an $A^3\Pi$ ionic core would be 2.83, consistent with n=3, $\delta=0.17$ or n=4, $\delta=1.17$. If, as the Franck-Condon calculations suggest, the third vibrational component of this state should be observable in the $[OH^+(X^3\Sigma^-), v^+=1]$ CIS spectrum then it must be masked by the strong NO contaminant

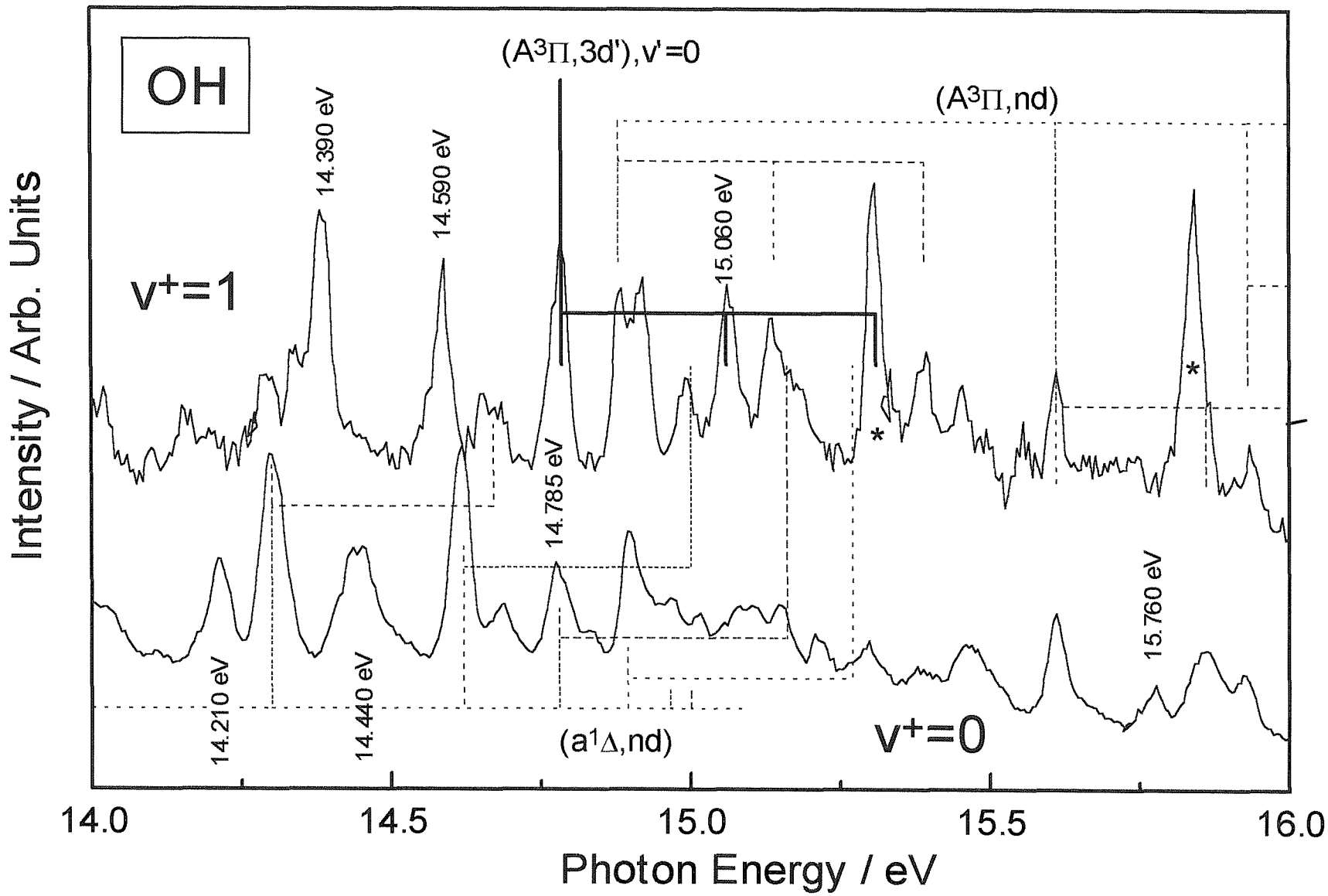

Figure 4.11: CIS spectra recorded for [$OH^+(X^3\Sigma^-)$, v^+=0 and 1] in the photon energy region 14.0-16.0 eV, showing overlap of the ($a^1\Delta$,nd) and ($A^3\Pi$,nd) Rydberg series (as dotted combs) and the positions of previously unassigned features. Peaks which may be due to NO resonances are marked with an asterisk (*). Vibrational combs are marked for OH*, v' resonances starting at v'=0 in each case.

at 15.30 eV (marked with an asterisk in Fig. 4.11). In support of an $A^3\Pi$ core for the excited Rydberg state, the photoelectron spectra recorded at 14.785 and 15.060 eV show extended vibrational profiles which are consistent with the assignment of these two features as $(A^3\Pi,nl\lambda),v'=0$ and 1; however, the relative intensities of the $v^+=2$ and $v^+=4$ components in the spectrum recorded at 15.060 eV are weaker than those in the spectrum recorded at 15.15 eV photon energy (an $(A^3\Pi,3d),v'=1$ resonance). In further support of this assignment, the CIS spectra of OD exhibit corresponding peaks at an appropriately contracted spacing. The question of whether the band at 14.785 eV corresponds to excitation to an $(A^3\Pi,nd)$ or $(A^3\Pi,ns)$ Rydberg state still remains, however. If the band at 14.785 eV was nominally assigned to an $(A^3\Pi,ns)$ excitation, as discussed earlier, then s-p mixing in the occupied Rydberg orbital at low n is expected to alter the derived value of δ significantly from the expected value of ~1.0. Hence, this band is assigned to a $(A^3\Pi,nd)$ excitation with n=3, δ=0.17.

The interpretation which is therefore favoured for the band at 14.785 eV is that it arises from excitation to the v'=0 level of an $(A^3\Pi,3d')$ state with the band at 15.060 eV being the v'=1 component (where the ' indicates a value of λ different to that of the nd series considered above). A separate d series can arise because a 3d orbital in $C_{\infty v}$ symmetry splits into $3d\sigma$, $3d\pi$, and $3d\delta$ components and each configuration $(A^3\Pi,3d\sigma)$, $(A^3\Pi,3d\pi)$ and $(A^3\Pi,3d\delta)$, gives rise to at least one doublet state which is formally allowed in a one-photon transition from the $X^2\Pi$ state of OH. Hence the 14.785 eV band is assigned to excitation to one $(A^3\Pi,3d')$ excited state with the band at 14.880 eV already having been assigned to excitation to another $(A^3\Pi,3d)$ state Bands associated with excitation to other $(A^3\Pi,nd')$ states (i.e., with n>3) were not resolved in this work.

Four other strong features in the CIS spectra of OH remain unassigned. Two occur in the $[X^3\Sigma^-, v^+=0]$ channel at 14.210 and 14.440 eV and two occur in the $v^+=1$ spectrum at 14.390 and 14.590 eV. All four can be seen in Fig. 4.11. None of these features occur strongly in both spectra and the spacing between peaks in the same CIS spectrum is less than the vibrational spacing in any known OH^+ state. The peaks in the $v^+=0$ channel at 14.210 and 14.440 eV are appropriately positioned to be v'=0 levels associated with v'=1 states observed in the $v^+=1$ CIS spectrum at 14.590 and

14.785 eV. Diagonal Franck-Condon factors of this type can arise from excitation to Rydberg states based on an $a^1\Delta$ or a $b^1\Sigma^+$ ionic core and only the latter ionic core assignment yields sensible values of n* (2.38 and 2.50), which could be interpreted as indicating excitation to ($b^1\Sigma^+$, 3pσ) and ($b^1\Sigma^+$, 3pπ) Rydberg states. This possible assignment is, however, inconsistent with the CIS spectra recorded for OD which show that the features at 14.210, 14.390, and 14.590 eV remain at approximately the same excitation energy, suggesting that they are all excitations to v′=0 vibrational levels. If this is so, then the absence of any significant peaks in the v^+=0 CIS spectrum at energies corresponding to peaks in the v^+=1 CIS spectrum (14.39 and 14.59 eV) is very puzzling, since a v′=0 Rydberg state based on any known ionic core should autoionize to the $X^3\Sigma^-$, v^+=0 level at least as strongly as to the $X^3\Sigma^-$, v^+=1 level. Finally, photoelectron spectra were recorded at photon energies corresponding to each unassigned feature and the OH envelopes were found to be significantly different from each other. The conclusion was therefore made that there is no Rydberg state assignment of any of these features (i.e., the peaks at 14.21, 14.44, 14.39, and 14.59 eV in Fig.4.11) which is consistent with the experimental evidence. It should be noted that a large number of valence states of OH have been calculated to lie in this excitation energy region[13,14,26] and that further analysis of the CIS spectra would benefit from more accurate determinations of the position and properties of these states.

In summary, all of the assignments made in the CIS spectra recorded in this work involve excitations to Rydberg states with $A^3\Pi$ or $a^1\Delta$ ionic cores and are consistent with photoelectron spectra recorded at the resonant photon energies. No firm evidence has been obtained for excitations to Rydberg states with $b^1\Sigma^+$ or $c^1\Pi$ ionic cores. In the case of $c^1\Pi$ based Rydberg states, this is because the $OH^+(c^1\Pi)\leftarrow OH\ (X^2\Pi)$ ionization energy (AIE expected at 18.30 eV)[20,23,24,25] is relatively high and transitions to Rydberg states with this ionic core are only expected above 16.60 eV excitation energy. In one of the earlier PIMS studies,[17] a Rydberg state was identified, with components at 13.18, 15.07, 15.75, and 16.07 eV, which was assigned to excitation to a ($b^1\Sigma^+$,ns) Rydberg series. However, this assignment could not be confirmed on the basis of CIS and PES results of this work. All of these features were observed in the present work; however, the peak at 13.18 eV is weak, and the peak at 16.07 eV would be coincident with the ($A^3\Pi$,4d),v′=2 and ($A^3\Pi$,6d),v′=0 features, already assigned in the above. As far as the remaining two features are concerned, only the peak at 15.75 eV is clearly seen in the v^+=0 channel, and it is also not seen in the

$v^-=1$ channel. In contrast, the peak at 15.07 eV is clearly seen in the $v^+=1$ channel, which contradicts the assignment of this feature to a $b^1\Sigma^+,v'=0$ Rydberg state since diagonal Franck-Condon factors are expected for autoionization from a Rydberg state based on a $b^1\Sigma^+$ core; in any case, this has been assigned in the present work as excitation to the $(A^3\Pi,3d'),v'=1$ state. Consequently, the only feature that could be assigned to a $(b^1\Sigma^+,5s)$ Rydberg state is the one at 15.75 eV, which would correspond to $\delta\sim1.0$. An alternative assignment would be to a $(b^1\Sigma^+,4d)$ state, with $\delta\sim0.0$.

4.2.5 Conclusions and Suggestions for Further Work

CIS spectra have been recorded for OH and OD in the 13.0-17.0 eV photon energy region. These spectra represent vibronically resolved relative photoionization cross sections at the fixed angle of collection used. Structure in these spectra has been analysed in terms of excitation to Rydberg states with $a^1\Delta$ and $A^3\Pi$ ionic cores, with an electron being excited from a 1π or 3σ valence molecular orbital to an nd Rydberg orbital.

The vibrational specificity of the CIS technique has allowed, for the first time, the positive identification of excitations to a number of Rydberg state excited vibrational levels of OH and OD. The vibrational profiles observed in the CIS spectra are in reasonable, but not exact, agreement with profiles obtained from Franck-Condon calculations. Photoelectron spectra of the first band of OH have been recorded at resonant photon energies and comparison of the vibrational envelopes with Franck-Condon computed envelopes provides support for the assignment of the CIS spectra. In some on-resonance photoelectron spectra, ionization to vibrational levels with $v^+>1$ of the $X^3\Sigma^-$ state of OH^+ and OD^+ has been recorded for the first time with up to six ionic vibrational levels being observed. An obvious extension of this work would be to probe the angular momentum composition of the free electron at resonance positions by carrying out angular distribution measurements at selected resonant photon energies.

This study has extended previous synchrotron PES work on reactive intermediates produced by microwave discharge of a flowing gas mixture[31,32,33] to the study of a short-lived molecule produced by an atom-molecule reaction. Other studies using the atom-molecule preparative route are planned.

4.3 References

1. R. P. Wayne, *Chemistry of Atmospheres* (Clarendon, Oxford, 1991).

2. F. J. Comes, *Angew. Chem. Int. Ed. Engl.* **33**, 1816 (1994).

3. D. J. Hucknall, *Chemistry of Hydrocarbon Combustion* (Chapman Hall, London, 1985); G. J. Mintoff and C. F. H. Tipper, *Chemistry of Combustion Reactions* (Butterworths, London, 1962).

4. A. Dalgarno and J. H. Black, *Rep. Prog. Phys.* **39**, 573 (1976); W. D. Watson, *Rev. Mod. Phys.* **48**, 513 (1976).

5. J. B. Nee and L. C. Lee, *J. Chem. Phys.* **81**, 31 (1984).

6. R. J. Cody, C. Maralejo, and J. E. Allen, *J. Chem. Phys.* **95**, 2491 (1991).

7. M. Collard, P. Kerwin, and A. Hodgson, *Chem. Phys. Lett.* **179**, 422 (1991).

8. E. de Beer, M. P. Koopmans, C. A. de Lange, Y. Wang, and W. A. Chupka, *J. Chem. Phys.* **94**, 7634 (1991).

9. E. de Beer, C. A. de Lange, J. A. Stephens, K. Wang, and V. McKoy, *J. Chem. Phys.* **95**, 714 (1991).

10. C. A. de Lange, in *High Resolution Laser Photoionization and Photoelectron Studies,* edited by I. Powis, T. Baer and C. Y. Ng (Wiley, Chichester, 1995).

11. J. C. Viney, *J. Mol. Spec.* **83**, 465 (1980).

12. A. E. Douglas, *Can. J. Phys.* **52**, 318 (1984).

13. E. F. van Dishoeck and A. Dalgarno, *J. Chem. Phys.* **79**, 873 (1983).

14. E. F. van Dishoeck, S. R. Langhoff and A. Dalgarno, *J. Chem. Phys.* **78**, 4552 (1983).

15. A. V. Nemukhin and B. L. Grigorenko. *Chem. Phys. Lett.* **276**, 171 (1997).

16. P. M. Dehmer, *Chem. Phys. Lett.* **110**, 79 (1984).

17. J. N. Cutler, Z. X. He and J. A. R. Samson, *J. Phys. B.* **28**, 4577 (1995).

18. R. T. Wiedmann, R. G. Tonkyn and M. G. White, *J. Chem. Phys.* **97**, 768 (1992).

19. S. Katsumata and D. R. Lloyd, Chem. Phys. Lett. **45**, 519 (1977).

20. H. van Lonkhuyzen and C. A. de Lange, Mol. Phys. **51**, 551 (1984).

21. D. J. Rodgers and P. J. Sarre, *Chem. Phys. Lett.* **143**, 235 (1988).

22. D. M. Hirst and M. F. Guest, *Mol. Phys.* **49**, 1461 (1983).

23. A. J. Merer, D. N. Malm, R. W. Martin, M. Horani and J. Rostas, *Can. J. Phys.* **53**, 251 (1975).

24. D. J. Rodgers and P. J. Sarre, *Chem. Phys. Lett.* **143**, 235 (1988).

25. D. M. Hirst and M. F. Guest, *Mol. Phys.* **49,** 1461 (1983).

26. I. Easson and M. H. L. Pryce, *Can. J. Phys.* **51**, 518 (1973).

27. R. P. Saxon and B. Liu, *J. Chem. Phys.* **85**, 2099 (1986).

28. R. de Vivie, C. M. Marion and S. D. Peyerimhoff, *Chem. Phys.* **112**, 349 (1987).

29. D. W. Turner, C. Baker, A. D. Baker and C. R Brundle, *Molecular Photoelectron Spectroscopy* (Wiley-Interscience, New York, 1971).

30. P. Erman, A. Karawajczyk, E. Rachlew-Kälne, and C. Strömholm, *J. Chem. Phys.* **102**, 3064 (1995).

31. J. M. Dyke, D. Haggerston, A. Morris, S. Stranges, J. B. West, T. G. Wright and A. E. Wright, *J. Chem. Phys.* **106**, 821 (1997).

32. J. M. Dyke, S. D. Gamblin, D. Haggerston, A. Morris, S. Stranges, J. B. West, T. G. Wright and A. E. Wright, *J. Chem. Phys.* **108**, 6258 (1998).

33. J. D. Barr, A. De Fanis, J. M. Dyke, S. D. Gamblin, A. Morris, S. Stranges, J. B. West, T. G. Wright and A. E. Wright, *J. Chem. Phys.* **109**, 2737 (1998).

34. K. P. Huber and G. Herzberg, *Molecular Spectra and Molecular Structure IV: Constants of Diatomic Molecules* (van Nostrand Reinhold Co., New York, 1979).

35. J. A. Stephens and V. McKoy, *Phys. Rev. Lett.* **62**, 889 (1989); J. A. Stephens and V. McKoy, *J. Chem. Phys.* **88**, 1737 (1988).

Chapter 5: A study of $O_2(a^1\Delta_g)$ with photoeletron spectroscopy using synchrotron radiation

5.1 Introduction and Previous work on $O_2(a^1\Delta_g)$

As oxygen is a major atmospheric constituent, vacuum ultraviolet photoionization of O_2, a process which occurs in the upper atmosphere through interaction with solar radiation, has been the subject of extensive investigations by photoionization mass spectrometry[1] and photoelectron spectroscopy.[2,3,4,5,6,7] The first excited state of oxygen, the $a^1\Delta_g$ state, is also an important atmospheric constituent. It is present in relatively high partial pressures in the stratosphere, being produed with $O(^1D)$ from photolysis of ozone, and is one of the strongest contributors to the atmospheric airglow.[8] Photoionization of $O_2(a^1\Delta_g)$ has been suggested as an important source of ions in the D region of the atmosphere to explain both the O_2^+ partial pressures and the total ion densities at these altitudes.[9,10,11] $O_2(a^1\Delta_g)$ ionization is also thought to be important at lower altitudes (<70 km) in providing a source of O_2^+ which can be involved, with NO, NO^+, and H_2O, in a sequence of reactions leading to the formation of protonated water clusters.[12,13]

The ground electronic configuration of O_2, which gives rise to the X, a, and b states, is

$$1\sigma_g^2 1\sigma_u^2 2\sigma_g^2 2\sigma_u^2 3\sigma_g^2 1\pi_u^4 1\pi_g^2$$

In the HeI photoelectron spectrum of $O_2(X^3\Sigma_g^-)$ five bands are observed,[2] corresponding to ionization to the O_2^+ states $X^2\Pi_g$, $a^4\Pi_u$, $A^2\Pi_u$, $b^4\Sigma_g^-$, and $B^2\Sigma_g^-$ with respective adiabatic ionization energies of 12.07, 16.10, 17.04, 18.17, and 20.30 eV. Removal of the $1\pi_g$ electron gives the $X^2\Pi_g$ state of O_2^+, removal of the $1\pi_u$ electron gives the $a^4\Pi_u$ and $A^2\Pi_u$ ionic states, and the $b^4\Sigma_g^-$ and $B^2\Sigma_g^-$ states arise from removal of the $3\sigma_g$ electron. For $O_2(a^1\Delta_g)$, electron removal from the $1\pi_g$ level gives $O_2^+(X^2\Pi_g)$, while loss of an electron from the $1\pi_u$ level gives $O_2^+(C^2\Phi_u)$ and $(A^2\Pi_u)$ and the $(3\sigma_g)^{-1}$ ionization gives $O_2^+(D^2\Delta_g)$. By recording a HeI photoelectron spectrum of discharged oxygen, and subtracting a spectrum recorded with the discharge off, well-resolved photoelectron bands have been

recorded for the ionizations $O_2^+(X^2\Pi_g)\leftarrow O_2(a^1\Delta_g)$, $O_2^+(A^2\Pi_u)\leftarrow O_2(a^1\Delta_g)$, $O_2^+(C^2\Phi_u)\leftarrow O_2(a^1\Delta_g)$, and $O_2^+(D^2\Delta_g)\leftarrow O_2(a^1\Delta_g)$.[14,15]

Rydberg excited states of $O_2(a^1\Delta_g)$ which are members of series which converge to the first ionic state, $O_2^+(X^2\Pi_g)$, have been studied in some detail by laser multiphoton ionization spectroscopy.[16,17,18,19,20,21] Also, the photoionization cross section of $O_2(a^1\Delta_g)$ has been measured between the ionization thresholds of the *a* and the *X* neutral states (11.09-12.07 eV).[22] Some resonant structure was observed in the photoionization efficiency curves obtained, but no excited state assignments were made. This excitation energy range is calculated to be too low for the observation of Rydberg states which are parts of series converging to $O_2^+(A^2\Pi_u)$, the lowest accessible excited state of O_2^+, so these resonant features probably correspond to vibrational autoionization from Rydberg states with an $O_2^+(X^2\Pi_g)$ core or autoionization from an excited state of valence character. Measurements of the absorption spectrum of $O_2(a^1\Delta_g)$ in the energy region 7.5-11.1 eV revealed excitation to Rydberg states which are parts of series converging to $O_2^+(X^2\Pi_g)$.[23] In this investigation strong npπ and weak npσ series were observed, in addition to a series tentatively assigned to excitation to nf orbitals.[23] Absorption spectra of $O_2(a^1\Delta_g)$ in the energy regions 7.6-9.6 and 13.7-14.8 eV have been observed by Katayama, Huffman, and co-workers.[24,25,26] In the earlier studies,[24,25] a vibrationally resolved band at ≈14.0 eV excitation energy was assigned to a $(C^2\Phi_u,3s\sigma_g)\ ^1\Phi_u\leftarrow a^1\Delta_g$ transition. Some of the vibrational components were rotationally resolved and an unusual alternating pattern of narrow and broad lines was observed in the vibrational members of this band, which was attributed to a combination of predissociation and autoionization. In the third study,[26] at lower excitation energy, an absorption of $O_2(b^1\Sigma_g^+)$ was observed, and some other diffuse features were assigned to $O_2(a^1\Delta_g)$ absorptions.

The objective of the work described in this chapter was to obtain more information on Rydberg states of $O_2(a^1\Delta_g)$ which lie above the first ionization threshold and to record photoelectron spectra at resonant photon energies, with the aim of obtaining extended vibrational structure.

5.2 Results and Discussion

A HeI photoelectron spectrum recorded with an oxygen discharge on and off is shown in Figure 5.1, with the assignment of the major features indicated in the caption. The 0.98 eV excitation energy of $O_2(a^1\Delta_g)$ relative to $O_2(X^3\Sigma_g^-)$ means that the first four vibrational components of the $O_2^+(X^2\Pi_g)\leftarrow O_2(a^1\Delta_g)$ band (labeled 1 in Figure 5.1) are observed before the onset of the more intense $O_2^+(X^2\Pi_g)\leftarrow O_2(X^3\Sigma_g^-)$ band (labeled 2). Also observed are features due to oxygen atoms, labeled as 3 and 5. The second and third bands of $O_2(a^1\Delta_g)$, arising from ionization to the $A^2\Pi_u$ and $C^2\Phi_u$ ionic states, occur in the regions labelled 4 and 6. These bands are not resolved in Figure 5.1, but can be clearly observed if the discharge is pulsed and a phase-sensitive method is used to detect photoelectron signals in-phase and out-of-phase with the discharge.[14,15,27] A photoelectron spectrum recorded using this method is shown in Figure 5.2 where signals due to $O_2(X^3\Sigma_g^-)$ are observed out-of-phase with the discharge (below the baseline in Figure 5.2) whereas those due to $O(^3P)$ and $O_2(a^1\Delta_g)$ are observed in-phase with the discharge (above the baseline in Figure 5.2). The $O_2^+(A^2\Pi_u)\leftarrow O_2(a^1\Delta_g)$ and the $O_2^+(C^2\Phi_u)\leftarrow O_2(a^1\Delta_g)$ bands can be clearly seen in this Figure. The measured separations in these vibrationally resolved bands gave ω_e=(898±30) cm^{-1} and $\omega_e x_e$=(14±5) cm^{-1}, ω_e=(1043±26) cm^{-1} and $\omega_e x_e$=(9±4) cm^{-1} in the $A^2\Pi_u$ and $C^2\Phi_u$ ionic states respectively.[14,15,27]

As the first four vibrational components of the $O_2^+(X^2\Pi_g)$, $v^+\leftarrow O_2(a^1\Delta_g)$, $v''=0$ band do not overlap with the $O_2^+(X^2\Pi_g)$, $v^+\leftarrow O_2(X^3\Sigma_g^-)$, $v''=0$ photoelectron band, CIS spectra can readily be recorded for these first four components of the first $O_2(a^1\Delta_g)$ photoelectron band. The CIS spectrum for $O_2^+(X^2\Pi_g)$, $v^+=2\leftarrow O_2(a^1\Delta_g)$, $v''=0$, recorded over the photon energy range 12.0-20.0 eV, is shown in Figure 5.3. Very low signals were observed between the ionization threshold (≈11.55 eV for $v^+=2$) and 12.0 eV because of low photon flux. The strongest features in Fig. 5.3 are two intense bands in the 14.0-15.0 eV region. Other signals were observed, notably weak features

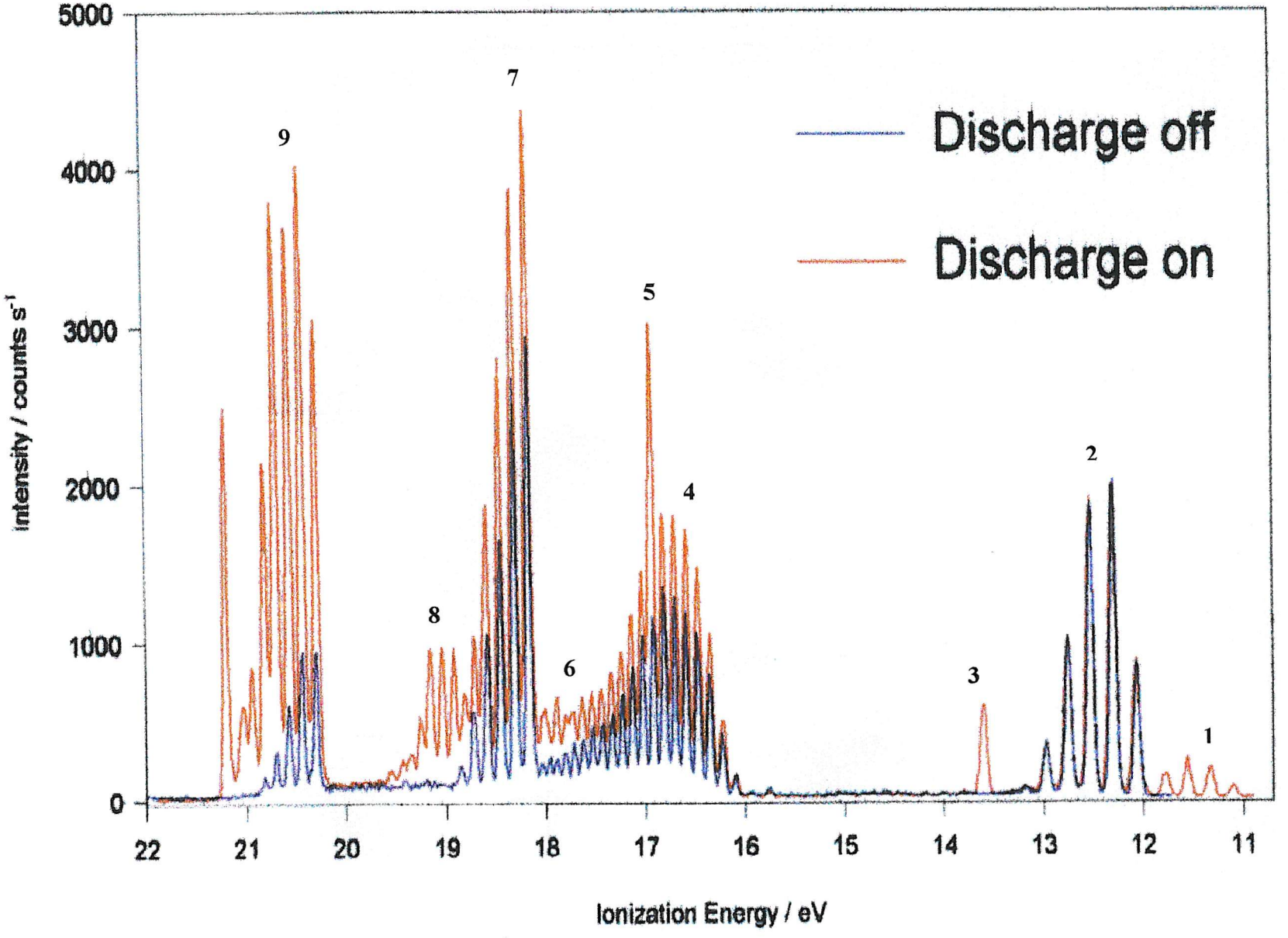

Figure 5.1:

HeI photoelectron spectrum recorded for discharged /undischarged oxygen. In this Figure, numbers are used as follows to label bands associated with the following ionizations

1. $O_2^+(X^2\Pi_g) \leftarrow O_2(a^1\Delta_g)$;
2. $O_2^+(X^2\Pi_g) \leftarrow O_2(X^3\Sigma_g^-)$;
3. $O^+(^4S) \leftarrow O(^3P)$
4. $O_2^+(a^4\Pi_u) \leftarrow O_2(X^3\Sigma_g^-)$
   $O_2^+(A^2\Pi_u) \leftarrow O_2(a^1\Delta_g)$;
5. $O^+(^2D) \leftarrow O(^3P)$;
6. $O_2^+(A^2\Pi_u) \leftarrow O_2(X^3\Sigma_g^-)$
   $O_2^+(C^2\Phi_u) \leftarrow O_2(a^1\Delta_g)$;
7. $O_2^+((b^4\Sigma_g^-) \leftarrow O_2(X^3\Sigma_g^-)$;
8. $O_2^+(D^2\Delta_g) \leftarrow O_2(a^1\Delta_g)$;
9. $O_2^+((B^2\Sigma_g^-) \leftarrow O_2(X^3\Sigma_g^-)$;

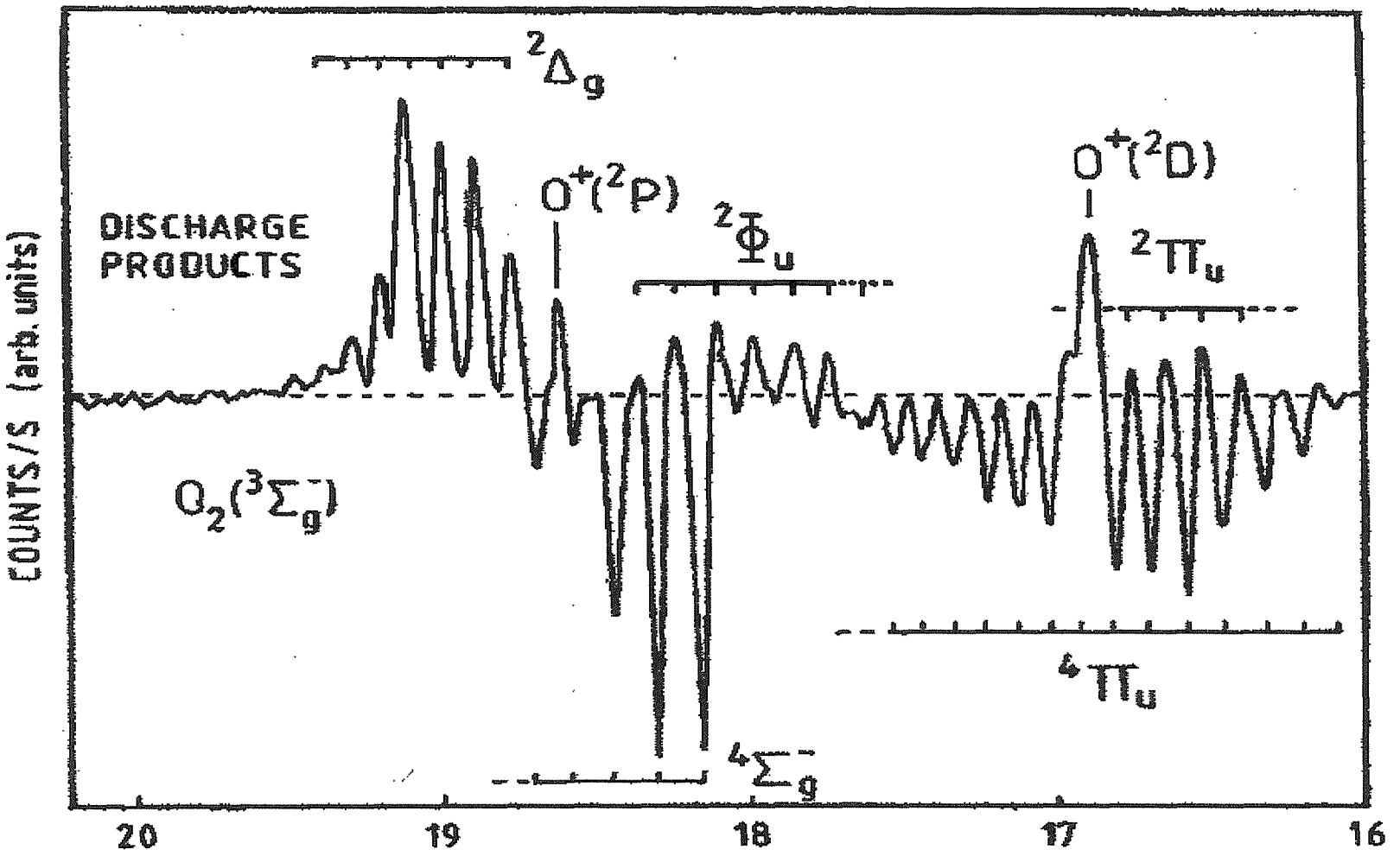

Figure 5.2: Phase-sensitive detection HeI photoelectron spectrum recorded for discharged oxygen. The discharge is pulsed and a phase sensitive detection method is used. Features above the horizontal baseline are in-phase with the discharge and features below are out-of-phase with the discharge. Hence the features above the baseline correspond to discharge products.

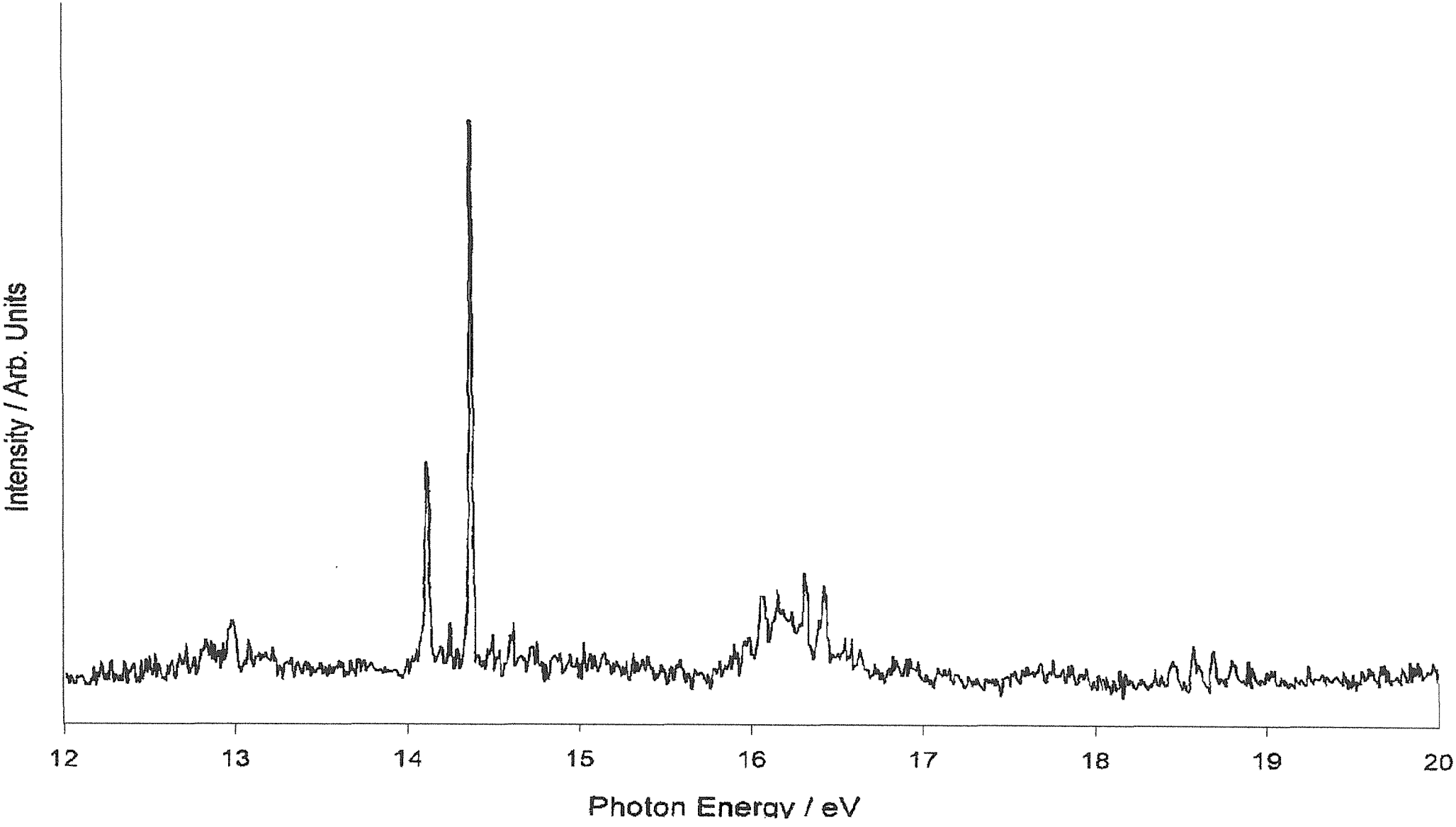

Figure 5.3: CIS spectrum recorded for $O_2^+(X^2\Pi_g)v^+=2 \leftarrow O_2(a^1\Delta_g)$, $v''=0$ over the photon energy region 12.0-20.0 eV

between 12.5 and 13.5 eV, a stronger, broad structured band at ≈16.0 eV and weaker features centred at approximately 18.5 eV. This CIS spectrum will be considered in three sections, (A): 14.0-15.5 eV, (B): 12.5-13.5 eV, and (C): 15.5-19.0 eV.

A. The 14.0-15.5 eV photon energy region

CIS spectra in this photon energy range have been recorded for the first four vibrational components of $O_2^+(X^2\Pi_g)$ and are shown in Figure 5.4. Each spectrum has been corrected for variation in the photon flux. Two bands, labelled A and B, dominate the spectra at 14.11 and 14.37 eV. It was not immediately obvious why only two intense bands were observed; they are approximately 2100 cm^{-1} apart, roughly twice the vibrational separation of any known excited state of O_2^+, so they cannot represent consecutive vibrational levels in a Rydberg state. The intensities of these bands are unusually high and photoelectron spectra recorded at these photon energies (shown later) demonstrate that these photon energies correspond to autoionization resonances of $O_2(a^1\Delta_g)$. The first two excited states of O_2^+ accessible from $O_2(a^1\Delta_g)$ are the $O_2^+(A^2\Pi_u)$ and $O_2^+(C^2\Phi_u)$ states, with adiabatic ionization energies of 16.06 and 17.51 eV, respectively.[14,15,27] Hence the possibility that bands A and B are both components of a Rydberg state with either an $O_2^+(A^2\Pi_u)$ or an $O_2^+(C^2\Phi_u)$ core was investigated initially, although it was noted that the A-B separation in Figure X.4 was too large to be two consecutive vibrational separations in a Rydberg state with an $O_2^+(A^2\Pi_u)$ core.

As mentioned previously, Katayama, Huffman, and co-workers[24,25] have observed absorption to an excited state of $O_2(a^1\Delta_g)$ in this photon energy region. In the experimental vacuum ultraviolet (vuv) absorption spectrum[24] not all vibrational levels in the excited state were observed and only a few vibronic bands were rotationally resolved. Analysis of the absorption spectrum yielded upper state constants of ω'_e=1071±4 cm^{-1}, $\omega_e x'_e$=8.3±0.8 cm^{-1}, and r'_e=1.374±0.0008 Å,[24] values which are sufficiently similar to the known constants of $O_2^+(C^2\Phi_u)$, derived from the analysis of the vibrationally resolved $O_2^+(C^2\Phi_u)\leftarrow O_2(a^1\Delta_g)$ photoelectron band, to imply Rydberg character for the excited state with an $O_2^+(C^2\Phi_u)$ core.

Figure 5.4:

CIS spectra recorded for $O_2^+(X^2\Pi_g)v^+ \leftarrow O_2(a^1\Delta_g)v''=0$ over the photon energy region 14.0-15.0 eV, for $v^+=0$, 1, 2, 3. The black symbols indicate the computed CIS relative intensities derived from Franck-Condon calculations.

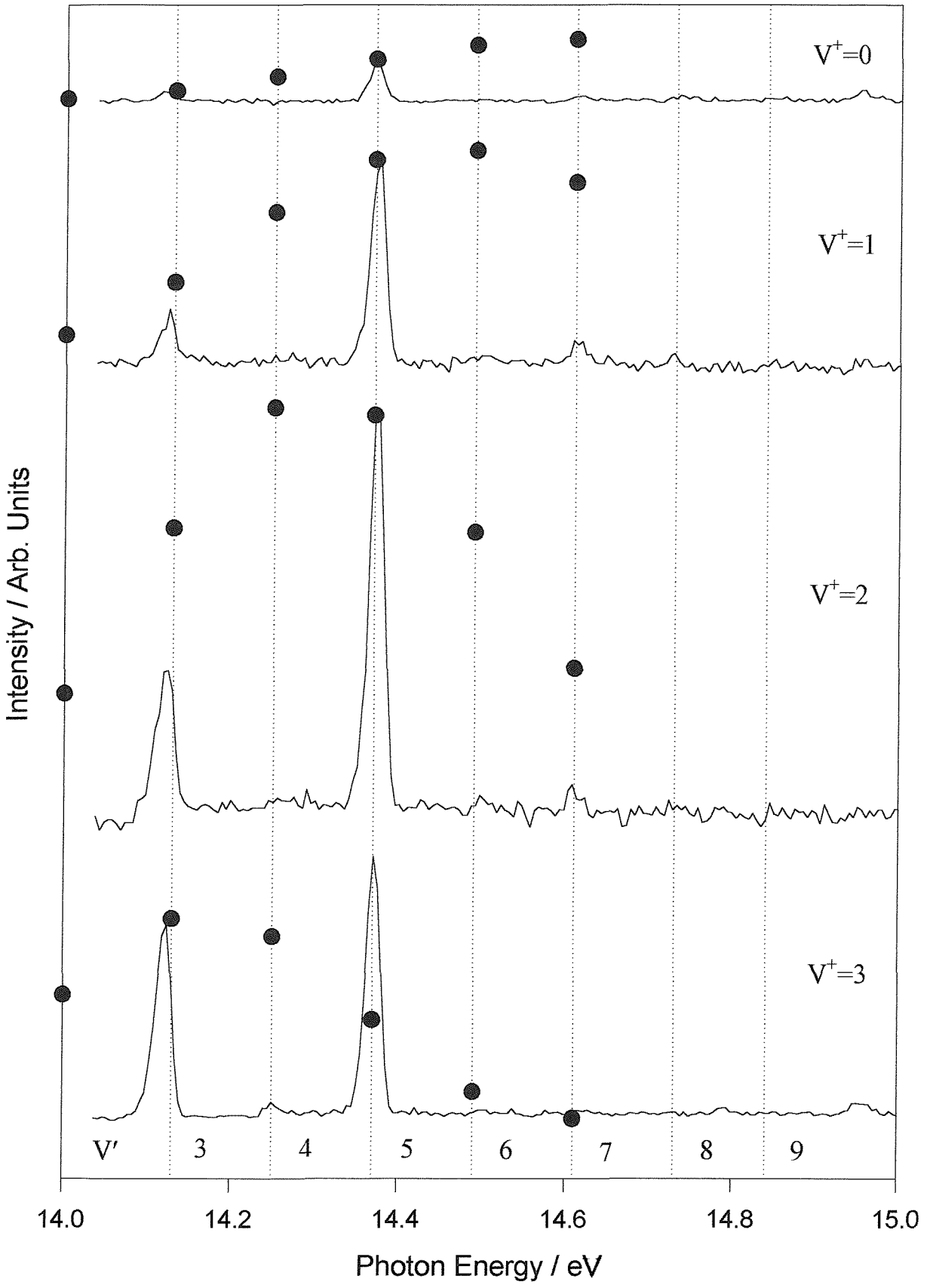

The v′=0 band occurs at 13.74 eV excitation energy which, when combined with the known adiabatic ionization energy (AIE) for $O_2^+(C^2\Phi_u)\leftarrow O_2(a^1\Delta_g)$ of 17.51 eV, gives an effective principal quantum number , n*, of 1.90.[24] This is consistent with n=3, δ=1.10 (where δ is the quantum defect) implying an outermost 3s Rydberg electron in the excited state.[28] The excited state is therefore labeled $(C^2\Phi_u,3s\sigma_g)\ p^1\Phi_u$ (the p label comes from the tables of Ref.29). This assignment implies that bands A and B correspond to excitation to v′=3 and v′=5 in the $p^1\Phi_u$ excited state. Closer inspection of Fig. 5.4 shows that a weak transition to v′=7 can be seen in some of the spectra.

An unusual feature of the vuv absorption band is that the vibrational components appear alternately sharp and diffuse.[24] Katayama *et al.* attribute this broadening to a combination of predissociation and autoionization in the vibrational levels in the excited $^1\Phi_u$ state.[24] The excitation energy at the band head and the appearance of each observed vibronic band of the $p^1\Phi_u\leftarrow a^1\Delta_g$ absorption taken from Ref.24 are summarised in Table 5.1 and these band head positions are marked as vertical dotted lines in Figure 5.4.

v′	E_{head}/eV	Appearance
0	...	Overlapped
1	13.87	Overlapped
2	14.00	Overlapped, diffuse
3	14.13	Well rotationally resolved
4	14.25	Diffuse
5	14.37	Well rotationally resolved
6	14.49	Diffuse
7	14.61	Reasonably well rotationally resolved
8	14.73	Poorly resolved
9	14.84	Diffuse

Table 5.1:
Summary of band head positions (E_{head}) and appearance of vibrational components in the $O_2(p^1\Phi_u)v' \leftarrow O_2(a^1\Delta_g)v''=0$ absorption band.

As outlined in Chapter 3, if CIS spectra only arise from autoionization processes then it is expected that they can be simulated using a product of Franck-Condon factors for the two steps involved, i.e., (a) and (b) in

$$O_2^+(X^2\Pi_g)v^+ \xleftarrow{b} O_2^*,\ v' \xleftarrow{a} O_2(a^1\Delta_g)v''=0,$$

where O_2^* is a Rydberg state with an $O_2^+(C^2\Phi_u)$ core. In these calculations each state is represented by a Morse potential specified using established values of r_e, ω_e, and

$\omega_e x_e$ for $O_2(a^1\Delta_g)$ and $O_2^+(X^2\Pi_g)$ (Ref.29) and the corresponding values for $O_2(p^1\Phi_u)$ from the vuv absorption study.[24] Franck-Condon factors were computed for (a) and (b) for a range of v′ values (e.g., v′=0-10) and a selected value of v^+ and simulated CIS spectra were derived taking the product of the two Franck-Condon factors. The results obtained are indicated by the solid black circles in Figure 5.4. As can be seen, the fit between experimental and computed relative intensities is poor. However, for the two clearly observed bands A and B, the overall trend is correct with the intensity of A rising with respect to B as v^+ increases. This poor agreement is probably a consequence of competition between autoionization and predissociation in the excited $p^1\Phi_u$ state; if the v′=3 level is predissociated slightly more efficiently than v′=5 then the intensity of the v′=3 level will be lower than calculated, as is observed. Indeed, in the vuv absorption spectrum,[24] the v′=3 absorption band is slightly less well resolved than the v′=5 band and from the rotational linewidths in the absorption spectrum approximate lifetimes of the v′=3 and v′=5 levels may be estimated, after allowance for the experimental contribution, as 1.8 and 2.6 ps, respectively. If it is assumed that predissociation of the v′=5 level is minimal, then 2.6 ps must represent the autoionization lifetime of this level. Predissociation of the v′=3 and 5 levels is presumably relatively slow while for the other vibrational levels it is much faster as little or no signals are seen for these levels in the CIS spectrum.

Photoelectron spectra of discharged oxygen recorded at photon energies corresponding to bands A and B in Fig 4.4 (14.11 and 14.37 eV) are shown in Figure 5.5 and 6, respectively. In each case comparison with spectra recorded with the discharge off allowed contributions from $O_2(a^1\Delta_g)$ and $O(^3P)$ to the discharged oxygen spectrum to be identified. Since in both Figs. 5.5 and 6 some of the photoelectron signals arising from ionization of $O_2(a^1\Delta_g)$ are partly obscured by stronger signals arising from $O_2(X^3\Sigma_g^-)$, a program has been used to deconvolute and remove the $O_2(X^3\Sigma_g^-)$ features from a spectrum recorded with the discharge on. The lowest trace in each Figure shows the contribution from $O_2(a^1\Delta_g)$, which represents the photoelectron spectrum of $O_2(a^1\Delta_g)$ at the two photon energies used over the ionization region 11.0-14.5 eV, except between 13.5 and 13.7 eV ionization energy where contributions from molecular and atomic oxygen overlap, making accurate deconvolution impossible. [The $O^+(^4S)\leftarrow O(^3P)$ ionization occurs at 13.61 eV.[30]] The spectra recorded at these photon energies with the discharge off [i.e., for the $O_2(X^3\Sigma_g^-)$ first band] show extra

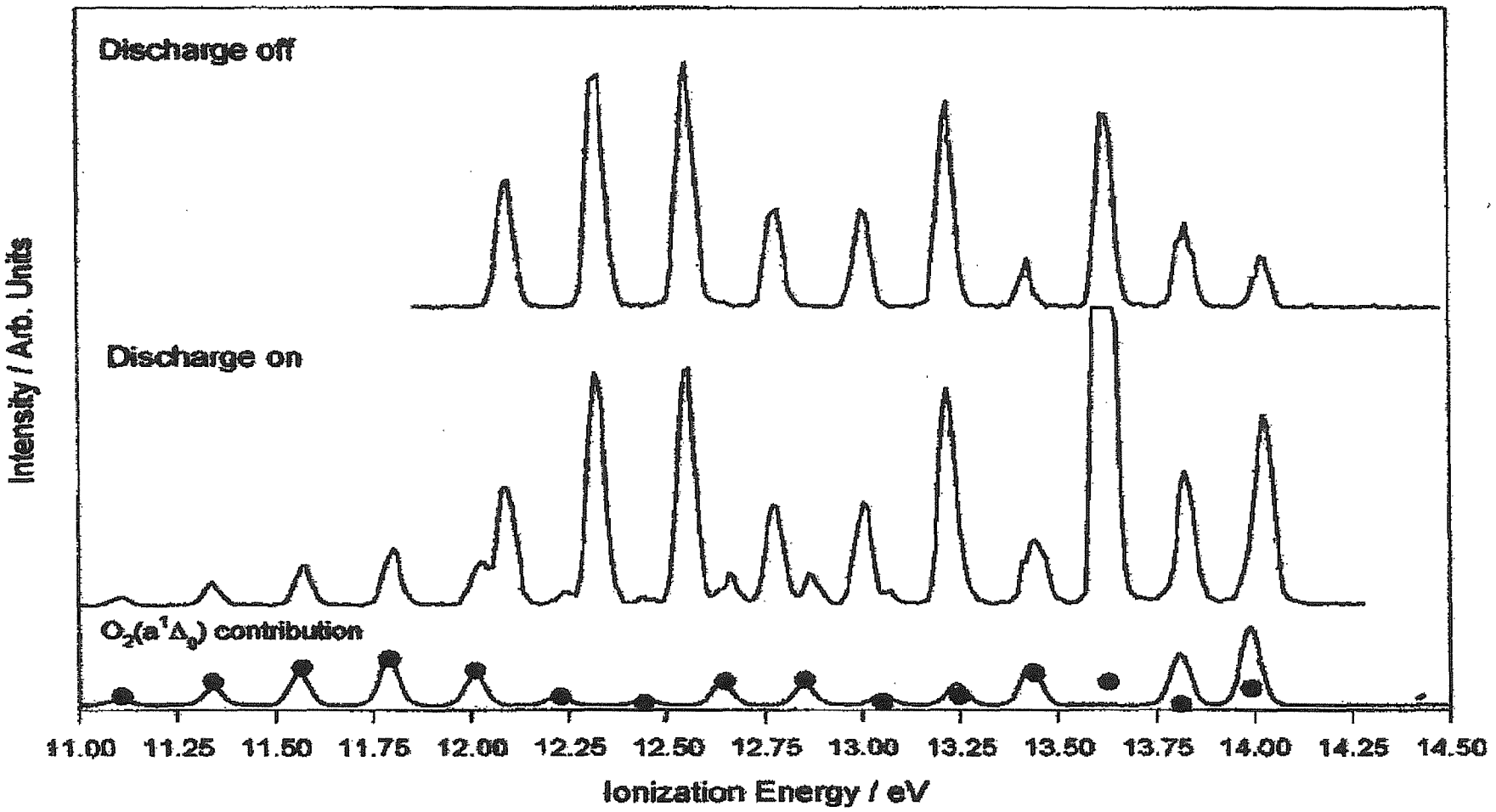

Figure 5.5: Photoelectron spectra recorded at hv=14.11 eV (i.e., at the position of band A in Fig. X.4) for discharged and undischarged oxygen, in the ionization energy region 11.0-14.1 eV. The black circles in the lower part of this figure represent relative vibrational intensities by summing the direct and autoionization computed envelopes.

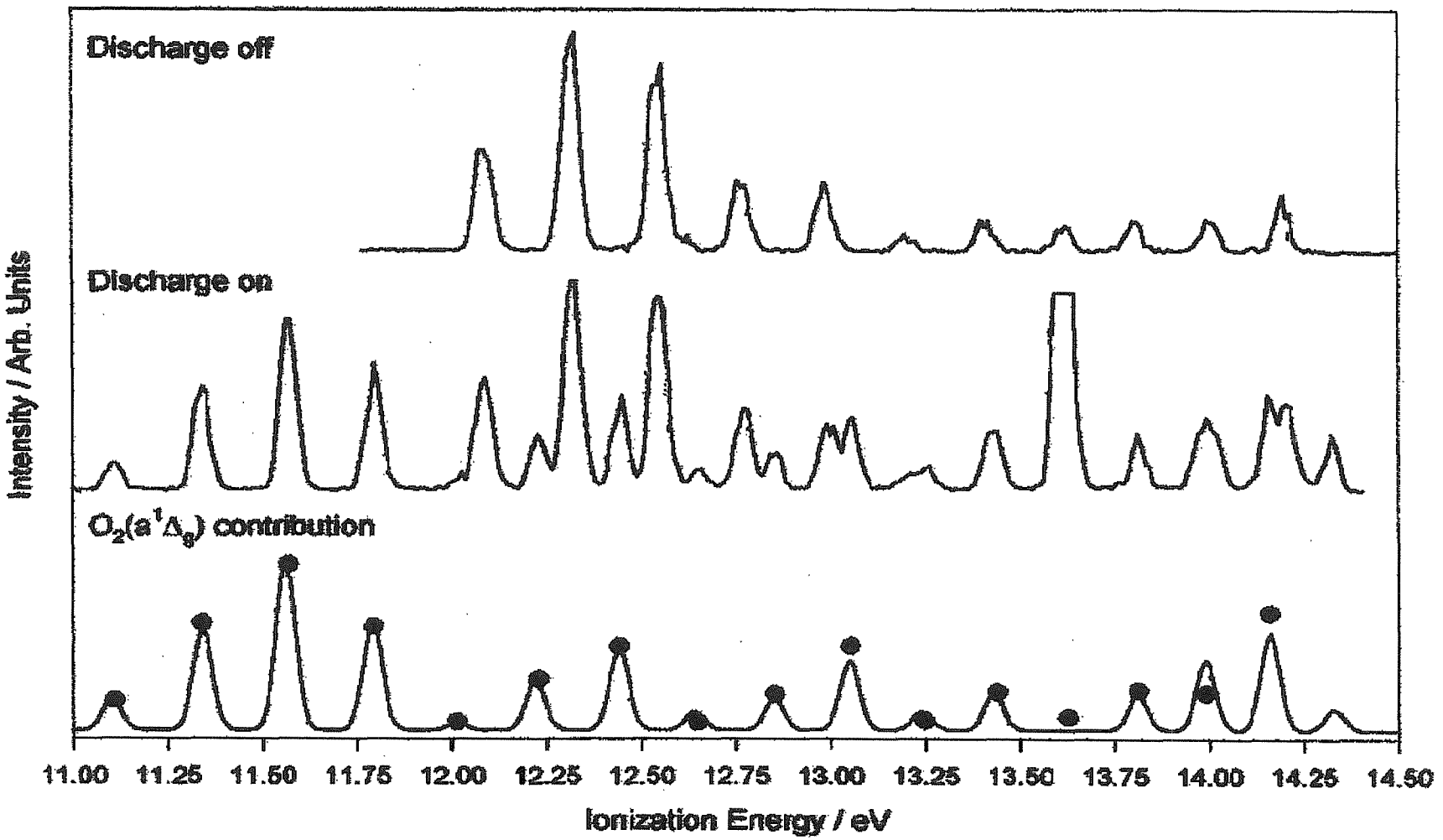

Figure 5.6: Photoelectron spectra recorded at hv=14.37 eV (i.e., at the position of band B in Figure 5.4) for discharged and undischarged oxygen, in the ionization energy region 11.0-14.4 eV. The black circles in the lower part of this Figure represent computed relative vibrational intensities obtained by summing the direct and autoionization computed envelopes.

vibrational structure compared with the band envelope recorded with HeI radiation. Also, instead of showing four vibrational components for the $O_2^+(X^2\Pi_g) \leftarrow O_2(a^1\Delta_g)$ ionization, as are observed in the HeI (21.22 eV) photoelectron spectrum, sixteen components are observed.

The $O_2(a^1\Delta_g)$ spectra in Figures 5.5 and 5.6 may be considered as arising from two contributions, one from direct photoionization and the other from autoionization from the resonant Rydberg state. Each of these processes will have an associated Franck-Condon envelope for population of the $O_2^+(X^2\Pi_g)$ state; accurate knowledge of the autoionization linewidth, Γ, and the Fano shape parameter, q, is required to allow the two envelopes to be scaled to simulate the entire resonant photoelectron spectrum.[31] However, as these parameters are not known a more empirical approach was taken. By using the intensity of the CIS background in Figure 5.4 as the intensity of the direct photoionization contribution and the band intensity if Fig. 5.4 on a resonance as the autoionization contribution, the respective Franck-Condon envelopes were scaled and summed to yield a calculated photoelectron spectrum at each photon energy. The vibrational component intensities obtained from this procedure are displayed as solid circles in Figs. 5.5 and 5.6 where the resonant states were assumed to be $p^1\Phi_u$, $v'=3$ and $p^1\Phi_u$, $v'=5$, respectively. As can be seen the agreement between the experimental and simulated envelopes is good. Computed photoelectron vibrational envelopes at hv=14.11 and 14.37 eV, which include both the direct and autoionization contributions, from selected vibrational levels of the $p^1\Phi_u$, v' state, with $v'=1$, 2, 3, 4, 5, and 6, are shown in Figs. 5.7(a) and 5.7(b), respectively. Comparisons of the experimental $O_2(a^1\Delta_g)$ vibrational envelope in Fig. 5.5 (at hv=14.11 eV) with the computed envelopes, only shows good agreement for $v'=3$ [in Fig. 5.7(a)]. A similar comparison of Fig. 5.6 (at hv=14.37 eV) with Fig. 5.7(b) only shows good agreement for $v'=5$ confirming the vibrational numbering of the resonance levels known from the vuv absorption study[24] and shown in Fig. 5.4.

The success of these Franck-Condon calculations in this and previous work on autoionization of $O_2(X^3\Sigma_g^-)$[32] implies that the characteristics of the reonances, in terms of autoionization linewidth, Γ, and shape parameter, q, are not important in cases where q is

Figure 5.7:

Computed vibrational envelopes for the first photoelectron band of $O_2(a^1\Delta_g)$, which include the direct and autoionization contributions, at photon energies of (a) 14.11 eV and (b) 14.37 eV. The hatched areas represent the autoionization contributions and the solid areas the direct contributions.

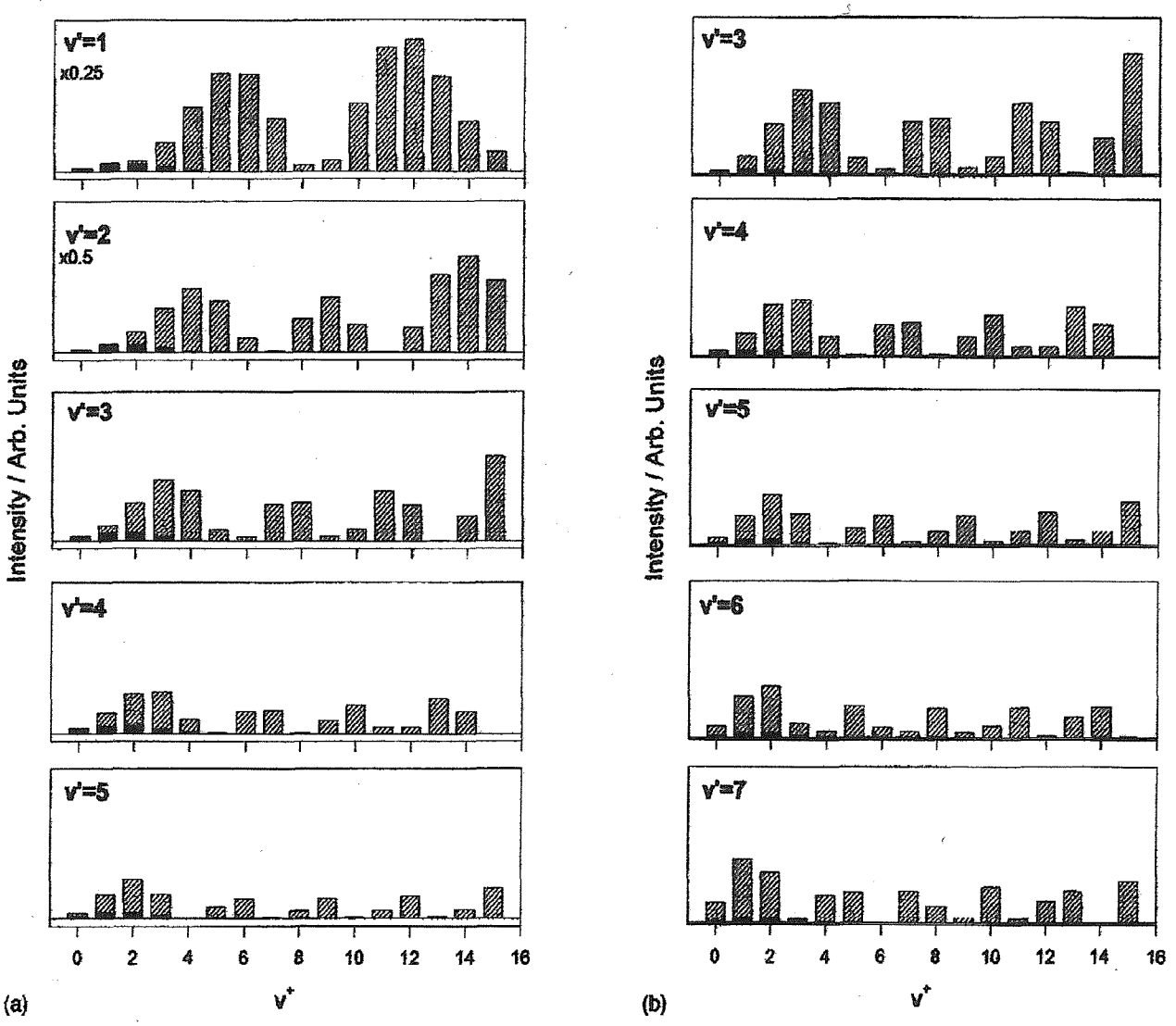

large, as is almost certainly the case for the resonances shown in Fig 5.4, in controlling ionic vibrational level populations produced by autoionization and direct ionization.

The perturbing states responsible for the vibrationally dependent predissociation that occurs in the $p^1\Phi_u$ state and competes with autoionization to the ground ionic state are not established although two dissociative $^1\Delta_u$ states and one dissociative $^1\Phi_u$ state have been proposed to cross the $p^1\Phi_u$ state.[24] Clearly further experimental and theoretical work is needed to establish the exact positions of these curves, the extent of their interaction with the $p^1\Phi_u$ state, and the nature of the observed vibrationally dependent predissociation. In summary, two strong resonances have been observed in the CIS spectra recorded for $O_2(a^1\Delta_g)$ between 14.0 and 15.5 eV. At these photon energies there is an enhancement in the photoionization cross section of $O_2(a^1\Delta_g)$ and photoelectron spectra recorded at these energies allow extra vibrational structure to be obtained. At hv=14.37eV, the $O_2(a^1\Delta_g)$ features are comparable in intensity with the $O_2(X^3\Sigma_g^-)$ photoelectron features even though the partial pressure ratio is ≈1:7. This implies that the $O_2(a^1\Delta_g)$ photoionization cross section is nearly an order of magnitude greater than the $O_2(X^3\Sigma_g^-)$ photoionization cross section at this photon energy. Also, the band associated with the $O^+(^4S)\leftarrow O(^3P)$ ionization at 13.61 eV is much more intense in Fig. 5.5 than Fig 5.6. This is because the photon energy used for Fig. 5.5, 14.11 eV, corresponds to a known $O^*\leftarrow O$ resonance ($a\ ^3P\leftarrow{}^3P$ transition) above the first ionization threshold of oxygen atoms.[30] This was confirmed by recording CIS spectra of the $O^+(^4S)\leftarrow O(^3P)$ band.

B. CIS spectra for O_2^+ ($X^2\Pi_g$) $v^+=0,1,2\leftarrow O_2(a^1\Delta_g)v''=0$ over the photon energe region 12.5-13.5 eV

As well as computing CIS spectra for a resonant Rydberg state with an $O_2^+(C^2\Phi_u)$ core, CIS simulations were performed as have been previously described for Rydberg states with $A^2\Pi_u$ and $D^2\Delta_g$ ionic cores. The results of these calculations are shown in Figure 5.8.

The 12.5-13.5 eV region of the experimental CIS specrum of $O_2(a^1\Delta_g)$ is shown in Figure 5.9 for all four available ionic vibrational channels. Each CIS channel includes one fairly strong, broad feature (labelled A, B, C and D in Figure 5.9) as well as several weaker bands. In this region of the CIS spectrum only Rydberg states based on the $A^2\Pi_u$ core should be

Figure 5.8:

Computed CIS envelopes for $O_2^+(X^2\Pi)v^+ \leftarrow O_2^*, v' \leftarrow O_2(a^1\Delta_g), v''=0$, where O_2^* represents a Rydberg state with an ionic core chosen as follows: (a)$O_2^+(A^2\Pi_u)$, (b)$O_2^+(C^2\Phi_u)$ and (c)$O_2^+(D^2\Delta_g)$.

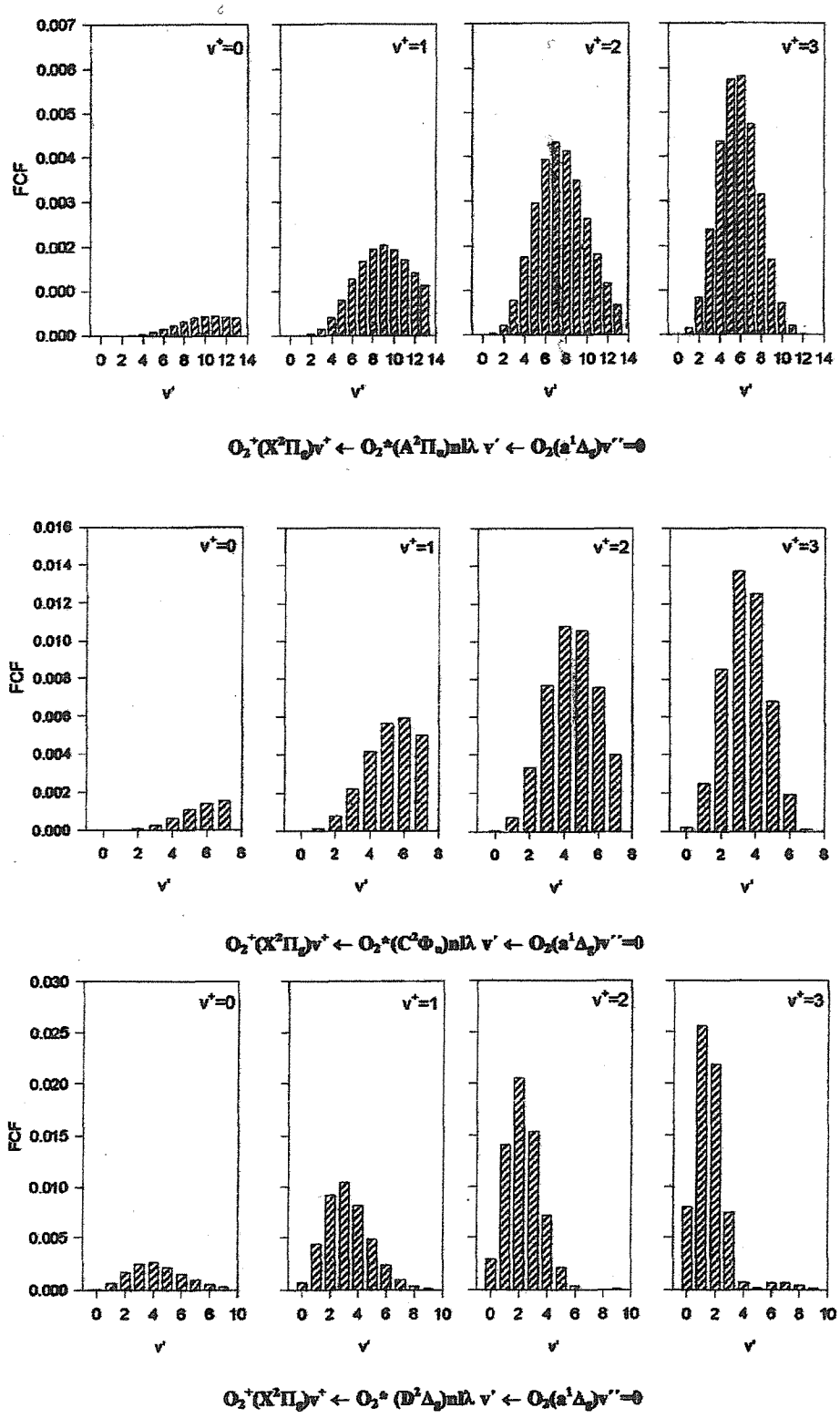

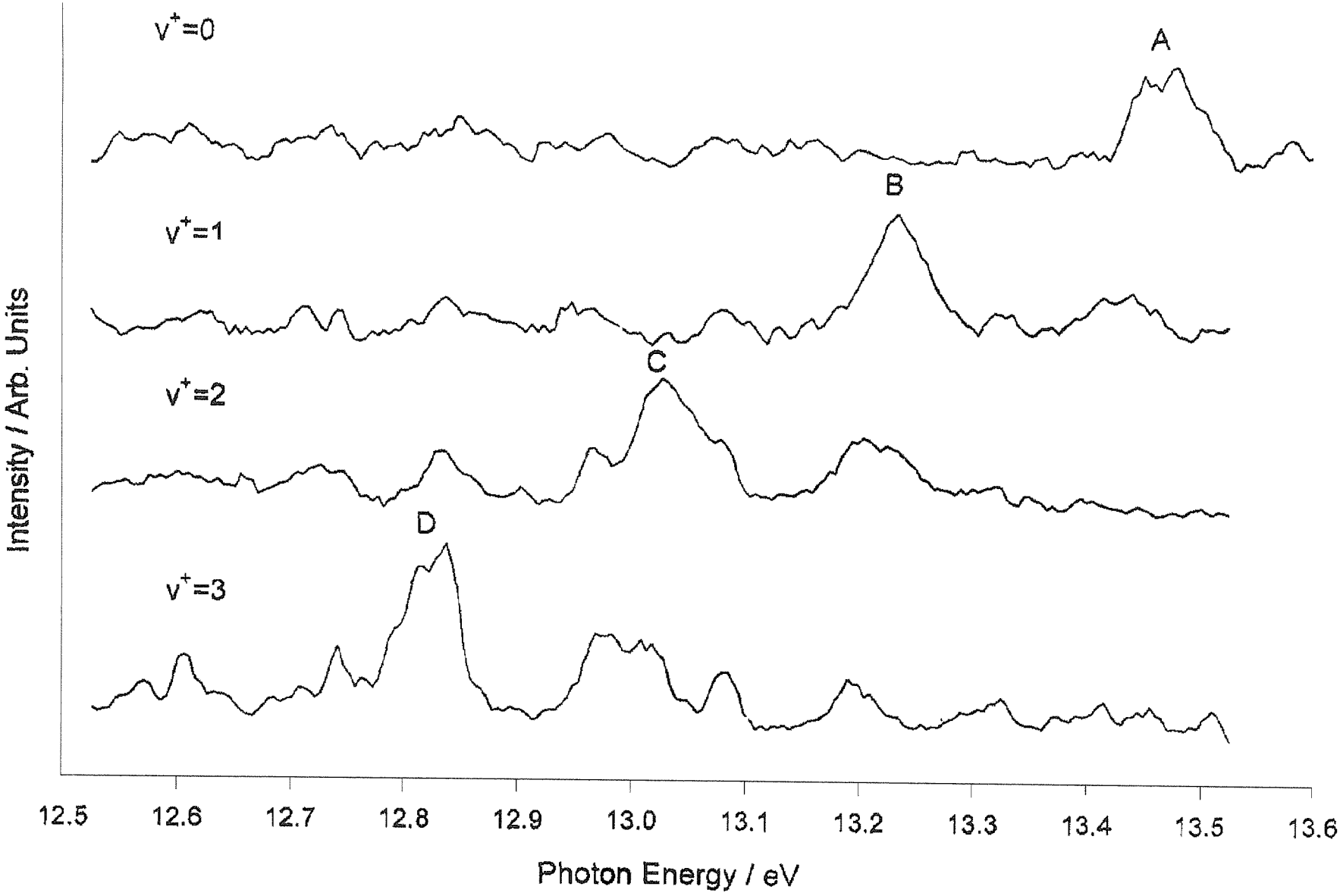

Figure 5.9: $O_2^+(X^2\Pi_g)v^+ \leftarrow O_2(a^1\Delta_g)v''=0$ CIS spectra recorded in the photon energy region 12.5-13.6 eV for $v^+=0,1,2$ and3.

accessible. The Franck-Condon simulations of the CIS envelopes for such states (Fig. 5.8) indicate a broad progression with the band maximum between v′=11 (for v^+=0) and v′=6 (for v^+=3). The v′=0 component is likely to be weak for v^+=0,1,2, and 3 and may not be observable. The $(A^2\Pi_u,3s\sigma_g)J^3\Pi_u$ Rydberg state has been well characterized by photoionization efficiency studies on $O_2(X^3\Sigma_g^-)$ and has ω_e=1010 cm^{-1} $\omega_e x_e$=3.7 cm^{-1}, δ=1.13, and T_o=13.14 eV.[33] Assuming the $^1\Pi_u$ counterpart to have a similar quantum defect, excitation to this singlet Rydberg state from $O_2(a^1\Delta_g)$ followed by autoionization to $O_2^+(X^2\Pi_g)$ would be observed in the region above 12.2 eV. A number of weaker features in Figure 5.9 may be components of a progression with spacings ≈1000 cm^{-1}, so that it is possible that they correspond to autoionization from $(A^2\Pi_u,3s\sigma_g)^1\Pi_u$ although no positive identification of a transition to this state can be made with the rather poor signal-to-noise ratios obtained.

The stronger resonances A, B, C, and D in Figure 5.9 exhibit unusual behaviour. Each autoionizes preferentially to a particular v^+ level with no appreciable intensity in other channels, implying strong Franck-Condon overlap of each O_2* v′ resonant level with only one v^+ level. As the vibrational quantum number in the $O_2^+(X^2H_g)$ state is increased by one from v^+=0, the dominant resonance moves to lower energy by about 1700 cm^{-1}. This separation is far higher than any vibrational separation in any known excited state of O_2^+, so bands A-D are unlikely to represent transitions to consecutive vibrational levels of Rydberg states built upon such cores. For example, if the O_2* state were of $(A^2\Pi_u,nl\lambda)$ character, features A-D would each have to be separated by two vibrational quanta; this seems highly implausible given that the experimental envelopes associated with bands A-D in Figure 5.9 are at odds with the simulated CIS envelopes in Figure 5.8.

The higher vibrational levels of $O_2^+(X^2\Pi_g)$ are separated by ≈1700 cm^{-1}, so bands A-D might be considered as transitions to members of Rydberg series converging to these high v^+ levels and autoionizing vibrationally. However, since the potential energy curves of the ground ionic state and Rydberg states with the same ionic core should be approximately parallel, a Δv=-1 propensity rule should apply.[34] This clearly cannot be the case for bands A-D with separations of up to 2.5 eV between he resonant features A-D and the ionization thresholds being observed in Figure 5.9.

It would appear that the stronger features A-D in Fig. 5.9 cannot be assigned to transitions to Rydberg states built on any known states of O_2^+. Instead the presence of an autoionizing valence (or mixed Rydberg-valence) state seems more likely. The interpretation which is favoured for bands A-D is that they arise from autoionization to $O_2^+(X^2\Pi_g)$ from vibrational turning points on the steeply rising part of the potential of a perturbed valence state. A schematic diagram showing part of an excited state potential and the $O_2^+(X^2\Pi_g)$ potential, which would give rise to CIS spectra of the type shown in Figure 5.9 is shown in Figure 5.10. Left-hand turning points of vibrational levels in the excited state potential, denoted by the solid black circles, are accessible from $O_2(a^1\Delta_g)$, $v''=0$ and are in this model accessed at 13.46 eV (A), 13.25 eV (B), 13.04 eV (C) and 12.84 eV (D). Further work is clearly necessary to elucidate the nature of these resonances.

C. $O_2^+(X^2\Pi_g)$ $v^+\leftarrow O_2(a^1\Delta_g)$ $v''=0$ CIS spectra recorded in the photon energy region 15.5-19.0 eV

Figure 5.11 shows the 15.5-17.0 eV region of the $O_2^+(X^2\Pi_g)$ $v^+=1,2,3\leftarrow O_2(a^1\Delta_g)v''=0$ CIS spectra. The $v^+=0$ signal proved to be too weak to enable reliable spectra to be recorded and is not shown. A number of features are observed in the $v^+=1,2$, and 3 spectra, many of which are reproduced in each ionic vibrational channel. The structure observed must arise from overlap of transitions to a number of Rydberg states, only one of which can be assigned with any confidence here.

The spacings between features G, H, I, and J in Figure 5.11 are constant at (950±30) cm^{-1} suggesting that these features are transitions to successive vibrational members of a Rydberg state based on the ionic states $C^2\Phi_u$ (ω_e=1042 cm^{-1}) or $D^2\Delta_g$(ω_e=995 cm^{-1}). (The O_2^+ $A^2\Pi_u$ state is eliminated as an ionic core as it has AIE=16.06 eV and ω_e=898 cm^{-1}). Despite the structured region observed to lower energy of band G in Figure 5.11, no clear component is observed at the correct spacing below this feature to extend the labelled G-J to lower energy.

Assuming that feature G (at 16.07 eV) corresponds to $v'=0$ in the upper state then effective quantum numbers of 3.07 and 2.23 are calculated for Rydberg states based on $C^2\Phi_u$ and $D^2\Delta_g$ ionic cores, from the known adiabatic ionization energies to the C and D ionic states

Figure 5.10: A schematic diagram showing part of an excited state potential and the $O_2^+(X^2\Pi)$ potential which would give rise to CIS spectra of the type shown in Figure 5.9. The positions of resonances A, B, C, and D (shown in Figure 5.9) from $O_2(a^1\Delta_g)v''=0$ are marked on the diagram. Left-hand turning points (marked by the solid circles) of vibrational levles in the excited state, denoted A, B, C, and D, are all accessible from $O_2(a^1\Delta_g),v''=0$ (r_e=1.2156 Å) and are in this model accessed at photon energies of 13.46 eV (A), 13.25 eV (B), 13.04 eV (C), and 12.84 eV (D).

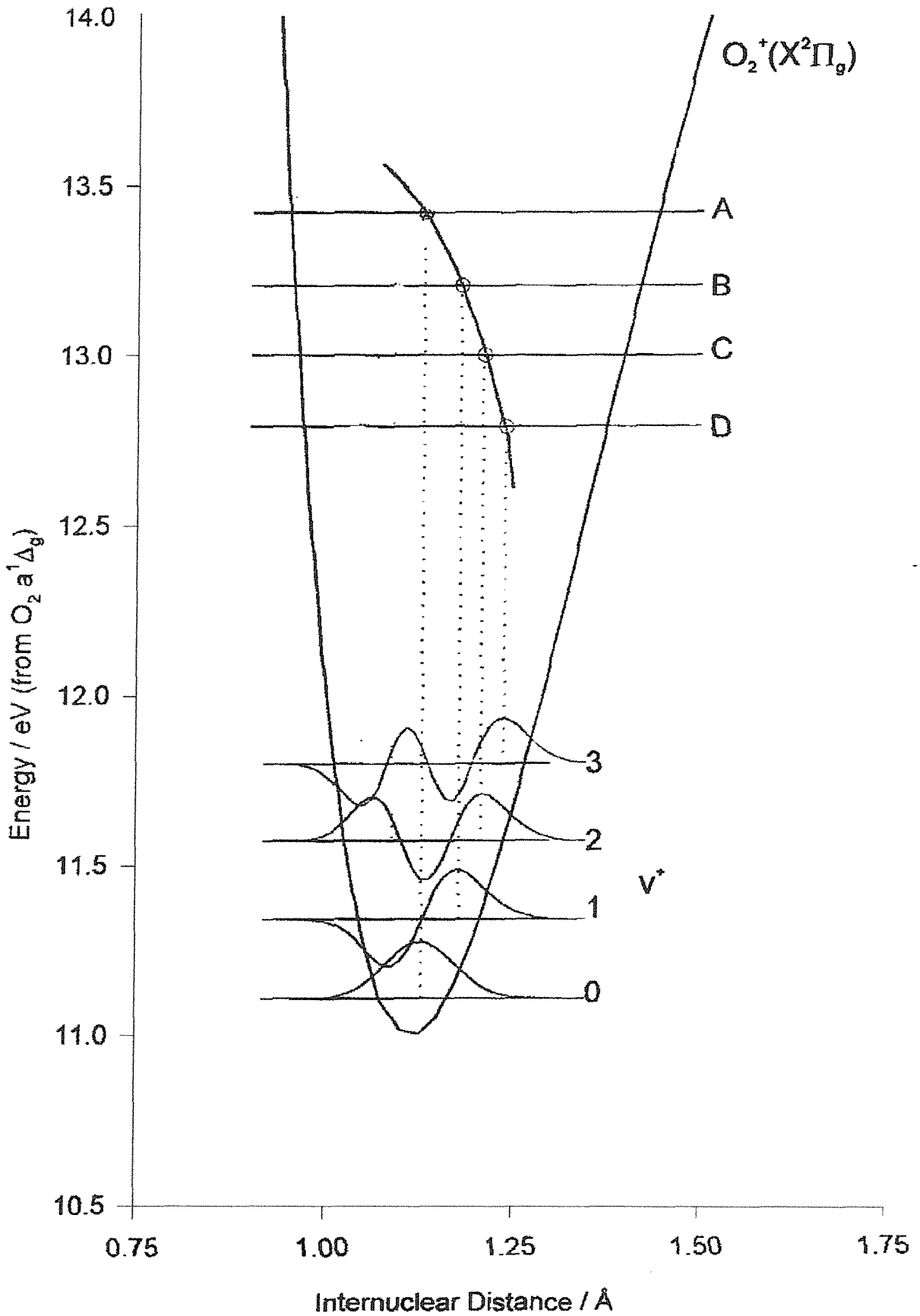

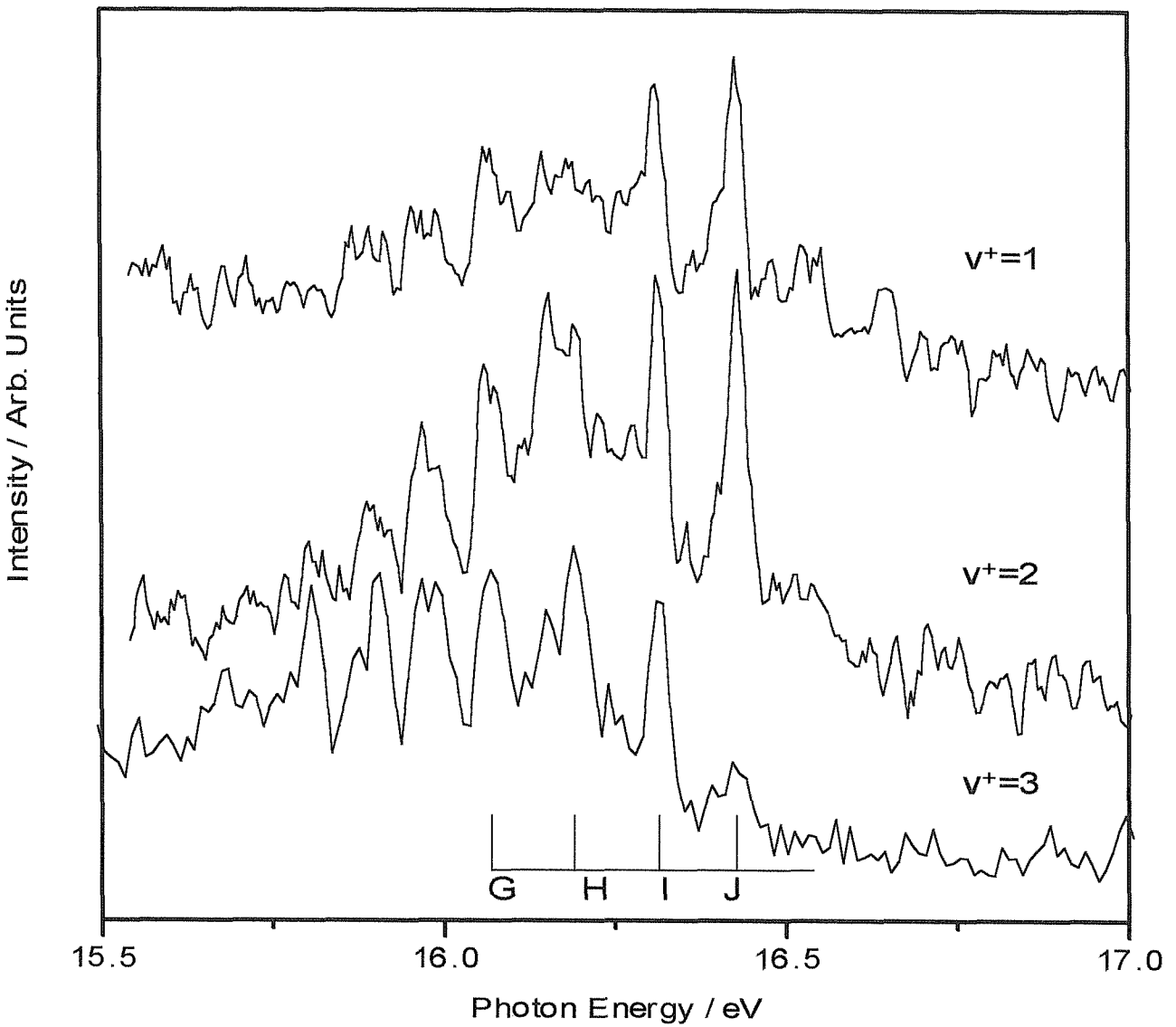

Figure 5.11: $O_2^+(X^2\Pi_g)$, $v^+ \leftarrow O_2(a^1\Delta_g)v''=0$ CIS spectra recorded in the photon energy region 15.5-17.0 eV, for $v^+=1$, 2, and 3.

from $O_2(a^1\Delta_g)$. These effective quantum numbers would be consistent with excitation to $(C^2\Phi_u,4s\sigma)^1\Phi_u$ or $(D^2\Delta_g,3p\pi_u)^1\Pi_u$, $^1\Phi_u$ states.[35] The latter assignment, corresponding to a $(D^2\Delta_g,3p\pi_u)$ (δ=0.77) state, is preferred since it has a lower value of n than that of the C state assignment and the observed vibrational spacings in the band labelled G-J in Fig 5.11 are closer to those of the D ionic state. This assignment is supported by the CIS simulations shown in Figure 5.8. These calculations indicate that the CIS envelope should peak at lower v′ values as v^+ increases, as is observed, and that for a Rydberg state with a $D^2\Delta_g$ ionic core, the v′=3 signal should be much weaker in the v^+=3 CIS spectrum than in the v^+=2 CIS spectrum. This is in agreement with a $(D^2\Delta_g,3p\pi_u)$ assignment in which feature J corresponds to v′=3. CIS calculations for a Rydberg state based on a $C^2\Phi_u$ ionic core suggest the opposite trend, i.e., that v′=3 autoionizes more strongly to v^+=3 than v^+=2, contrary to the experimental observation. The observed intensity of the v′=0 component, feature G in Figure 5.11, is greater than expected from the CIS simulations but this is understandable as it is overlapped by an unassigned band to low photon energies. Although more features are observed in Fig 5.11, no other vibrational progressions can be unambiguously identified.

In summary, bands G-J in Fig 5.11 are assigned to excitation to a $(D^2\Delta_g,3p\pi_u)$ state even though the $(C^2\Phi_u,4s\sigma_g)$ $^1\Phi_u$ state is expected in this region and the transition to the $(C^2\Phi_u,3s\sigma_g)$ $^1\Phi_u$ state at lower energy is particularly intense (Fig 5.4). This assignment means that a broad weak band centred at ≈17.75 eV (see Fig. X.3) in both the v^+=1 and v^+=2 CIS spectra can be assigned to the excitation O_2^* $(D^2\Delta_g,4p\pi_u)\leftarrow O_2(a^1\Delta_g)$.

The final photon energy region in which discrete structure was observed was 18.2-19.2 eV. CIS spectra recorded for $O_2^+(X^2\Pi_g)v^+$=1,2, and 3 over this range are shown in Figure 5.12. Once again the v^+=0 signal proved to be too weak to record reliable spectra. Relatively strong features labelled K,L,M,N, and O form a clear vibrational progression with a mean spacing of (940±30) cm^{-1}. A second, weaker progression which partly overlaps the first (labelled K′, L′, M′, N′ and O′ in Fig. X.12), can also be identified and has a mean vibrational spacing of (1000±30) cm^{-1}.

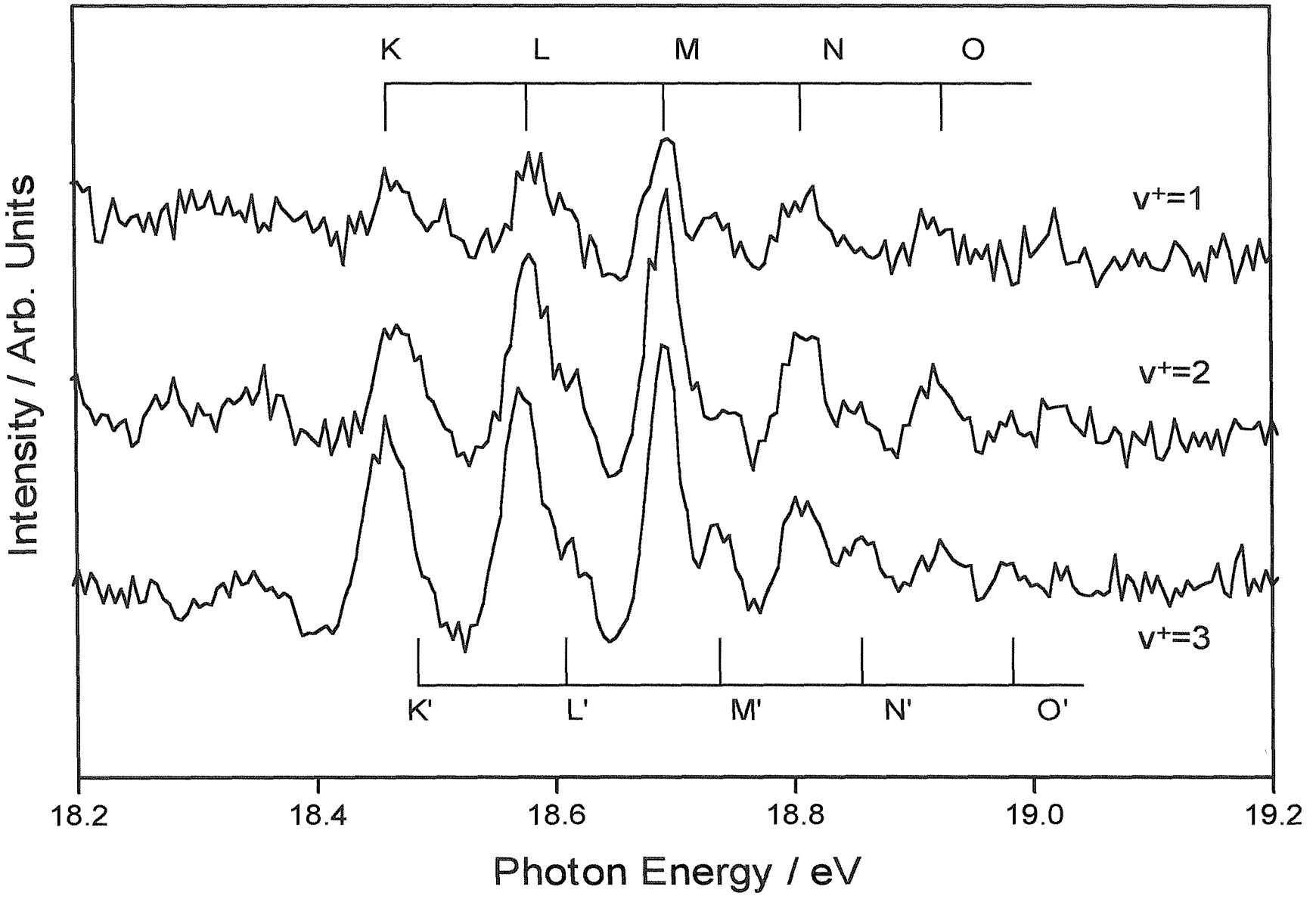

Figure 5.12: $O_2^+(X^2\Pi_g)v^+ \leftarrow O_2(a^1\Delta_g)v''=0$ CIS spectra recorded in the photon energy region 18.2-19.2 eV, for $v^+=1,2$, and 3.

The only well-characterized state of O_2^+ accessible from $O_2(a^1\Delta_g)$ above 18.0 eV photon energy is the $D^2\Delta_g$ state with an adiabatic ionization energy of 18.81 eV from $O_2(a^1\Delta_g)$.[14,15,27] Assuming feature K (at 18.46 eV) to correspond to the first component of a vibrational progression, the effective principal quantum number of the associated Rydberg state based on a $D^2\Delta_g$ ionic core is calculated to be 6.23, suggesting a ($D^2\Delta_g$,7pπ) (δ=0.77) assignment.[25] However, the high value of n and the absence of any experimental evidence of members of this series with n=5 or 6 at lower photon energies (although the 3p and 4p components have been observed) does not support this interpretation. Also, the CIS simulations of Fig 5.8 are not consistent with this assignment as, if the ionic core is $D^2\Delta_g$, the CIS vibrational profiles are calculated to change with v^+, in contrast to the very unusual experimental observation that the CIS vibrational profile is essentially the same in all v^+ channels.

An ionic state of unknown symmetry has been observed by Baltzer *et al*[3] as a weak progression between the vibrational components of the $O_2^+(B^2\Sigma_g^-) \leftarrow O_2(X^3\Sigma_g^-)$ band in the high-resolution photoelectron spectrum of ground state oxygen. Baltzer *et al*[3] analysed the vibrational structure in the observed photoelectron spectrum band to yield ω_e=830 cm^{-1} in the ionic state and suggested that this state might be a $^2\Delta_g$ state. The adiabatic ionization energy to this state is 20.35 eV, from $O_2(X^3\Sigma_g^-)$, and 19.37 eV from $O_2(a^1\Delta_g)$, although it is not known if it is accessible from $O_2(a^1\Delta_g)$. However, if the feature K in Fig. 5.12 is the first component of a transition to a Rydberg state with this ionic core, then an effective principal quantum number of 3.87 can be derived for the excited Rydberg state. This may correspond to a state with the excited electron in a 4dσ_g, 4dπ_g (δ=0.13) or 5sσ_g(δ=1.13) Rydberg orbital, any one of which is also plausible for the state associated with the second vibrational series (K′,L′,M′,N′,O′). However, for this ionic state to be accessible from both the $X^3\Sigma_g^-$ and $a^1\Delta_g$ neutral states, it must have $^2\Pi_u$ or $^2\Pi_g$ symmetry contrary to the suggestion of Balzer *et al.*[3] that it is a $^2\Delta_g$ state. In summary, the two vibrational progressions observed in the CIS spectra of $O_2(a^1\Delta_g)$ recorded in the 18.2-19.2 eV region must remain unassigned until the ionic states accessible from $O_2(a^1\Delta_g)$ in the ionization energy region 20-22 eV have been fully characterized.

5.3 Conclusions

In conclusion, the variable photon energy facility of a synchrotron source has enabled CIS spectra of $O_2(a^1\Delta_g)$ to be recorded and hence has allowed highly excited singlet states of $O_2(a^1\Delta_g)$ above the first ionization threshold to be investigated. This has established wavelengths in the vacuum ultraviolet region in which the photoionization cross section of this atmospherically important species is enhanced. The largest increase in photoionization cross section occurs at photon energies of 14.11 and 14.37 eV. The excited Rydberg state associated with these resonances has been assigned and photoelectron spectra of the first band of $O_2(a^1\Delta_g)$ recorded at these resonant energies exhibit extended vibrational structure with sixteen vibrational components being observed compared to only four components observed in the off-resonance spectra. Suggestions are made for assignment of the weaker structure observed in the CIS spectra.

5.4 References

1. P. M. Dehmer and W. A. Chupka, *J. Chem. Phys.* **62**, 4525 (1975).

2. O. Edqvist, E. Lindolm, L. E. Selin and L. Asbrink, *Phys. Scr.* **1**, 25 (1970).

3. P. Baltzer, B. Wannberg, L. Karlsson, M. Carlsson Gothe and M. Larsson, *Phys. Rev. A.* **45**, 4374 (1992).

4. K. Ellis, R. I. Hall, L. Avaldi, G. Dawber, A. McConkey, L. Andric and G. C. King, *J. Phys. B.* **27**, 3415 (1994).

5. F. Merkt and P. M. Guyon, *J. Phys. Chem.* **99**, 15775 (1995).

6. W. Kong and J. W. Hepburn, *Int. J. Mass Spectrom. Ion Processes.* **159**, 27 (1996).

7. T. Akahori, Y. Morioka, T. Tanaka, H. Yoshii, T. Hayaishi and K. Ito, *J. Chem. Phys.* **107**, 4875 (1997).

8. G. Marston, *Chem. Soc. Rev.* **33** (1996).

9. D. M. Hunter and M. B. McElroy, *J. Geophys. Res.* **73**, 2421 (1968).

10. W. F. J. Evans, D. M. Hunter, E. J. Llewellyn and A. Vallance-Jones, *J. Geophys. Res* **73**, 2885 (1968).

11. R. P. Wayne, *Adv. Photochem.* **7**, 311 (1969).

12. E. E. Ferguson and F. C. Fehsenfeld, *J. Geophys. Res.* **74**, 5743 (1969).

13. E. E. Ferguson, F. C. Hehsenfeld and D. L. Albritton, in *Gas-Phase Ion Chemistry,* edited by M. T. Bowers (Academic, New York, 1979), Vol. 1.

14. N. Jonathan, A. Morris, M. Okuda, K. J. Ross and D. J. Smith, *J. Chem. Soc., Faraday Trans.* **70**, 1810 (1974).

15. H. van Lonkhuyzen and C. A. de Lange, *J. Electron. Spectrosc. Relat. Phenom.* **27**, 255 (1982).

16. H. Park, L. Li and W. A. Chupka, *J. Chem. Phys.* **92**, 61 (1990).

17. H. Park, L. Li and W. A. Chupka. *Chem. Phys. Lett.* **162,** 317 (1989).

18. R. J. Yokelson, R. J. Lipert and W. A. Chupka, *J. Chem. Phys.* **97**, 6144 (1992); **97**, 6153 (1992).

19. A. Sur, R. S. Friedman and P. J. Miller, *J. Chem. Phys.* **94**, 1705 (1991).

20. R. D. Johnson, G. R. Long and J. W. Hudgens, *J. Chem. Phys.* **87**, 1977 (1987).

21. R. Ogorzalec Loo, W. J. Marinelli, P. L. Houston, S. Arepelli, J. R. Wisenfeld and R. W. Field, *J. Chem. Phys.* **91**, 5185 (1989).

22. R. E. Huffman, D. E. Paulsen, J. C. Larrabee and R. B. Cairns, *J. Geophys. Res.* **76**, 1028 (1971).

23. R. J. Collins, D. Husain and R. J. Donovan, *J. Chem. Soc., Faraday Trans.* **69**, 145 (1973).

24. D. H. Katayama, R. E. Huffman and Y. Tanaka, *J. Chem. Phys.* **62**, 2929 (1975).

25. R. E. Huffman, J. C. Larrabee and Y. Tanaka, *J. Chem. Phys.* **46**, 2231 (1967).

26. D. H. Katayama, S. Ogawa, M. Ogawa and T. Tanaka, *J. Chem. Phys.* **67**, 2132 (1977).

27. H. van Lonkhuyzen, Ph.D thesis, Free University, Amsterdam, 1984.

28. E. Lindolm, *Ark. Fys.* **40**, 117 (1969); C. Y. R. Wu, *J. Quant. Spectrosc. Radiat, Transf.* **37**, 1 (1987).

29. K. P. Huber and G. Herzberg, *Molecular Spectra and Molecular Structure IV Constants of Diatomic Molecules* (van Nostrand Reinhold, New York, 1979).

30. C. E. Moore, *Atomic Energy Levels, Volume 1,* Circular of the National Bureau of Standards 467, 1949 (U.S. Govt, Printing Office, Washington D.C.).

31. A. L. Smith, *Philos. Trans. R. Soc. London, Ser. A* **268**, 169 (1970).

32. J. H. D. Eland, *J. Chem. Phys.* **72**, 6015 (1980).

33. E. Nishitani, I. Tanaka, K. Tanaka, T. Kato and I. Koyano, *J. Chem. Phys.* **81**, 3429 (1984).

34. J. Berkowitz, *Photoabsorption, Photoionization and Photoelectron Specroscopy* (Academic, New York, 1979); J. Berkowitz and W. A. Chupka, *J. Chem. Phys.* **51**, 2341 (1969).

35. E. Lindolm, *Ark. Fys.* **40**, 117 (1969); C. Y. R. Wu, *J. Quant. Spectrosc. Radiat. Transf.* **37**, 1 (1987).

Chapter 6: Experimental apparatus for REMPI spectroscopic studies of van der Waals complexes

The basic REMPI apparatus used in this work consists of a tunable laser beam focussed into a low pressure gas. Ions created by the laser pulse are mass analysed using a time-of-flight (ToF) analyser. The photoions traverse the ToF tube before collection using a set of multichannel plates. The current at a selected ToF window is then amplified and the resultant signal is recorded as a function of laser wavelength. An overview of the apparatus used for this procedure is shown schematically in Figure 6.1 and the operation of the major components is discussed in this chapter.

6.1 The Photon Source

The tunable near-ultraviolet radiation (220-350nm) used in the REMPI experiments was provided by the frequency doubled output of an excimer[1,2,3] pumped dye laser[2,3,4]. The excimer laser (Lumonics PulseMaster 842) used was operated using XeCl as the active medium. In this excimer laser, the excited state complex Xe*Cl is produced by a ~30kV transverse electrical discharge in Xe (1.5%), HCl (0.06%) and Ne (balance). This is quickly followed by radiative decay (308nm) to the unbound ground state of XeCl which has a dissociation time on the order of a vibrational period, around 10^{-13} s. This bound-free transition ensures a very favourable lifetime ratio of upper and lower levels and hence population inversion is achieved.

The monochromatic radiation produced by the excimer laser (typical power per pulse was ~150mJ at a repetition rate of 10Hz) was used to pump a dye laser which emitted tunable visible radiation. The active medium of the dye laser consists of large organic dye molecules dissolved in a solvent such as an alchohol or water. The dyes used[5] have a wide range of structures, but they all have in common a planar skeleton with a conjugated π-electron system delocalised over a large part of the molecule. This high degree of delocalisation has the important consequence that the highest occupied and lowest unoccupied molecular orbitals are close together, with their energy difference corresponding to the visible region of the electromagnetic spectrum. Furthermore the oscillator strengths for allowed transitions in dye molecules are usually quite large as a result of the large dipole moments which are present in these molecules.

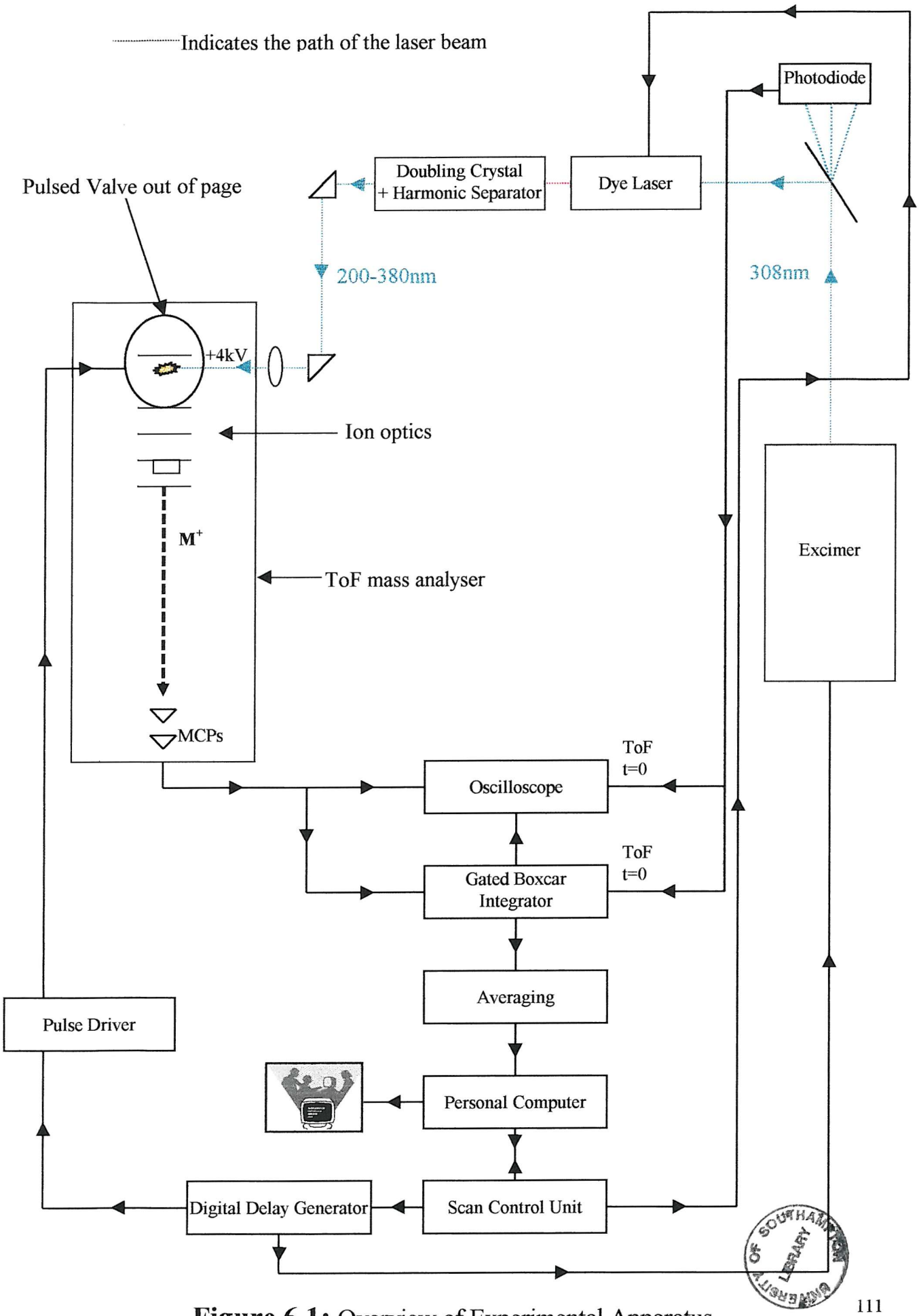

Figure 6.1: Overview of Experimental Apparatus

The pump transition, provided by the excimer radiation, corresponds to excitation from the ground state of the dye molecule (S_0) in solution to an excited singlet state (S_1). This is rapidly followed by collisional relaxation to the lower levels of S_1. The laser radiation is produced by stimulated emission from the lower vibrational levels of S_1 which, as a consequence of the Frank-Condon principle, terminate in vibrationally excited levels of S_0.

On entering the dye laser, the excimer beam is split into two parts (laser cavities). A lower intensity part goes to the oscillator and a more intense part to the amplifier. Tuning within the broad emission curves of the dye molecules is accomplished by making the cavity loss in the oscillator larger than the gain for most frequencies. To achieve this, one of the cavity mirrors is replaced by a diffraction grating which reflects radiation of wavelength λ only in those directions θ satisfying the Bragg condition[3]

$$2d\sin\theta = n\lambda \qquad \ldots(6.1)$$

where d is the spacing between the lines of the grating and n is the order of diffraction. Wavelengths not satisfying equation (6.1) are not fed back along the oscillator axis and consequently have large losses. Thus the bandwidth of the laser is greatly reduced, and tuning is accomplished by rotation of the grating. The output beam from the oscillator passes through an amplifying dye cell, the pumping of which is delayed to avoid amplification of prompt fluorescence from the oscillator, to give a final power on the order 10 $mJpulse^{-1}$. The linewidth of this beam is mostly determined by the groove density and number of illuminated grooves of the grating and was approximately 0.1cm^{-1} in this work[6].

Frequency doubling of the dye laser output was achieved using KD*P (KD_2PO_4) and BBO (β-BaB_2O_4) crystals for the 300-360nm and 222-300nm wavelength ranges respectively[7]. This phenomenon, known as second harmonic generation, is only achieved at the relatively high electric field intensities which are generated by the dye laser. Under these circumstances non-linear terms in the expression (6.2) which relate the electric polarisation, P, induced in the crystal to the electric field, strength E, of the laser radiation become significant.[8]

$$P = \varepsilon_0\left(\chi E + \chi_2 E^2 + \chi_3 E^3\right) \qquad \ldots(6.2)$$

In this equation, ε_0 is the vacuum permittivity, χ is the dimensionless linear susceptibility constant, and χ_2 and χ_3 represent non-linear susceptibilities. If the laser radiation has an oscillating electric field strength which can be written as, $E=E_0\sin\omega t$, where E_0 is the amplitude of the electric field and ω is the angular frequency (rad s^{-1}) it can be seen that the induced electric polarization will be given by equation 6.3.

$$P = \varepsilon_0 \chi E_0 \sin\omega t + \frac{\varepsilon \chi_{20}}{2} E_0^2 (1 - \cos 2\omega t) + \frac{\varepsilon \chi_{30}}{4} E_0^3 (3\sin\omega t - \sin 3\omega t) + \ldots \qquad \ldots(6.3)$$

Finally, the Maxwell equation[8] (6.4)

$$\nabla^2 E - \varepsilon_0 \mu_0 \frac{\delta^2 E}{\delta t^2} = \mu_0 \frac{\delta^2 P}{\delta t^2} \qquad \ldots(6.4)$$

then infers that the second harmonic term in the polarization P should act as a source for a second-harmonic contribution to the electric field E.

Efficient second-harmonic generation requires the pump and second harmonics to be *phase-matched*. The method of phase-matching used in this work utilizes the birefringence of the uniaxial crystals used for second-harmonic generation. Only two types of wave can propagate in such a crystal, namely, waves plane-polarized perpendicular to the plane formed by the optic axis (along which direction the refractive index is independent of the direction of polarization) and the axis of propagation (ordinary waves), and waves plane-polarized parallel to this plane (extraordinary waves). The refractive index for ordinary waves is denoted by n_0. The refractive index, n_e, of an extraordinary wave has an angular dependence upon its angle of propagation, θ, relative to the optic axis given by the relation (6.5)

$$\frac{1}{n_e(\omega,\theta)^2} = \frac{\cos^2\theta}{n_o^2(\omega)} + \frac{\sin^2\theta}{n_e^2(\omega)} \qquad \ldots(6.5)$$

Hence the dye laser output is propagated into the crystal as an extraordinary wave at an angle θ chosen such that equation (6.6) holds.

$$n_0(2\omega) = n_e(\omega,\theta) \qquad \ldots(6.6)$$

The second-harmonic wave is generated as an ordinary wave propagating in the direction θ, since this is the only direction and polarization for which there is phase matching and substantial second harmonic generation. In practice maximum second harmonic generation is maintained by synchronously tuning the angle of the crystal with the wavelength of the dye laser, according to a user pre-set tracking curve. After transmission through the crystal the radiation is returned along its original path via a compensator block which is situated to mirror image the position of the crystal. Finally the frequency doubled radiation is separated from the fundamental using a harmonic separator which consists of four prisms set at Brewster angles and two beam stops which are oriented to block the fundamental while allowing the second harmonic to pass through. Right-angled prisms, made from either crystalline quartz or UV fused silica (synthetic quartz) were used to steer the laser radiation into the ionization chamber. Where high power densities were required, the laser radiation was focussed into the ionization region using a quartz lens of the appropriate focal length. Calibration of the laser wavelength scale was achieved by comparison with appropriate multiphoton ionization spectra of NO together with atomic transitions of Kr and Xe[9], the specific transitions depending on the region of interest.

6.2 Vacuum System

The vacuum system used in this work consisted of an ionisation chamber, onto which was built a time-of-flight (ToF) tube with a length of ~1m. A large diffusion pump (Edwards E250, 2130 ls^{-1}) backed by a rotary pump (Edwards ED660, 40m^3h^{-1}) was used to evacuate the ionisation chamber and this provided a base pressure on the order of 10^{-5}mbar. The ToF tube and ion detection system was pumped by two diffusion pumps (Edwards E08, 1300ls^{-1}, and Edwards E06M3A, 650ls^{-1}) each backed by a rotary pump (Edwards E2M8, 9.5m^3h^{-1}, and Edwards E2M6, 5.6m^3h^{-1}) giving rise to a base pressure on the order of 10^{-6} mbar. The diffusion pumps attached to the ToF tube were both fitted with liquid nitrogen traps to improve pumping efficiency.

6.3 Sample Preparation

The problem in preparing a suitable sample of van der Waals molecules for spectroscopic study arises from the fact that the van der Waals bond is weak and under ordinary conditions is unstable with respect to dissociation by binary collisions. Of the various approaches used to solve this synthesis problem, the most appropriate for spectroscopic study is to work on a system that is not in thermodynamic equilibrium. A supersonic expansion[10,11] (housed in an X,Y,Z translatable mount positioned above the ionization region) was used to generate the sample where the molecule of interest, either neat or in a carrier gas, is expanded from a relatively high stagnation pressure (~4 atm) through a small orifice (diameter=440μm) into the ionisation chamber (pressure~10^{-5} mbar). The expansion cools the translational degrees of freedom of the gas mixture, and in the post-nozzle region of the expansion, the cold translational bath acts as a refrigerant for the other degrees of freedom. The supersonic expansion then serves two purposes. A low temperature environment is provided, where the most probable relative kinetic energy in a binary collision is very much less than van der Waals binding energies. Under these conditions van der Waals molecules, once formed, are stable with respect to collisions with the surrounding gas. The second function of the supersonic expansion is the simplification of the spectrum by depopulation of excited rotational and vibrational states. This is particularly important in the spectroscopic study of van der Waals molecules since intermolecular bonds tend to be weak and long, which implies low frequency vibrations and small rotational constants.

6.4 Time-of-Flight Mass Analysis

After photoionization, the sample of interest is accelerated towards the collector by a series of constant electric fields. The velocity of ions in a free flight path is a function of the ratio of their charge, q, to their mass, m[12]. Therefore, when the ions reach the collector they have separated into bunches of different q/m values. If only singly charged ions are present, the lightest group reaches the collector first and they are followed by groups of successively heavier mass. Therefore each laser shot produces a mass spectrum which is easily obtained by connecting the ion collector to the vertical plates of an oscilloscope. The unique advantage of ToF mass spectrometry in this work is the speed with which a spectrum can be obtained conveniently. This allows the carrier of a particular multi-photon ion signal to be easily identified and, if necessary, more than one species can be monitored simultaneously.

The ion optics system used in this work was based on the two-field acceleration design of Wiley and McLaren[13]. The resolution of a ToF mass spectrometer depends on its ability to reduce the time spread caused by the ever-present initial space and kinetic energy distributions. The problem of an initial energy spread can be reduced significantly by applying a strong electric field, but since the acquired energy of the ions depends greatly on their position before acceleration this will only serve to promote broadening arising from the spatial factor. Hence space resolution and energy resolution place opposite requirements on the system. The best over-all resolution is a compromise between the two, which the two-field system (usually one weak and one strong) provides[14]. The ion extraction arrangement, shown in Fig 6.2, consists of a series of 25mm-diameter plates, each held at a constant potential with respect to ground. The two electric fields generated between plates A (~3000V) and B (~1000V) and plates B and C (ground) were used to extract the ions from the interaction region. The ions then pass through a 3-element Einzel lens system which focuses them along a 1m long field-free drift tube. The Einzel lens consisted of a focussing plate D (~500V) and a plate E set at ground potential. Plates B,C and E had tungsten-mesh-covered apertures (diameter=10mm) cut through their centre to allow the passage of ions.

After traversing the field-free domain, the ions were detected by a resistance-matched pair of 25mm-diameter microchannel plates (Galileo 1396-0050). A copper plate, known as the Faraday plate, collects the amplified current that is monitored by a digital storage oscilloscope (GOULD 4062) which is triggered (this defines ToF=0) by a signal from the photodiode initiated by scattered light from the excimer laser.

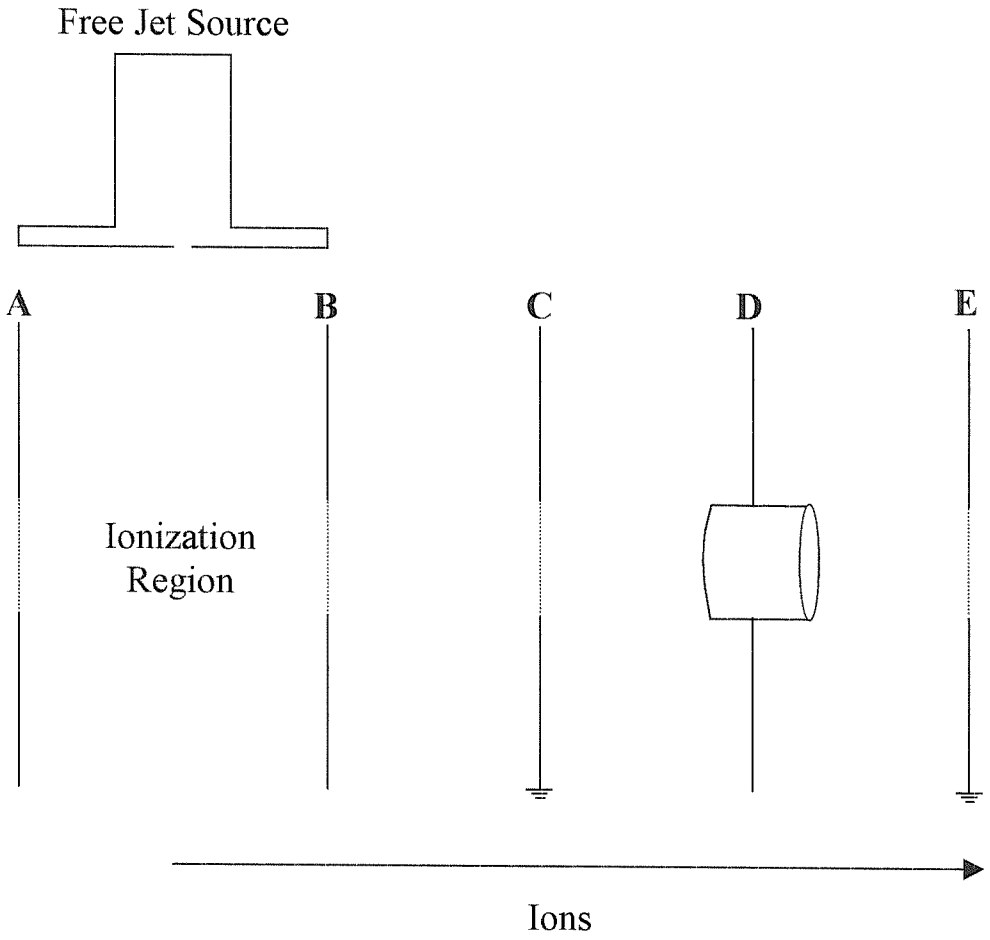

Figure 6.2: Ion Extraction System

6.5 Recording REMPI Spectra

Before recording a spectrum, the REMPI signal was optimized by making small adjustments to the ion acceleration voltages and laser beam orientation. The wavelength scanned spectra associated with selected mass channels were then collected by a Boxcar integrator (SRS SR250) which was interfaced to an IBM PC compatible computer. A dye laser scan control unit (SCU) controlled the firing and wavelength position of the laser system via a set of user defined parameters (scan start and finish wavelength in nm, step size in nm, repetition rate in Hz and number of shots per wavelength position).

A scan begins when the SCU, initiated by the PC running Stanford Systems SRS 265 software, steps the dye laser to the first wavelength position required. The doubling crystal moves synchronously, according to a pre-optimized curve, with the diffraction grating in order to achieve optimum phase matching as the wavelength changes. Once the grating and crystal are in position, the SCU then signals the beginning of a laser shot series by triggering a delay generator (SRS DG535). Ten laser shots (or more if more precise data are required) are fired, with each preceded by a gas pulse formed by enabling (using an IOTA ONE general valve corporation pulse driver) a high speed solenoid pulsed valve, (General Valve Corporation, Series 9). The valve is constructed of corrosion resistant materials and can operate with very short pulses up to stagnation pressures of 85 atm. The photodiode, mentioned earlier, signals time ToF=0 by triggering the SR250 boxcar which, after a delay appropriate to the mass of the species of interest, integrates the ion signal arriving in a gate of user-defined width. The SR250 boxcar averages over the 10 shots and converts the result into digital form for transmission to the computer via an RS232 interface. The SCU then steps the dye laser wavelength to the next position, and the process is repeated until the end of the scan is reached. Survey scans were recorded with stepsize 0.01nm whereas detailed work used the smaller 0.004nm stepsize, resulting in better resolution. The SR265 software allowed display, storage, scaling and manipulation of the data obtained.

6.6 Summary

In this chapter, the experimental apparatus and operating procedures employed in the REMPI spectroscopic studies of Ar·NO , Kr·NO, and $(CO)_2$ have been described.

6.7 References

1. *Lumonics Excimer-500 Reference Manual*, Lumonics Inc. Kanata, Ontario, Canada.

2. D. L. Andrews, *Lasers in Chemistry*, Springer-Verlag, Berlin, (1986).

3. J. M. Hollas, *High Resolution Spectroscopy*, Butterworths, London (1982).

4. Lumonics HyperDye-300 Reference Manual, Lumonics Inc. Kanata, Ontario, Canada.

5. *Exciton Laser Dye Catalogue*, Exciton Inc., Ohio, USA (1989).

6. *Lumonics Excimer-500 Reference Manual*, Lumonics Inc., Kanata, Ontario, Canada (1986).

7. *Lumonics Hypertrak-1000 SHG Option Reference Manual*, Lumonics Inc., Kanata, Ontario, Canada (1988).

8. E. Hecht, *Optics*, 2nd Edition, Addison-Wesley, Reading, Massachusetts (1987).

9. C. Moore, *Atomic Energy Levels*, circular 467, United States National Bureau of Standards (1949).

10. R. E. Smalley, L. Wharton and D. H. Levy, *Acc. Chem. Res.*, **10**, 139 (1977).

11. R. E. Smalley, L. Wharton and D. H. Levy, *J. Chem. Phys.*, **63**, 4977 (1975).

12. V. H. Dibeler, *Anal. Chem.* **26**, 58 (1954).

13. W. C. Wiley and I. H. McLaren, *Rev. Sci. Instrum.* **26**, 1150 (1955).

14. M. Tabrizchi, *PhD Thesis*, University of Southampton (1996).

Chapter 7 Theoretical methods used to interpret (2+1) REMPI spectra of 'Rare-Gas'-NO Complexes

7.1 Introduction

This chapter describes the theory used to interpret the (2+1) REMPI spectra of the Ar·NO and Kr·NO complexes associated with the $\widetilde{E}^2\Sigma^+ \leftarrow \widetilde{X}^2\Pi$ two-photon electronic transition. In the recorded spectra the structure due to intermolecular vibrations of the complex is completely resolved, but it was only possible to partially resolve rotational structure due to the rotation of the complex about the *a* inertial axis. In order to reproduce the observed transition energies and intensities, and hence obtain accurate molecular parameters, for each electronic state, it is necessary to take into account the full Hamiltonian (Eqn 7.1) for the problem for each state which, within the Born-Oppenheimer approximation, may be written as the sum of electronic, vibrational and rotational contributions.

$$H_{TOT} = H_{ELECTRONIC} + H_{VIBRATIONAL} + H_{ROTATIONAL} \qquad \ldots(7.1)$$

Under favourable circumstances it may be possible to calculate an accurate potential energy surface in a given electronic state by *ab initio* or semi-empirical treatments of the many electron problem. It would be necessary to have accurate potential energy surfaces available for each electronic state in order to calculate vibrational frequencies and Franck-Condon factors and hence fit the vibrational structure observed in the spectrum.. Although an accurate potential energy surface exists for the ground ($\widetilde{X}^2\Pi$) state of Ar·NO[1,2], no accurate electronic structure calculations have been performed on the Rydberg ($\widetilde{E}^2\Sigma^+$) state. As a result, the approach taken in this work is to calculate the rotational structure of a particular vibronic component in the $\widetilde{E}^2\Sigma^+ \leftarrow \widetilde{X}^2\Pi$ (2+1) REMPI spectrum and then include the electronic and vibrational parts of the Hamiltonian empirically.

The model used is based upon the formalism presented by Fawzy *et.al*[3], where matrix elements required for calculating rotational energy levels for a planar complex consisting of an open-shell diatomic molecule and a closed-shell partner were derived. Also included in Ref. [3] were transition-moment matrix elements needed for calculating intensities in single-photon electric-dipole allowed transitions, with the excitation localized on the open-shell diatomic fragment. The approach is extended to two-photon transitions following the

method of Meyer[19]. In this approach the matrix elements of the two-photon absorption operator are generated by rotating the nonvanishing spherical tensor components of the corresponding transition in the bare NO molecule into the principal axis system of the complex. This chapter first describes the two-photon spectroscopy of the isolated NO molecule and then shows how this theory may be extended to explain the rotational structure observed in the two-photon spectra associated with the Rg·NO complexes.

7.2 Two-Photon Spectroscopy of NO

The single-photon absorption and emission spectra of the NO molecule have been investigated extensively by many different groups[4]. The ground electronic state of NO has the configuration:

$$1\sigma^2 2\sigma^2 3\sigma^2 4\sigma^2 5\sigma^2 1\pi^4 2\pi$$

The excited states of the NO molecule can be classified into one of two types: either valence or Rydberg. Excitation of an electron out of the filled closed shell molecular orbitals into the antibonding 2π orbital leads to valence states. The two lowest excited configurations of this type are

$$1\pi^4 2\pi \rightarrow 1\pi^3 2\pi^2, \qquad \text{States Obtained: } a^4\Pi,\ B^2\Pi,\ L^2\Pi,\ ^2\Phi,\ ^2\Pi$$

and

$$5\sigma^2 2\pi \rightarrow 5\sigma 2\pi^2, \qquad \text{States Obtained: } b^4\Sigma^-,\ B'^2\Delta,\ G^2\Sigma^-,\ I^2\Sigma^+$$

Of these nine valence excited states, seven have been observed spectroscopically[4]. Excitation of an electron from one of the closed shells into Rydberg orbitals leads to a series of Rydberg states which converge to electronically excited states of the NO^+ ion. So far, four such series have been identified. This work is concerned with Rydberg states converging to the ground $X^1\Sigma^+$ ionic state of NO which are produced when an electron is excited from the 2π anti-bonding orbital into a Rydberg orbital, denoted as $nl\lambda$. These states are characterized by vibrational constants ω_e and rotational constants B_e almost identical with ω_e=2377cm^{-1} and B_e=2.002cm^{-1} of NO^+, $X^1\Sigma^+$.

7.2.1 Transition Energies

As was mentioned in (7.1), the energy of a rovibronic state is treated as a sum of electronic, vibrational and rotational contributions. Therefore, for a transition between two states, the total energy change, ΔE, can be written as (7.2)

$$\Delta E = \Delta E^{EL} + \Delta G(v) + \Delta F(J) \qquad \ldots(7.2)$$

where ΔE, ΔG and ΔF are the electronic, vibrational and rotational contributions respectively. In this work the contribution of an electronic energy change ΔE is assumed to have a constant value for a given transition. The vibrational contribution to the total transition energy, $\Delta G(v)$, was discussed in Chapter 3.

In order to evaluate the rotational, $\Delta F(J)$, contribution to the transition energy, it is necessary to consider the various sources of angular momentum that are present in a molecule and how they couple together. There are four sources of angular momentum in a diatomic molecule: the spin of the electrons (**S**), their orbital angular momenta (**L**), the rotation of the nuclear framework (**R**), and the nuclear spin (**I**). There are several different interactions that can couple these momenta together to varying extents, forming a resultant that is always designated **J**. Of the wide range of coupling approximations which may result from these interactions, Hund proposed five which are most commonly occurring. These are referred to as Hunds coupling cases (a), (b), (c), (d) and (e). If rotational states are expressed in terms of a basis of functions corresponding to a particular coupling case, the Hamiltonian, H, can be separated into a part, H^0, which has only diagonal matrix elements between a given set of states. The remaining part, H′, then corresponds to deviations of the true system from that described by the Hunds coupling case, and contains the appropriate off-diagonal matrix elements. The coupling cases most relevant to this work (cases (a) and (b)) are described below and are characterized by a set of rigorously good quantum numbers only if H′ is ignored. If the total Hamiltonian, H, is considered then its eigenvalues are unaffected by the 'choice' of coupling case, so long as the basis forms a complete set of functions.

Hund's Case (a)

The good quantum numbers in Hund's case (a), shown as a vector diagram in Figure 7.1, are J,S,Λ,Σ and Ω.[8] Here, Λ and Σ are the components of the electronic and spin angular momenta of the electrons respectively, parallel to the internuclear axis. This case is appropriate when the spin-orbit coupling term in the total hamiltonian, H_{so}, is large compared to the rotational term H_{rot} but is small compared to the splitting between states of different Λ. This results in **S** being strongly coupled to Λ and therefore also, indirectly, to the internuclear axis; the quantum number Σ is then well defined. The total angular momentum, **J**, is then given by the vector sum of the component parallel to the internuclear axis, Ω=Σ+Λ, and the component perpendicular to this axis, **R**, which arises from rotation of the nuclear framework.

Hund's Case (b)

In Hund's case (b), also shown as a vector diagram in Figure 7.1, the good quantum numbers are J, S, N and Λ. This case is appropriate for an electronic state when the spin-orbit coupling term, H_{so}, is small compared to H_{rot}. Under these circumstances L but not S is quantised along the internuclear axis; **R** and **Λ** couple to form a resultant **N**, which then couples with **S** to form a resultant **J.**

The rotational energies may be obtained by formulating the total Hamiltonian in terms of the various angular momentum operators **J, N, S, R** and **L** and selecting suitable basis functions for the problem. Secular equations can then be constructed and diagonalized to obtain the eigenvalues and eigenvectors.

Figure 7.1: Hund's Coupling Cases for an open-shell diatomic

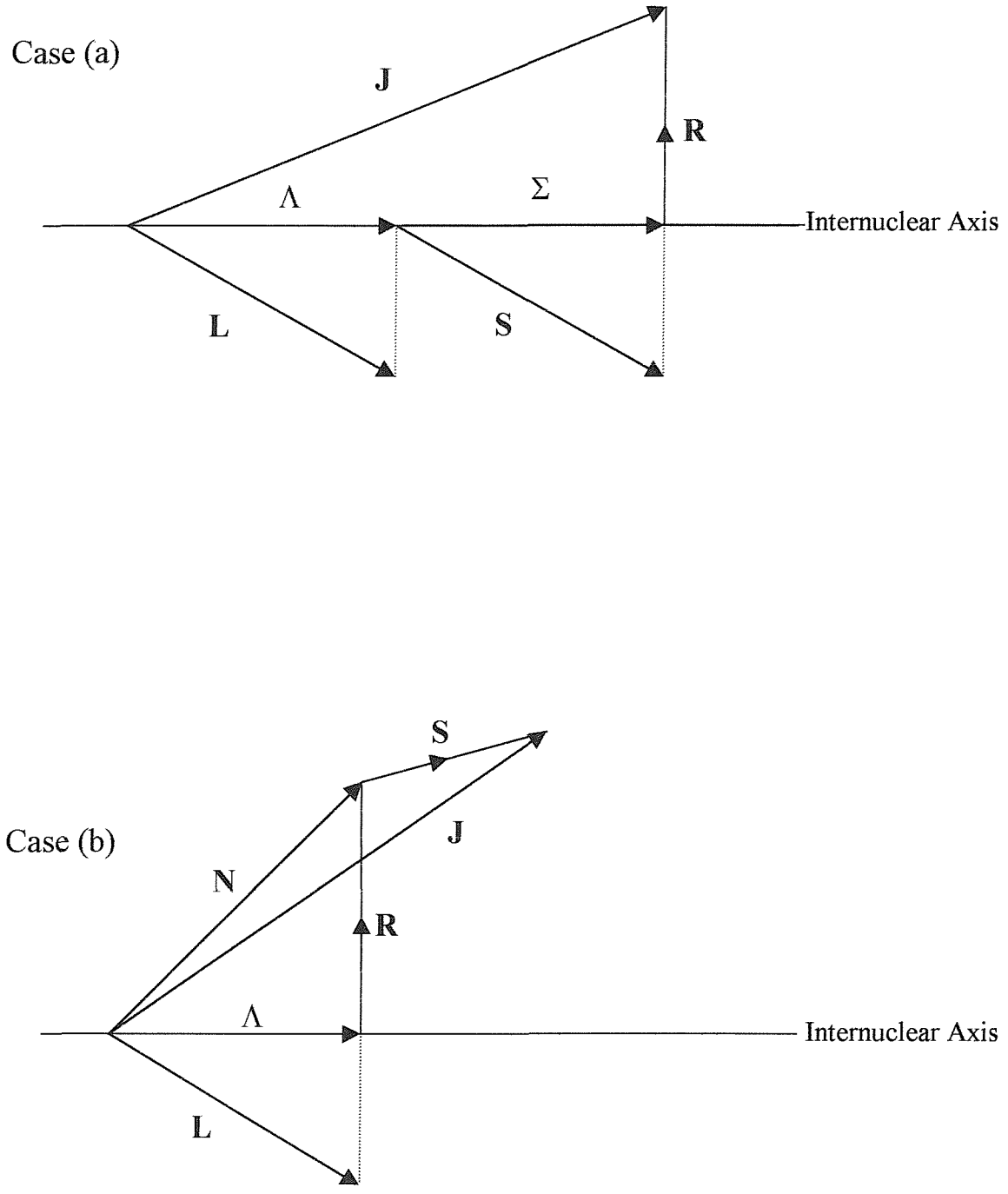

If the vibronic expectation value (7.5),

$$\left\langle \hat{H}_{el} + \hat{H}_{vib} \right\rangle = E_{ev} \qquad \ldots(7.5)$$

is treated as a constant for a given state then only the effects of the rotational (7.6) and spin-orbit (7.7) parts of the total Hamiltonian need to be considered when evaluating the rotational energy levels. H_{rot} and H_{so} can then be written as follows:-[5]

$$\begin{aligned} H_{rot} &= B(R)^2 = B(J-L-S)^2 \qquad \ldots(7.6) \\ &= B(J^2 - J_z^2) + B(S^2 - S_z^2) + B(L^2 - L_z^2) \\ &- B(J^+L^- + J^-L^+) - B(J^+S^- + J^-S^+) + B(L^+S^- + L^-S^+) \end{aligned}$$

$$H_{so} = AL \cdot S = AL_z S_Z + A\frac{L^+S^- + L^-S^+}{2} \qquad \ldots(7.7)$$

In these equations,

$$J^{\pm} = J_x \pm iJ_y \qquad L^{\pm} = L_x \pm iL_y \qquad S^{\pm} = S_x \pm iS_y$$

are raising and lowering operators.

In the $X^2\Pi$ state of NO the lower rotational energy levels are sufficiently approximated by the case Hund's (a). The associated energy level pattern consists of two widely separated $^2\Pi_{3/2}$ and $^2\Pi_{1/2}$ spin-orbit components, both having the same rotational constant, rotational energy $E_J = BJ(J+1)$, and very similar potential energy curves.

For the $\widetilde{E}^2\Sigma^+$ Rydberg state of NO[5] there are two case (b) basis functions,

$$\left| n, \Lambda = 0, S = \frac{1}{2}, \Sigma = \frac{1}{2} \right\rangle \left| v \right\rangle \left| JM \right\rangle = \left| {}^2\Sigma_{1/2} \right\rangle$$

$$\left|n,\Lambda=0,S=\frac{1}{2},\Sigma=-\frac{1}{2}\right\rangle\left|v\right\rangle\left|JM\right\rangle=\left|{}^{2}\Sigma_{-1/2}\right\rangle$$

and diagonalization of the Hamiltonian matrix (using all of 7.6) in this basis set gives two degenerate spin-rotation terms, F_1(e parity) and F_2(f parity), each with rotational energy E_J=BN(N+1). For the F_1 levels N is J-1/2 while for the F_2 levels N is J+1/2. Inclusion of the spin rotation term

$$\hat{H}_{SR}=\gamma N\cdot S \qquad \ldots(7.8)$$

where γ is the spin-rotation coupling constant, splits the F_1 and F_2 levels by the amount $\gamma\left(N+\frac{1}{2}\right)$ which is too small to observe in this work.

By using these rotational energy expressions for the $E^2\Sigma^+$ and $X^2\Pi$ states and applying the appropriate selection rules (see 7.2.2) the line positions within a particular vibronic transition can easily be predicted.

7.2.2 Two Photon Transition Intensities

Electromagnetic radiation may be considered as having oscillating electric and magnetic fields perpendicular to the propagation direction. Since the interaction of the magnetic field with a molecule is usually several orders of magnitude smaller that that of the electric field it is neglected in this work. Also, since the wavelengths of the radiation being used are longer than the species under investigation, the electric field across the molecule at any instant may be assumed to be uniform. This is known as the electric dipole approximation. The electric dipole interaction Hamiltonian may be represented as[6,7]

$$H=-\mu.E=-(\mu.\varepsilon_a)E_a\cos\omega_a t \qquad \ldots(7.9)$$

where μ is the molecular electric dipole moment, E is the electric field strength of magnitude E_a and unit polarization ε_a, and ω_a is the radiation frequency. Time dependent perturbation theory may used to calculate the probability of an n-photon transition from an

initial state $|g\rangle$ to a final state $|f\rangle$[8]. For example, the transition probability for a single photon transition is given by

$$P_{f\leftarrow g}(t) \propto I\left|\langle f|\varepsilon.\mu|g\rangle\right|^2 \frac{\sin^2\left[(\omega_{fg}-\omega)t/2\right]}{(\omega_{fg}-\omega)^2} \qquad \ldots(7.10)$$

where ω_{fg} is the frequency required for the transition f←g, I is the radiation intensity, and ω is the frequency of the incident radiation. Expression (7.10) contains a dependence on time and assumes completely monochromatic radiation. The observed transition rate is an integral over all of the transition probabilities to which the perturbing electric field can drive the system. If the density of states is written $\rho(E)$, where $\rho(E)$ is the number of final states accessible under the influence of the perturbation then the total transition probability is

$$P_{f\leftarrow g}(t) = \int P_{f\leftarrow g}(t)\rho(E)dE \qquad \ldots(7.11)$$

Evaluating this integral[8], and then taking the first derivative with respect to time, yields the transition rate which is given by

$$W_{f\leftarrow g} \propto \left|\langle f|\varepsilon.\mu|g\rangle\right|^2 \rho(E) \qquad \ldots(7.12)$$

The most significant term in equation (7.12) is the square of the transition moment, $R_{fg} = \langle f|\varepsilon\mu|g\rangle$ since this factor depends on the properties of the molecule and the polarization of the radiation.

For multiphoton processes the transition moment R_{fg} must be evaluated at higher perturbation orders. A two-photon transition proceeds from the ground $|g\rangle$ state, through a virtual intermediate state $|v\rangle$ and reaches the final state $|f\rangle$. The virtual state $|v\rangle$ can be expanded in terms of the complete basis of real states $|i\rangle$ with energies $\hbar\omega_i$, as follows:-

$$|v\rangle = \sum_i c_i|i\rangle \qquad \ldots(7.13)$$

The form of the generalised transition moment is[6,7]

$$
\begin{aligned}
R_{fg} &= \varepsilon_a \langle f|\mu_a|g\rangle \\
&+ \varepsilon_a \varepsilon_b . \sum \left\{ \frac{\langle f|\mu_b|i\rangle\langle i|\mu_a|g\rangle}{\hbar(\omega_{ig} - \omega_a)} + \frac{\langle f|\mu_a|i\rangle\langle i|\mu_b|g\rangle}{\hbar(\omega_{ig} - \omega_b)} \right\} \\
&+ \varepsilon_a \varepsilon_b \varepsilon_c . \sum_i \sum_j \left\{ \frac{\langle f|\mu_c|j\rangle\langle j|\mu_b|i\rangle\langle i|\mu_a|g\rangle}{\hbar^2(\omega_{ig} - \omega_a)(\omega_{jg} - (\omega_a + \omega_b))} + \textit{five permutations} \right\} \\
&+ \ldots
\end{aligned}
\qquad \ldots(7.14)
$$

where the first three terms represent one, two and three photon transitions. For the purposes of calculating transition intensities it is more convenient to express the transition moment, R_{fg} in terms of dimensionless cartesian polarization tensors and cartesian tensors of molecular transition matrix elements.

R_{fg} then becomes[9],

$$
\begin{aligned}
R_{fg} &= T(\varepsilon_a).T_{fg}(\mu) \\
&+ T(\varepsilon_a \varepsilon_b).T_{fg}(A) \\
&+ T(\varepsilon_a \varepsilon_b \varepsilon_c).T_{fg}(B) \\
&+ \ldots
\end{aligned}
\qquad \ldots(7.15)
$$

where T(μ), T(A) and T(B) are the operators of the dipole vector, the polarisability tensor and the first hyperpolarisability tensor, giving rise to one, two, and three photon transitions respectively. For one-colour excitation (i.e. $\omega_a = \omega_b = \omega$), the permutations in Eqn (7.14) collapse to individual terms, weighted according to the n! possible orderings of the n photons. In this case T(μ), T(A) and T(B) are given by

$$T_{fg}(\mu) = \langle f|\mu|g\rangle \qquad \ldots(7.16)$$

$$T_{fg}(A) = 2\sum_i \frac{\langle f|\mu|i\rangle\langle i|\mu|g\rangle}{\hbar(\omega_{ig} - \omega)}$$

$$T_{fg}(B) = 6\sum_i\sum_j \frac{\langle f|\mu|j\rangle\langle j|\mu|i\rangle\langle i|\mu|g\rangle}{\hbar^2(\omega_{ig} - \omega)(\omega_{jg} - 2\omega)}$$

The overall transition rate for a two-photon transition is then given by

$$W_{fg} \propto I^2\left|T(\varepsilon\varepsilon).T_{fg}(A)\right|^2 \qquad \ldots(7.17)$$

In Eqn(7.17) the polarization tensors are expressed in the laboratory or space-fixed frame (SFF), whilst the tensor expressing the molecular transition matrix element $T_{fg}(A)$ is expressed in the molecule-fixed frame (MFF). In order to calculate rotational line strength factors, the MFF tensors must be transformed into the SFF. The simple rotational transformation properties of spherical tensors, T^k can be utilized to solve this problem most succinctly. An irreducible spherical tensor, T^k has 2k+1 components denoted by T^k_p, where k is the rank of the tensor and p, which can take the values, p=0, ±1, …, ±k, labels the component. When reduced into their irreducible spherical tensor components, the cartesian polarisation tensor and the first hyperpolarisability tensor become[9]

$$T(A) = T^0(A) + T^2(A) \qquad \ldots(7.18)$$
$$T(B) = T^1(B) + T^3(B)$$

As has been mentioned above, the non-zero vibronic matrix elements of T(A), which are defined in the molecular axis system, must be rotated to the space-fixed axes of the polarization tensors for insertion into eqn(7.17). This is achieved by the use of the following transformation[10]

$$T^k_p = \sum_q D^{k*}_{pq}(\omega)T^k_q \qquad \ldots(7.19)$$

where the q component is in the MFF and the p component is in the SFF. The factor D^{k*}_{pq} is a Wigner rotation matrix[11]. When evaluating the matrix elements of each $T^k_p(A)$,the rovibronic wavefunctions for the $|g\rangle$ and $|f\rangle$ states may be expressed as products of vibronic $|\eta\rangle$, and rotational $|JM\Omega\rangle$ (for a diatomic with Hund's case (a) coupling) functions. As a consequence the matrix elements can be factorised as follows

$$\begin{aligned}\langle f|T^k_p|g\rangle &= \langle \eta_f |\langle J_f M_f \Omega_f |T^k_p| J_g M_g \Omega_g\rangle |\eta_g\rangle \\ &= \sum_q \langle \eta_f |T^k_q|\eta_g\rangle \langle J_f M_f \Omega_f |D^{k*}_{pq}(\omega)| J_g M_g \Omega_g\rangle\end{aligned} \qquad \ldots(7.20)$$

The last matrix element in eqn.(7.20) which involves only the rotational part of the wavefunction is given by[9,12]

$$\begin{aligned}&\langle J_f M_f \Omega_f |D^{k*}_{pq}(\omega)| J_f M_f \Omega_f\rangle = (-1)^{p-q+M_g-\Omega_g} \\ &\times\left[(2J_f+1)(2J_g+1)\right]^{1/2}\begin{pmatrix} J_f & k & J_g \\ M_f & -p & -M_g\end{pmatrix}\begin{pmatrix} J_f & k & J_g \\ \Omega_f & -q & -\Omega_g\end{pmatrix}\end{aligned} \qquad \ldots(7.21)$$

where the final two terms are Wigner 3-j symbols[11]. Substitution of Eqns (7.20) and (7.21) into the expression for the two photon transition rate (Eqn 7.17) allows the line strength for transitions between states with Hund's case (a) coupling to be derived[9,12].

$$\begin{aligned}\sum_{M_f}\sum_{M_g}|R_{fg}|^2 &= \sum_{k=0,2}\left[\sum_p \frac{|T^k_{-p}(\varepsilon\varepsilon)|^2}{2k+1}\right] \\ &\times\left[\sum_q |\langle \eta_f |T^k_q(A)|\eta_g\rangle|^2 (2J_f+1)(2J_g+1)\begin{pmatrix} J_f & k & J_g \\ \Omega_f & -q & -\Omega_g\end{pmatrix}^2\right]\end{aligned}$$

$$\ldots(7.22)$$

In this equation, J_f and J_g are the final and initial state rotational quantum numbers, Ω_f and Ω_g are the final and initial state total electronic angular momentum quantum numbers $(\Omega = \Lambda + \Sigma)$, k is the rank of the tensor operator that carries the transition and p and q are the components k, k-1, ..., -k of the tensor operator in the molecule in the space fixed and

molecule fixed frames respectively. Equation (7.22) can be used for a general n-photon transition between Hund's case (a) states if the appropriate changes are made to the tensor operators.

7.2.3 Selection Rules

The factor, $\left|\left\langle \eta_f \left| T_q^k(A) \right| \eta_g \right\rangle\right|^2$, in Eqn(7.22) is the square of the vibronic transition moment and may be further simplified by applying the Born-Oppenheimer approximation to separate out electronic $|\Psi\rangle$, and vibrational $|\nu\rangle$, terms of the vibronic wavefunction. The vibronic transition moment then reduces to a product of an electronic transition moment and a Franck-Condon factor (c.f. 3.1). The Franck-Condon factors, between the initial and final states, may then be used to estimate the expected relative intensities of multiphoton transitions to different vibrational levels of the final electronic state. The vibronic transition moment gives rise to the electronic selection rules for a multi-photon transition. For an allowed transition, $T_q^k(\hat{O})$, where $\hat{O} = \mu, A, B \quad etc$, must transform as the direct product of the initial and final state symmetries in the point group of the molecule. The transformation properties of the components of $T_q^k(\hat{O})$ for the $C_{\infty v}$ and $D_{\infty h}$ point groups are presented in Table(7.1).

Table 7.1 **Transormation properties of the components $T_q^k(\hat{O})$ of the transition tensor for the $C_{\infty v}$ and $D_{\infty h}$ point groups[13]**

k	q	$C_{\infty v}$	$D_{\infty h}$
0	0	Σ^+	Σ_g^+
1	0 ±1	Σ^+ Π	Σ_u^+ Π_u
2	0 ±1 ±2	Σ^+ Π Δ	Σ_g^+ Π_g Δ_g
3	0 ±1 ±2 ±3	Σ^+ Π Δ Φ	Σ_u^+ Π_u Δ_u Φ_u

The rotational selection rules are embodied by the factor in equation (7.22):-

$$\theta_k(g,f) = (2J_f+1)(2J_g+1)\begin{pmatrix} J_f & k & J_g \\ \Omega_f & -q & -\Omega_g \end{pmatrix}^2 \qquad \ldots(7.23)$$

and for an n-photon transition, carried by the k-th rank tensor component T_q^k can be expressed as[9]:

$$\Delta J = J_f - J_g = 0,\pm 1,\pm 2,\ldots,\pm k \qquad \ldots(7.24)$$
$$\Delta\Lambda = \Lambda_f - \Lambda_g = \pm q$$

7.3 Two-Photon Spectroscopy of Van der Waals Complexes involving NO and a Closed Shell Atom

This section describes the model used for the analysis of the rotational structure of two-photon transitions in van der Waals complexes containing a closed shell atom and the NO molecule. The model is based on previous work of Mills *et al.*[14] and Fawzy *et al.*[15] who treated the eigenvalue problem for a rigid rotor type complex with non-zero electronic orbital and spin angular momenta.

Non-linear binary complexes containing one open-shell diatomic molecule (NO) and one closed-shell partner can be thought of as asymmetric rotors with unquenched orbital and spin angular momenta. The theoretical complications in such systems arise from interactions among the four angular momenta in the complex; they are the electron orbital and spin motions, the overall rotational motion of the complex, and the internal rotational motion of the diatomic. The model described here neglects the effect of internal rotation of the NO molecule, focussing instead upon the effects of interactions of the overall rotation and the electron orbital and spin angular momenta. This is expected to be a good approximation for those energy levels that are populated under the extremely low temperature of about 2K in the molecular beam environment. Under these circumstances the complex will have a relatively well-defined bending angle and equilibrium geometry. This may especially be the case for excited Rydberg states where there is a strong degree of charge-induced dipole interaction. Also, due to the limited resolution of the laser based experiments performed in this work in comparison with a microwave experiment, effects resulting from hyperfine interactions are neglected.

7.3.1 The Co-ordinate System

The total angular momentum of the system can be written as:-

$$J = R + L + S \equiv N + S \qquad \ldots(7.25)$$

which is the sum of the end-over-end rotation (**R**), the electron orbital angular momentum (**L**), and the electron spin (**S**), where both **L** and **S** are molecule quantized and have components Λ and Σ, respectively, along the NO axis. The major complications with this model arise because there are two axis systems to consider: (i) An axis system coincident with the principal axes of inertia of the nonlinear complex is important because the complex is an asymmetric rotor. (ii) An axis system with one axis parallel to the open shell diatomic molecule direction is important because the electron orbital angular momentum and the spin angular momentum will be quantized along that direction.

The vector operators in Eqn(7.25) must be considered as components in the two axis systems, as shown in Figure 7.2. The unprimed axis system is defined with respect to the principal axis (PA) system of the complex while the primed axis system is attached to the NO molecule. The x′, y′, z′ system has its z′ axis locked to the internuclear direction of the NO molecule, and its y′ axis perpendicular to the plane of the complex. The x, y, z system has its z axis along the inertial A axis of the complex (approximately coincident with the line joining the centre of mass of the NO molecule and the centre of mass of the closed-shell partner) and its y axis along the inertial C axis, which is necessarily perpendicular to the plane in a planar complex. The angle between the z and z′ axes is represented by θ.

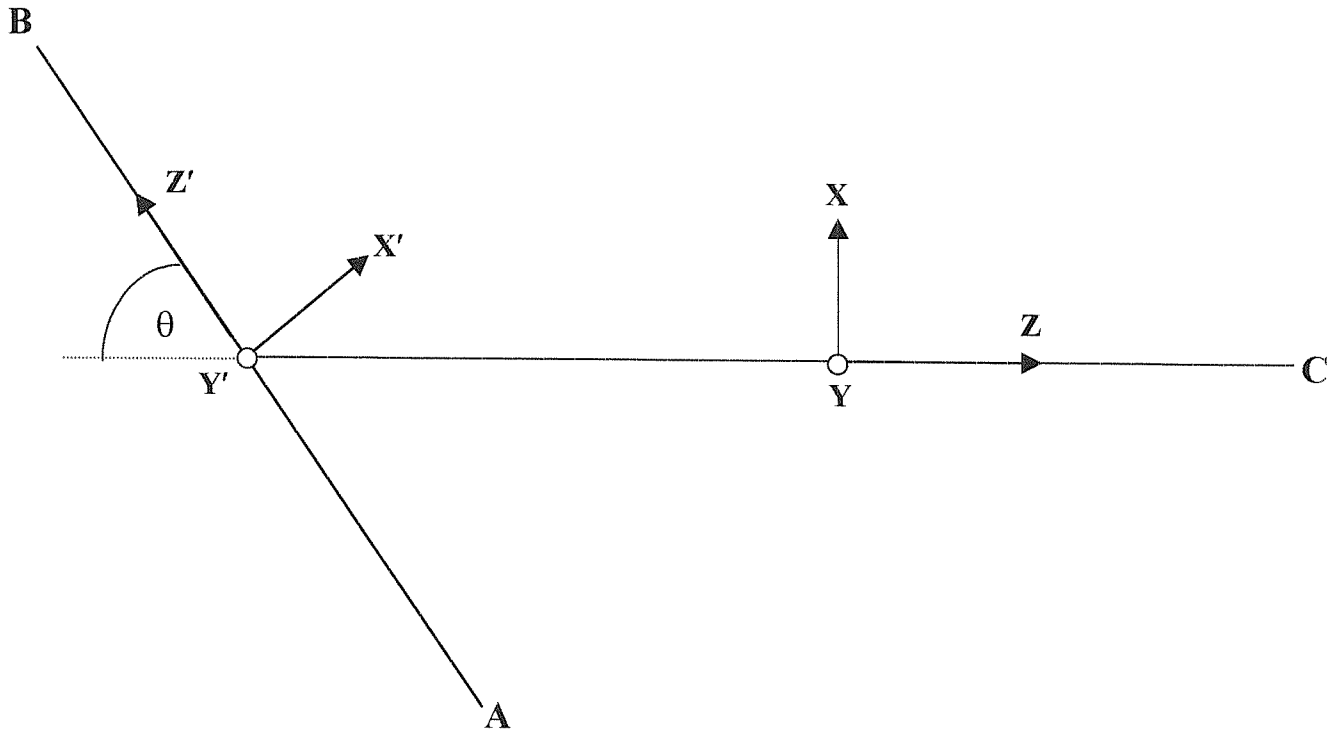

Figure 7.2:
Definition of axis systems for a planar complex consisting of an open-shell diatomic AB and a closed-shell partner C.

Having established the two co-ordinate systems, the components of angular momenta referring to the PA system can then be expressed in terms of linear combinations of the components referring to the NO frame, as follows:-

$$\begin{aligned} \mathbf{L}_x &= \mathbf{L}_{x'} \cos\theta + \mathbf{L}_{z'} \sin\theta \\ \mathbf{L}_y &= \mathbf{L}_{y'} \\ \mathbf{L}_z &= \mathbf{L}_{x'} \sin\theta + \mathbf{L}_{z'} \cos\theta \end{aligned} \qquad \ldots(7.26)$$

Similarly, the individual components of the spin operator can be expressed in terms of the components referring to the NO frame.

7.3.2 Transition Energies

For each state involved in an electronic transition, the approximate Hamiltonian for the problem consists of the following terms

$$H = H_{rot} + H_{SO} + H_q \qquad \ldots(7.27)$$

These terms represent respectively the rotational, spin-orbit and orbital angular momentum quenching contributions. For a system with molecule-quantized electron spin and orbital angular momentum (i.e., similar to a Hund's case (a) representation), the rotational Hamiltonian is given by[8]

$$H_{rot} = A(\mathbf{J}_z - \mathbf{L}_z - \mathbf{S}_z)^2 + B(\mathbf{J}_x - \mathbf{L}_x - \mathbf{S}_x)^2 + C(\mathbf{J}_y - \mathbf{L}_y - \mathbf{S}_y)^2 \qquad \ldots(7.28)$$

where A, B, and C are the conventional rotational constants for the complex. It is assumed, as will almost always be the case because of the long van der Waals bond in the complexes investigated, that the z axis, which connects the centre of mass of the open-shell diatomic fragment and the centre of mass of the closed-shell partner, is the a inertial axis of the complex. For a planar molecule, the inertial c axis must always be perpendicular to the molecular plane, which corresponds in the above coordinate system to the y direction. Also, because of the long van der Waals bond, the complex is expected to be a near symmetric-top prolate rotor. Since in Eqn (7.25) **L** and **S** are quantized along the NO z axis, H_{rot} needs

to be expanded using Eqn(7.26). The rather complex result of this expansion is contained in Refs. 3 and 14.

The spin-orbit Hamiltonian, H_{SO} is given by

$$H_{SO} = a\mathbf{L}'_z\mathbf{S}'_z \qquad \ldots(7.29)$$

where a is the spin-orbit coupling constant. Competing with the spin-orbit coupling, in a doubly degenerate electronic state, is the quenching term H_q. This is caused by the presence of the rare gas atom which lifts the degeneracy of the NO π_x and π_y orbitals. This interaction leads to a barrier to free orbital motion and to a slight quenching of the orbital angular momentum of the odd electron within the complex. The orbital angular momentum quenching is incorporated for an electronic state of given Λ by a term of the form[3]

$$H_q = \frac{1}{2}\varepsilon\left[(\mathbf{L}^+)^{2\Lambda} + (\mathbf{L}^-)^{2\Lambda}\right] \qquad \ldots(7.30)$$

where $(L^{\pm})^{2\Lambda}$ are normalized versions of $(L_x \pm iL_y)^{2\Lambda}$. The quenching term, ε is proportional to the magnitude of the splitting between the two potential surfaces of A′ and A″ symmetry, obtained from the Π state, and must be set to zero when the complex is linear. It is invariant to the sign of the bending angle when the complex is bent. In a Π state a positive value of ε places the state of A″ symmetry at a higher energy than the state of A′ symmetry[3]. A more elaborate function of the vibrational and electronic co-ordinates is required to characterize the true vibronic origins of the quenching, but Eqn(7.30) is adequate for the MPI probing technique.

In choosing the molecular basis set it is assumed that electronic states in the open-shell diatomic are separated from each other by energies which are large compared to the interaction energy with the closed-shell partner. In this case electronic states of the complex can be described in terms of orbitals localized on the open-shell diatomic fragment.. The electronic orbital wavefunctions are therefore of the form $|\eta L\Lambda\rangle$ where Λ is the orbital angular momentum projection quantum number along the z′ axis and η can for simplicity be

taken to be the labelling letter (e.g. X,A,B,a,b) for the electronic state of the diatomic molecule.

The "natural" direction to use for quantizing the electron spin projection depends on the specific problem. In a Π state with large spin-orbit interaction compared to Coriolis interaction energies BJ, CJ, and AK, it would be natural to quantize S along the z′ axis. However, in a Σ state it would be natural to quantize S along either the near-symmetric-top z axis or along the laboratory fixed Z axis. In this work the spin angular momentum operator is defined with respect to a frame attached to the NO molecule so that the quantum number Σ represents the projection of S along the diatomic internuclear direction z′.

Rotational basis set wavefunctions are given by[16,17]

$$\left|PJM_J\right\rangle = \left[(2J+1)/8\pi^2\right]^{1/2} D^{(J)}_{P,M_J}(\chi,\theta,\phi) \qquad \ldots(7.31)$$

where P and M_J represent projections of the total angular momentum J along the molecule-fixed z axis and the laboratory fixed Z axis, respectively.

The complete basis set wavefunctions thus have the simple product form

$$\left|\eta\Lambda\Sigma\right\rangle\left|JMP\right\rangle \qquad \ldots(7.32)$$

and may be used to construct a matrix representation of the total molecular complex Hamiltonian (7.27) where the **L** and **S** operators are defined with respect to the NO frame using Eqns. (7.26). Non-vanishing matrix elements involving wave functions with signed values for both Λ and Σ are given in Refs 3 and 14. Eigenvalues and eigenfunctions may then be determined by numerical diagonalisation of this matrix.

7.3.3 Transition Intensities[18,19]

As was mentioned previously the two-photon transition matrix element is of the form

$$\widetilde{S}_{if} = \sum_{jm} \langle f | \widetilde{\mathbf{T}}^{(1)}_{\mathbf{m}}(LAB) P^{(J)}_{m} | i \rangle \qquad \ldots(7.33)$$

where $P^{(J)}_{m}$ is the polarization tensor and $\widetilde{\mathbf{T}}^{(1)}_{\mathbf{m}}$ is the two-photon absorption operator. In order to derive an expression for the two-photon transition matrix elements of the complex, it must be assumed that excitation is confined exclusively to the NO moiety. The spherical tensor components for the two-photon transition in the NO molecule may then be transformed to the principal axis of the complex by a single rotation[19]. The angle of rotation Θ'' defines the orientation of the internuclear axis in the NO molecule with respect to the principal axis system, (PA''), of the complex.

$$\mathbf{T}^{(1)}_{\mathbf{k}}(PA'') = \sum_{\tilde{k}} \mathbf{T}^{(1)}_{\tilde{\mathbf{k}}}(NO) D^{(J)^*}_{\tilde{k}k}(0, \Theta'', 0) \qquad \ldots(7.34)$$

The spherical components of the two-photon transition operator $\widetilde{\mathbf{T}}^{(1)}_{\mathbf{m}}$ (LAB) defined in a laboratory fixed frame can now be expressed in terms of the corresponding components for the bare NO molecule

$$\widetilde{\mathbf{T}}^{(1)}_{\mathbf{m}}(LAB) = \sum_{k,\tilde{k}} \mathbf{T}^{(1)}_{\tilde{\mathbf{k}}}(NO) D^{(J)^*}_{k\tilde{k}}(0, \Theta'', 0) D^{(J)^*}_{mk}(\omega'') \qquad \ldots(7.35)$$

where ω'' represents the orientation of the principal axis system (PA'') of the ground electronic state of the complex with respect to a laboratory fixed frame. Eqn(7.33) then takes the form

$$\begin{aligned} \widetilde{S}_{if} &= \sum_{jm} \langle f | \widetilde{\mathbf{T}}^{(1)}_{\mathbf{m}}(LAB) P^{(J)}_{m} | i \rangle \qquad \ldots(7.36) \\ &= \sum_{jm} \sum_{k} \langle f | \mathbf{T}^{(1)}_{\tilde{\mathbf{k}}}(NO) D^{(J)^*}_{k\tilde{k}}(0, \Theta'', 0) \times D^{(J)^*}_{mk}(\omega'') P^{(J)}_{m} | i \rangle \end{aligned}$$

In this expression the electronic part of the wave function refers to the NO frame while the NO frame is defined with respect to the PA″ system, where PA″ is the principal axis system of the ground state. The final state wave function must also be specified with respect to this system. The extreme floppiness of van der Waals complexes can result in considerable changes of the vibrationally averaged structure on electronic excitation. To account for this possibility another principal axis system PA′ is introduced, representing the vibrationally averaged structure of the excited state. Since the transition matrix elements are evaluated using the PA″ system, the rotational part of the excited state wave function must be expressed in terms of functions which depend on the orientation of the PA″ system. For a triatomic molecule, the two co-ordinate frames will only differ in the orientation of their z and x axes since the y axis is perpendicular to the molecular plane[20]. The rotational wavefunction for the excited state then becomes

$$\left|J_f M_f P_f\right\rangle = \sqrt{\frac{2J_f+1}{8\pi^2}} \sum_{\tilde{P}} D^{(J_f)^*}_{\tilde{P}P_f}(0,\gamma,0) D^{(J_f)^*}_{M_f\tilde{P}}(\omega'') \qquad \ldots(7.37)$$

where the angle γ specifies the orientation of the z′ axis in the (x″,z″) plane of the PA″ system.

With the aid of the above transformations the two-photon transition matrix elements for the complex may be derived, and the final somewhat complex result can be found in Ref. 19.

7.4 Methods of Analysis

Computer programs used to calculate transition energies and intensities within the model described in this chapter were written in Turbo Pascal by Professor Henning Meyer, University of Georgia. All the spectra observed in this work were assigned to (2+1) REMPI processes. The reasonable assumption was made that if the photon fluence was high enough to bring about the less probable 2-photon step, then this step, rather than the much faster one-photon ionisation step, would determine the intensity of the overall MPI transition. This would have the result that the transition intensities would show no dependance on the ionisation step, and therefore the rotational linestrengths for the 2-photon resonant step should be sufficient to account for the relative intensities of the rotational lines in a vibronic

band. In addition the intensities were multiplied by a factor that represented the Boltzmann rotational population distribution of the initial state at a specified temperature.

The width of experimental rotational lines observed in this work was mainly determined by four factors: lifetime broadening, Doppler broadening, laser linewidth and power broadening. Of these, lifetime broadening is generally the smallest contributor for long-lived states. A state observed by a multiphoton absorption generally lies at the equivalent of vacuum ultra-violet (VUV) wavelengths for a single-photon transition from the ground state, and would be expected to have a radiative lifetime of $\sim 10^{-8}$ s, resulting in a lifetime broadening of ~ 0.0005 cm^{-1}. The laser linewidth was mentioned in Chapter 6 and would be expected to contribute $\sim 0.24 cm^{-1}$ for a two-photon absorption at $70000 cm^{-1}$. The power broadening is essentially a lifetime broadening effect arising from the reduction of the excited state lifetime by the use of intense laser radiation to induce multiphoton transitions. Since most of the processes observed in this work were (2+1) MPI processes, the 2-photon absorption controls the overall intensity. By contrast the final single-photon ionisation step has a high cross-section compared to the multiphoton absorption, and will thus occur very rapidly, causing an effective reduction in the upper state lifetime at high laser powers. This may result in significant lifetime broadening, often observed to be of the order of a few wavenumbers at high laser power. Experimentally this factor was found to be very important, and careful optimization of all experimental conditions to allow the use of minimum power density in the laser focus was critical to obtain well-resolved spectra.

In order to reproduce the observed spectra the structural parameters θ, r_{NO} and $R_{NO\text{-}Rg}$ are required for each electronic state. Additional parameters are the spin-orbit constant, a, and the orbital angular momentum quenching parameter ζ. Using the available constants for the ground electronic state (taken from the microwave work of Mills *et.al*[14]) there are five unknown parameters which remain: θ', $R'_{NO\text{-}Rg}$, r'_{NO}, a', and ζ'. Due to the limited resolution in the experiments, the spectra are not sensitive to the NO-Rg distance $R'_{NO\text{-}Rg}$. For all simulations reported in this work, $R'_{NO\text{-}Rg}$ has been fixed to 3.30 Å. The final simulations were produced by empirically matching vibrational spacings and Franck-Condon factors with the observed spectrum.

7.5 Conclusions

This chapter describes how the rotational structure of two-photon spectra of van der Waals complexes involving an open shell diatomic molecule may be analysed using a rigid rotor Hamiltonian where the relevant components of the two-photon absorption operator of the diatomic are transformed to the principal axis system of the complex. This approach has been used to simulate the $\widetilde{E}^2\Sigma^+ \leftarrow \widetilde{X}^2\Pi$ two-photon spectra of Ar·NO and Kr·NO recorded in this work and comparison of the experimental and simulated spectra is made in Chapter 8.

7.6 Refernces

1. M. H. Alexander, *J.Chem.Phys.* **111**, 7426 (1999).

2. M. H. Alexander, *J.Chem.Phys.* **111**, 7435 (1999).

3. W. M. Fawzy and J. T. Hougen, *J.Mol.Spec.* **137**, 154 (1989).

4. E. Miescher and K. P. Huber, *Int. Rev. Sci, Phys. Chem,* **3**, 37 (1976) Butterworths.

5. P. Bernarth, *Spectra of Atoms and Molecules,*

6. S. A. Boggis, *PhD Thesis,* University of Southampton (1991).

7. J. Baker, *PhD Thesis,* University of Southampton ().

8. P. W. Atkins, *Molecular Quantum Mechanics,* OUP, Oxford (1997).

9. R. N. Dixon, J. M. Bayley and M. N. R. Ashfold, *Chem. Phys.* **84**, 21 (1984).

10. R. N. Zare, *'Angular Momentum'*, Wiley, New York (1986).

11. M. E. Rose, *'Elementary Theory of Angular Momentum'*, Chapman and Hall, London (1957).

12. C. Maïnos, Y. Le Duff and E.Boursey, *Mol.Phys.* **56**, 1165 (1985).

13. M. N. R. Ashfold and J. D. Howe, *Ann. Rev. Phys. Chem.* **45**, 57 (1994).

14. P. D. A. Mills, C. M. Western and B. J. Howard. *J. Phys. Chem.* **90**, 3331 (1986).

15. W. M. Fawzy and J. T. Hougen, *J. Mol. Spec.* **137**, 154 (1989).

16. J. T. Hougen, *J. Chem. Phys.* **37**, 1433 (1962); *J. Chem. Phys.* **39**, 358 (1963).

17. E. P. Wigner, *Group Theory*, Academic Press, New York (1959).

18. H. Meyer, *J. Chem. Phys.* **107**, 7721 (1997).

19. H. Meyer, *J. Chem. Phys.* **107**, 7732 (1997).

20. J. T. Hougen and J. K. Watson, *Can. J. Phys.* **43**, 298 (1965).

Chapter 8: The $\widetilde{E}^2\Sigma^+$ State of Rg·NO Complexes Studied Using REMPI Spectroscopy (Rg=Rare Gas)

8.1 Previous Work

The rare gas-nitric oxide molecules Rg·NO have recently been studied by a variety of techniques and a good understanding of the electronic spectroscopy and photophysics of these species is emerging. The potential curves for various electronic states have been probed directly by techniques such as laser induced fluorescence (LIF) and multiphoton ionization (MPI), as well as indirectly by scattering experiments.

The interest in these species stems from the fact that for the ground state, Rg·NO ($\widetilde{X}^2\Pi$), the rare gas atom lowers the cylindrical symmetry of the NO molecule, breaking the degeneracy of the π orbitals, in which the unpaired electron resides. This has the effect of splitting the orbitals into two components of A′ and A″ symmetry, under C_s symmetry. This may be viewed as a Renner-Teller-type quenching of the orbital angular momentum. Howard and co-workers have studied the effect this has on the rotational spectroscopy of ground state Ar·NO,[1,2] based on a theoretical model developed for that system.[3] That work showed that the $\widetilde{X}^2\Pi$ state of Ar·NO is T-shaped, with the Ar atom slightly off the axis of the T, and slightly closer to the nitrogen atom (the Jacobi bond length and bond angle were 3.71 Å and 85°, respectively). The spectroscopy indicated that the $^2\Pi$ electronic character of the NO moiety was only slightly quenched by the presence of the Ar atom, in a Renner-Teller type interaction. Recent *ab initio* calculations have also indicated that the complex is T-shaped[4], with a small splitting between the A′ and A″ surfaces. In addition, the barrier to linearity was calculated to be ca. 20 cm^{-1}, with vibrational frequencies of 16 cm^{-1} for the intermolecular stretch, and 10 cm^{-1} for the intermolecular bend.[4]

There have been no other spectroscopic studies on the ground state of Rg·NO complexes, but intermolecular potentials were derived for Ar·NO , Kr·NO, and Xe·NO from scattering studies, which led to estimates of the potential well depth[5]. He·NO was studied by *ab initio* molecular orbital studies. Two relatively recent studies yielded very different results: the first study by Zolotoukhina and Kotake[6] concluded that the complex was linear, with a He·ON configuration. In contrast, Yang and Miller[7] concluded that the complex was T-shaped. A recent *ab initio* study[8] concurs with the result of Yang and Miller, but notes that

the surface is extremely flat, and that great care must be taken with respect to the treatment of basis set superposition error (BSSE). This varies with orientation, and can lead to differing conclusions regarding the calculated geometry for different levels of theory and basis set. The dissociation energy of the ground state of Ar·NO has been derived spectroscopically by Tsuji *et al.*[9] as 88 cm^{-1}.

Most of the electronic spectroscopic studies of Rg·NO complexes have been performed using resonance-enhanced multiphoton ionization (REMPI) spectroscopy. For the $\tilde{A}^2\Sigma^+$ state, (1+1) or (1+1′) REMPI studies were made, whereas for the other states (2+1) REMPI schemes were employed.

The first reported bound-bound transitions of Ar·NO were by Miller[10], but the reported spectra were rather poorly resolved. Later McQuaid and coworkers[11] and Tsuji *et.al*[12] both reported well-resolved (1+1) REMPI spectra, but were unable to assign the observed structure. Bush *et.al*[13] were the first to attempt such an assignment, based upon the idea that the long intermolecular bond in a near T-shaped molecule leads to the *a* inertial axis of the molecule being almost coincident with this bond. This means that rotation of the molecule about this bond is more or less equivalent to rotation of the NO molecule about this axis, since the Ar atom will not contribute much to the motion. In the spectrum the region to higher wavenumber of the origin, assigned as excitation of the intermolecular stretch, resembles the $A^2\Sigma^+ \leftarrow X^2\Pi$ transition in NO, as expected for a T-shaped geometry of the complex. The region to lower wavenumber, the origin, is rather simpler in character, and cannot be explained by a T-shaped $\tilde{A}^2\Sigma^+$ state. In fact a near-linear geometry is required to explain the lack of structure. Tsuji *et.al* derived the dissociation energy of the $\tilde{A}^2\Sigma^+$ state as 44cm^{-1} (Ref. 9), which included an analysis of structure above the dissociation limit; from this value they were also able to derive the dissociation energy of the $\tilde{X}^2\Pi$ state as 88cm^{-1}, as noted earlier.

The first observation of the $\tilde{A}^2\Sigma^+ \leftarrow \tilde{X}^2\Pi$ transition for another Rg·NO complex was that for Kr·NO[14], by Bush *et.al*. The spectrum is rather complicated, and it was not possible to assign it in any great detail; however, the dissociation energy of the $\tilde{A}^2\Sigma^+$ state could be estimated from the energy range of observed structure in the spectrum, giving a value of ≈110cm^{-1}. The fact that the origin of this transition was almost coincident with the origin of

the $A^2\Sigma^+ \leftarrow X^2\Pi$ transition in bare NO implied that the dissociation energy of the $\tilde{X}^2\Pi$ state was also $110cm^{-1}$, within experimental error. Similarly, the recently obtained spectrum for the corresponding transition in Xe·NO is also rather complicated[15], and again no assignment was possible. The range of this spectrum allowed the dissociation energy of the $\tilde{A}^2\Sigma^+$ state of Xe·NO to be estimated as $157cm^{-1}$, and this, combined with the red shift of the spectrum from the corresponding NO transition yielded an estimate of the $\tilde{X}^2\Pi$ state dissociation energy as $121cm^{-1}$. As noted in Ref. 15, the $\tilde{A}^2\Sigma^+$ states of He·NO and Ne·NO are likely to be very weakly bound, given the expected trend in bonding for the other Rg·NO complexes. No $\tilde{A}^2\Sigma^+ \leftarrow \tilde{X}^2\Pi$ spectra have been reported for these species.

Other studies have also been reported on the spectroscopy of the $\tilde{A}^2\Sigma^+ \leftarrow \tilde{X}^2\Pi$ transition of Ar·NO . Miller and Cheng[16] reported the (2+2) REMPI spectrum of this transition, which was very broad, and they associated this with dissociative behaiviour in the upper state. Much earlier, Levy and coworkers[17] had reported broad LIF spectra, which they had assigned as being caused by transitions to a dissociative part of the upper potential. Very recently, Gauyacq and coworkers[18] have reported LIF spectra of the $\tilde{A}^2\Sigma^+ \leftarrow \tilde{X}^2\Pi$ transition. The spectra resemble very closely the previously reported REMPI spectra by other workers. There are, however, two features to higher wavenumber in the LIF spectra, which were not seen in the recent studies. The assignment of these features in Ref. 18 was to above-dissociation resonances, and this assignment was supported by *ab initio* claculations.

The $\tilde{C}^2\Pi$ state of Ar·NO was first studied by Sato *et.al*[19] in a (2+1) REMPI experiment. A short series of peaks was observed, which were assigned to excitation of a progression of the intermolecular stretch. Miller and Cheng[20] observed $\tilde{C}^2\Pi \leftarrow \tilde{X}^2\Pi$ REMPI spectra for Ne·NO, Ar·NO and Kr·NO. In this work, although the Ar·NO spectrum was very similar to those reported by Sato, the Ne·NO spectrum only consisted of two features. The Kr·NO spectrum was the most complicated with a strong progression of five features, as well as some additional structure; this structure was better resolved in a later study[21], where two progressions were assigned. The $\tilde{C}^2\Pi \leftarrow \tilde{X}^2\Pi$ REMPI spectrum of Xe·NO was also reported in the latter study although the spectrum was recorded in the Xe^+ mass channel exclusively. The structure observed in the Kr·NO $\tilde{C}^2\Pi \leftarrow \tilde{X}^2\Pi$ spectrum has recently been

reinterpreted[22] in the light of the assigment of similar structure in the corresponding Ar·NO spectrum by Meyer[23]. As noted earlier, for T-shaped weakly-bound complexes, such as the Rg·NO complexes, the *a* inertial axis is almost coincident with the intermolecular bond, and so the Rg atom does not contribute substantially to the moment of inertia about the *a* axis, giving rotational structure very similar to that of uncomplexed NO, as with the $\widetilde{A}^2\Sigma^+ \leftarrow \widetilde{X}^2\Pi$ transition. The model used by Meyer to simulate the (2+1) REMPI spectra of the $\widetilde{C}^2\Pi \leftarrow \widetilde{X}^2\Pi$ transition in Kr·NO is the same as presented in Chapter 7 of this work. The simulations presented in Ref. 23 were consistent with a T-shaped geometry for the $v_{NO}'=2$ vibrational level of the $\widetilde{C}^2\Pi$ state, but it is not inconceivable that there are some small deviations. For the $\widetilde{C}^2\Pi$ ($v_{NO}'=0$) level of Ar·NO and Kr·NO, it was deduced that the geometry is skewed away from T-shaped, giving a geometry similar to that of the cation. The $\widetilde{C}^2\Pi \leftarrow \widetilde{X}^2\Pi$ transition has also been studied very recently by Gauyacq and coworkers[18] but no detailed analysis of the structure was presented. The spectrum of the $\widetilde{C}^2\Pi \leftarrow \widetilde{X}^2\Pi$ transition in Xe·NO also appears to show the same type of structure, but attempts in Southampton to obtain spectra with a better signal-to-noise ratio than that of Miller's spectrum have so far proved unsuccessful.

The $\widetilde{D}^2\Sigma^+$ state has only been observed for Ar·NO by Miller and Cheng[16] using (2+1) REMPI spectroscopy, where a long progression of ≈ 12 features were observed. There is a hint of extra structure within these bands, and it would be of great interest to re-record these spectra with better resolution to see if rotational structure similar to that seen in spectra accessing other electronic states is present.

The *ab initio* study of Ref. 18 led to an attempt at reassigning this structure to a state which consists of highly-mixed $\widetilde{C}^2\Pi/\widetilde{D}^2\Sigma^+$ character (where the A′ component of the $\widetilde{C}^2\Pi$ state interacts with the $\widetilde{D}^2\Sigma^+$ state in C_s symmetry); further, the spectrum is assigned in reference [18] to transitions to a saddle point of the surface. This assignment requires confirmation, owing to the rather approximate *ab initio* treatment employed.

One surprising aspect of the $\widetilde{D}^2\Sigma^+ \leftarrow \widetilde{X}^2\Pi$ spectrum is its great difference from the $\widetilde{C}^2\Pi \leftarrow \widetilde{X}^2\Pi$ spectrum, even though both excited electronic states are derived from the 3p Rydberg orbital of NO. Although the transition energy is similar, the length of the

progression seen is much longer in the case of the $\widetilde{D}^2\Sigma^+ \leftarrow \widetilde{X}^2\Pi$ transition. Indeed, this long progression, and the large dissociation energy that may be calculated from the red shift of the spectrum from the origin of the $D^2\Sigma^+ \leftarrow X^2\Pi$ transition in NO and the known dissociation energy in the ground state of Ar·NO, giving a value of D_0=932cm^{-1}, suggests that there is something peculiar about this state. Certainly, the calculated Rydberg orbital radius, from a simple one electron formula (Eqn. 7.2), is very similar to that for the $\widetilde{C}^2\Pi$ state and so similar non-Rydberg behaviour is expected, yet the $\widetilde{D}^2\Sigma^+$ appears to have a dissociation energy close to that of the cation (≈950cm^{-1}), compared to D_0=422cm^{-1} for the $\widetilde{C}^2\Pi$ state. The high dissociation energy of the $\widetilde{D}^2\Sigma^+$ state is especially surprising, given the lower value for the $\widetilde{E}^2\Sigma^+$ state (see later), which is expected to be more Rydberg like, as the radial extent of the 4s orbital is greater than the 3pσ orbital.

Of the possible valence states, only the $\widetilde{B}^2\Pi$ state of Ar·NO has been studied by Miller and Cheng[16] using (2+1) REMPI spectroscopy. A weak spectrum, consisting of three features was observed: two of these were assigned to excitation of vibrational levels of the $\widetilde{B}\,^2\Pi_{1/2}$ component, with the third being due to excitation to the v_{str}'=1 of the $\widetilde{B}\,^2\Pi_{3/2}$ component. The dissociation energy of the $\widetilde{B}^2\Pi$ state may be calculated as 131 cm^{-1} from the spectral shift of the band origin and the known dissociation energy of the ground state, which is small compared to the $\widetilde{C}^2\Pi$ and $\widetilde{D}^2\Sigma^+$ states. The weaker bond is to be expected, as there is no Rydberg character present for this state, which corresponds to a $\pi^3\pi^{*2}$ valence configuration.

It is clearly of interest, given that the bonding of the lower electronic states of the Rg·NO complexes is far from cationic-like, to investigate the higher electronic states of Rg·NO complexes. The $\widetilde{E}^2\Sigma^+$ state (arising from excitation from the outermost electron in a π* orbital to the 4sσ orbital) of the Ar·NO and Kr·NO is studied and discussed in the next section.

8.2 Results and Discussion

Typical time-of-flight (TOF) spectra showing the presence of NO^+ and Ar·NO^+ ions are shown in Figure 8.1. No indication was found for a correlation of the NO^+ signal with the

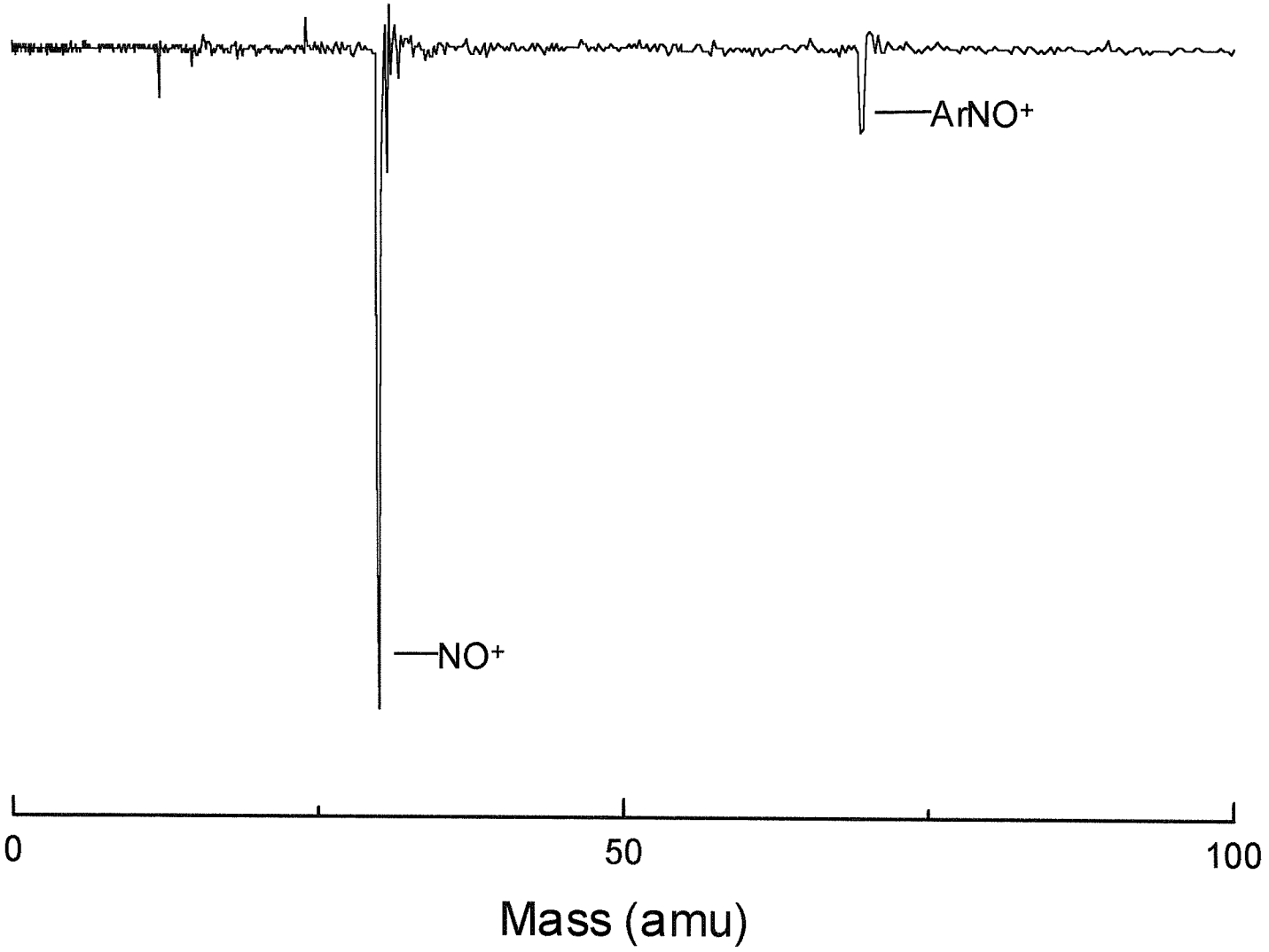

Figure 8.1: Time of Flight Spectrum showing the presence of NO^+ and $Ar{\cdot}NO^+$ ions

signal at mass=70amu (assigned to Ar·NO^+). In combination with the sharpness of this signal and the lack of observation of any higher Ar_x·NO_y signals, this is very strong evidene for its correct assignment as being due to direct absorption and detection of the Ar·NO species, rather than ionization of any higher or mixed clusters.

The spectrum shown in Figure 8.2 was obtained by monitoring the mass signal corresponding to 70amu in the two-photon wavenumber range 60350-60700 cm^{-1}. The possibility of a single-photon transition can be disregarded since there are no bound NO excited states below 44,000 cm^{-1},[25] whilst the lowest excited state of Ar is located at 93,143 cm^{-1} [24]. The only possible electronic states of NO that the transition can be associated with are the $B'^2\Delta$ and the $E^2\Sigma^+$ states (see fig 8.3), accessed via a two-photon transition. The band cannot be associated with the $\widetilde{B}'^2\Delta \leftarrow \widetilde{X}^2\Pi$ Ar·NO transition, since such an assignment would infer an unreasonably low dissociation energy for the Ar·NO excited state. The band is therefore assigned to the (2+1) REMPI spectrum of the $\widetilde{E}^2\Sigma^+ \leftarrow \widetilde{X}^2\Pi$ transition of Ar·NO .

The spectral shift, $\Delta\nu$ of a Rg·NO band origin from that of the origin of the correponding spectrum of NO is given by

$$\Delta\nu = D_0'' - D_0' \qquad \ldots(8.1)$$

where D_0'' and D_0' are the zero-point dissociation energies of the lower and upper states respectively. If the weak feature at 60368cm^{-1} is taken to be the origin of the transition (v_s,v_b=0,0) then the dissociation energy of the $\widetilde{E}^2\Sigma^+$ state may be calculated as 582 cm^{-1} since the dissociation energy of Ar·NO in the $\widetilde{X}^2\Pi$ ground state has already been determined spectroscopically by Tsuji *et.al*[9] (88 cm^{-1}) and the position of the origin of the $E^2\Sigma^+ \leftarrow X^2\Pi$ transition in NO (60863 cm^{-1}) has been previously determined by absorption spectroscopy[25] and was confirmed by measurements in this work (see Figure 8.3).

A close inspection of the spectrum in Figure 8.2 shows that it consists of a repeated pattern of two closely spaced features, with each pair accompanied by a weaker feature a little further to the blue. This profile would appear to be too complicated to be accounted for by

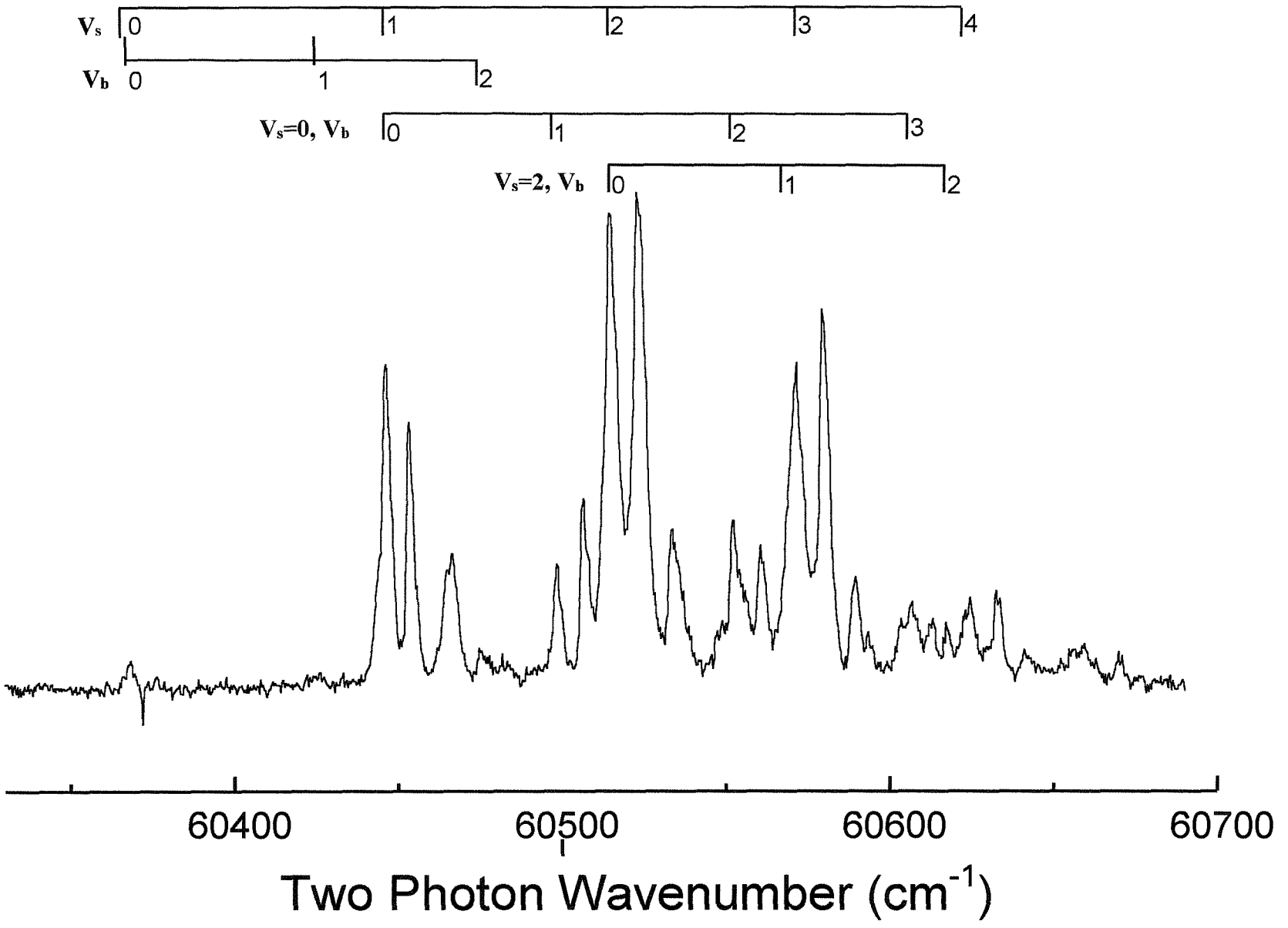

Figure 8.2: The (2+1) REMPI Spectrum of the $\tilde{E}^2\Sigma^+ \leftarrow \tilde{X}^2\Pi$ Transition of Ar·NO

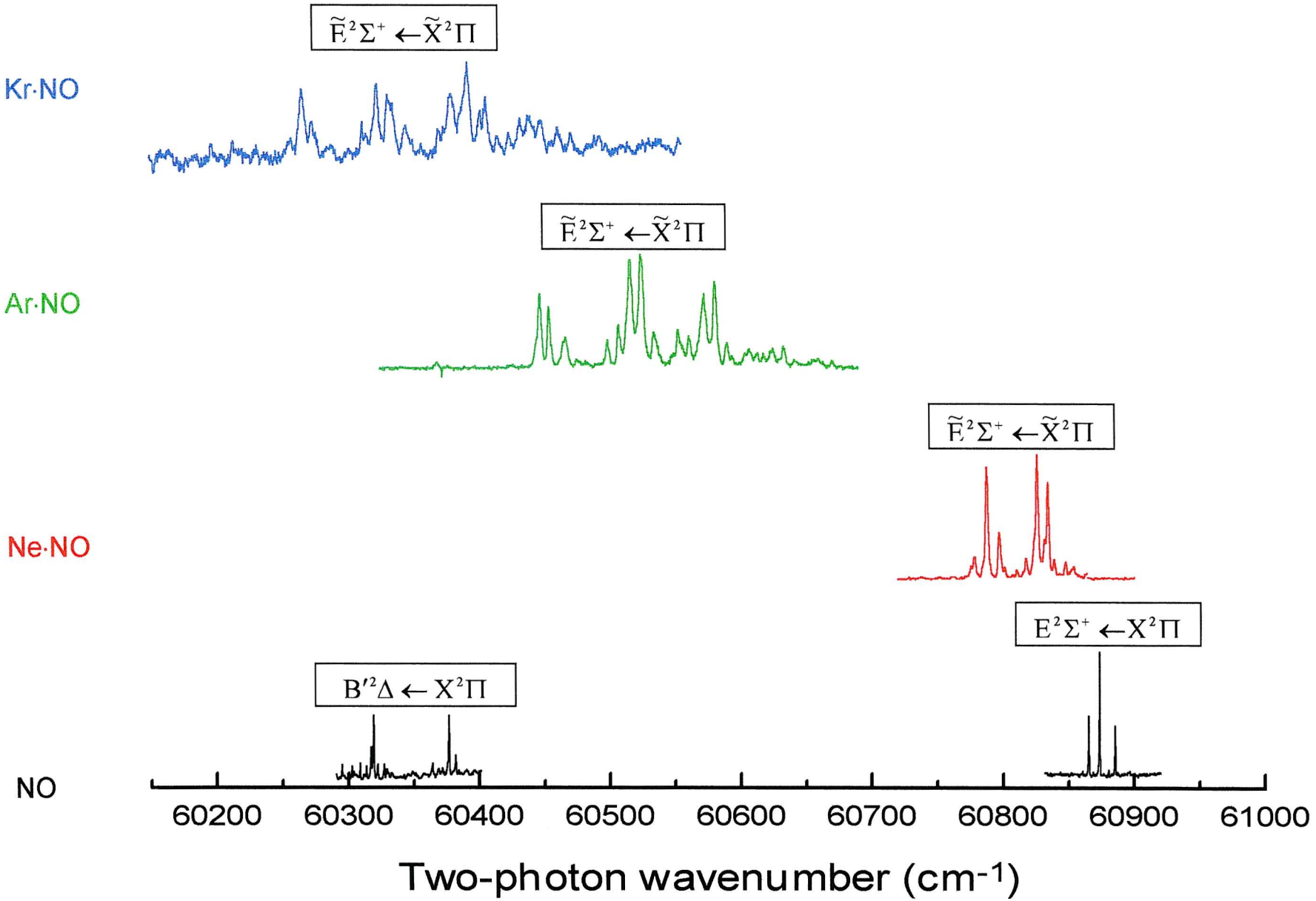

Figure 8.3: Overview of the Rg·NO$^+$ spectra present in the energy range of interest

an electronic transition involving a T-shaped ground state to a linear excited state configuration where a progression of single features containing unresolved structure due to end-over-end rotational transitions would be expected. The repeating structure observed in the spectrum is very similar to that observed in the (2+1) REMPI spectrum of the $E^2\Sigma^+ \leftarrow X^2\Pi$ transition in free NO (Fig 8.3). This would suggest that the Ar·NO complex has a similar T-shaped structure in the $\widetilde{E}^2\Sigma^+$ state to that found in the $\widetilde{A}^2\Sigma^+$ and $\widetilde{C}^2\Pi$ states where the *a* inertial axis is almost coincident with the intermolecular bond, and so the Rg atom does not contribute substantially to the moment of inertia, giving a rotational structure very similar to that of uncomplexed NO. In this case the rotational structure associated with each vibronic component of the transition is characteristic of a mixed *a,c-type* transition in a near prolate symmetric top molecule.

Although it is possible to assign some vibrational structure in the spectrum in Figure (8.2), the overlap of different band systems makes an unambiguous analysis difficult to achieve, without an interpretation of the rotational structure. This is a common feature in the electronic spectroscopy of van der Waals molecules where the rotational energy in a transition can be comparable to the energies of the intermolecular stretching and bending levels. In order to achieve a vibrational analysis the rotational structure within each vibronic component was analysed using the rigid rotor model described in Chapter 7.

In free NO, the rotational structure of the two photon $E^2\Sigma^+ \leftarrow X^2\Pi$ transition is determined by the single tensor component $T_{-1}^{(2)}$.[26] Transforming this component to the complex axis system gives rise to the simulated contours displayed in Figure 8.4 (a). For comparison, part of the experimental spectrum is shown in Figure 8.4(b). For these simulations the NO bond distance was fixed to the value found for the $E^2\Sigma^+$ state of NO (1.1 Å)[25]. As mentioned in Chapter 7, the simulations are not sensitive to the NO-Ar distance $R'_{NO\text{-}Ar}$ whilst the spin orbit coupling parameter a′ and the orbital angular momentum quenching parameter ξ′ do not contribute for a Σ state. This leaves the structural angle θ′ to which the simulations are quite sensitive. As can be seen by comparing with the experiment, the best fit is achieved for a skewed structure which deviates from the T-shape geometry by about 25°. The absolute position of the Ar atom cannot be determined in this work since the simulated contours are very similar for the angles θ′=65° and 115°.

Figure 8.5 compares the experimental spectrum with profiles calculated at 55°, 65°, 75°; as can be seen, the best overall fit if found of the θ=65° geometry.

The entire spectrum may be reproduced by shifting and adding contours which result from the nonvanishing $T_{-1}^{(2)}$ component (Figure 8.6). Three major vibrational progressions can be identified in this way. Perhaps the most obvious is the intense pure stretching progression which is accompanied by structure to the red of each component. Since this accompanying structure to the red of the main rotational contour did not appear in the rotational simulation it is assigned to bands involving the bending vibration. Structure in the bending vibration is expected to be very weak in intensity due to the large change in internuclear distance on excitation from the $\widetilde{X}^2\Pi$ state to the $\widetilde{E}^2\Sigma^+$ state. The resulting poor overlap of vibrational wavefunctions is a consequence of a lesser degree of anisotropy in the $\widetilde{X}^2\Pi$ state, where the intermolecular bending mode can be treated as near-free in-plane rotation of NO around the van der Waals bond, coupled with stronger anisotropy of the intermolecular potential surface in the $\widetilde{E}^2\Sigma^+$ state where the bending mode is restricted to behave more like a conventional bending vibration. By the same reasoning, one might also expect that excitation of the stretching mode should facilitate some oscillator strength towards the bending mode, thus giving rise to progressions involving bend-stretch vibrations. The deviation of the structure from 90° T-shaped in the $\widetilde{E}^2\Sigma^+$ state, as determined from the rotational contour analysis, will enhance the intensity of these transitions even further. Consequently, weak bending features are assigned to excitation of pure bending levels whereas those that are more intense are attributed to excitation of bend-stretch combinations. The simulated contours match the progression members involving one or more quanta of bending vibration for structures which deviate even more from the T-shaped geometry. The opposite trend is found for the members of the pure stretch progression. The band assignments, positions, bond angle and intensity factors used to simulate the spectrum are listed in Table 8.1.

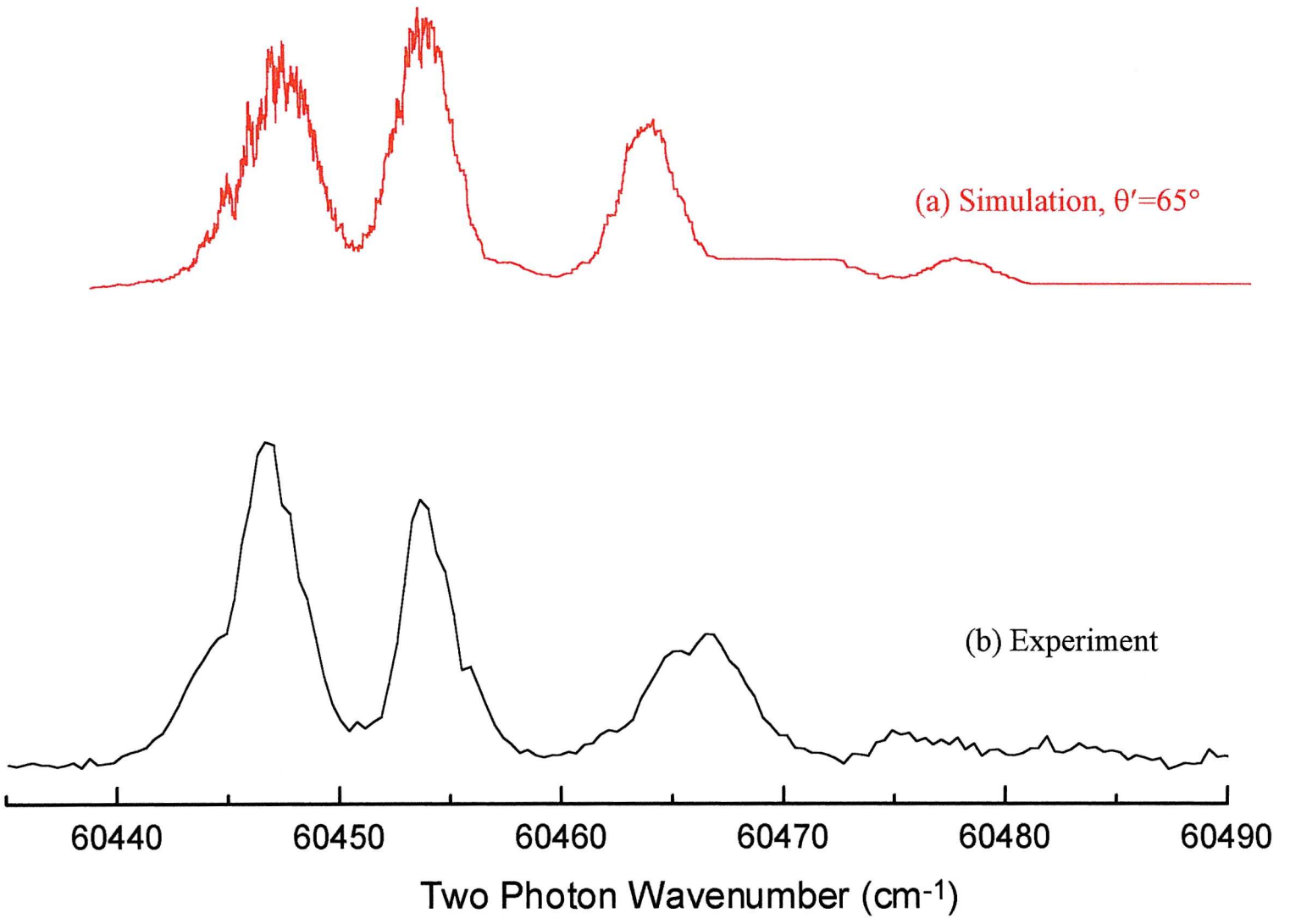

Figure 8.4: Simulated Rotational Contours for the vibrational component (v_s, v_b)=(0,1) of the $\widetilde{E}^2\Sigma^+ \leftarrow \widetilde{X}^2\Pi$ transition of Ar·NO

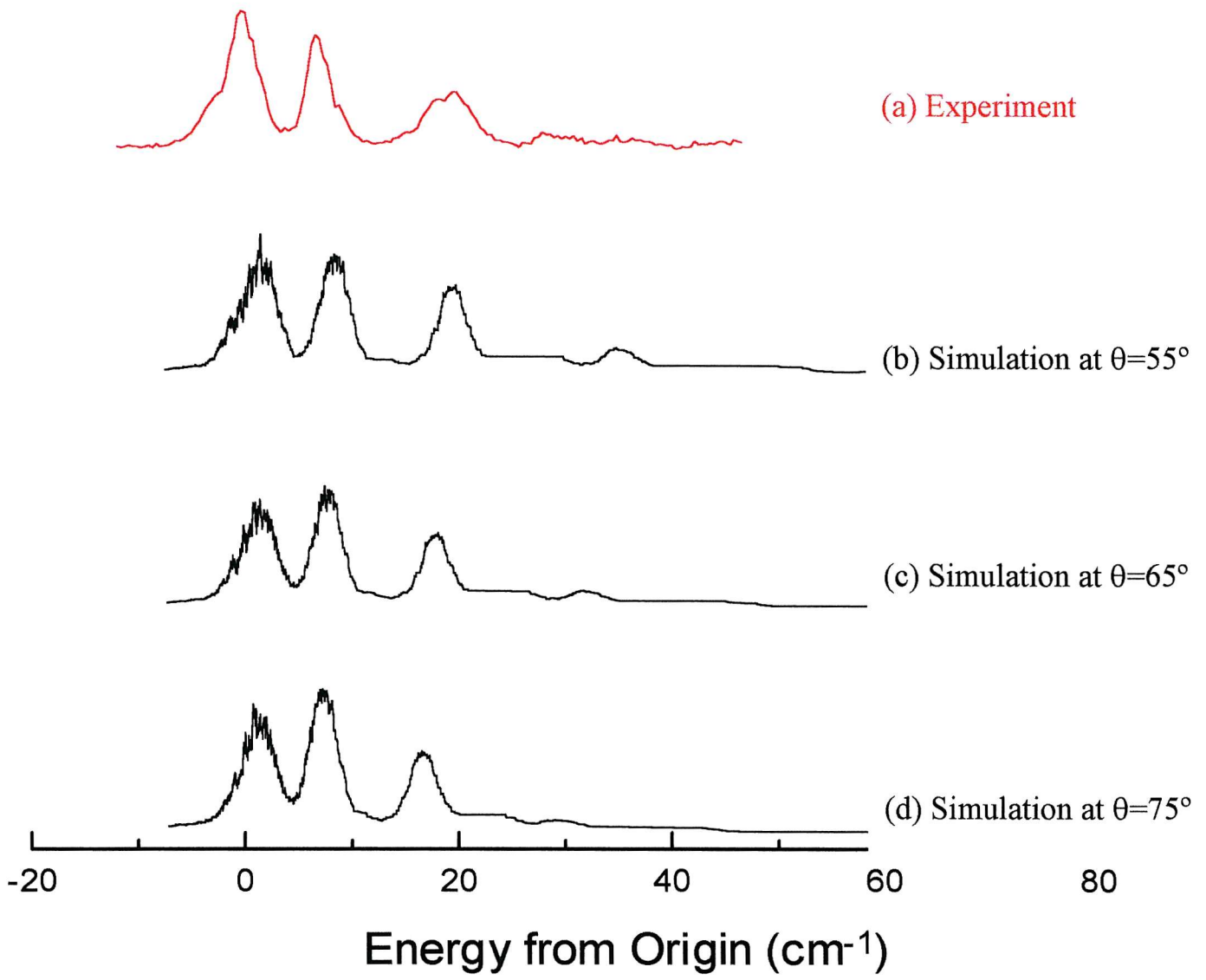

Figure 8.5: Comparison of the experimental $(v_s,v_b)=(1,0)$ vibronic component of the $\tilde{E}^2\Sigma^+ \leftarrow \tilde{X}^2\Pi$ transition of Ar·NO with profiles simulated at different geometries

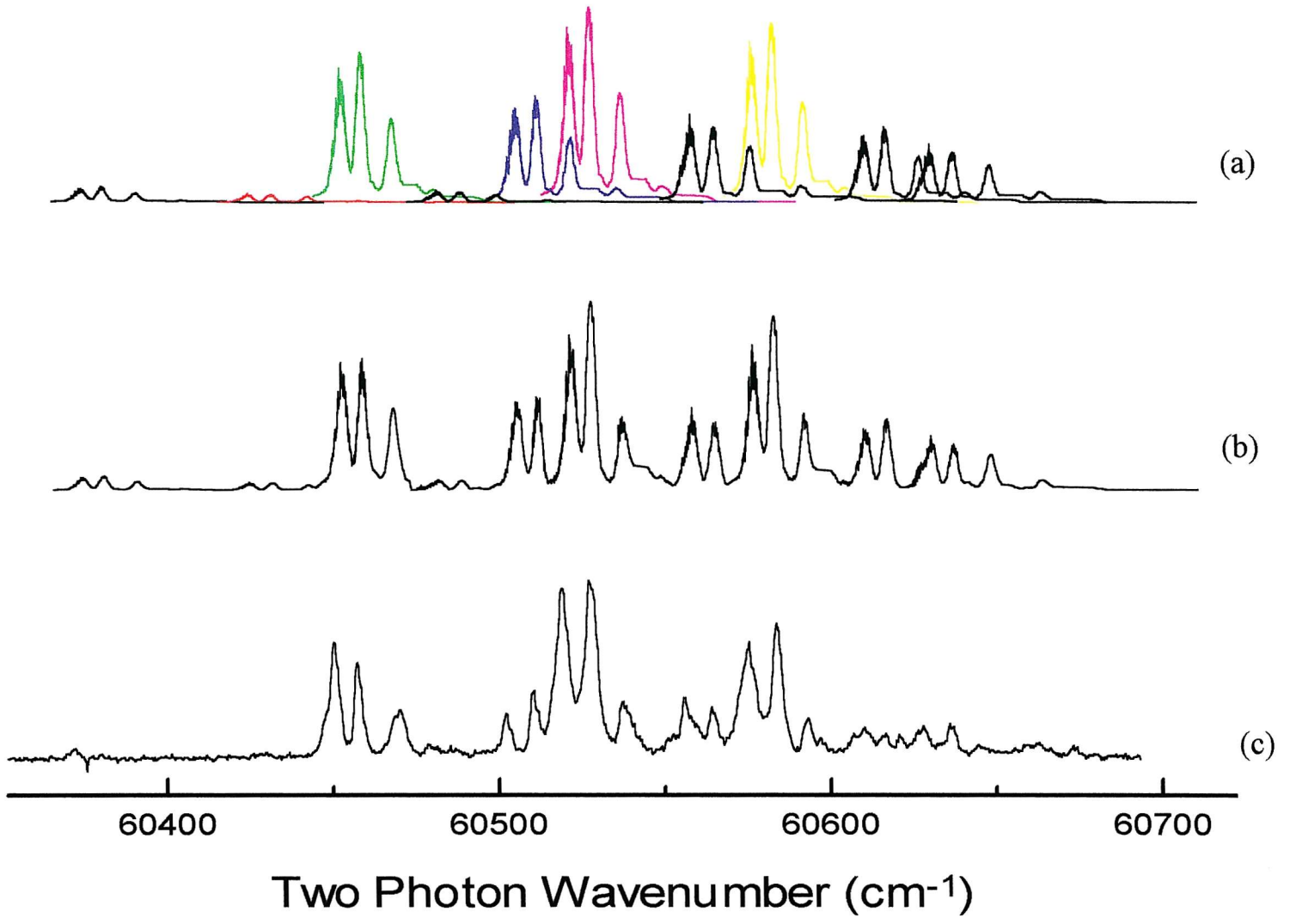

Figure 8.6: Fitting the vibrational structure exhibited by the (2+1) REMPI spectrum of the $\tilde{E}^2\Sigma^+ \leftarrow \tilde{X}^2\Pi$ trasnition of Ar·NO . **(a)** Individual vibrational component indicated by different colours, **(b)** Sum of (a), **(c)** experiment

(v_s', v_b')	**Two-Photon Wavenumber (cm^{-1})**	$\theta'(°)$
(0,0)	60368.6	65
(1,0)	60446.0	70
(2,0)	60515.3	70
(3,0)	60572.3	70
(4,0)	60625.0	70
(0,1)	60425.6	60
(0,2)	60475.5	60
(1,1)	60498.2	65
(1,2)	60553	60
(1,3)	60606.4	65
(2,1)	60568.6	70
(2,2)	60617.9	60

Table 8.1: Band assigments and excited state (θ') bond angles used to simulate the (2+1) REMPI Spectrum of the $\tilde{E}^2\Sigma^+ \leftarrow \tilde{X}^2\Pi$ transition of Ar·NO

Some caution in interpreting these structural parameters is appropriate[27]. The rigid rotor Hamiltonian used in the model described in Chapter 7 is derived from the complete Hamiltonian by taking an approximate average over the vibrational wavefunction of the

complex. Therefore, each term in the rigid rotor Hamiltonian represents a structural average.Inspection of the Hamiltonian matrix elements
(Ref. 28) shows that they have an angular dependence that is always either of the form cos θ, $\cos^2\theta$, or sin θ cos θ. It is the vibrational average of these angle functions that dictates the form of the spectrum. It can be shown that these important quantities may be approximated by the following: $\langle\cos\theta\rangle = \langle 1-(1/2\theta^2)\rangle$, $\langle\cos^2\theta\rangle = \langle 1-\theta^2\rangle$ and $\langle\sin\theta\cos\theta\rangle = \langle\theta-(5/(6\theta^3))\rangle$ for small θ. For a van der Waals molecule exhibiting a wide-amplitude bending vibration, $\langle\theta\rangle \neq \langle\theta^2\rangle^{1/2}$ and so it may be necessary to allow the values for $\langle\cos\theta\rangle$, $\langle\cos^2\theta\rangle$ etc. to differ from the corresponding value calculated using the average bond angle θ. For the $\tilde{E}^2\Sigma^+ \leftarrow \tilde{X}^2\Pi$ transition in Ar·NO, it turns out that it is not necessary to take this vibrational averaging into account and the angular dependant matrix elements of the Hamiltonian were calculated using the average bond angle θ.

The (2+1) REMPI spectrum of the $\tilde{E}^2\Sigma^+ \leftarrow \tilde{X}^2\Pi$ transition in Kr·NO proved much more difficult to obtain than for Ar·NO. As Figure 8.3 shows, the Kr·NO $\tilde{E}^2\Sigma^+ \leftarrow \tilde{X}^2\Pi$ (2+1) REMPI spectrum occurs in the same energy region as the (2+1) REMPI spectrum of the $B'^2\Delta \leftarrow X^2\Pi$ transition in free NO. It was found that saturation of the MCPs occurred when passing through these NO resonances, due to the large number of NO^+ ions formed. This saturation affected the signal output for several microseconds and thus interfered with the Kr·NO^+ signal at longer time-of-flight. Hence many of the recorded (2+1) REMPI spectra of the $\tilde{E}^2\Sigma^+ \leftarrow \tilde{X}^2\Pi$ transition of Kr·NO contained sharp parasitic NO features. Attempts were made to "block" the parasitic NO^+ signal by applying a pulsed voltage to the MCPs, so that they are effectively inactive during the time period when the NO^+ ions arrived. These proved unsuccessful due to "ringing" complications caused by the short duration high voltage that was necessary. The best quality spectra were recorded by subtracting the signal in a time gate very close to the Kr·NO^+ signal (effectively the NO^+ signal) from the Kr·NO^+ signal itself; a technique adopted previously in the study of Ar·NO[29].

The best quality (2+1) REMPI spectrum obtained of the $\tilde{E}^2\Sigma^+ \leftarrow \tilde{X}^2\Pi$ transition of Kr·NO is shown in Figure 8.7. As was the case for Ar·NO it seems that several features arising

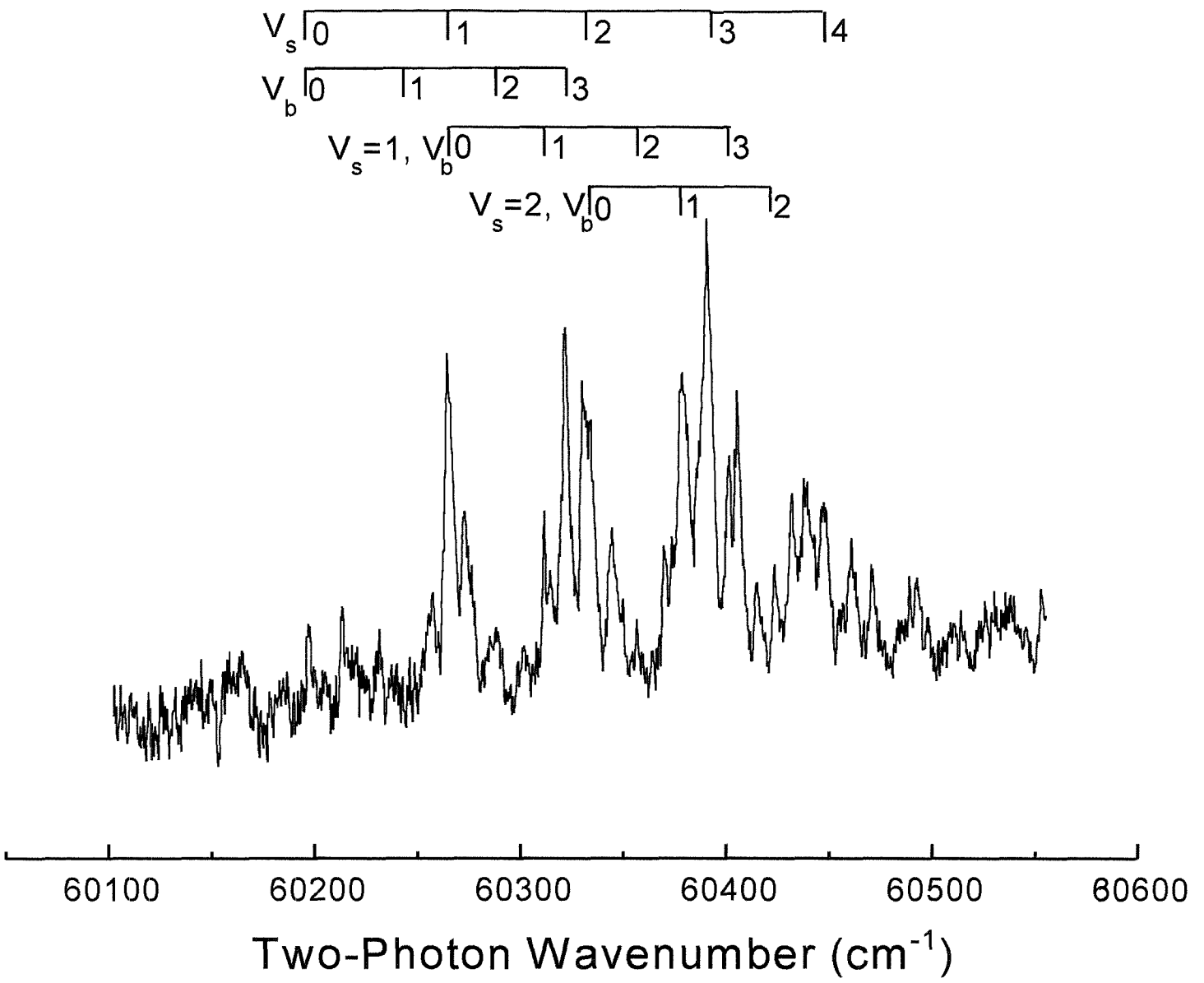

Figure 8.7: (2+1) REMPI Spectrum of the $\widetilde{E}^2\Sigma^+ \leftarrow \widetilde{X}^2\Pi$ Transition in KrNO

from excitation of bending modes are built onto a main stretching progression. The low signal:noise ratio in the spectrum prevents a definitive identification of the origin of the transition. In order to arrive at a consistent assignment with the corresponding Ar·NO spectrum, the first strong band is assigned as the second member of the stretch progression. Consequently the origin would be expected to occur one quantum of stretch vibration to the red of the first strong feature at approximately 60200 cm^{-1}, which does appear to coincide with a weak feature on the spectrum. The red shift of the complex band system from the origin [$Q_{11}(1/2)$] of the corresponding transition in free NO is 664 cm^{-1}. The dissociation energy of the ground, $\widetilde{X}^2\Pi$ state of Kr·NO is known from *ab initio* calculations[30] to be 110cm^{-1}. Hence the dissociation energy of the $\widetilde{E}^2\Sigma^+$ state of Kr·NO can be calculated with the aid of Eqn (8.1) as 774 cm^{-1}.

As was the case for Ar·NO an unambiguous vibrational assignment is not possible without the aid of a similar rotational analysis. Again the rotational structure of the two photon $\widetilde{E}^2\Sigma^+ \leftarrow \widetilde{X}^2\Pi$ transition is determined by the single tensor component $T_{-1}^{(2)}$.[31] A slightly more skewed geometry than Ar·NO was found to best fit the Kr·NO spectrum. The complete spectrum was simulated in the same way as for Ar·NO and is displayed in Figure 8.8 together with a comparison with the experimental spectrum. The band assignments, positions, excited state bond angle and intensity factors used to simulate the spectrum are listed in Table 8.2.

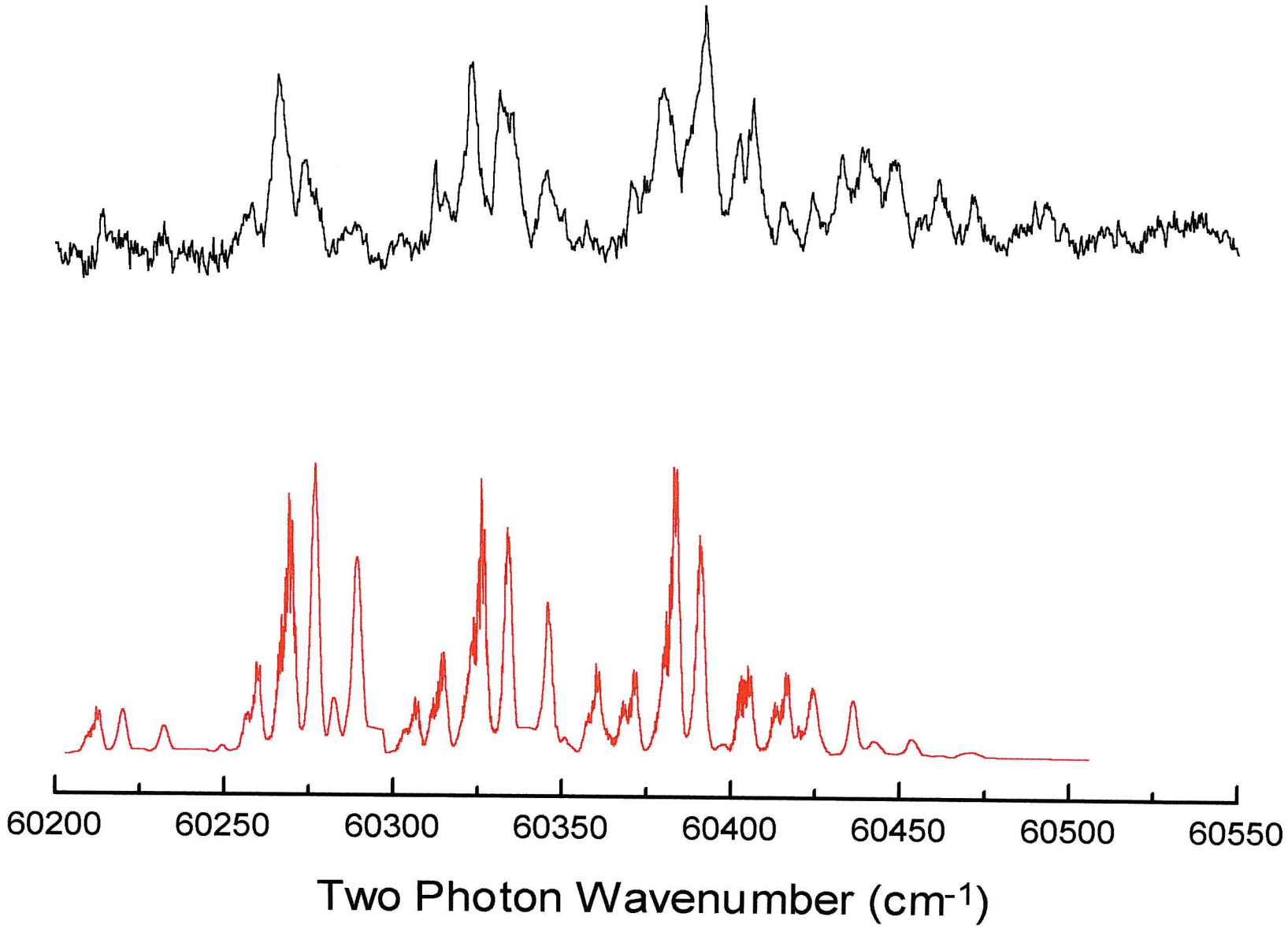

Figure 8.8: Simulation of the (2+1) REMPI Spectrum of the $\widetilde{E}^2\Sigma^+ \leftarrow \widetilde{X}^2\Pi$ Transition in Kr·NO

(V_s, V_b)	Two Photon Wavenumber (cm^{-1})	θ(°)
(0,0)	60197.0	55
(1,0)	60267.2	60
(2,0)	60334.6	60
(3,0)	60395.1	60
(4,0)	60451.3	60
(0,1)	60245.2	55
(0,2)	60290.4	55
(0,3)	60324.7	55
(1,1)	60313.5	60
(1,2)	60358.7	55
(1,3)	60402.9	60
(2,1)	60379.8	60
(2,2)	60422.6	55

Table 8.2: Band assignments and excited state bond angles (θ′) used to simulate the (2+1) REMPI spectrum of the $\widetilde{E}^2\Sigma^+ \leftarrow \widetilde{X}^2\Pi$ transition in Kr·NO

Substantial insight into the type of intermolecular forces which are dominant in the electronic states of these complexes may be gained from the information derived from the spectra. Table 8.3 lists the vibrational frequencies and dissociation energies found for Ar·NO in the various electronic states studied to date.

Electronic State	ω_e(stretch) (cm^{-1})	ω_e(bend) (cm^{-1})	D_0 (cm^{-1})	ref
$\widetilde{X}^2\Pi$	16	11	88	9,4
$\widetilde{A}^2\Sigma^+$	30	-	44	9,35
$\widetilde{C}^2\Pi$	54	39	413	22
$\widetilde{E}^2\Sigma^+$	90	61	582.1	*This work*
Ar·NO $^+$ $\widetilde{X}^1\Sigma^+$	94	79	941	35

Table 8.3: Dissociation energies and intermolecular frequencies determined for Rydberg states of Ar·NO

It would seem from these values that the dissociation energy and intermolecular vibrational frequencies determined for the $\widetilde{E}^2\Sigma^+$ state of Ar·NO indicate a significant step towards ionic character. This observation may be rationalised by considering the different contributions to the intermolecular forces which dominate on changing from one electronic state to another. The expectation value for the radius of a Rydberg orbital, R_{Ryd} may be calculated from the formula:

$$R_{Ryd} = \frac{1}{2Z}\left[3n^{*2} - l(l+1)\right] \qquad \ldots(8.2)$$

where R_{Ryd} is in bohr, l is the azimuthal quantum number and n* is the effective quantum number (n*=n-δ, δ is the quantum defect). Calculated values of R_{Ryd} for the NO electronic

states of interest, using the appropriate T_0 values together with the adiabatic ionization energy of NO (74,721.7cm^{-1})[32] are shown in Table (8.4).

Electronic State	Rydberg Orbital Character	T_0 / cm^{-1}	δ	R_{Ryd} / Å
$\widetilde{A}^2\Sigma^+$	3sσ	44200.2	1.10	2.86
$\widetilde{C}^2\Pi$	3pπ	52371	0.78	3.38
$\widetilde{E}^2\Sigma^+$	4sσ	60863.8	1.19	6.27

Table 8.4: Calculated expectation Rydberg orbital radii

Given that the atomic diameter of Ar is 3.52 Å[33], it can be seen that for the n=3 Rydberg states ($\widetilde{A}^2\Sigma^+$ and $\widetilde{C}^2\Pi$) the Ar atom must lie, on average, outside the mean radius of the Rydberg electron. In this situation the repulsive exchange interaction between the Rydberg electron and the Ar electron cloud is expected to introduce substantial non-Rydberg behaviour. The dependence of this interaction upon the orientation of the van der Waals axis relative to the spatial orientation of the Rydberg orbital is illustrated by the contrasting $\widetilde{A}^2\Sigma^+$ and $\widetilde{C}^2\Pi$ intermolecular potentials since the NO 3sσ Rydberg electron is distributed isotropically whereas the 3pπ(A″) electron is distributed out of the molecular plane. For the n=4 Rydberg state ($\widetilde{E}^2\Sigma^+$) the Ar atom is situated, on average, within the orbit of the Rydberg electron. In this case the charge-charge induced dipole interaction between the ionic core of NO and Ar is expected to be dominant, resulting in a deep well in the potential energy surface, which has a much closer resemblance to the potential of the ionic ground state. Nevertheless, the $\widetilde{E}^2\Sigma^+$ state has the outermost electron in a 4s orbital which has some electron density in the core region. Therefore, it is not too surprising that the dissociation energy as well as the intermolecular vibrational frequencies are close to but still lower than the experimental values determined for the cationic complex[34,35]

The geometries found for the $\widetilde{E}^2\Sigma^+$ states of the Rg·NO complexes all deviate considerably from that known for the electronic ground, $\widetilde{X}^2\Pi$ state (θ=85°)[2]. Recent *ab initio* calculations agree that for the ionic complex NO^+-Ar there is a similar deviation from the T-

shaped geometry, although the absolute structure of the cationic complex is still in doubt. Wright *et al.*[36] computed a Potential energy surface with a minimum at θ=65°, placing the Ar atom on the N side of the complex. In an *ab initio* study by Robbe *et al.*[37], a minimum structure is found with θ=105°, locating the Ar atom on the O side of the complex in the cation. The calculated dissociation energies and NO-Ar stretching frequencies are very similar in both studies, but there is a substantial difference in the computed bending frequencies which differ by nearly a factor of 2. The experimental results of this work (where θ deviates from the T-shaped geometry by 20°-25°) would seem to be in best agreement with the surface of Wright *et.al*, although it must be bourne in mind that the spectroscopically derived excited state angle reflects the vibrationally averaged structure rather than the minimum geometry. In addition, the larger bending frequency found for the $\tilde{E}^2\Sigma^+$ state is in better agreement with the predictions of Wright *et.al.*[36] Again though, some caution should be exercised, since the bending levels calculated for each computed potential energy surface exhibit opposite anharmonic effects. The surface of Robbe *et.al*[37] shows a pure bending progression with increasing intervals while the surface of Wright *et al.* predicts decreasing intervals. In both cases, the most dramatic change occurs for the first level. If the first level is disregarded, then both surfaces yield a spacing between adjacent bending levels of about 60 cm^{-1}. This value lies within 15% of the experimental value found for the $\tilde{E}^2\Sigma^+$ state.

8.3 Conclusions and Suggestions For Further Work

Two-photon REMPI spectra have shown that the intermolecular potential energy surface of electronically excited Rg·NO complexes approach those of the ionic species, $Rg{\cdot}NO^+$, when the radial extent of the NO Rydberg orbital exceeds the intermolecular distance. The rotational structure observed in the spectra has been analysed in terms of the non-vanishing tensor components of the two-photon absorption operator associated with the corresponding transition in the uncomplexed diatomic molecule (NO). The rotational energy levels of the complex have been determined in this analysis using the extended rigid rotor model originally proposed by Mills *et.al.*[2].

The analysis of the rotational structure observed in the (2+1) REMPI spectra of Ar·NO and Kr·NO indicate a significant deviation in the $\tilde{E}^2\Sigma^+$ state from the T-shaped geometry found in the ground state of the complexes. This deviation is found to be more pronounced for

levels involving one or two quanta of the bending vibration. It was found that for both Ar·NO and Kr·NO the spectra could be adequately simulated by calculating Hamiltonian matrix elements using the average bond angle θ. This indicates a small degree of vibrational averaging and hence a fairly rigid complex structure. This is in contrast to studies of lower Rydberg states[22], where it was necessary to allow values for some angular terms in the Hamiltonian matrix to differ from the corresponding value calculated using the average bond angle θ. This finding is consistent with the increased well depth of the $\widetilde{E}^2\Sigma^+$ state potential compared to those of the lower Rydberg states, as shown from the much larger red shift of the spectrum from that of the corresponding transition in free NO.

In comparing Ar·NO to Kr·NO, the spectra indicate both a larger dissociation energy and a greater deviation from T-shaped geometry for the Kr·NO complex. This would be consistent with a stronger charge induced dipole interaction for the complex involving the larger, more polarisable Kr atom. The NO^+ ion has a charge distribution which has more charge on the nitrogen than the oxygen[38]. The greater deviation from T-shaped geometry found for the $\widetilde{E}^2\Sigma^+$ state of Kr·NO is probably a consequence of the more polarizable Kr atom being attracted towards the more positively charged nitrogen atom where the charge/induced dipole interaction will be greatest, and the electron-electron repulsion energy will be smallest. It must be noted that the rotational analysis is only sensitive to a relative change in bond angle and so the absolute geometry of the complex cannot be determined from the experiments in this work. However, the vibrational frequencies and angular deviation from a T-shaped geometry are in good agreement with *ab initio* calculations[36,38] which predict that the Rg atom resides on the nitrogen side of the NO molecule. Further support for this conclusion may be deduced by comparing with the Rg·CO complexes where the lightest rare gas atom is found to prefer the oxygen end of the CO molecule, whereas the heavier atoms tend to have a more T-shaped geometry[39]. The CO molecule is known to be polarized $^{\delta-}C\text{-}O^{\delta+}$, and so it seems that electron-electron repulsion is the dominant effect in determining which linear conformer the complexes prefer.

Although not many van der Waals complexes have been studied by two-photon spectroscopy, this work and previous work of others would seem to provide encouragement by providing an analysis of the spectra using a simple extension of the original rigid rotor model proposed by Mills *et.al*[12] and Fawzy and Hougen[28]. Rotational analysis of the spectra

not only enables the extraction of information concerning the vibrationally averaged structures but it also provides the key to the analysis of the vibrational band structure and the determination of intermolecular frequencies.

Further work on these complexes is warranted. It may be possible to probe more vibrational levels of the $\tilde{E}^2\Sigma^+$ state by first exciting the complexes to the $\tilde{A}^2\Sigma^+$ state in a (1+1′+1′) REMPI scheme, providing more information on Kr·NO by virtue of enhanced Franck Condon factors involved in the $\tilde{E}^2\Sigma^+ \leftarrow \tilde{A}^2\Sigma^+$ transition. Also, it would be clearly of interest to investigate the electronic spectroscopy of even higher (n>4) Rydberg states in order to establish at what point convergence to the respective cations occurs. Such work would provide a stern theoretical challenge since many of the higher Rydberg states will overlap and could be subject to perturbations. Higher resolution spectra, especially those which resolved the end-over-end rotational structure of the complexes, would be invaluable in providing a deeper insight into the structure and dynamics of these species.

It is hoped that the detailed understanding of the Rg·NO complexes that has been built over the last decade will provide a solid foundation, both theoretically and experimentally, for the study of complexes formed between NO and a molecule, such as CH_4 and N_2. Molecular complexes of NO^+ with N_2, CO_2 and H_2O are thought to play important roles in upper atmospheric chemistry (See Chapter 1), as well as in ion mobility spectrometry, and so a detailed understanding of their spectroscopy is of great interest for these reasons, as well as for purely scientific reasons. The (1+1) REMPI spectrum of the $\tilde{A}^2\Sigma^+ \leftarrow \tilde{X}^2\Pi$ transition of N_2·NO, recorded by the Southampton MPI group, has already been published[40]. The analysis of the spectrum is difficult since the geometry of the complex is unknown in either state. Initial *ab initio* calculations on the ground state of N_2·NO have revealed a fairly flat potential energy surface consisting of several minima separated by rather small barriers[41]. It may be necessary to gather more information on the ground state before any other studies on the complex can proceed.

A possible route to this information could be an 'ion dip' or 'hole burning' experiment[42,43,44,45] , a technique which has been used to observe the electronic spectrum of a single isomer which would otherwise be embedded in the spectra of other isomers. The approach exploits the fact that, subsequent to electronic excitation by laser irradiation,

relatively few molecules find their way back to the initial rovibronic levels spanned by the bandwidth of the excitation laser. Photophysical processes such as internal conversion, intersystem crossing, emission to other levels, and ionization by absorption of an additional photon as well as photochemical processes such as predissociation and isomerization can all contribute to the reduction of the repopulation of the initial levels. Therefore, it is possible to significantly reduce the population of a subset of ground-state molecules by simply tuning a laser into resonance with an excited electronic state. For the N_2·NO problem a 'probe' laser would be fixed to a wavelength corresponding to a known[40] $\widetilde{A}^2\Sigma^+ \leftarrow \widetilde{X}^2\Pi$ transition energy. A second 'hole-burning' laser would then be scanned across the $\widetilde{A}^2\Sigma^+ \leftarrow \widetilde{X}^2\Pi$ transition. A delay (typically 100s of ns) would be introduced between the light pulses in order to distinguish between the signals produced by the different lasers. The data would then appear as dips in the probe laser signal as the hole-burning laser is scanned through transitions involving the same initial rovibronic levels of the species being probed. Hopefully this would serve to simplify the present congested spectrum[40] which is hindered by the prescence of several energetically similar ground state isomers.

8.4 References

1. B. J. Howard, C. M. Western, and P. D. Mills, *Discuss. Faraday Soc.* **73**, 129 (1982).

2. P. D. A. Mills, C. M. Western, and B. J. Howard, *J. Phys. Chem.* **90**, 4961 (1986).

3. P. D. A. Mills, C. M. Western, and B. J. Howard, *J. Phys. Chem.* **90**, 3331 (1986).

4. M. H. Alexander, *J. Phys. Chem.*, **99**, 7725 (1993); T. Schmeltz, P. Rosmus and M. H. Alexander, *J. Phys. Chem.*, **98**, 1073 (1994).

5. H. Thuis, S. Stolte and J. Reuss, *Chem. Phys.*, **43**, 351 (1979); H. H. W. Thuis, S. Stolte, J. Reuss, J. J. H. van den Biesen and C. J. N. van Meijdenberg, *Chem. Phys.*, **52**, 211 (1980); P. Casavecchia, A. Laganà and G. G. Volpi, *Chem. Phys. Lett.*, **112**, 445 (1984).

6. T. N. Zolotoukhina and S. Kotake, *J. Chem. Phys.* **99**, 2855 (1993).

7. M. Yang and M. H. Alexander, *J. Chem. Phys.* **103**, 6973 (1995).

8. E. P. F. Lee and T. G. Wright, *J. Chem. Phys.*, **109**, 157 (1998).

9. T. Tsuji, K. Shibuya and K. Obi, *J. Chem. Phys.* **100**, 5441 (1994).

10. J. C. Miller, *J. Chem. Phys.* **90**, 4031 (1989).

11. M. J. McQuaid, G. W. Lemire and R. C. Sausa. *Chem. Phys. Lett.* **227**, 54 (1994).

12. K. Tsuji, K. Shibuya and K. Obi, *Laser Chem.* **15**, 157 (1995).

13. A. M. Bush, J. M. Dyke, P. Mack, D. M. Smith and T. G. Wright, *J. Chem. Phys.* **108**, 406 (1998).

14. A. M. Bush, J. M. Dyke, P. Mack, D. M. Smith and T. G. Wright, *J. Chem. Phys.* **105**, 9804 (1996).

15. P. Mack, J. M. Dyke and T. G. Wright, *J. Chem. Soc. Faraday Trans.* **94**, 629 (1998).

16. J. C. Miller and W. C. Cheng, *J. Chem. Phys.* **89**, 1647 (1985).

17. P. R. R. Langridge-Smith, E. Carrasquillo and D. H. Levy, *J. Chem. Phys,* **74**, 6513 (1981).

18. N. Shafizadeh, P. Bréchignac, M. Dyndgaart, J. H. Fillion, D. Gauyacq, B. Lévy, J. C. Miller, T. Pino and M. Raoult, *J. Chem. Phys.* **108**, 9313 (1998).

19. K. Sato, Y. Achiba and K. Kimura, *J. Chem. Phys.* **81**, 57 (1984).

20. J. C. Miller and W. C. Cheng, *J. Phys. Chem.* **89**, 1647 (1985).

21. J. C. Miller, *J. Chem. Phys.* **86**, 3166 (1987).

22. P. Mack, J. M. Dyke, D. M. Smith, T. G. Wright and H. Meyer, *J. Chem. Phys.* **109**, 4361 (1998).

23. H. Meyer, J. Chem. Phys. **107**, 7732 (1997).

24. C. Moore, *Atomic Energy Levels,* circular 467, Umited States National Bureau of Standards (1949).

25. E. Miescher and K. P. Huber, *Int. Rev. Sci, Phys. Chem,* **3**, 37 (1976) Butterworths.

26. H. Meyer, *J. Chem. Phys.* **102**, 3151 (1995).

27. D. D. Nelson, Jr., G. T. Fraser, K. I. Peterson, K. Zhao, W. Klemperer, F. J. Lovas, and R. D. Suenram, *J. Chem. Phys.* **85**, 5512 (1986); H. B. Quian, D. Seccombe, and B. J. Howard, *ibid.* **107**, 7658 (1997).

28. W. M. Fawzy and J. T. Hougen, *J. Mol. Spec.* **137**, 154 (1989); P. D. A. Mills, C. M. Western and B. J. Howard, *J. Phys. Chem.* **90**, 3331 (1986).

29. A. M. Bush, J. M. Dyke, P. Mack, D. M. Smith and T. G. Wright, *J. Chem. Phys,* **105**(22), 9804 (1996).

30. J. Fleniken, Y. Kim and H. Meyer, *J. Chem. Phys.* **109**, 8940 (1999).

31. H. Meyer, *J. Chem. Phys.* **102**, 3151 (1995).

32. E. Miescher and K. P. Huber, *Int. Rev. Sci, Phys. Chem,* **3**, 37 (1976) Butterworths.

33. Chemistry and Physics data book (1995).

34. M. Takahashi, *J. Chem. Phys.* **96**, 2594 (1992).

35. A. M. Bush, J. M. Dyke, P. Mack, D. M. Smith and T. G. Wright, *J. Chem. Phys.* **108**(2), 406 (1998).

36. T. G. Wright, V. Spirko and P. Hobza, *J. Chem. Phys.* **100**, 5403 (1994); T. G. Wright, *J. Chem. Phys.* **105**, 7579 (1996).

37. J. M. Robbe, M. Bencheikh and J. P. Flament, *Chem. Phys. Lett.* **210**, 170 (1993).

38. T. G. Wright, *J. Chem. Phys.* **105**, 7579 (1996).

39. K. A. Walker, T. Ogata, W. Jäger, M. C. L. Gerry and I. J. Ozier, *J. Chem. Phys.* **106**, 7519 (1997).

40. P. Mack, J. M. Dyke, D. M. Smith and T. G. Wright, *Chem. Phys. Lett.* **284**, 423 (1998).

41. E. P. F. Lee, *Private Communication.*

42. R. J. Lipert and S. D. Colson, *J. Phys. Chem.* **93,** 3894 (1989).

43. M. R. Hockridge, E. G. Robertson and J. P. Simons, *Chem. Phys. Lett.* **302**, 538 (1999).

44. R. J. Graham, R. T. Kroemer, M. Mons, E. G. Robertson, L. C. Snoek and J. P. Simons, *J. Phys. Chem. A.* **103**, 9706 (1999).

45. M. Schmitt, U. Henrichs, H. Müller and K. Kleinermanns, *J. Chem. Phys.* **103**, 9918 (1995).

Chapter 9-REMPI Spectroscopy of the $X^1\Sigma^+ + C^1\Sigma^+ \leftarrow X^1\Sigma^+ + X^1\Sigma^+$ Transition of $(CO)_2$

9.1 Previous Work on the CO Dimer

Carbon monoxide is a fundamental species in molecular spectroscopy, being widely used as a wavelength standard, a probe for surfaces, and a means to trace the distribution of interstellar matter in the universe.[1] However, in spite of the extensive literature on the spectroscopy of weakly bound molecular complexes, only a few observations of the CO dimer have been reported. The first of these was made twenty years ago by Vanden Bout *et.al.*,[2] who measured five microwave lines of $(CO)_2$ by means of molecular beam electric resonance spectroscopy (one at $\approx$ 1.5GHz and a quartet at $\approx$ 16 GHz). These authors were not, however, able to assign these lines. More recently, Havenith *et.al.*[3] studied the infrared spectrum of the CO dimer in the 2146 cm^{-1} region ,the CO stretching vibration region, and assigned a group of 19 lines as P-, Q-, and R-branch transitions of a K=2$\leftarrow$1 sub-band. However, Brookes *et.al.*[4], showed that their analysis was inconsistent with detailed observations of the same spectrum at different temperatures. Subsequently, Roth *et.al.*[4] reported 15 unassigned transitions of the CO dimer in the millimeter wave region (142-172 GHz), confirming their carrier by isotopic substitution. Later, Brookes *et.al.*[5] reported the observation and analysis of the infrared spectrum of the CO dimer in the 2139-2152 cm^{-1} region, the CO stretching region. These measurements were made by direct infrared absorption of a tuneable diode laser beam by a supersonic jet expansion of CO diluted in Ne. By changing the expansion conditions and the regions of the jet probed, spectra were obtained at different effective rotational temperatures in the range of about 1 to 12K. Over 120 observed transitions were assigned in terms of 13 sub-bands involving 24 lower state (ν_{CO}=0) and 36 upper state ($\nu_{CO=1}$) rotational energy levels of the complex with total angular momentum values of J=0 to 9. These levels fall into two groups corresponding to distinct isomers with intermolecular separations of either about 4.0 or 4.4 Å. The 4.4 Å isomer is the ground state of the complex, while the 4.0 Å isomer is a very low-lying (0.88 cm^{-1}) excited state, but this energy ordering is inverted in the ν_{CO}=1 level.

A potential energy surface for $(CO)_2$ has been calculated by Van der Pol *et.al.*[6] using *ab initio* values for the electrostatic and first order exchange interactions and dispersion coefficients. This surface showed considerable nonrigidity, with a number of minima

differing in energy only by small amounts (10-20 cm^{-1}) and separated by small barriers (10-20 cm^{-1}). Later, this surface was used by Bunker *et.al.*[7] to calculate bound energy levels of the dimer. Recently, Meridith and Stone[8] refined the earlier CO dimer potential surface calculation and also determined energy levels and wave functions. This new surface differs in detail from the earlier one,[6] but also shows a number of energy minima with different geometries separated by small barriers. Brookes *et.al.*[5] noted that calculations using MP4, CCSD(T), and SAP methods indicate that the potential surface is especially difficult to calculate precisely because of sensitivity to electron correlation effects. Both published potentials feature a planar global minimum with a short intermolecular separation (≈3.8 Å) and an O-bonded T-shaped configuration. They also show at least one secondary minimum, also planar, with a much larger separation (≈4.4 Å) and a C-bonded T-shaped configuration. It would be tempting to associate these two geometries with the two isomers observed in the work of Brookes *et.al*[5]. However, it must be realized that a range of geometries will contribute to the wave function of each state of the complex, so that the isomers are not really distinct. Clearly the effects of interchange tunneling motions among equivalent geometries are important for the CO dimer, as in the well-studied cases of the HCl and HF dimers[9]. It seems that an understanding of the structure and internal dynamics of the ground state of the CO dimer is far from complete at present, although substantial progress has been made with more advanced calculations and improved spectroscopic measurements.[5]

Spectra of many other complexes containing CO have been studied in both the infrared and microwave regions[10]. Most relevant to this work is CO-N_2, which is isoelectronic with $(CO)_2$. Xu and McKellar[10] observed the spectrum of CO·N_2 in the CO stretching region, and assigned 5 sub-bands involving states with K=0 and 1 for ν_{CO}=0 and K=0,1, and 2 for ν_{CO}=1. One significant difference between $(CO)_2$ and CO·N_2 is that excitation of the CO stretch in the CO dimer involves vibrational degeneracy arising from the two identical monomers. There is no such effect in CO·N_2, since the CO and N_2 vibrations are well separated (2143 cm^{-1} and 2359 cm^{-1}, respectively). Rare gas-CO complexes (Rg-CO) exhibit increasing free rotation of the CO subunit as the polarisability of the rare gas atom decreases (Rg=Kr[11], Ar[12], Ne[13], He[14,15]). CO forms fairly rigid complexes with some molecules
(e.g. CO-CO_2[16], CO-OCS[17], CO-HF[18]), but the effects of large-amplitude internal motion are evident in other systems such as CO-H_2[19]. The N_2 dimer is also isoelectronic with

$(CO)_2$, but the absence of allowed dipole transitions has so far prevented high resolution spectroscopic studies, and only lower resolution data are available.[20] *Ab initio* studies[21] of $(N_2)_2$ indicate a considerable degree of internal rotational freedom.

Of particular relevance to a spectroscopic study of Rydberg states of the CO dimer is the carbon monoxide dimer ion $(CO)_2^+$, of which there has been several investigations. $(CO)_2^+$ was first observed in a high pressure mass spectrometric investigation employing electron impact ionization with variable electron energy.[22] The appearance energy was reported as 12.8±0.3 eV. Combined with the adiabatic ionization energy of the CO molecule (14.014 eV)[23], this would correspond to a binding energy of the $(CO)_2^+$ ion of 1.21±0.3eV.

The first photoionization study of CO cluster beams was conducted by Linn *et.al.*[24] . By measuring photoionization efficiency curves (PIE) they determined the appearance energy of $(CO)_2^+$ as 13.05±0.04 eV. By applying the same technique Ding *et.al.*[25] deduced a value of 13.15eV. In an experiment with energy selected cluster ions the first ionization energy of $(CO)_2$ was later determined to be 12.73±0.05 eV by Norwood *et.al.*[26,27] . However, this was considered to represent an upper limit to the ionization energy since the experiment might have been influenced by dissociative ionization of larger clusters. Again combined with the adiabatic ionization energy of CO (14.014 eV)[23] and the binding energy of neutral $(CO)_2$ of 18 meV[28] this would lead to a binding energy of the carbon monoxide dimer ion of 1.30±0.05 eV. In a Selected Ion Flow Drift Tube (SIFDT) experiment the thermal activation energy for the dissociation of $(CO)_2^+$ ions[29] was determined as 1.1-1.3 eV. While most of the relevant experimental results suggest a binding energy on the order of 1.3 eV, a significantly higher value was reported by Chen and Holmes.[30] In that work the heat of formation of $(CO)_2^+$ was determined by electron impact ionization of several precursors. The binding energy of the $(CO)_2^+$ ion was deduced to be larger than 1.96 eV. This would make it one of the strongest bonds ever observed in an ionized van der Waals dimer.

The first *ab initio* calculation of the $(CO)_2^+$ ion was reported by Beebe and Sabin.[31] Knight *et al.* described *ab initio* CI calculations of the nonlinear *trans* bent ^2B_u ground state (point group C_{2h}) of the $(CO)_2^+$ ion.[32] Stimulated by photodissociation experiments of the $(CO)_2^+$ ion, Blair *et al.*[33] performed extensive *ab initio* calculations of the ground and excited states

of this ion. For the ground state of $(CO)_2^+$ at the UMP2/6-31G* level, the global minimum was again observed as a trans planar geometry (C_{2h} symmetry) with a C-C bond length of 1.505 Å and a CCO bond angle of 144.3°. The binding energy of the $(CO)_2^+$ ion was reported as D_e=2.68 eV. The zero point dissociation energy (D_0) could not be deduced since no vibrational frequencies were calculated. The C_{2h} symmetry was recently confirmed by an infrared study of $(CO)_2^+$ isolated in a solid neon matrix.[34]The most advanced calculations on the $(CO)_2^+$ ion were carried out by Mähnert *et al.*[35] . They also found a global minimum with a trans planar (C_{2h}) geometry, and also reported vibrational frequencies.

There is no report in the literature of any electronic spectroscopy of the CO dimer or any other CO containing van der Waals molecule to date.

9.2 Results and Discussion

A typical time-of-flight (TOF) spectrum showing the presence of CO and $(CO)_2^+$ ions is shown in Figure 9.1. This was recorded at a laser wavelength of 230nm. No indication was found for a correlation of the CO^+ signal with the signal at mass=56amu (assigned to $(CO)_2^+$), as the laser wavelength is scanned. In combination with the sharpness of the $(CO)_2^+$ signal, this is very strong evidence for its correct assignment as being due to multiphoton ionization and detection of the $(CO)_2$ species, rather than ionization and fragmentation of any possible higher or mixed clusters. Due to its relatively large two-photon absorption cross section[36], the CO^+ ion signal is observed at all wavelengths in this region, whereas the $(CO)_2^+$ ion signal is observed only at resonant frequencies.

Figure 9.2 shows the spectrum recorded in the $(CO)_2^+$ mass channel in the two-photon energy range 85680-87560 cm^{-1}. The appearance of the spectrum depended greatly on the delay time between the opening of the nozzle and the firing of the laser. At longer delay times, where more rotational and vibrational levels of the ground state complex are expected to be populated, the spectrum is much more complicated. The possibility of a single-photon transition can be disregarded since there are no bound CO excited states below 55,825 cm^{-1}.[37] The only possible electronic states of CO that the transition can be associated with are the $C^1\Sigma^+$ ($3p\sigma$) and $E^1\Pi$ ($3p\pi$) states which lie at 91916 cm^{-1} and 92903 cm^{-1} above the ground state respectively. Since no evidence could be found for a structured spectrum to the red of the $E^1\Pi \leftarrow X^1\Sigma^+$ transition, the spectrum is assigned to the (2+1) REMPI spectrum of the $X^1\Sigma^+ + C^1\Sigma^+ \leftarrow X^1\Sigma^+ + X^1\Sigma^+$ transition of $(CO)_2$.

If the feature at 86190 cm^{-1} is assumed to be the origin of the $(CO)_2$ transition, then this would represent a red-shift of 6200 cm^{-1} from the $C^1\Sigma^+_{v'=0} \leftarrow X^1\Sigma^+_{v''=0}$ two-photon transition of CO. This red-shift combined with the ground state dissociation energy of $(CO)_2$ known from *ab initio* calculations[38,39,40] (D_0=93 cm^{-1}) allows the dissociation energy of the $X^1\Sigma^+ + C^1\Sigma^+$ state of $(CO)_2$ to be estimated as 6300 cm^{-1}. This value is much lower than that found for the ground state of the ion (D_e=14,520 cm^{-1}) by Mähnert *et.al*[35] from the dissociative ionization of $Ar\cdot(CO)_2$ clusters. However, the estimate in this work is expected to be very much a lower limit since it is likely that for such a large change in geometry, transitions to

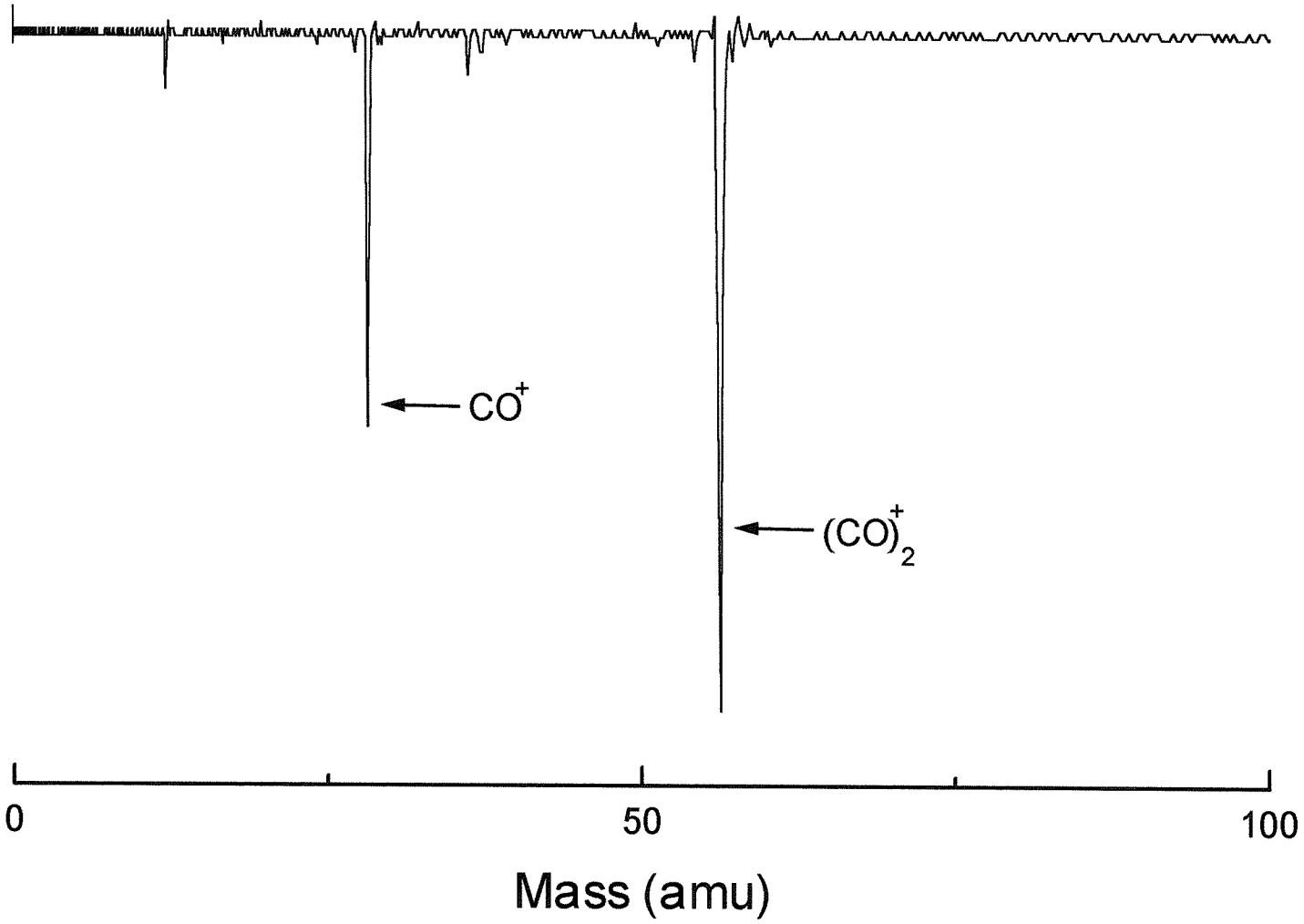

Figure 9.1: Time-of-flight mass spectrum showing the presence of CO and $(CO)_2^+$ ions, recorded at a laser wavelength of 230nm.

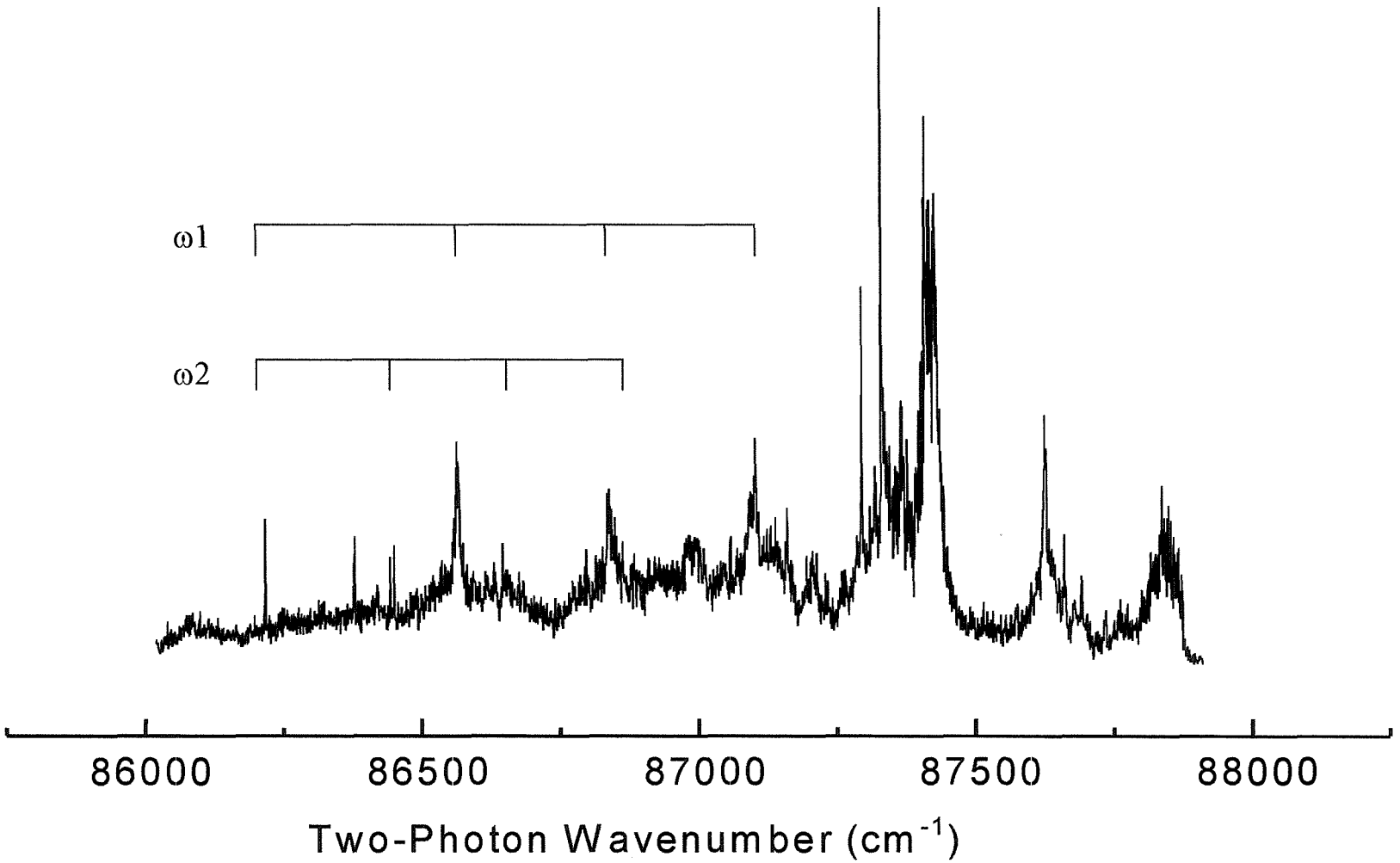

Figure 9.2:
(2+1) REMPI Spectrum of the $X^1\Sigma^+ + C^1\Sigma^+ \leftarrow X^1\Sigma^+ + X^1\Sigma^+$ Transition of $(CO)_2$. Regular separations observed in the spectrum are assigned to progressions in the symmetric stretching (ω1) and symmetric bending (ω2) vibrations.

the first few vibrational levels in the excited state have low intensities and are not observed. Moreover, the excited state is obtained by promoting an electron from the outermost occupied orbital in CO (a σ bonding orbital) to a 3sσ Rydberg orbital. Thus the 3sσ orbital has some electron density in the core region and so the dissociation energy would be expected to fall short of the ionic value.

Evidently there is a significant difference in equilibrium geometry between the neutral van der Waals dimer and the ion. Hence it is unsurprising that long progressions of vibrational structure are observed in the spectrum. It is unlikely that the spectrum will display any resolved rotational structure. End-over-end rotational structure will not be observable at the level of resolution attained (≈0.6 cm^{-1}), whilst the rotation of a single CO subunit is expected to give rise to a single peak for the $C^1\Sigma^+_{v'=0} \leftarrow X^1\Sigma^+_{v''=0}$ transition. The similarity of the rotational constants for the $C^1\Sigma^+_{v'=0}$ state (B_e=1.9533 cm^{-1})[37] and the $X^1\Sigma^+_{v''=0}$ state (1.93 cm^{-1})[37] causes the overlap of transitions from higher rotational levels in the ground state. The O and S branches, which are also expected for a two-photon $\Sigma\leftarrow\Sigma$ transition (the P and R branches are forbidden because of parity selection rules), are 2 to 3 orders of magnitude weaker than the Q branch and are not observed using linearly polarized radiation, as used in this work. Hence even if the complex had a T-shaped excited state geometry then rotation about the *a* inertial axis would only be expected to give rise to a single feature in the spectrum.Therefore only a vibrational analysis is possible with the spectrum in Figure 9.2.

Several regular progressions are observed in the spectrum. Given the large change in intermolecular distance between the ground $(CO)_2$ $X^1\Sigma^+ + X^1\Sigma^+$ (4.0-4.4 Å)[5] and the excited $(CO)_2$ (ground ionic state (~ 1.8 Å)),[35] one would certainly expect strong excitation of the intramolecular symmetric stretching mode. A progression in one or more of the bending modes would also be expected considering the predicted change in geometry from roughly T-shaped in the ground state to the *trans* (C_{2h}) structure in the excited state. By comparison with the vibrational frequencies calculated for the ground state of the ion in Ref. 35, whilst bearing in mind that the corresponding intramolecular frequencies in the Rydberg state will be slightly lower in energy (since the Rydberg electron will penetrate the ionic core and perturb the intermolecular interaction between the two CO molecules) it is possible to

tentatively assign two progressions of ~ 300 cm^{-1} and ~ 180 cm^{-1} to the symmetric stretching (ω_1) and symmetric bending (ω_2) intermolecular vibrations respectively.

9.3 Conclusions and Suggestions for Further Work

Preliminary results have been presented for the (2+1) REMPI spectrum of the $X^1\Sigma^+ + C^1\Sigma^+ \leftarrow X^1\Sigma^+ + X^1\Sigma^+$ transition of the CO dimer. The observed band origin allows the dissociation energy in the upper state to be estimated as 6300 cm^{-1}. Although this value is still large for an ionized van der Waals molecule, it is less than the predicted dissociation energy of the ground state of the ion. Two progressions in the spectrum are assigned as being due to the symmetric stretching and symmetric bending vibrations.

In order to improve the analysis of the spectrum, it will be necessary to establish a better understanding of the structure and dynamics of the species in its ground state. The extreme fluxional behaviour indicated by the calculations and experiments to date would appear to suggest that this would be a rather formidable theoretical challenge. A full analysis of the MPI spectrum could facilitate a study of $(CO)_2^+$ by ZEKE spectroscopy, since it would then be possible to selectively probe different parts of the ionic potential surface by exciting different vibrational levels of the intermediate state. Such a study would provide an interesting contrast with similar work on the NO dimer[41]. In the case of the CO dimer the dipole moments of the CO monomers would point in opposite directions in the ionic state, since it is known that neutral CO has its dipole moment aligned $^{\delta-}C\text{-}O^{\delta+}$, whereas CO^+ is aligned $^{\delta+}C\text{-}O^{\delta-}$.[42] This would certainly explain the contrasting geometries implied in this and previous work for the ground (T-shape) and excited (*trans* C_{2h}) states. It may be worthwhile recording the REMPI spectrum with circularly polarised light since under these circumstances the O and S branches of the monomer transition are relatively stronger and may aid a rotational analysis of the complex spectrum from which structural parameters could be derived.

9.4 References

1. W. Klemperer. *Nature,* **227**, 1230 (1970).

2. P. A. Vanden Bout, J. M. Steed, L. S. Bernstein and W. Klemperer, *Astrophys. J.* **234**, 503 (1979).

3. M. Havenith, M. Petri, C. Lubina, G. Hilpert and W. Urban, *J. Mol. Spectrosc.* **167**, 248 (1994).

4. M. D. Brookes and A. R. W. McKellar, *Chem. Phys. Lett.* **287**, 365 (1998).

5. M. D. Brookes and A. R. W. McKellar, *J. Chem. Phys.* **111**, 7321 (1999).

6. A. van der Pol, A. van der Avoird and P. E. S. Wormer, *J. Chem. Phys.* **92**, 7498 (1990).

7. P. R. Bunker, P. Jensen, S. C. Althorpe and D. C. Clary, *J. Mol. Spectrosc.* **157**, 208 (1993).

8. A. W. Meredith and A. J. Stone, *J. Phys. Chem.* **102**, 434 (1998).

9. M. D. Schuder, C. M. Lovejoy, R. Lascola, and D. J. Nesbitt, *J. Chem. Phys.* **99**, 4346 (1993).

10. Y. Xu and A. R. McKellar, *J. Chem. Phys.* **104**, 2488 (1996).

11. A. R. W. McKellar, *J. Mol. Spectrosc.* **158,** 100 (1993).

12. Y. Xu and A. R. W. McKellar, *Mol. Phys.* **88**, 859 (1996).

13. R. W. Randall, A. J. Cliffe, B. J. Howard and A. R. W. McKellar, *Mol. Phys.* **79**, 1113 (1993).

14. C. E. Chuaqui, R. J. Le Roy and A. R. W. McKellar, *J. Chem. Phys.* **101**, 39 (1994).

15. M. C. Chan and A. R. W. McKellar, *J. Chem. Phys.* **105**, 7910 (1996).

16. R. W. Randall, J. P. L. Summersgill and B. J. Howard, *J. Chem. Soc. Faraday Trans.* **86**, 1943 (1990).

17. M. D. Brookes, D. J. M. Clift, R. J. Low, J. M. Brown and B. J. Howard, *Mol. Phys.* **88**, 899 (1996).

18. Z. Wang, J. W. Bevan, *J. Chem. Phys.* **91**, 3335 (1989).

19. A. R. W. McKellar, *Chem. Phys. Lett.* **186**, 58 (1991).

20. A. R. W. McKellar, *J. Chem. Phys.* **88**, 4190 (1988).

21. J. R. Stallcop and H. Partridge, *Chem. Phys. Lett.* **281**, 212 (1997); A. Wada, H. Kanamori, and S. Iwata, *J. Chem. Phys.* **109**, 9434 (1998).

22. M. S. B. Munson, F. H. Field, and J. L. Franklin, *J. Chem. Phys.* **37**, 1790 (1962).

23. S. G. Lias, J. E. Bartmess, J. F. Liebman, J. L. Holmes, R. D. Levin and W. G. Mallard, "Gas phase ion and neutral thermochemistry", *J. Phys. Chem. Ref. Data.* **17** (1988).

24. S. H. Linn, Y. Ono, and C. Y. Ng, *J. Chem. Phys.* **74**, 3342 (1981).

25. A. Ding, J. H. Futrell, R. A. Cassidy, L. Cordis, and J. Hesslich, *Surf.Sci.* **156**, 282 (1984).

26. K. Norwood, J. H. Guo, G. Luo, and C. Y. Ng, *J. Chem. Phys.* **88**, 4098 (1988).

27. K. Norwood, J. H. Guo, G. Luo, and C. Y. Ng, *J. Chem. Phys.* **90**, 6026 (1989).

28. A. van der Pol, A. van der Avoird, and P. E. S. Wormer, *J. Chem. Phys.* **92**. 7498 (1990).

29. J. Golsik, V. Skalsky, C. Praxmarer, D. Smith, W. Freysinger and W. Lindinger, *J. Chem. Phys.* **101**, 3792 (1994).

30. H. Chen and J. L. Holmes, *Int. J. Mass. Spectrom. Ion Proc.* **133**, 111 (1994).

31. N. G. F. Beebe and J. R. Sabin, *Chem. Phys. Lett.* **24**, 389 (1974).

32. L. B. Knight, Jr., J. Steadman, P. K. Miller, D. E. Bowman, E. R. Davidson and D. Feller, *J. Chem. Phys.* **80,** 4593 (1984).

33. J. T. Blair, J. C. Weisshaar, J. E. Carpenter and F. Weinhold, *J. Chem. Phys.* **87**, 392 (1987).

34 .W. E. Thompson and M. E. Jacox, *J. Chem. Phys.* **95**, 735 (1991).

35. J. Mähnert, H. Baumgärtel and K. Weitzel, *J. Chem. Phys.* **103**, 7016 (1995).

36. M. P. McCann, C. H. Chen, I. Datskou and S. Evans, *Chem. Phys.* **174**, 417 (1993).

37. K. P. Huber and G. Herzberg, *Molecular Spectra and Molecular Structure IV: Constants of Diatomic Molecules* (van Nostrand Reinhold Co., New York, 1979).

38. A. Van der Pol, A. van der Avoird and P. E. S. Wormer, *J. Chem. Phys.* **92**, 7498 (1990).

39. A. W. Meredith and A. J. Stone, *J. Phys. Chem.* **102**, 434 (1998).

40. P. R. Bunker, P. Jensen, S. C. Althorpe and D. C. Clary, *J. Mol. Spectrosc.* **157**, 208 (1993).

41. B. Urban, A. Strobel and V. E. Bondybey, *J. Chem. Phys.* **111**, 8939 (1999).

42. K. A. Walker, T. Ogata, W. Jäger, M. C. L. Gerry, I. Ozier, *J. Chem. Phys.* **106**, 7519 (1997).

Chapter 10: Estimation of the Number of Ions in a Quadrupole Ion Trap Mass Spectrometer

10.1 Introduction

The advent of soft ionizing techniques such as electrospray ionization (ESI)[1,2]and matrix assisted laser desorption-ionization (MALDI) have allowed the analysis of large biological molecules using mass spectral techniques. The compact quadrupole ion trap (QIT)[3,4] is particularly suited to such a task with adequate mass range and resolution, together with the structural information which MS^n scan modes can provide. The interfacing of an electrospray ion source to a quadrupole ion trap (ES-QIT)[5] is thus a powerful analytical tool that may be applied to a wide range of species including drugs, DNA, RNA, sugars, peptides, and proteins.

Detection limits of analytes measured in ES-QIT mass spectrometers are generally on the order of fmols, with the lowest limits being recorded when an isolation step is used to accumulate and/or isolate only the ion(s) of interest[6]. These detection limits are usually defined empirically as the minimum amount of sample which produces a specified mass spectral signal-to-noise ratio under a set of standard conditions[7]. A detection limit defined in this way includes a composite measure of factors such as sample volatility, ionization efficiency, ion trapping efficiency, ion stability towards collisions or reactions, trap size and shape, detection circuit.

In a particular experiment it may be of interest to know the absolute number of trapped ions that contribute to a detected signal since this knowledge could provide a direct measure of, for example, ionization efficiency or ion trapping efficiency. Ideally one would like to be able to determine accurately the minimum and the maximum number of detectable trapped ions. It might be expected that this information could be obtained directly from the detection limits described above by estimating the various loss mechanisms that occur between sampling and detection. However, the various factors on which the detection limit depend are not easy to separate and may also be variable in different environments.

Several novel approaches to this problem have been described previously, all using ion cyclotron resonance mass spectrometry (FT/ICR/MS). In a study by Hunter *et.al*[8], a dc voltage was applied to one of the trapping plates in order to attract positive ions which were then counted using an electrometer. An alternative method developed by McIver *et.al*[9] used

known electron ionization cross sections to calculate the number of ions present by measuring the electron beam duration, emission current and ionisation volume. Both of these methods give no direct indication of the extent of ion loss during and after the excitation process and would not be appropriate for an ion injection technique such as ES-QITMS where trapping efficiencies are typically fairly low. Addressing this problem, Limbach *et.al*[10] determined the absolute number of trapped ions by comparing the experimentally observed signal voltage to that calculated for a single ion orbiting at the (measured) ICR orbital radius of the ion packet. Although this method provides a good lower bound of the absolute number of ions present, it is based upon the assumption that all ions orbit in a tight coherent packet in the trap mid-plane.

Recently, Senko *et.al*[11] statistically compared high resolution FTMS spectra of horse Myglobin with model isotopic distributions in order to assign accurately the monoisotopic mass. Since the level of error between the calculated and experimental distributions correlates with the number of ions that contribute to the isotopic distribution, the authors were also able to obtain an estimate of the number of ions trapped in the FTMS cell. This method would be inappropriate in the case of the much smaller molecules for which QIT-MS is able to resolve C^{13}/C^{12} isotopic distributions.

In this work we also use naturally occurring isotope ratios to estimate the number of ions present in the trap. The experiment involves repeatedly scanning the isotopic profile of a particular ion, to obtain the mean proportion $\overline{p}$ and associated standard deviation σ of each component. Since the naturally occurring isotope proportion p is known, an estimate for the number of ions n can be obtained from the resulting probability distribution using the following equation, which is the normal approximation to the binomial distribution.

$$n \approx p(1-p)/\sigma^2 \qquad \ldots(10.1)$$

10.2 Experiment

Experiments were performed on a Finnigan MAT LCQ LC/MS^n quadrupole ion trap mass spectrometer and, for comparison, a Bruker ESQUIRE quadrupole ion trap mass spectrometer. Both instruments were equipped with an electrospray ionization (ESI) source. A diagram of the ESQUIRE system is shown in Figure 10.1. The major components of this instrument are (i) the spray chamber where ions are transferred from the sample solution, (ii)the ion transport and focussing region which conveys the ions into the ion trap, (iii) the ion trap analyser where ions are separated according to their mass-to-charge ratio (*m/z*) and (iv) the detection system where the ion signal is measured. In both the LCQ and ESQUIRE spectrometers the pressure drops from atmospheric pressure (1013 mbar = 760 Torr) in the spray chamber through about 0.1 mbar in the focussing region to approximately 5×10^{-6} mbar in the chamber surrounding the ion trap and detector. These different pressure regions are achieved using turbomolecular and rotary pumps.

10.2.1 The Electrospray Ion Source

Electrospray ionization (ESI) is a technique which allows the transfer of ions from solution to the gas phase. This method has several advantages over other mass-spectrometric ionization techniques. The unique ability to produce intact multiply charged ions allows the creation of highly charged forms of very large molecular weight compounds which may be analysed on virtually all mass spectrometers. The fact that samples under analysis must be introduced in solution results in a natural compatibility of the technique with many types of separation techniques most suitable for many chemical and biological species. Further, the extreme "softness" of the process (ESI) permits the preservation in the gas phase of noncovalent interactions between molecules which existed in solution, as well as the study of three-dimensional molecular conformations.

The ESQUIRE spray chamber, housing the electrospray source and sampling capillary, is shown in Figure 10.2. The sample is introduced into the spray chamber through a nebulizer which is at right angles to the sampling capillary. The nebulizer consists of a very fine needle which resides inside a tube that adds nebulizing gas (nitrogen) to the sample stream.

Figure 10.1: Overview of the ESQUIRE Ion Trap Mass Spectrometer

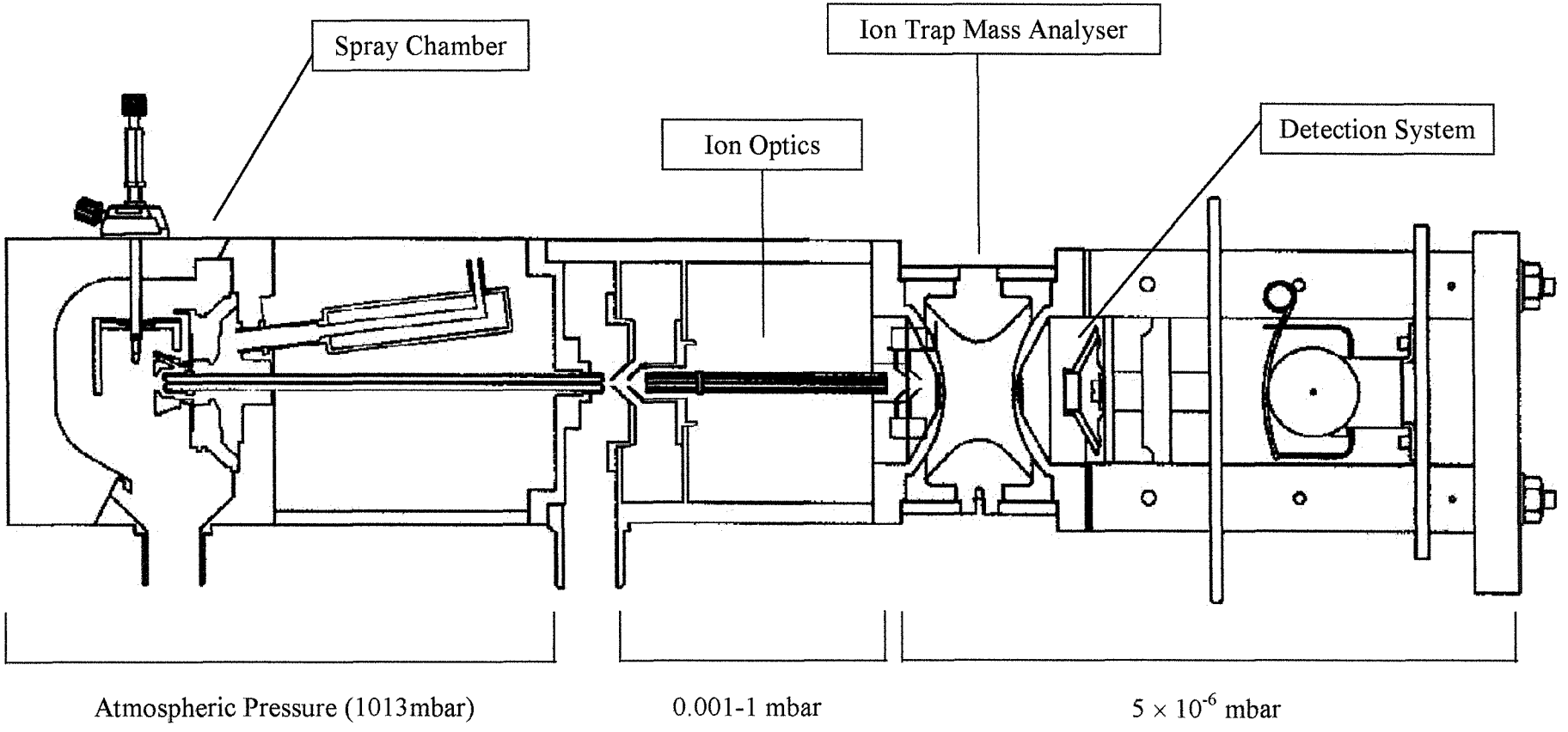

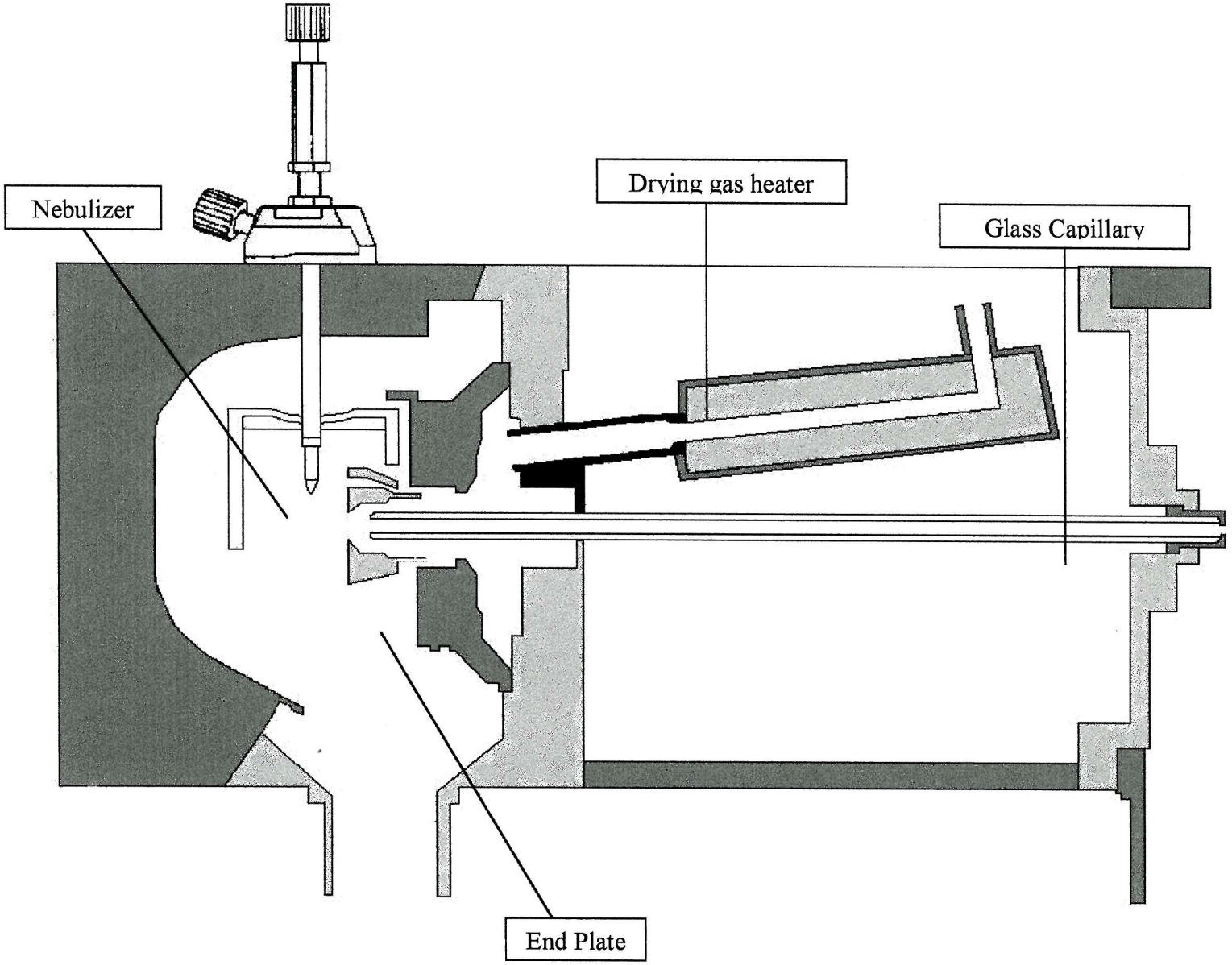

Figure 10.2: The spray chamber on the ESQUIRE ion trap mass spectrometer

On passing through the nebulizer the sample solution is broken into droplets both by the strong shear forces generated by the nebulizing gas and the strong electrostatic field generated between the nebulizer needle tip (at ground potential) and the end plate (a polished metal disk centred around the entrance of the glass capillary) at 2-6kV. As the droplets disperse (Figure 10.3), ions of one polarity are preferentially attracted to the droplet surface by the electrostatic field. The type of ions formed depends on the composition of the liquid sprayed, and ions may be produced via mechanisms such as proton transfer, hydride abstraction, charge exchange, association or electron capture.

Before analysis, the sample must be desolved to yield a bare $[M+H_n]^{n+}$ ion. This is achieved using a counter flow of heated nitrogen which evaporates the solvent, decreasing the droplet diameter and forcing the predominantly like-surface charges closer together. When the force of the resulting coulomb repulsion equals that of the surface tension of the droplet (the Rayleigh limit), the droplet explodes, producing charged daughter droplets that are subject to further evaporation. This process repeats itself, and droplets with a high surface-charge density are formed. When the potential per unit area reaches approximately 10^8 V/cm^2, ion evaporation occurs. Ions are then pushed through the capillary entrance by the pressure gradient between the spray chamber and the low pressure ion focussing reigion. After traversing the glass capillary, the ions are directed through a pair of skimmers which remove the bulk of the drying gas. Finally the ions are transported to the ion trap via a series of electrostatic lenses which must be optimized for the *m/z* range of interest.

For each of the species used in this study the electrospray conditions and ion lens voltages were optimized for maximum signal:noise before each set of experiments.

10.2.2 The Quadrupole Ion Trap Mass Analyser

The theory of the quadrupole ion trap has been reviewed extensively[12,13]. The instrument operates on the basis of first storing ions and then facilitating their detection according to their mass/charge (*m/z*) ratio. As shown in Figure 10.4, it consists of an arrangement of three electrodes wherein gaseous ions may be held by application of electric fields. A central electrode (known as the ring electrode) having the form of a hyperboloid of two sheets is located between two hyperboloids of one sheet (known as the end-cap electrodes).

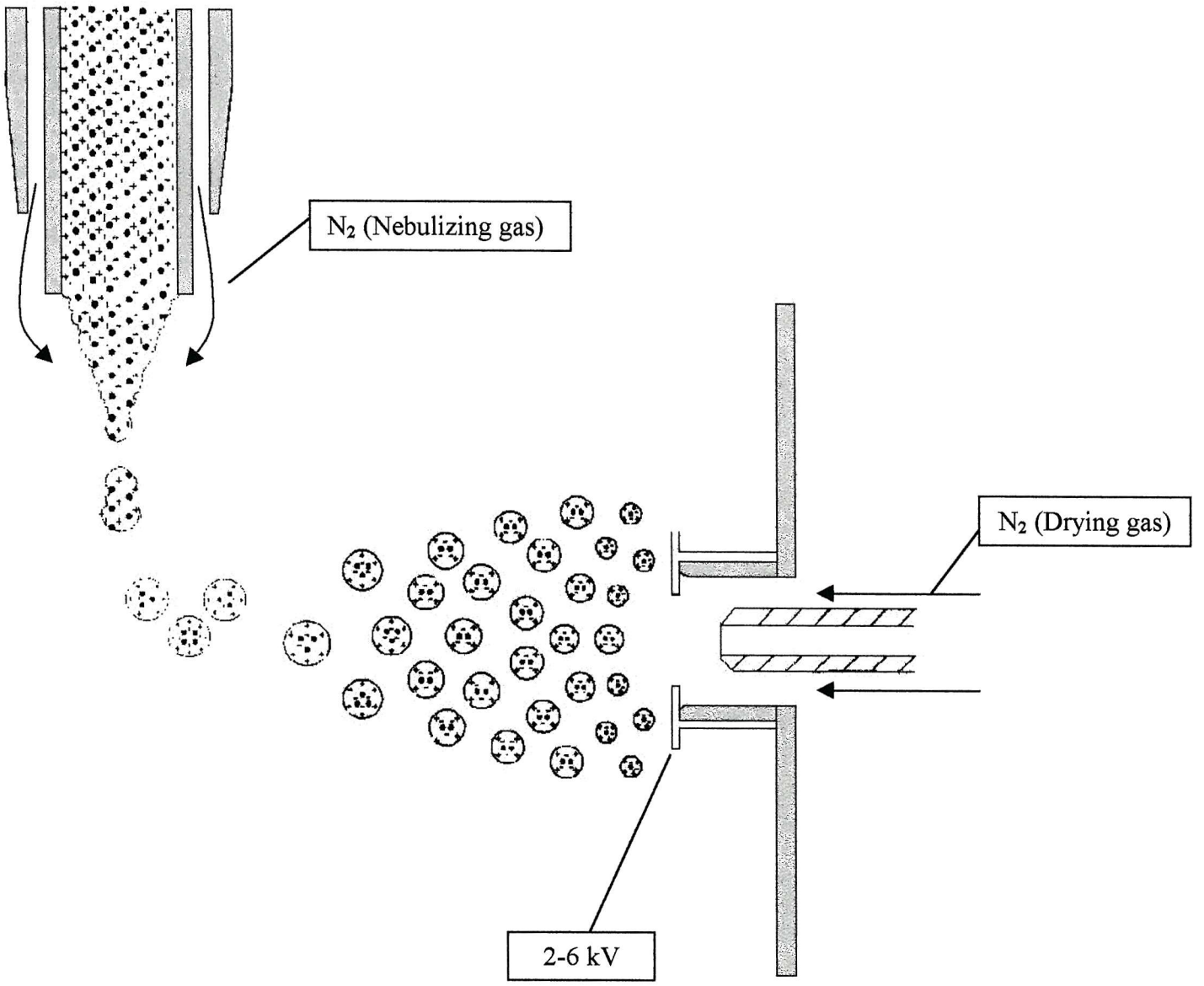

Figure 10.3: The Electrospray process within the spray chamber

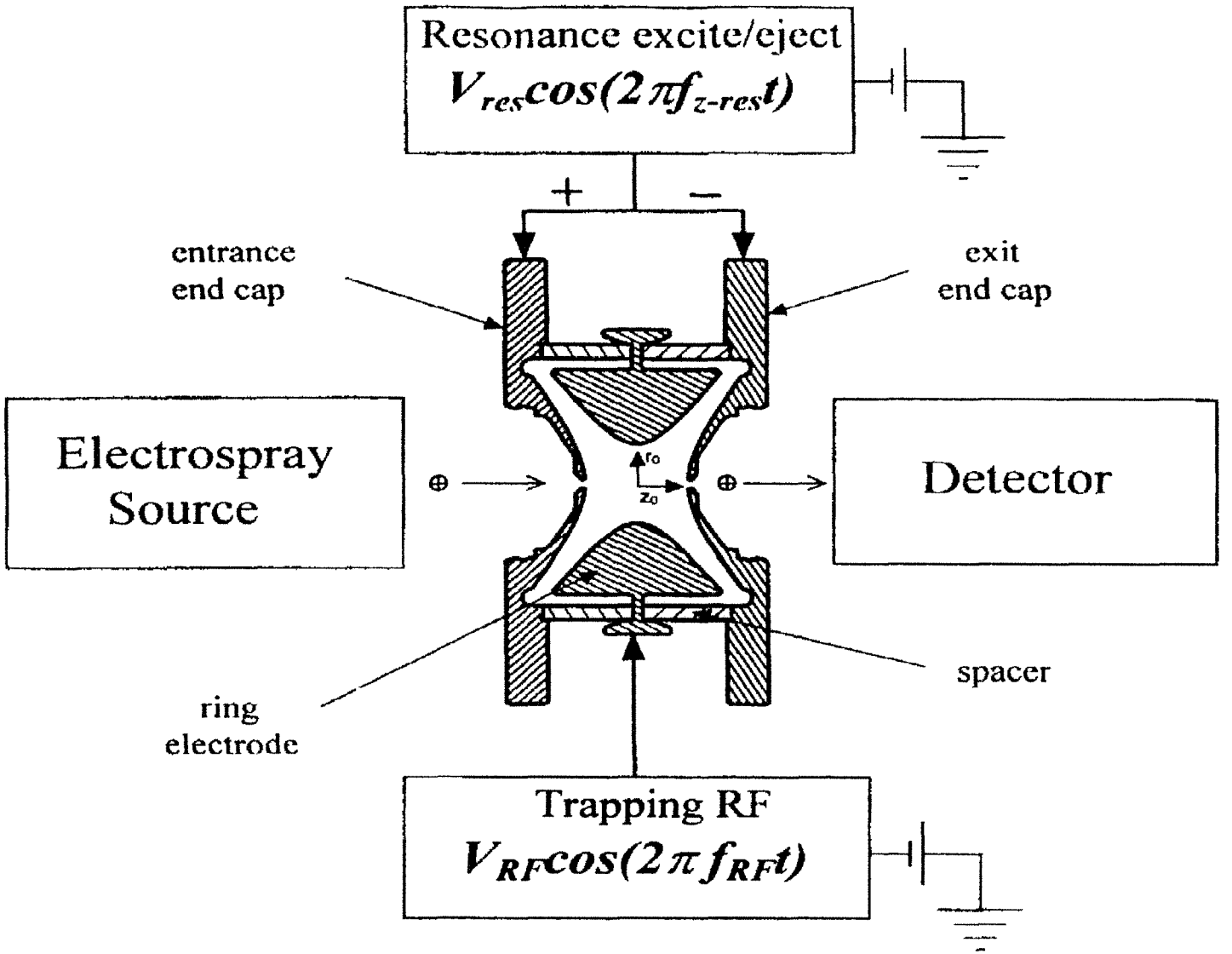

Figure 10.4: The ion trap mass analyser

In the normal mode of use, the end-cap electrodes are connected to earth potential while a radiofrequency (RF) oscillating potential is applied to the ring electrode. The shape of the potential, ϕ, developed within the trap is then given by

$$\phi = \frac{1}{2}(U - V\cos\Omega t)\frac{(x^2 + y^2 + 2z^2)}{r_0^2} + \frac{U - V\cos\Omega t}{2} \qquad \ldots(10.2)$$

where U represents the maximum DC potential and V the maximum RF potential applied between the ring and the end-cap electrodes, Ω is the angular frequency of the RF potential, and r_0 is the internal radius of the ring electrode. Ions injected into the trap by the electrospray source are focused and defocused along the z axis and vice versa in the radial plane by the periodic reversal of this field caused by the oscillation of the RF potential.

The differential equation of motion for a singly charged positive ion is readily obtained from

$$\frac{d^2\vec{r}}{dt^2} = -\frac{e}{m}\nabla\phi \qquad \ldots(10.3)$$

which, in the field given by Eqn 10.2 becomes

$$\frac{d^2u}{dt^2} = \frac{\alpha e}{m(r_0^2 + 2z_0^2)}[U + V\cos(\Omega t)]u \qquad \ldots(10.4)$$

where α=-2 for u=r and α=4 for u=z. This equation is of a similar form to the Mathieu equation[14]

$$\frac{d^2u}{d\xi^2} + (a_u + 2q_u\cos 2\xi)u = 0$$

where

$$\xi = \frac{\Omega t}{2}$$

$$a_z = -2a_x = -2a_y = -\frac{16eU}{m(r_0^2 + 2z_0^2)\Omega^2}$$

and

$$q_z = -2q_x = -2q_y = \frac{8eV}{m(r_0^2 + 2z_0^2)\Omega^2}$$

The a_u and q_u parameters are fundamental to the operation of the ion trap since they determine whether the ion motion is stable (the ions remain trapped) or unstable (the ions escape the trap). Plotting and overlapping the solutions to the Mathieu equation in (a,q) space for the r and z dimensions forms the quadrupole ion trap stability diagram, a portion of which is shown in Figure 10.5.

This diagram defines the areas within which the axial (z) and radial (*r*) components of motion are stable. In this work the analytical use of the ion trap relies upon the *mass-selective ejection* of ions[15]. Of the ions which are injected into the trap by the electrospray source, a range of *m/z* values may be held in stable orbits by virtue of the RF potential. As the amplitude of the RF potential is increased, the motion of the ions becomes progressively more energetic, such that they develop unstable trajectories along the z axis. Then, in order of increasing *m/z* values, the ions exit the device through holes in one of the end-cap electrodes and impinge on a detector. In this way, a mass spectrum is generated. Since q_z is inversely proportional to mass, high mass-to-charge ratio ions have a lower q_z value than low mass-to-charge ions. Therefore the mass-selective instability scan described above may be represented on the instability diagram by progressing across (a_z, q_z) coordinates until the right-hand boundary is reached. From the stability diagram there follows an important consequence: the existence of a cut-off mass. There is always a lowest mass stable in the field, with all other lower masses unstable in the field.

Figure 10.5

Stability diagram for the ion trap plotted in (a_z,q_z) space. The points marked M_1, M_2, and M_3 ($M_1<M_2<M_3$) refer to the (a_z,q_z) coordinates of three ions: M_1 has already been ejected, M_2 is on the point of ejection and the species M_3 is still trapped.

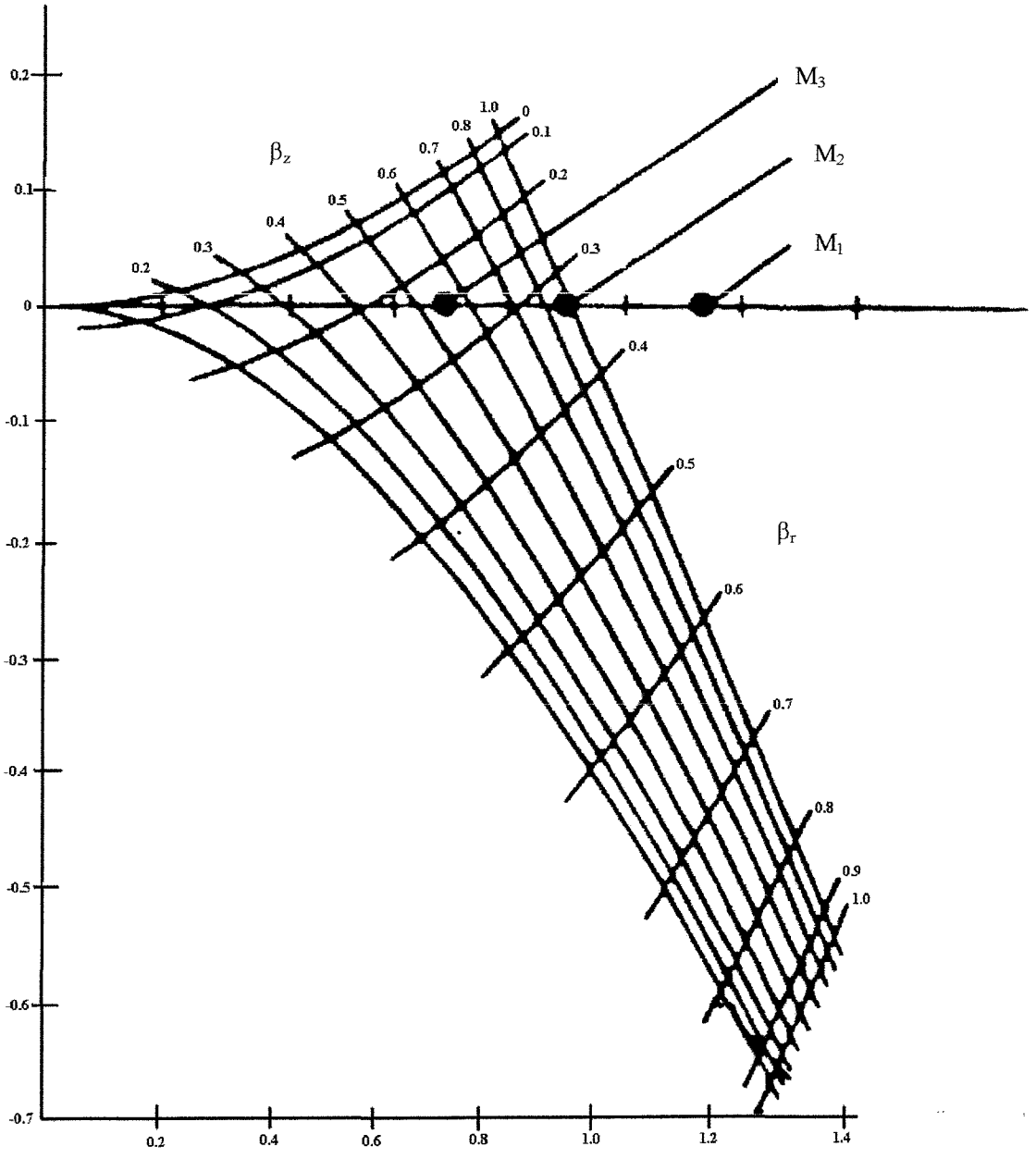

The range of masses that can be stored in the field thus has a lower limit, the cut-off mass. The cut-off mass is determined by the RF level on the ring electrode with its corresponding secular frequency being given by one half of the RF drive frequency. Theoretically, there is no upper limit to the storable mass range. However, for practical purposes and thermal reasons, there is an upper limit. This upper limit is about 20-30 times the cut-off mass; ions with an *m/z* above this limit are not efficiently trapped by the RF field. The lines drawn across the region of stability are known as iso-β lines and describe the detailed trajectories of the ions at each point. These have the general appearance of a Lissajous curve and are of the mathematical form

$$u_0(t) = A_u \sum_{n=-\infty}^{+\infty} C_{2n,u} \cos\left((2n+\beta_u)\frac{\Omega}{2}t\right) + B_u \sum_{n=-\infty}^{+\infty} C_{2n,u} \sin\left((2n+\beta_u)\frac{\Omega}{2}t\right) \quad \textbf{...(10.6)}$$

where A_u and B_u are arbitrary constants and the $C_{2n,u}$ coefficients give the amplitudes of the allowed modes of motion. The magnitude of these coefficients falls off rapidly as n increases so that only trajectories corresponding to n=±1, ±2 are of practical significance. Ions of a specific mass-to-charge ratio have a fundamental frequency, f_h, (h=0) of motion unique to their q_z value which may be calculated from the β_u value. F_h can be expressed in terms of β_u as follows

$$f_h = (hf_{rf} \pm \beta_u f_{rf}/2) \quad \text{...(10.7)}$$

Resolution, peak height, and sensitivity are greatly improved if the mass-selective instability scan mode is supplemented with resonance ejection whereby a dipole signal $[V_{res}\cos(2\pi f_{z-res}t)]$ is applied to the end caps with frequency equal to the fundamental resonant frequency of the ion. The ZOOM scan mode used by the LCQ spectrometer uses this principle in order to eject ions of unwanted *m/z* before the mass-selective instability scan. In this way it is possible to increase the trap concentration of the species of interest, thus enhancing sensitivity.

10.2.3 The Geometry of the LCQ and ESQUIRE Ion Trap Analysers

The discussion in section 10.2.2 is based upon the ion trap geometry defined by Equation 10.8

$$r_0^2 = 2z_0^2 \qquad \ldots(10.8)$$

where r_0 is the internal radius of the ring electrode and $2z_0$ is the closest distance between the two end-cap electrodes. This is known as the *perfect* geometry and is necessary for a purely quadrupole field if one neglects any other disturbances. In the early 1980s, however, researchers at Finnigan Corporation observed that ion traps built with the specific geometry of Equation 10.8 demonstrated poor mass accuracy. Mass assignments were shifted and errors were compound dependent. Although not well understood, Syka[16] has suggested that these mass shifts are due to a difference in ion radial distributions that occur because of the different ion collision cross sections, the high pressure of helium in the trap, and the effects of higher order fields that are caused by field imperfections resulting from the entrance and exit holes. Mass shifts were reduced to negligible deviations by spacing the end caps outward by a factor of $0.11\,z_0$. Syka has proposed that such an alteration of the geometry improves the homogeneity of the quadrupole field near the centre of the trap where the ions are stored. The LCQ spectrometer uses this "stretched" ion trap geometry whereas the ESQUIRE makes use of a "multipole-superimposed" ion trap in which the mainly quadrupolar field has contributions from hexapolar, octapolar and even higher-order fields. The effect is created by a slight change to the angle of the asymptotes associated with the hyperbolic profile formed by the electrodes.

10.2.4 Scan Modes and Sample Preparation

Both spectrometers have the option of automatic gain control (AGC). This method divides the scan function into two stages, known as the *prescan* and the *analytical scan*. A *prescan* is rapid and is used to determine the analytical scan injection time so that space charge effects caused by an over abundance of ions are avoided.

Both the LCQ and the ESQUIRE spectrometers have several different scan modes, the choice of which depends upon the type of species being analysed and the nature of the information that is required. Since this work requires the measurement of adjacent isotopic peaks, it was necessary to operate at high resolution ($m/\Delta m \approx 10{,}000$ at m/z 2000). This is achieved by reducing the scan rate of the QIT and supplementing this scan with an appropriate resonance-ejection voltage (c.f. Equation 10.7).
On the LCQ instrument, the ZOOM mode was used in which an ion-isolation step preceded the main scan function. In order to isolate the ions of interest (with a window of width equal to $10m/z$ centred on the sample mass) a continuous band of frequencies at all β_z values corresponding to the unwanted m/z range is required. In practice a sum-of-sines tailored waveform consisting of many discrete frequencies is simpler to implement and is used by the LCQ. For comparison experiments on the ESQUIRE spectrometer, a very similar isolation step was performed in order to replicate the LCQ ZOOM mode as closely as possible.

The samples were infused at a flow rate of 3 μL/min using methanol:water (50:50 mixture, 0.1% formic acid) as a solvent. The biological samples, Bradikinin (Sigma chemical co., Product no:B3259) and Porcine (Pancreastrin fragment 33-49, Sigma chemical co., Product no:P2919) were prepared with a concentration of 5 pmol/μL. Caffeine was prepared with a concentration of 0.02 mg/mL. All spectra were obtained in the positive ion mode to generate both singly and multiply protonated ions.

The raw data files produced by the spectrometer software were converted into an appropriate format and analysed using the Program "Convert" which was written using Visual Basic 6.

10.3 Theory

Quadrupole ion trap mass spectrometry is capable of resolving $^{13}C/^{12}C$ isotopic profiles for low charge states (+1, +2) of fairly large molecular weight organic compounds (up to ~1800 amu). Clearly if an infinite number of ions are sampled by the ion trap analyser then the relative intensities of the profile components will only fluctuate according to the natural variability of the $^{13}C/^{12}C$ isotope ratio[17]. In a real series of experiments the extent of this fluctuation depends upon the number of ions that are sampled by the ion trap analyser.

Each experiment is considered to involve a sample of size n (unknown) ions from an infinite distribution of ions of which the mean probability (naturally occurring), p_1, p_2,...,p_N of observing each species is known. This then defines a discrete probability distribution for the observed proportions $x_1, x_2, .., x_N$. The probability of observing a particular isotope proportion, P(r) is given by the expression

$$P(r) = {}^{n}C_{r}\, p^{r}(1-p)^{n-r} \qquad \ldots(10.9)$$

where r/n is the observed proportion. These probabilities define a discrete probability distribution customarily called the *binomial distribution*. The probabilities are obtained when the expression

$$1 = [p + (1-p)]^{n} = \sum_{r=0}^{n} {}^{n}C_{r}\, p^{r}(1-p)^{n-r} \qquad \ldots(10.10)$$

is expanded by the binomial theorem. For this application it is more convenient to approximate the binomial distribution so that in any particular experiment the proportion of ions r/n containing a particular isotope will be distributed normally with a mean p and standard deviation, σ, given by :-

$$\sigma = \sqrt{p(1-p)/n} \qquad \ldots(10.11)$$

In order to estimate the value of n the experiment is repeated a large number (500) of times, thus providing an estimate for the standard deviation, σ. Since the mean proportion, p is already known (see below) the absolute number of ions present in the trap can be estimated from the equation

$$n \approx p(1-p)/\sigma^2 \qquad \ldots(10.12)$$

10.4 Results and Discussion

A selection of small haloalcohols were first used to validate the technique. These were chosen so that strong isotopic patterns were exhibited in the mass spectrum. Figure 10.6 shows the mass spectrum obtained from a solution of chloroethanol using methanol/water (50:50 mixture) as a solvent. Chloroethanol is first protonated and then looses a water molecule yielding $ClCH_2CH_2^+$.

$$ClCH_2CH_2OH + H_3O^+ \rightleftharpoons ClCH_2CH_2OH_2^+ + H_2O$$

$$ClCH_2CH_2OH_2^+ \overset{-H_2O}{\rightleftharpoons} ClCH_2CH_2^+$$

The spectrum shows the expected[18] ~3:1 ratio of the $Cl^{35}CH_2CH_2^+$ and $Cl^{37}CH_2CH_2^+$ species. The statistical method described in section 10.3 was used to calculate the absolute number of trapped ions for a series of AGC values. The result of this experiment is shown in Figure 10.7. The error bars associated with this data were deduced from five repeated experiments at each point. Other data (not shown) were also collected with the AGC facility disabled. It was found that the AGC facility did not affect the number of trapped ions since very similar numbers were calculated for corresponding ion injection times in each mode. As expected the number of trapped ions increases linearly with AGC value. The data point at AGC=5e7 corresponds to a spectral signal-to-noise ratio of approximately 3:1, which would conform with previous definitions of detection limits in mass spectrometry. At greater AGC values than AGC=9e7, space charge effects begin to broaden the individual ion peaks and thus it is not possible to monitor the individual isotopes.

Having successfully applied the technique to chloroethanol, the next experiments involved the use of larger organic molecules and in particular the more practically relevant small peptides and protein fragments. Figure 10.8 shows the mass spectra obtained using solutions of (i) caffeine, (ii) the +2 charge state of bradikinin and (iii) the +2 charge state of Porcine. As was the case for chloroethanol the AGC facility did not affect the number of trapped ions. Figure 10.9 shows the number of ions determined at a series of injection times using (i) caffeine and (ii) porcine on the LCQ spectrometer. Again the plots cover the complete dynamic range for detection of these ions.

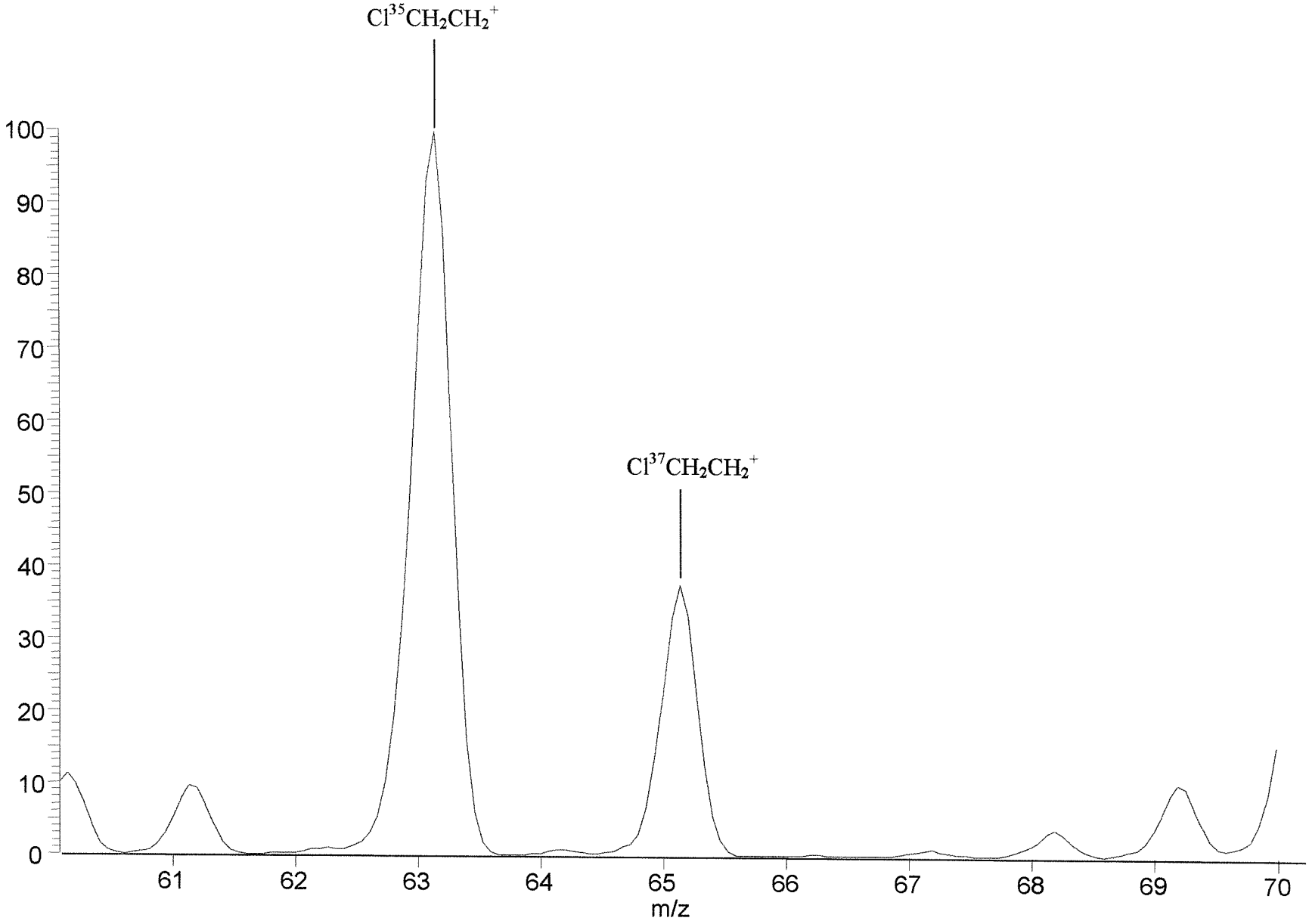

Figure 10.6: Mass spectrum obtained using Chloroethanol in Methanol/Water (50:50)

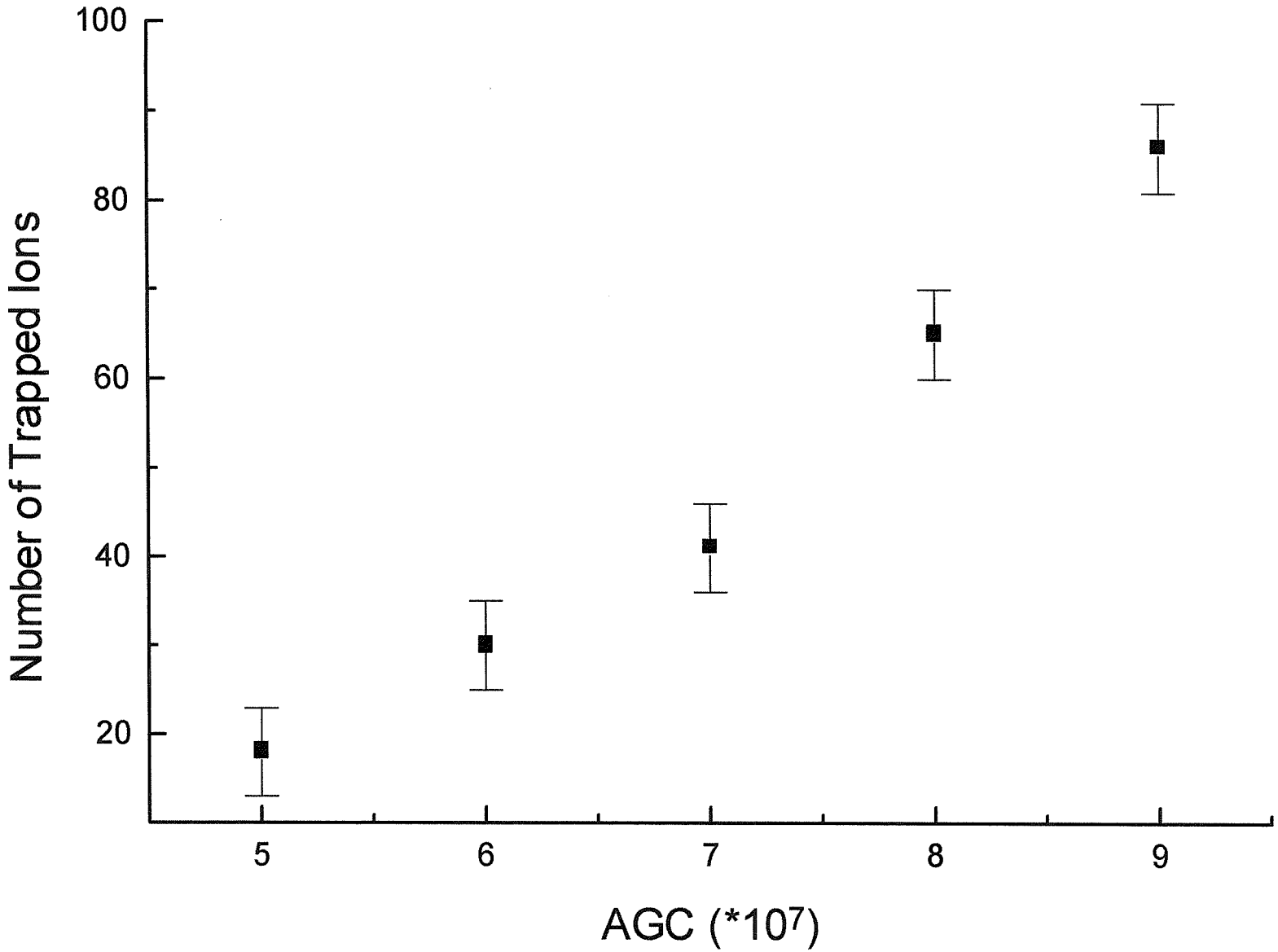

Figure 10.7: Chloroethanol on the LCQ

Figure 10.8(i): Caffeine

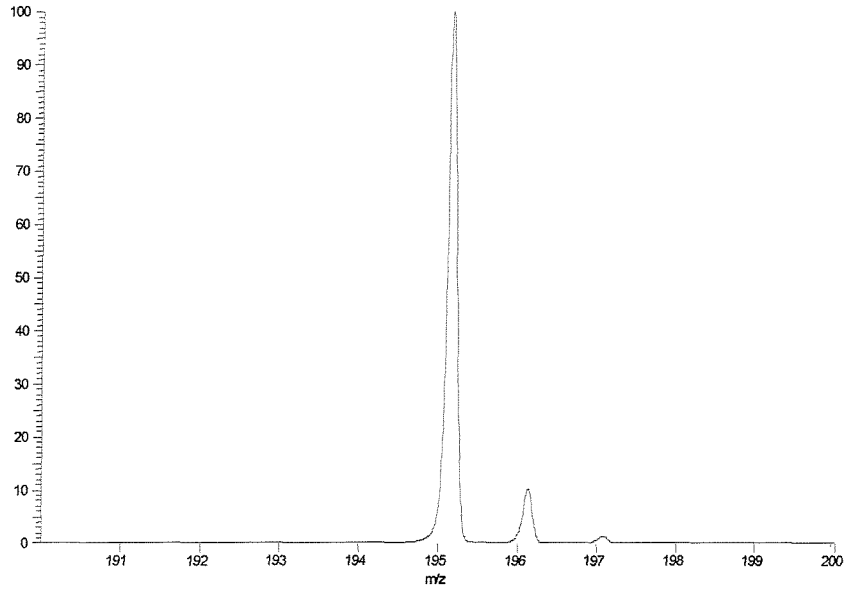

Figure 10.8(ii): Bradikinin

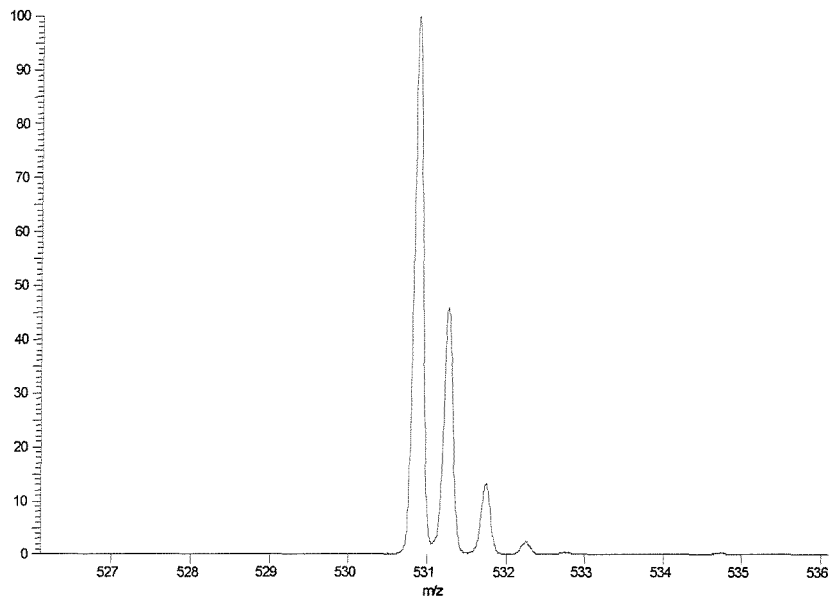

Figure 10.8(iii): Porcine

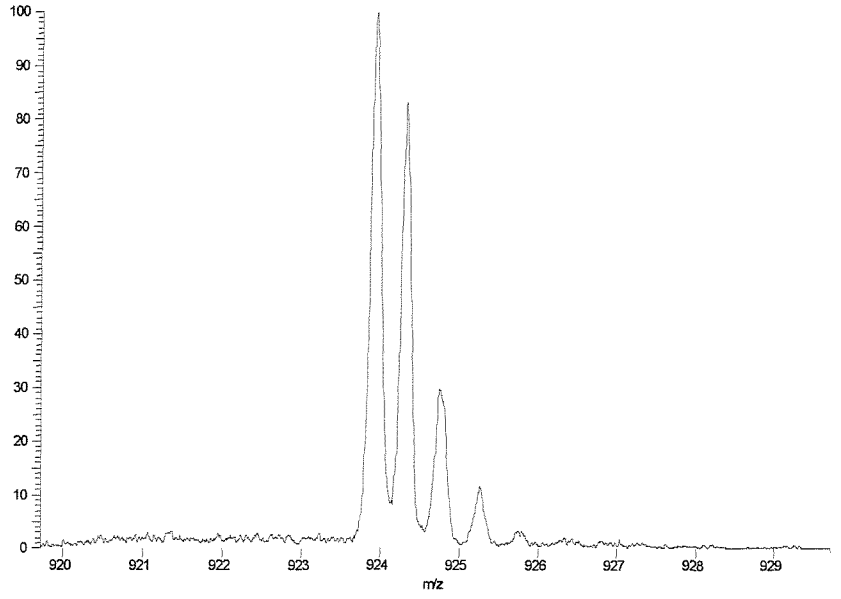

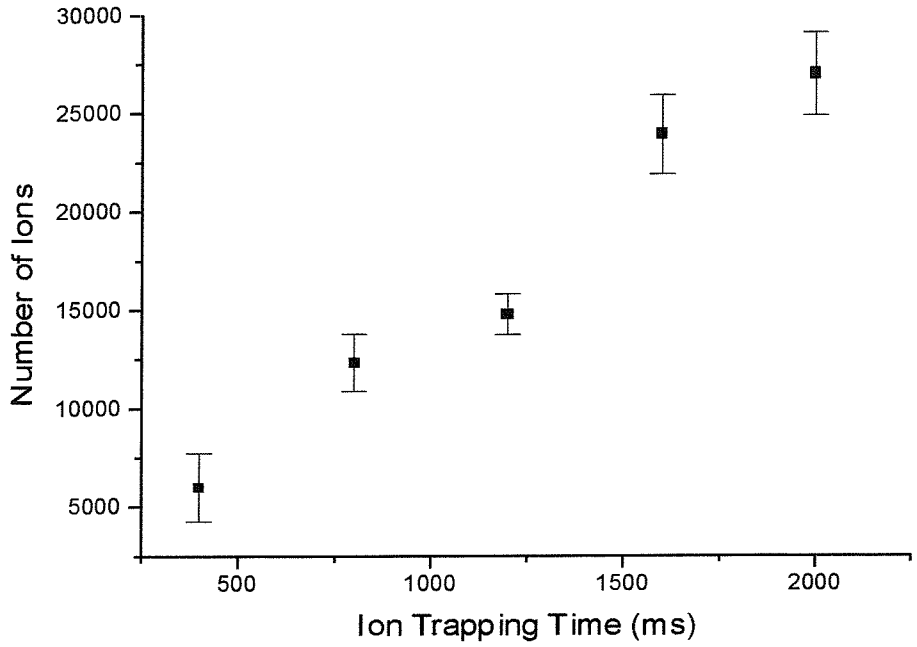

Figure 10.9(i): Caffeine

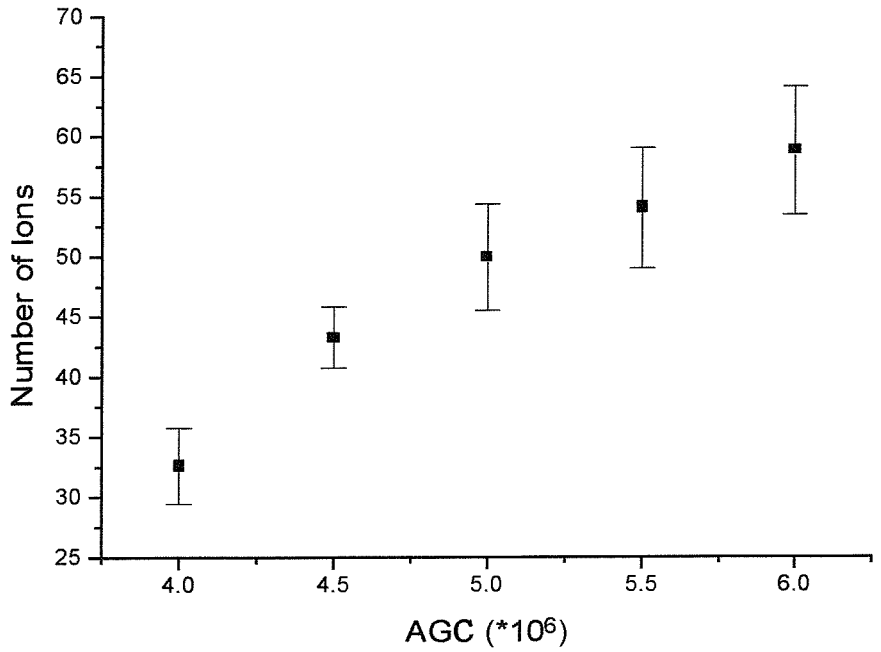

Figure 10.9(ii): Porcine

It is clear that a much greater number of caffeine ions than porcine ions can be detected whilst still being able to resolve the individual isotopes in the mass spectrum. This is presumably a consequence of the much smaller caffeine ions occuying less space in the trap.

The trapping efficiencies of the LCQ and ESQUIRE spectrometers, using the (+2) charge state of Bradikinin are compared in Figure 10.10. It would seem that more detectable ions are trapped by the LCQ than the ESQUIRE for the same ion injection times. The most likely explanation for this difference would seem to be the contrasting electrospray ion source designs used by the two different instruments. Amongst other differences, the nebulizer spray on the ESQUIRE is directed at right angles to the sampling capillary whereas the LCQ directs the spray straight at the capillary. Also the modifications of the *perfect* ion trap geometry, introduced to improve mass accuracy, are different for the two spectrometers (see X.3). The injected ions would therefore be expected to experience contrasting field strengths and shapes when they enter the trap. In a recent study by Quarmby *et.al*[19], a model for the process by which injected ions are trapped was developed using SIMION v6.0 to simulate the electrostatic field within the LCQ ion trap. A similar model, with parameters chosen to simulate the ESQUIRE ion trap, may provide some insight as to the apparent difference in trapping efficiency of the two spectrometers.

10.4 Conclusions

A statistical method for the determination of the absolute number of trapped ions in a quadrupole ion trap mass spectrometer is demonstrated. As expected the results vary according to the species of interest and experimental conditions used. Comparisons between the LCQ and ESQUIRE spectrometers are inconclusive. The difference in trapping efficiencies inferred from the preliminary data could be due to a number of factors such as ionization source design or discrepancies in the extent of kinetic energy damping which occurs on injection into the trap. In order to investigate this further additional data needs to be collected using an extensive *m/z* range of compounds on each instrument. A theoretical model to simulate the injection and storage of ions in the ESQUIRE ion trap would also be an advantage.

Figure 10.10: Comparison between LCQ and ESQUIRE Spectrometers using Bradikinin (+2)

(i) LCQ

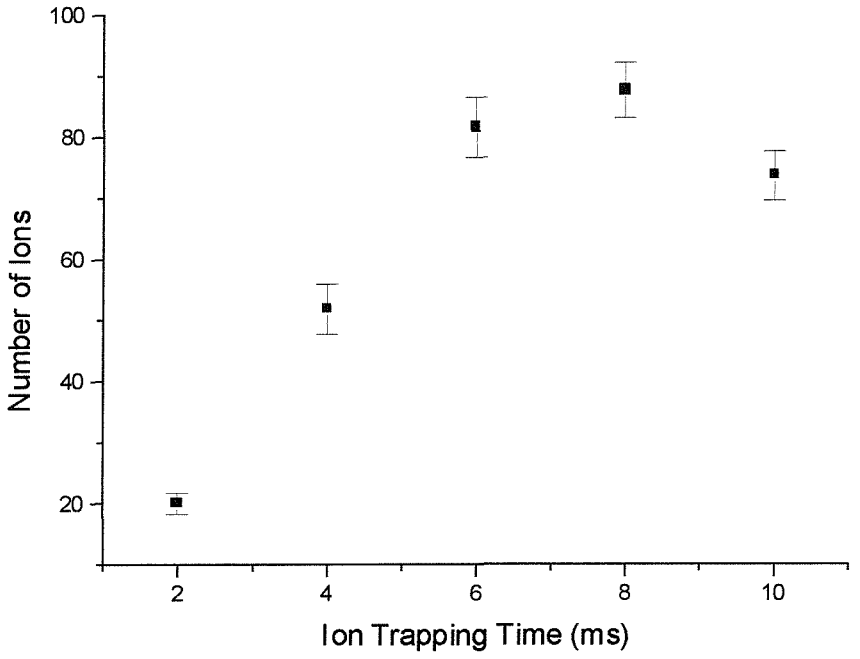

(ii) ESQUIRE

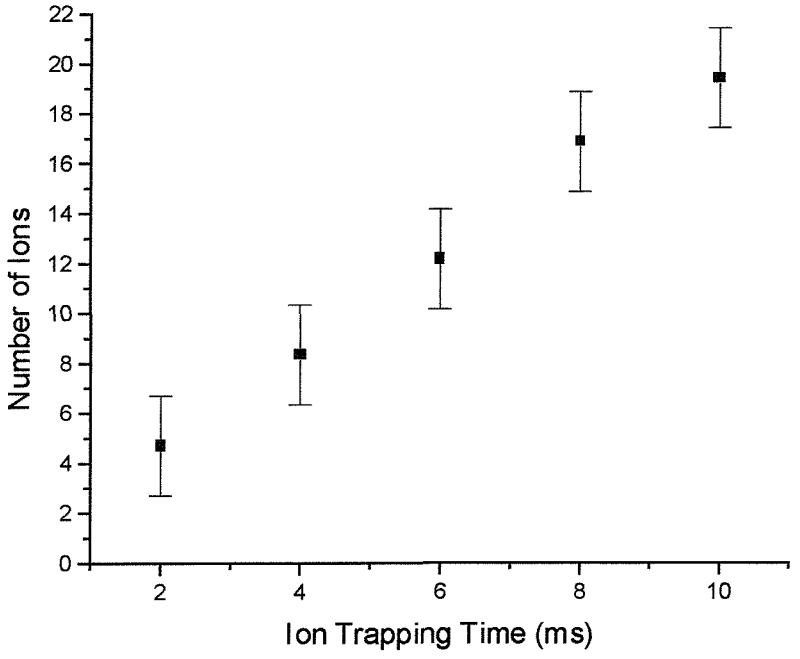

10.5 References

1. M. Dole, L. L. Mach, R. L. Hines, R. C. Mobley, L. D. Ferguson, M. B. Alice. *J. Chem. Phys.* **49**, 2240 (1968).

2. J. B. Fenn, M. Mann, C. K. Meng, S. F. Wong. *Mass Spectrom. Rev.* **9**, 37 (1990).

3. W. Paul, Z. Steinwedel. *Z. Naturforsch.* **8a**, 448 (1953).

4. W. Paul, H. Steinwedel. *Z. Naturforsch.* **104**, 672 (1956).

5. G. J. Van Berkel, G. L. Glish, S. A. McLuckey. *Anal. Chem.* **63**, 1284 (1990).

6. M. A. Moseley, J. W. Jorgenson, J. Shabanowitz, D. F. Hunt, K. B. Tomer. *J. Am. Soc. Mass. Spectrom.* **3**, 289 (1992).

7. T. M. Sack, D. A. McCrery, M. L. Gross. *Anal. Chem.* **57**, 1290 (1985).

8. R. L. Hunter, M. G. Sherman, R. T. McIver. *Int. J. Mass Spectrom. Ion Phys.* **50**, 259 (1983).

9. R. T. McIver, R. L. Hunter, E. B. Ledford, M. J. Locke and T. J. Francl. *Int. J. Mass Spectrom. Ion. Phys.* **39**, 65 (1981).

10. P. A. Limbach, P. B. Grosshans and A. G. Marshall. *Anal. Chem.* **65**, 135 (1993).

11. M. W. Senko, S. C. Beu and F. W. McLafferty. *J. Am. Soc. Mass.Spectrom.* **6**, 229 (1995).

12. R. E. March, J. F. J. Todd, *Practical Aspects of Ion Trap Mass Spectrometry*, CRC, New York, (1995).

13. R. E. March, H. E. Hughes, *Quadrupole Storage Mass Spectrometry*, Wiley, New York, (1989).

14. E. Mathieu, *J. Math. Pure Appl.* **13**, 137 (1868).

15. G. C. Stafford, P. E. Kelley, J. E. P. Syka, W. E. Reynolds, J. F. J. Todd. *Int. J. Mass Spectrom. Ion. Proc.* **60**, 85 (1984).

16. *Practical Aspects of Ion Trap Mass Spectrometry*; R. E. March, J. F. Todd. Eds, CRC Press, Boca Raton, Fl, 1995, Vol. 1, Ch. 1.

17. R. C. Beavis, *Anal. Chem.* **65**, 496 (1993).

18. *Handbook of Chemistry and Physics,* CRC Press (1977).

19. S. T. Quarmby and R. A. Yost, *Int. J. Mass. Spec,* **190/191**, 81 (1999).

CHAPTER 11: CONCLUSIONS AND FURTHER WORK..

Chapter 11: Conclusions and Further Work

The aim of the work presented in this thesis was to study unstable species in the gas phase using spectroscopic methods. This objective has been achieved through two separate studies: the investigation of various Rg·NO complexes using REMPI spectroscopy; and the study of OH and $O_2(a^1\Delta_g)$ using photoelectron spectroscopy with a synchrotron radiation source. A further aim was to devise a method to determine the number of ions contained in a quadrupole ion trap mass spectrometer.

11.1 Photoelectron spectroscopy of short-lived molecules using synchrotron radiation

In terms of the synchrotron studies on $O_2(a^1\Delta_g)$ and OH, constant ionic state spectra (CIS) of these molecules reveal for the first time a complex array of autoionising Rydberg states that exist within these systems at excitation energies below 20 eV. CIS spectroscopy has been shown to be an effective complement to photoionisation efficiency studies by allowing autoionisation to be examined as a function of the final ionic state vibrational level. Also, photoelectron spectra of OH and $O_2(a^1\Delta_g)$ have been recorded at photon energies in resonance with autoionisaing transitions observed in the CIS spectra, with the enhanced vibrational structure observed providing improved values for the constants ω_e and $\omega_e x_e$ in the ground ionic states. The study of OH extended previous synchrotron PES work on reactive intermediates produced by microwave discharge of a flowing gas mixture[1,2,3] to the study of a short-lived molecule produced by an atom-molecule reaction.

There are a number of refinements to the spectrometer that could be made to further enhance this work. The installation of a multichannel detector should allow samples with low partial pressures or photoionisation cross-sections to be studied. This would also allow the rapid collection of frames of data, so that signal stability should become less critical in CIS spectra. This will require new software to be written, to control the mutidetector. Given sufficient signal stability, it may also be possible to obtain two-dimensional photoelectron spectra, which have been shown to provide a detailed picture of autoionisation in small molcules[4]. The incorporation of ion detection, such as by a quadrupole mass spectrometer or a time-of-flight mass analyser, would permit not only the identification of all species in the ionisation region, but also the performance of photoelectron-photoion coincidence (PEPICO) measurements.[5] Such an experiment would distinguish between overlapping

photoelectron signals that arise from ionisation of different species, which are a common problem in PES.

Despite the success of these studies, none of the molecules can be said to have been completely characterised in the process. Many of the assignments of CIS resonances are tentative, owing to the complicated or weak spectra; in a few cases it might be useful to record these spectra again, under improved conditions (such as with the multichannel detector installed) to confirm or challenge the analyses presented in this thesis. The proposed improvements to the spectrometer should allow the resolution of many of the uncertainties in the spectra obtained in this project, and should prevent the same problems from occurring in future investigations.

Several short-lived species may be produced by the fluorine abstraction method, such as CH_3 from $CH_4 + F$[6]. The reactants and by-products of such mixtures can present several problems, such as contamination of the spectrometer and spectral congestion, but useful information could be obtained from a successful experiment. Other production methods, such as pyrolysis of a solid sample, or laser photodissociation, could also be attempted, but these also have experimental obstacles that must be overcome.

Having established the viability of the method, the future lies in extending it from diatomic studies published so far[1,2,3,7] to other species produced by atom-molecule reactions, in particular polyatomic molecules. Recent successful work on the angle resolved photoelectron spectroscopy of $O_2(a^1\Delta_g)$[8], means that both the dynamic variables, partial cross sections and photoelectron angular distributions, can now be measured. This information should lead to a detailed understanding of the photoionization process for short-lived molecules in the future.

11.2 REMPI Spectroscopy of rare gas-NO complexes and $(CO)_2$

The structure and bonding of Ar·NO and Kr·NO have been studied using REMPI spectroscopy. The main aim was to characterize the $\widetilde{E}^2\Sigma^+$ state of these complexes in order to facilitate a ZEKE study of $Ar{\cdot}NO^+$ and $Kr{\cdot}NO^+$ using the $\widetilde{E}^2\Sigma^+$ state as the resonant intermediate state. The two-photon $\widetilde{E}^2\Sigma^+ \leftarrow \widetilde{X}^2\Pi$ transition in Ar·NO and Kr·NO has been studied using one-colour REMPI spectroscopy. The (2+1) REMPI spectra were recorded

and then simulated using a rigid rotor model[9] in which relative intensities are calculated in terms of the non-vansishing tensor components of the two-photon absorption operator associated with the corresponding transition in uncomplexed NO. The resolution of the REMPI spectra of Ar·NO and Kr·NO recorded in this work was not sufficient to resolve transitions associated with end-over-end rotation of the complex, and the neglect of this rotational motion in the model, therefore, was not a significant problem.

Analysis of the (2+1) REMPI spectra of Ar·NO and Kr·NO indicated larger dissociation energies and significant deviations from the T-shaped geometry found in the ground and $\tilde{A}^2\Sigma^+$ state of the complexes. The interpretation given for these differences is that in the $\tilde{E}^2\Sigma^+$ state the radius of the Rydberg electron orbit is greater than the diameter of the Rg atom and so a charge-induced dipole interaction dominates, similar to $Rg{\cdot}NO^+$, whereas for the ground and lower electronic states the Rg atom lies outside the Rydberg electron radius and the charge of the NO^+ core is screened.

As mentioned previously, it is hoped that the work presented in this thesis on the $\tilde{E}^2\Sigma^+$ state of Ar·NO and Kr·NO will be valuable to the future interpretation of ZEKE spectra of the corresponding cations. Takahashi used a (2+1′) REMPI process to perform ZEKE experiments on Ar·NO using the $\tilde{C}^2\Pi$ state as a resonant level[10], and (1+1′) ZEKE experiments have been performed in Southampton using the $\tilde{A}^2\Sigma^+$ state as an intermediate level[11]. It is clear from those two experiments that ZEKE experiments via the $\tilde{A}^2\Sigma^+$ state yield information on the high-lying vibrational levels of the $Ar{\cdot}NO^+$ cation, whereas those via the $\tilde{C}^2\Pi$ state yield information regarding the low-lying levels. This arises since the intermolecular bond length of the $\tilde{A}^2\Sigma^+$ state is >4.5 Å, whereas in the cation it is *ca.* 3 Å; on the other hand the $\tilde{C}^2\Pi$ state has a bond length closer to that of the cation. In general, therefore, it may be anticipated that using different electronic states as resonant states in ZEKE experiments will yield information on a wide range of vibrational levels of the $Rg{\cdot}NO^+$ ions. There are four main areas in which to extend the work already performed on the electronic and photoelectron spectroscopy of Rg·NO complexes:

(i) to study higher-lying Rydberg states, thus investigating the convergence of these to those of the cation

(ii) to use different resonant vibronic levels to record ZEKE spectra, to give more information on the cations of the $Rg{\cdot}NO^+$ species

(iii) to continue the previous *ab initio* studies of the Southampton group[12] in order to produce accurate potential energy surfaces, and to calculate accurate rovibronic levels of the cations. These potential energy surfaces will be very anharmonic, owing to the weakly-bound nature of these species, and will prove a useful test for the theoretical techniques involved.

(iv) To identify the REMPI spectra of electronic states which are valence, rather than Rydberg in character, and to identify the lowest electronic state, corresponding to the $2p\sigma^* \leftarrow 2p\pi^*$ transition.

A natural extension of the work on the Rg·NO complexes is to study NO·X complexes, where the ligand X is an atmospherically important species (e.g. H_2O, CO_2, N_2, O_2, CH_4. This work will provide accurate data (vibrational frequencies of the corresponding cations, and adiabatic ionization energies), which can be combined with *ab initio* results to yield enthalpies, entropies and free energies of formation and reaction which may be input into thermodynamic cycles, yielding enthalpies of ligand-switching and clustering reactions. Recently the Southampton group reported an observation of the $\tilde{A}^2\Sigma^+ \leftarrow \tilde{X}^2\Pi$ transition in $NO{\cdot}N_2$. As was explained in Chapter 8, the analysis of this spectrum is hindered by the presence of several isomers in the ground state separated by fairly small energy barriers[13]. It may be necessary to gather information on the ground state using 'ion dip' or 'hole burning' experiments (see chapter 8) before a detailed analysis of the REMPI spectrum can be attempted.

Preliminary results were presented for the (2+1) REMPI spectrum of the $X^1\Sigma^+ + C^1\Sigma^+ \leftarrow X^1\Sigma^+ + X^1\Sigma^+$ transition of the CO dimer. The observed band origin allowed the dissociation energy in the upper state to be estimated as 6300 cm^{-1}. Two progressions in the spectrum were assigned as being due to the symmetric stretching and symmetric bending vibrations. In order to provide a more detailed interpretation of the spectrum it will be necessary to establish a better understanding of the structure and dynamics of the species in its ground state.

At present the MPI apparatus is being redesigned to separate the molecular beam production apparatus from the high voltage ion lens region. This is necessary, as arcing occurs between the pulsed valve and the kV voltages on the ion lens, causing massive disruption of the ion signals. Thus, there will be a preskimmer chamber, containing the pulsed valve, separated by a skimmer from the ionization chamber, which will contain the electron and ion optics and microchannel plate detectors. Turbomolecular pumps will be used as opposed to the oil diffusion pumps on the present apparatus since this will remove any contamination of the time-of-filght spectrum by background oil signals (large hydrocarbons) which have hampered the detection of weak signals in the past. The pumping system will also have increased capacity, allowing work at high gas pulse repetition rates (> 10 Hz), without stalling the pumps, as presently occurs.

11.3 Determination of the number of ions in a quadrupole ion trap mass spectrometer

A statistical method for the determination of the absolute number of trapped ions in a quadrupole ion trap mass spectrometer was demonstrated. As expected the results varied according to the species of interest and experimental conditions used. Comparisons between the two different models of spectrometer (LCQ and ESQUIRE) prooved inconclusive. In order to extend this work, additional data neeeds to be collected using a greater *m/z* range of compounds on the different instruments.

11.4 References

1. J. M. Dyke, D. Haggerston, A. Morris, S. Stranges, J. B. West, T. G. Wright and A. E. Wright, *J. Chem. Phys.* **106**, 821 (1997).

2. J. M. Dyke, S. D. Gamblin, D. Haggerston, A. Morris, S. Stranges, J. B. West, T. G. Wright and A. E. Wright, *J. Chem. Phys.* **108**, 6258 (1998).

3. J. D. Barr, A. DeFanis, J. M. Dyke, S. D. Gamblin, A. Morris, S. Stranges, J. B. West, T. G. Wright and A. E. Wright, *J. Chem. Phys.* **109**, 2737 (1998).

4. A. A. Cafolla, T. Reddish and J. Comer, *J. Phys. B: At. Mol. Opt. Phys.* **22,** L273-L278 (1989).

5. J. H. D. Eland, *Int. J. Mass Spectrom. Ion Phys.* **8**, 143-151 (1972).

6. A. R. Ellis, PhD Thesis, University of Southampton (1985).

7. J. D. Barr, A. DeFanis, J. M. Dyke, S. D. Gamblin, N. Hooper, A. Morris, S. Stranges, J. B. West and T. G. Wright, *J. Chem. Phys.* **110**, 345 (1999).

8. L. Beeching, A. DeFanis, J. M. Dyke, S. D. Gamblin, N. Hooper, A. Morris and J. B. West, *J. Chem. Phys.* **112**, 1707 (2000)

9. P. D. A. Mills, C. M. Western and B. J. Howard, *J. Phys. Chem.* **90**, 3331 (1986).

10. M. Takahashi, *J. Chem. Phys.* **96**, 2594 (1992).

11. A. M. Bush, J. M. Dyke, P. Mack, D. M. Smith and T. G. Wright, *J. Chem. Phys.* **108**, 406 (1998).

12. E. P. F. Lee, P. Soldán and T. G. Wright, *J. Phys. Chem. A.* **102**, 6858 (1998).

13. E. P. F. Lee, *Private Communication.*